Unified approach to jet installation noise using mathematical modelling and spectral analysis of jet turbulence

Sarah A. Stirrat

This thesis is submitted in partial fulfilment for the degree of
Doctor of Philosophy (PhD)
at the University of Strathclyde

February 2024

This thesis is the result of the author's original research. It has been composed by the author and has not been previously submitted for examination which has led to the award of a degree.

Signed: Sarah Stirrat

Date: 28/11/23

Abstract

The acoustic analogy has been used as a method of jet noise prediction for several decades. Goldstein's generalised acoustic analogy showed that jet noise can be formulated as the product of a spectral tensor which contains the jet turbulence statistics and the propagator which controls how the acoustic waves propagate to the far field. In this approach the turbulence enters through the spectral tensor (linearly related to the space-time Fourier transform of the Reynolds stress auto-covariance). The Afsar et al (2011) formulation for heated jets in axisymmetric turbulence showed that the generalised analogy can be related to 11 independent components of the spectral tensor.

The main objective of this thesis is to carry out a detailed numerical analysis of the turbulence statistics using LES of four jets. We investigate various turbulence approximations in the spectral tensor model and its impact on acoustic predictions. Our aim is to discover whether universality of turbulence scales exists across Mach number and jet temperature ratio. We found that for jet noise predictions, universality was confirmed across acoustic Mach number, when the jet temperature ratio was fixed. Notably, universality was also found across jet temperature ratio at the peak frequency ($St = 0.2, \theta = 30$). We also find several approximations can be made in the spectral tensor calculation to reduce computational complexity.

This thesis also considers edge noise, utilising parallel programming across a graphic processor unit to increase computational speed of the predictions as well as improved analytical modelling including optimisation to obtain more accurate acoustic predictions across a range of subsonic Mach number. These results are then combined with the jet noise results to investigate installation effects.

Acknowledgements

Firstly, I would like to thank my supervisor Dr Zamir Koshuriyan for not only giving me the opportunity to undertake this PhD but also for his guidance and support throughout this journey. Without your encouragement and sharing your technical knowledge this PhD would not have been possible.

I would also like to thank my second supervisor Dr Edmondo Minisci for the valuable discussions regarding the optimisation aspect of this thesis. Thanks also go to Dr Ioannis Kokkinakis for his guidance and support in the GPU parallelisation area of this project. Your enthusiasm for computing motivated me greatly in the first year of my PhD journey.

I would also like to thank Dr Adrian Sescu from Mississippi State University who invited me to the university and gave me much appreciated support and guidance while I was there. Thank you for giving me the use of your LES code and sharing your technical knowledge.

This PhD would not have been possible without the financial support from EPSRC who funded this PhD project. My research visit to Mississippi State University would not have been possible without the Rebecca Fraser scholarship which I received from Mr Colin McLatchie, the Amelia Earhart Fellowship from Zonta International, the JM Lessells travel scholarship from the Royal Society of Edinburgh and funding from the Scottish International Education Trust. Thank you all, I greatly appreciate the support.

I would like to thank my friends, Gemma and Tish. I appreciate all the times you have listened to me and supported me despite the distance between us. Speaking with you both has never failed to cheer me up.

Lastly, I would like to thank my family. None of this would have been possible without your unwavering support of me throughout the years. You have seen me through the ups and downs, encouraged me to not give up and listened to all my worries. Thank you for always believing in me.

Contents

List of Figures

List of Tables

Nomenclature

List of Abbreviations

CAA Civil Aviation Authority

CFD Computational fluid dynamics

DE Differential evolution

DNS Direct numerical simulations

$FW-H$ Ffowcs Williams-Hawkings

GA Genetic algorithm

$ICAO$ International Civil Aviation Organisation

$IDEA$ Inflationary differential evolution algorithm

LES Large eddy simulation

LHS Left hand side

MBH Monotonic basin hopping

$MP-AIDEA$ Multi-population adaptive inflationary differential evolution algorithm

$OASPL$ Overall sound pressure level

PSO Particle swarm optimisation

RHS Right hand side

SPL Sound pressure level

tke Turbulent kinetic energy

WHO World Health Organisation

List of Symbols

$\boldsymbol{\eta}$ Spatial separation

$\Delta^{(m)}$ Dispersion relation

ϵ Rate of dissipation

γ Specific heat ratio

λ Wavelength

μ_∞ Dynamic viscosity

$\Phi^*_{\nu j \mu l}$ Acoustic spectral tensor

ψ Azimuthal coordinate

$\Psi^*_{\nu j \mu l}$ Physical spectral tensor

ρ Density

τ Temporal separation

τ Time (jet)

τ_{ij} Stress tensor

θ Far field angle of the observer

B Velocity decay constant

c Speed of sound

c_∞ Speed of sound in the far-field

D_j Jet diameter

E Total energy

f Frequency

G_μ Adjoint Green's function

H Step function

h Enthalpy

h_0 Stagnation enthalpy

$H_m^{(1)}$ Hankel transform

I Acoustic spectrum

$I^{[1]}$ Acoustic spectrum (Momentum-flux)

$I^{[2]}$ Acoustic spectrum (Coupling)

$I^{[3]}$ Acoustic spectrum (Enthalpy-flux)

$J^{(m)}$ Invariant

k Turbulent kinetic energy

k_1 Streamwise wavenumber

k_∞ Thermal conductivity

L_R Rayleigh operator

M Eddy convection Mach number

m Mode

$M_j = U_j/c_0$ Jet Mach number

$Ma = U_j/c_\infty$ Acoustic Mach number

p Pressure

Pr Prandtl number

r Radial coordinate

$R_{\nu j \mu l}$ Reynolds stress

Re Reynolds number

S Spread rate

$St = fD_j/U_j$ Strouhal number

T Temperature

t Time (far-field)

TR Temperature ratio of jet compared to ambient air

U Streamwise meanflow velocity

U_c Convective velocity

U_j Jet velocity

v_i Velocity

$W(w_1^{(m)}, w_2^{(m)})$ Wronskian

$w_1^{(m)}, w_2^{(m)}$ Linearly independent homogeneous solutions to a Sturm-Liouville problem

x_i Observer (far-field) coordinates

y_1 Streamwise coordinate

y_i Source (jet) coordinates

Chapter 1

Introduction

1.1 Motivation for Research

Aircraft noise has been recognised as a significant problem since the advent of the jet engine in the mid twentieth century. The jet engine was much noisier than the preceding propeller engines and at this time flight became more commonplace which further exasperated the problem.

Currently, over one million people in the UK are exposed to aircraft noise which exceeds World Health Organisation (WHO) limits over a 24-hour period and the health impacts relating to this, such as hearing loss and cardiovascular disease [1], are estimated to cost the government £540 million each year [2]. Furthermore, the WHO estimate that 1 million healthy-life years are lost in Western Europe alone due to environmental noise (aviation noise being the biggest source), with cardiovascular disease contributing to the majority of these deaths [3].

Aircraft noise is naturally a larger issue close to busy airports, for example, Heathrow airport impacts more people than any other European airport, and is classed as 'significantly annoying' by the UK Civil Aviation Authority (CAA) [4]. This will only worsen as airports expand, for example, in 2020 Tokyo Haneda airport adjusted flight paths to increase the number of flights by 50 per day, this has resulted in an increase of 10dB, resulting in 80dB aircraft noise in certain areas, which could have ill effects on health [5]. If the London Heathrow airport expansion goes ahead, which Heathrow CEO John Hollad-Kaye believes it will [6], an estimated 2.2 million people will be exposed to increased aircraft noise

[7]. Although Heathrow is a large contributor to the UK economy, increased noise pollution has been linked to cognitive impairment and behavioural issues in children, sleep disturbance, obvious hearing damage and other consequent health issues [1].

Covid-19 disrupted the aviation sector in 2020, bringing a halt to domestic and international flights. Its impact is still being felt three years later with continued reduction in demand [8]. However, forecasts predict there could be bounce-back within this decade with 2.5 million additional flights by 2029 in Europe alone [8]. Therefore jet noise control remains a high priority in aviation.

Over the last few decades a vast amount of research in the area in combination with tightening airport regulations has resulted in a reduction of noise by roughly 20EPNdB (effective perceived noise takes into account not only the magnitude of noise but also the frequency and duration) despite the increase of aircraft size and weight over that time [9]. However, although individual aircraft are becoming quieter, due to the volume of aircraft in the skies, the overall noise levels are still rising so it remains a prevalent issue.

This reduction in aircraft noise has been largely motivated by noise regulations enforced by the International Civil Aviation Organisation (ICAO). Although some noise control measures were first introduced by airports in the 1960s, the first international noise certification standards were issued in 1972 by the ICAO in Annex 16, Volume I to the Convention on International Civil Aviation. They defined three locations where noise should be measured: lateral, flyover, and approach. These are shown in Figure. 1.1.

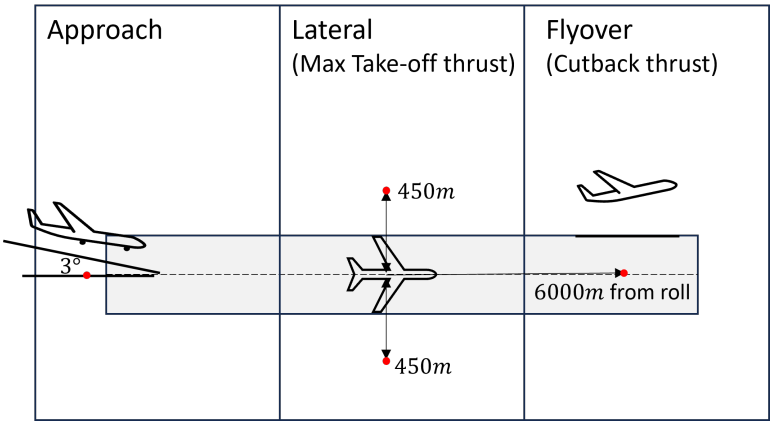

Figure 1.1: Noise measurement locations for certification of aircraft (ICAO, Annex 16, vol. I)

These noise regulations have become more stringent over the years, which is shown in Figure. 1.2. The initial regulations which were defined in Chapter 2 of Annex 16 were tightened in Chapter 3 following the introduction of the bypass engine since it enabled a large reduction in noise, this applied to all aircraft certified prior to 2006. The Chapter 4 stipulations were introduced after more noise reduction technologies were included in aircraft design. Most recently, in 2013, Chapter 14 legislation was introduced which further tightened regulations by 7EPNdB. It is important to note that these noise regulations refer to the 'noise at source', i.e. they will be considered in the design phase of aircraft development. The ICAO takes a balanced approach to noise reduction, meaning that they think each airport should address their own specific noise issues by considering: noise at source, land-use planning and management, operational procedures, and operating restrictions.

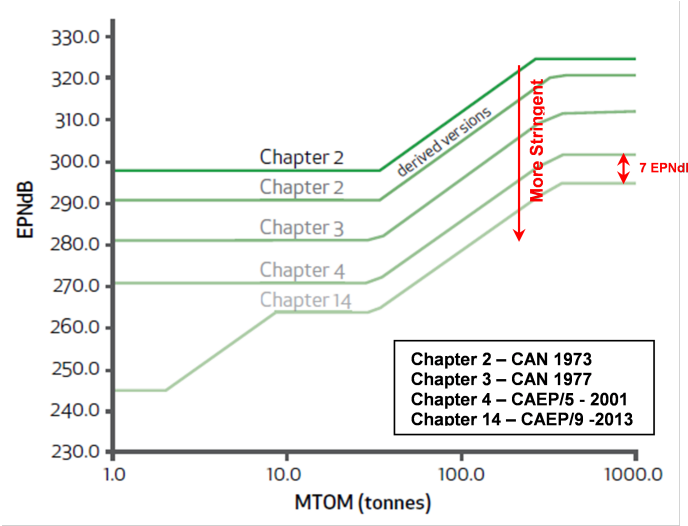

Figure 1.2: ICAO Noise regulations for subsonic jets [10]

Before discussing aircraft noise in more detail, it is prudent to have a deeper understanding of what constitutes noise and how it is measured. Noise is commonly defined as unwanted sound, where sound can be described as a combination of two main components: frequency and loudness. Human hearing is estimated to be able to hear from 20-20,000 Hz, with the ability to hear higher frequencies decreasing with age due to hearing loss. There are several units that we can use to measure noise, these being decibel (dB), 'A-weighted' decibel (dBA) and the equivalent perceived noise decibel (EPNdB). The decibel

is the basic logarithmic scaling for sound measurements, where an increase of 3dB represents a doubling of the sound pressure which relates formally to a doubling of power, however note that this is the minimum sound pressure increase that can actually be heard. Therefore, in practice an increase of 10dB is required before sound is subjectively found to be twice as loud. Additionally, we must remember that the human ear perceives sound differently depending on frequency; two sounds can have the same dB but we can hear the high frequency while not being able to hear the low frequency, A-weighting accounts for this by applying a filter so that sound measurements using this unit are a better representation of the sound we can actually hear. Aircraft noise regulations however are stated in terms of EPNdB, which additionally takes into account the length of time over which the noise occurs, since humans find noise more annoying the longer its duration, and it is more damaging to health.

1.1.1 Jet Noise

Aircraft noise is clearly very complex but it can be split into two main groups: engine noise and airframe noise. The airframe noise is that relating to the interaction of the freestream air with surfaces of the aircraft such as the fuselage, flaps, landing gear etc. The engine noise is produced from internal moving components (such as the fan) and the high speed turbulent jet. Most noise is produced from the engine, especially on takeoff. On approach the noise contribution is more or less equal between the engine and airframe [11]. The noise relating to the high speed jet can be categorised into two areas: jet noise which considers only the isolated jet; and jet surface interaction which takes into account the installation effects, i.e. how the jet interacts with surfaces of the aircraft.

Turbulence in jets is made up of small-scale and large scale structures, as depicted in Figure. 1.3. The small scale structures have been found to be more dominant in producing high-frequency noise, and the large scale structures are more dominant in producing low-frequency noise.

Lighthill [12] showed that jet noise was proportional to the eighth power of the jet velocity, therefore when the turbofan engine was introduced in the 1960s jet noise was largely reduced. The introduction of a stream of air through the bypass duct not only improved the efficiency of the aircraft but also reduced the velocity

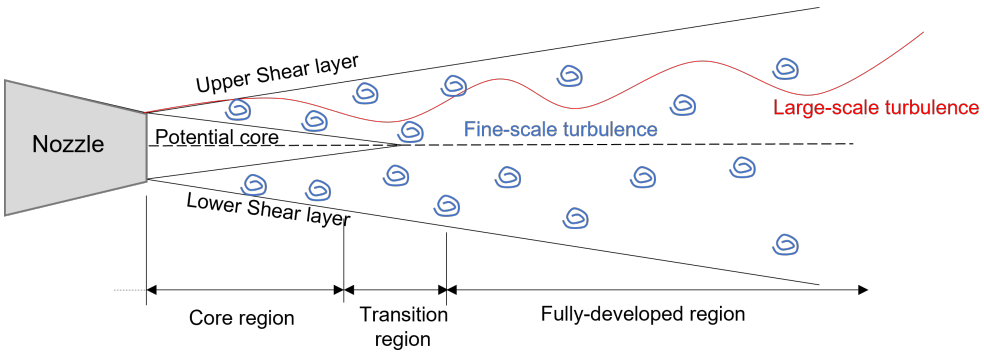

Figure 1.3: Regions of turbulent jet

of the jet which consequently reduced the jet noise. However, we have reached the bypass limit so further reductions to jet noise require smaller changes such as the inclusion of chevron shaped nozzles, and this requires a deeper understanding of the flow field and the production of noise.

Lighthill formulated the acoustic analogy which rewrites the Navier Stokes equations in terms of a linear wave equation which can be solved for the unknown variables if we assume the turbulence is known, and is therefore an 'acoustic source term' in the Navier-Stokes equations. At the time of its introduction it was impossible to know the turbulence structure however, over the past decades computational power has increased significantly allowing simulations to be carried out to find the turbulence statistics which can then be used within the acoustic analogy to predict the noise.

1.1.2 Edge Noise

Since commercial jets have the engines mounted beneath the wings of the aircraft and large bypass ratios mean that they are mounted close to the wing, there is a significant interaction between the jet and the trailing edge of the wing. This interaction was shown to increase the low frequency sound, particularly in the sideline locations (perpendicular to the wing). Therefore when carrying out noise predictions, it is also important to consider this interaction, which is known as 'installation effect'. Several methods have been developed to do this, and they are discussed in the literature review.

This thesis is split into two parts, looking at both jet noise and edge noise and finally combining prediction models into a 'hybrid' method for the prediction of

the full installation noise signature. The latter will be restricted to the jet and edge noise spectra.

1.2 Research Questions and Objectives

We currently do not have full information on the turbulence structure of jets across a range of acoustic Mach number (Ma) and jet temperature ratio (TR). This has lead to approximations of the turbulence being used in existing research which has the potential of introducing error in acoustic predictions and conclusions. Hence the research questions that we pose are as follows:

1. How does acoustic Mach number and jet temperature ratio affect turbulence statistics?
2. Can certain correlation functions be neglected?
3. Is there universality for the spectral tensor across Ma and TR?
4. Can jet surface interaction noise be better predicted using more faithful representation of the turbulence?

These questions will be answered in this thesis via targeting the main objectives:

- RO1: Obtain raw turbulence data for several acoustic Mach numbers and jet temperature ratio using LES simulations;
- RO2: Calculate the propagator using LES mean flow data;
- RO3: Calculate turbulence statistics using this LES data;
- RO4: Use LES turbulence statistics to calculate the spectral tensor analytically and validate numerically;
- RO5: Combine the propagator and spectral tensor to predict the jet noise spectrum;
- RO6: Expand the jet surface interaction model and use optimisation techniques to achieve better predictions and utilise GPU parallelisation to speed up the program;

- RO7: Combine jet surface interaction with jet noise to obtain the overall noise production

1.3 Roadmap of the Thesis

Figure 1.4 shows the structure of this thesis and indicates which research objectives are tackled in each chapter.

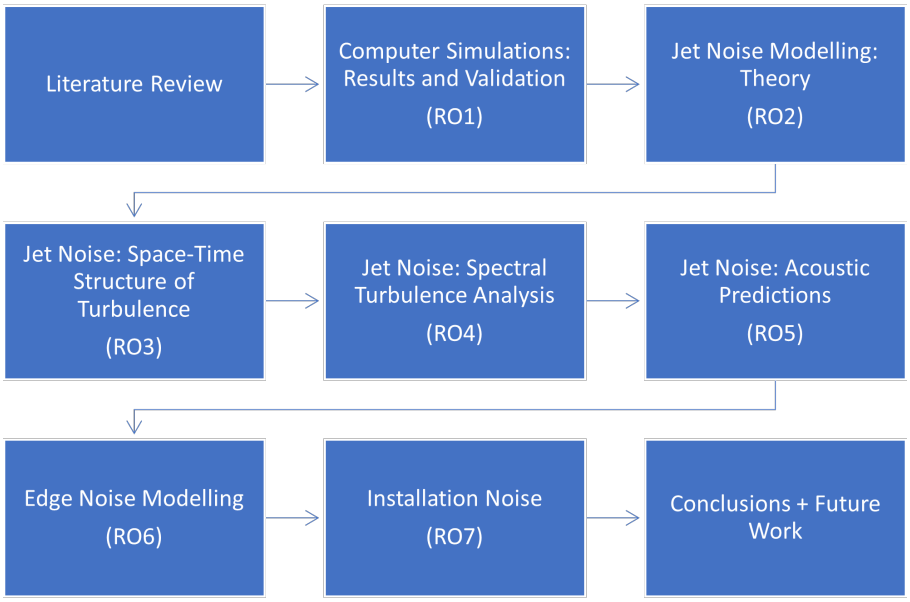

Figure 1.4: Roadmap of thesis

1.4 Scientific Contribution

The results obtained in this thesis have been disseminated at several conferences and journal publications listed below:

Journal Articles Published

- Stirrat, Afsar, Minisci (2021) Assessment of optimization methods for aero-acoustic prediction of trailing-edge interaction noise in axisymmetric jets, *MDPI Mathematics*.

Journal Articles in Preparation

- Koshuriyan, Stirrat (2024) On the universality of turbulence parameters in jet interaction noise models.
- Stirrat, Koshuriyan, Sescu (2024) Subsonic jet noise modelling by spectral turbulence reconstruction using large eddy simulation.
- Koshuriyan, Stirrat, Kokkinakis (2024) Analytical approximations of the acoustic spectrum for an installed axisymmetric jet flow.

Conference Papers

- Afsar, M. Z., Stirrat, S. A. & Kokkinakis, I, W. (2020) AIAA-2020-2564 - Investigation of fast GPU-based algorithms for jet-surface interaction noise calculations. *AIAA Aviation*, 15–19th June 2020.
- Stirrat, S., Afsar, M. Z. & Kokkinakis, I. W. (2020) Investigation of parallel computing for jet-surface interaction noise calculations. *33rd Scottish Fluid Mechanics Meeting* – Heriot Watt University, Edinburgh, UK. 28th May 2020.
- Stirrat, S., Afsar, M. Z., Minisci, E. & Kokkinakis, I. W. (2020) Using Optimisation Techniques within a Rapid-Distortion Theory Framework to Improve Trailing Edge Noise Predictions. *17th International Conference on Flow Dynamics*. Sendai, Japan, Oct. 28-30th, 2020.
- Stirrat, S., Afsar, M. Z., Minisci, E. & Kokkinakis, I. W. (2020) Modelling the trailing edge noise using optimisation techniques within a rapid distortion theory framework. *73rd Annual Meeting of the APS Division of Fluid Dynamic2s*, November 22–24, 2020; Virtual
- Afsar, M. Z. & Stirrat, S. (2021) The role of the spanwise correlation length in low-frequency sound radiation by turbulence/surface interaction in circular jets. *British Applied Mathematics Colloquium* , Glasgow, Tuesday 6th April – Friday 9th April 2021.
- Afsar, M. Z., Stirrat, S. and Sescu, A. (2021) The effect of the streamwise spatial development of Reynolds stress auto-covariance tensor on the

low-frequency acoustic spectrum of a high-speed supersonic air jet. *18th International Conference on Flow Dynamics.* Sendai, Japan, Oct. 27-29th, 2021.

- Stirrat, S., Koshuriyan, M.Z.A. (2022) Mapping the parameter space of trailing-edge noise spectrum– aero acoustic modelling and optimization, *2nd International Conference on Computational Methods and Applications in Engineering.* Mississippi State University, Starkville, MS, USA, 2022.

- Stirrat, S., Koshuriyan, M.Z.A. (2022) Optimized aero-acoustic modeling of trailing-edge noise for an axisymmetric jet interacting with a flat plate at arbitrary vertical locations, *35th Scottish Fluid Mechanics Meeting*, SAMS, Oban, UK, 2022.

- Stirrat, S., Koshuriyan, M.Z.A. & Sescu, A. (2023) - Examination of the acoustic spectrum in the generalized acoustic analogy for heated flows - temperature coupling effects vs direct enthalpy flux generated noise, *20th International Conference on Flow Dynamics.* Sendai, Japan, Nov. 6-8th, 2023.

- Koshuriyan, M.Z.A., Stirrat, S. & Sescu, A. (2023) - Taylor's Hypothesis in High-order Turbulence Correlations, *20th International Conference on Flow Dynamics.* Sendai, Japan, Nov. 6-8th, 2023.

Chapter 2

Literature review

2.1 Jet Noise Modelling

Modelling jet noise has been a topic of investigation for over half a century, with computational aeroacoustics becoming the main focus of research in the past 30 years. To predict jet noise we need to capture both the jet turbulence and the propagation of the acoustic waves to the far field. This can be determined through two main routes: direct numerical computation and hybrid approaches. Direct numerical computation aims to numerically resolve both the turbulent jet and also the sound propagation to the far field. Hybrid approaches, on the other hand, split the domain into regions, one containing the turbulent jet where the Navier Stokes equations can be solved, and the other in the far field where the acoustic propagation can be found using acoustic theory. Three main hybrid methods have emerged: the two source model, wave packet models of turbulence, and acoustic analogies. Figure 2.1 displays the different methods of hybrid jet noise modelling and some of the major contributors.

This thesis deals primarily with the acoustic analogy framework and uses computational fluid dynamics (CFD) to obtain the flow statistics. Hence, this section will focus mostly on the development of the acoustic analogies and the evolution of the use of CFD within them. Direct numerical computation, the two-source model and wave packets will also be briefly discussed to enable a greater appreciation of the field.

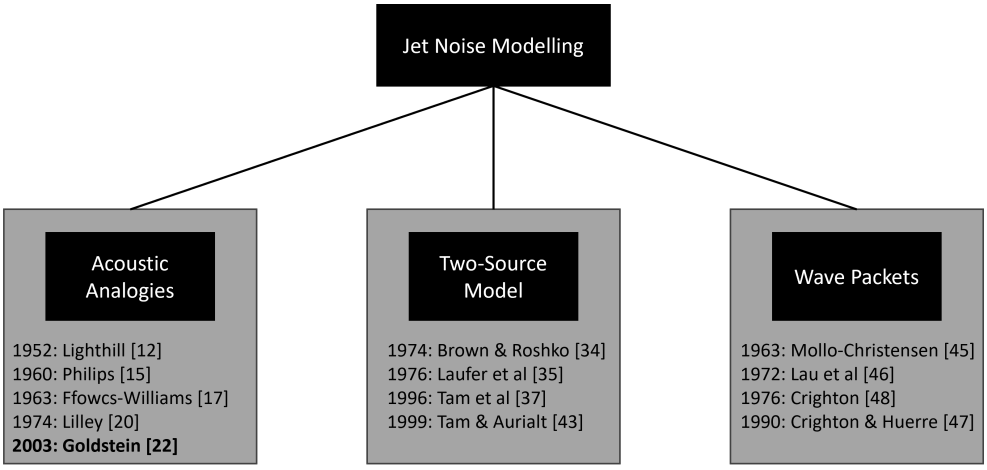

Figure 2.1: Main analytical methods of calculating jet noise (some of the main contributors to each method are listed - Goldstein is emphasised as this is the analogy that is used within this thesis)

2.1.1 Direct Numerical Computation

As mentioned, direct numerical computation involves solving the Navier Stokes equations in the entire domain. This can be done using several techniques, which were recently reviewed by Brès and Lele [13]. Direct numerical simulations (DNS) use a very fine grid to resolve the viscous scales of turbulence, naturally this is computationally expensive and only possible for low Reynolds number flows. Large eddy simulations (LES) are more popular as they are less computationally expensive as a coarser grid can be used since only the large scale motions are resolved. The small scales are either filtered out (implicit LES) or included using sub-grid scale modelling (explicit LES). Hybrid approaches can also be used to reduce computational requirements, such as combining LES with the Reynolds Averaged Navier-Stokes (RANS) equations, one example of this is detached eddy simulations (DES) where RANS is used close the the nozzle walls and LES is used for the free-shear flow where the turbulent length scale is larger than the grid size. More recently a Lattice Boltzmann method has also been used for jet surface interaction [14].

2.1.2 Acoustic Analogy

The field of aeroacoustics emerged in 1952 when Lighthill [12] published his acoustic analogy which was the first attempt at a method which could estimate

the intensity of the jet noise using the details of the fluid flow itself. His acoustic analogy rewrote the Navier Stokes equations into a linear wave equation which could then be solved using classical acoustics.

Figure 2.2 shows the problem split into source and observer variables, the source region describes the turbulent flow region, and the observer region is in the far field where there is no turbulent motion.

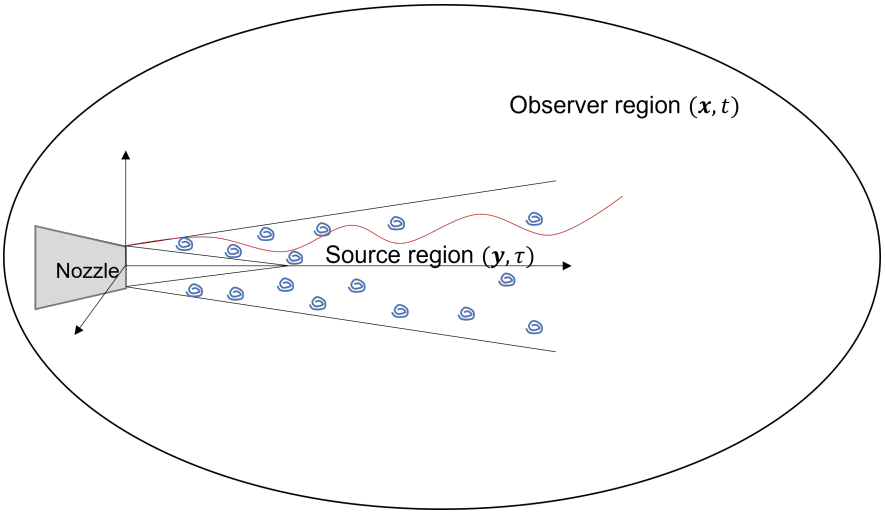

Figure 2.2: Source and observer regions

He showed that the Navier Stokes equations could be exactly written as a linear wave equation for a medium at rest with a quadrupole source term. He used the continuity and momentum equations:

$$\frac{\partial \rho}{\partial \tau} + \frac{\partial}{\partial y_j}(\rho v_j) = 0 \tag{2.1.1}$$

$$\frac{\partial}{\partial \tau}(\rho v_i) + \frac{\partial}{\partial y_j}(\rho v_i v_j) + \frac{\partial p}{\partial y_i} - \frac{\partial}{\partial y_j}\tau_{ij} = 0 \qquad i = 1, 2, 3 \tag{2.1.2}$$

where ρ is the density of the fluid, v_j is the velocity, p is the pressure and τ_{ij} is the stress tensor $\tau_{ij} = \mu(\partial v_i/\partial x_j + \partial v_j/\partial x_i)$, where μ is the dynamic viscosity. Then, by taking the time derivative of the continuity equation and subtracting the divergence of the momentum equation, this resulted in:

$$\frac{\partial^2 \rho}{\partial \tau^2} + \frac{\partial^2}{\partial \tau \partial y_j}(\rho v_j) - \left[\frac{\partial^2}{\partial y_i \partial \tau}(\rho v_i) + \frac{\partial^2}{\partial y_i \partial y_j}(\rho v_i v_j) + \frac{\partial^2 p}{\partial y_i \partial y_i} - \frac{\partial^2}{\partial y_i \partial y_j}\tau_{ij}\right] = 0 \tag{2.1.3}$$

$$\frac{\partial^2 \rho}{\partial \tau^2} = \frac{\partial^2}{\partial y_i \partial y_j}(\rho v_i v_j) + \frac{\partial^2 p}{\partial y_i \partial y_i} - \frac{\partial^2}{\partial y_i \partial y_j}\tau_{ij} \tag{2.1.4}$$

which, subtracting $c^2\nabla^2\rho$ from both sides, (where c is the speed of sound) gives the wave equation form:

$$\frac{\partial^2\rho}{\partial\tau^2} - c^2\nabla^2\rho = \frac{\partial^2}{\partial y_i \partial y_j}(\rho v_i v_j) + \frac{\partial^2 p}{\partial y_i \partial y_i} - \frac{\partial^2 \tau_{ij}}{\partial y_i \partial y_j} - c^2\frac{\partial^2\rho}{\partial y_i \partial y_i} \tag{2.1.5}$$

This can be written succinctly as:

$$\frac{\partial^2\rho}{\partial\tau^2} - c^2\nabla^2\rho = \frac{\partial^2 T_{ij}}{\partial y_i \partial y_j} \tag{2.1.6}$$

where $T_{ij} = \rho v_i v_j + \delta_{ij}(p - c^2\rho) - \tau_{ij}$. The wave operator on the left hand side of (2.1.6) is the usual wave equation operator on a homogeneous (constant c) medium. At this point no approximations have been made, therefore (2.1.6) is an exact representation of the Navier Stokes equations, where the source term includes the convection of sound with the flow, the variable speed of sound, and dissipation through viscosity.

For the subsonic Mach numbers that were considered by Lighthill, viscous terms, small fluctuations in density and conduction could be ignored, meaning that the strength could be approximated by $T_{ij} = \rho v_i v_j$. Since the source term is assumed known this equation can be solved using a Green's function. Lighthill's acoustic analogy shows that there is an analogy between density fluctuations in any real flow and small amplitude density fluctuations that would occur in a stationary fictitious flow with a quadrupole distribution of strength T_{ij} (which is assumed known) and speed of sound c. Doing this leads to the solution:

$$\rho' = \frac{\partial^2}{\partial x_i \partial x_j}\int_{V(\boldsymbol{y})} \frac{T_{ij}(\boldsymbol{y}, t - |\boldsymbol{x}-\boldsymbol{y}|/c)}{4\pi c^2|\boldsymbol{x}-\boldsymbol{y}|} d\boldsymbol{y} \tag{2.1.7}$$

After rewriting derivatives from jet field variable $\boldsymbol{y}$ on the right hand side of (2.1.6) to $\boldsymbol{x}$. For low subsonic Mach numbers the source region is compact (i.e. $T_{ij}(\boldsymbol{y}, t-|\boldsymbol{x}-\boldsymbol{y}|/c \approx T_{ij}(\boldsymbol{y}, t-x/c), x = |\boldsymbol{x}|)$, and the solution (2.1.7) is simplified to $O(1/x)$:

$$\rho' \sim \frac{1}{4\pi c^2 x}\frac{\partial^2}{\partial x_i \partial x_j}\int_{V(\boldsymbol{y})} T_{ij}(\boldsymbol{y}, t - x/c) d\boldsymbol{y} \tag{2.1.8}$$

If we look at the dimensions of this equation, letting U_j, D_j represent the characteristic velocity/length respectively then the characteristic frequency is $f \sim U_j/D_j$ and characteristic wavelength is $\lambda = c/f \sim cD_j/U_j = D_j/M_j$, $\partial/\partial x_i \sim$

$1/\lambda = M_j/D_j$, and the integral $\int_V \sim D_j^3$. Since, Lighthill approximates $T_{ij} = \rho v_i v_j \sim \rho_0 U_j^2 = \rho_0 c^2 M_j^2$, the density fluctuations scale as:

$$\begin{aligned} \rho' &\sim \frac{1}{c^2 x}\Big(\frac{M_j}{D_j}\Big)^2 D_j^3(\rho_0 c^2 M_j^2) \\ &\sim \frac{\rho_0 D_j M_j^4}{x} \end{aligned} \tag{2.1.9}$$

Therefore the mean square density fluctuation scales as:

$$\overline{\rho'^2} \sim \Big(\frac{\rho_0 D_j}{x}\Big)^2 M_j^8 \tag{2.1.10}$$

Hence, the sound intensity scales as the eighth power of the velocity. This was one of the main findings of Lighthill's work and is known as the 'eighth power law'. This link between jet velocity and sound intensity explains why increasing the bypass ratio at fixed net thrust, which resulted in lower jet speeds, also decreased the jet noise.

At the time, this analogy was only useful for describing gross properties of the acoustic field such as the eighth power law. It could not provide accurate spectral noise predictions since (for different reasons) the near field measurement of T_{ij} was not known.

As noted however, some of the estimates of turbulence and mean flow refraction of sound in Lighthill's work are not valid for supersonic flows, hence further studies were done to find appropriate 'analogies' that explicitly included the latter and improved modelling of the former. One of which was by Philips [15], who followed a similar approach to Lighthill except expressing the problem in terms of pressure fluctuations rather than density fluctuations. In this formulation the convection and variation of the speed of sound are gathered in the left-hand side of the equations rather than in the source terms (as was done in Lighthill [12]) and cannot be neglected. However, similar to Lighthill's analogy there was no explicit representation of meanflow convection in the wave operator. But Lighthill recognised that the quadrupole sources would be convected with the flow, and included a 'scaling factor' independent of the meanflow to account for this; Ffowcs-Williams [16] then modified this factor slightly to account for Doppler convection (when sound by a moving source propagates to a fixed observer). Ffowcs-Williams [17] extended Lighthill's acoustic analogy for this and found that the intensity of a high-speed jet would scale with the third power

of the jet velocity. Both this and Lighthill's scalings have been confirmed with several experiments. So, they found that the intensity of a supersonic jet scaled as:

$$I \sim \frac{\bar{\rho}^2 U^8}{\rho_0 c^5} \Big(\frac{D}{|\boldsymbol{y}|} \Big)^2 \frac{1}{|1 - M\cos\theta|^5} \tag{2.1.11}$$

where M is the eddy convection Mach number and θ is the far field angle of the observer. This put a prefactor of the type (2.1.11) which obviously introduces a singularity for supersonic jets when $M\cos\theta = 1$, this is termed the 'critical layer' [18].

As we have mentioned, neither Lighthill nor Ffowcs-Williams explicitly included the effects of mean flow refraction in the acoustic analogy. Figure 2.3 (adapted from [19]) shows that refraction will clearly occur since the local velocity at point B is greater than point A. At different points the local fluid flow will have different velocities and unless the jet is isothermal, the speed of sound is also dependent on location. Lilley [20] modified the acoustic analogy to be more reliable for heated jets by including the effects of mean flow refraction. This was done through the rearrangement of the Navier Stokes equations, primarily using the energy equation to replace the $\delta_{ij}(p' - c^2\rho')$ term which Lighthill neglected, this results in a source term related to enthalpy and kinetic energy. The kinetic energy term was determined to be small enough to be neglected.

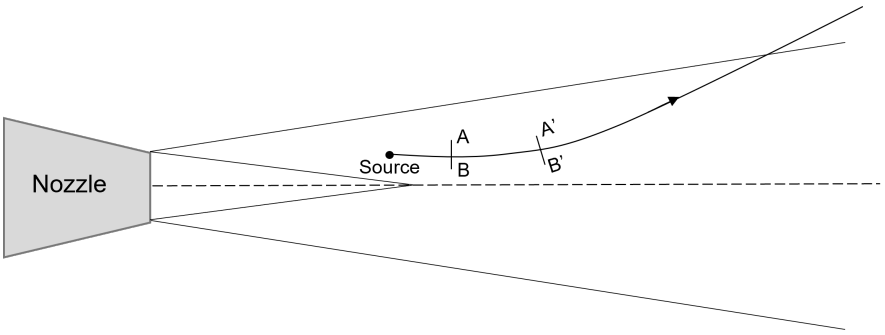

Figure 2.3: Meanflow refraction

Lilley's equation is appropriate for a parallel mean flow (i.e. $\boldsymbol{v}(\boldsymbol{y}) = \boldsymbol{e}_1 U(r)$) which is a good approximation for unheated subsonic jets [21]. However even this approach in which the wave operator in (2.1.6) includes mean flow gradient dU/dr) results in a Green's function solution that can potentially become unbounded at subsonic and supersonic speeds. The unboundedness in the Lilley equation approach were for two reasons:

1. The Green's function possesses a discrete spectrum of instabilities (i.e. points in the streamwise wavenumber k_1) where the dispersion relation $\Delta(\omega, k_1) = 0$ (defined by (4.2.38) and (A.2.5)), one of these points will render the Green's function solution singular.

2. At supersonic speeds the coefficients of the space-time Fourier transform of the Lilley equation will be unbounded on the critical layer (see (4.2.20)).

Both of the above issues can be remedied by including a spreading mean flow. Goldstein [22] did this in his Generalised Acoustic Analogy (GAA). This is the most general acoustic analogy and the one that is used in this thesis. He found that Lighthill's analogy and the subsequent forms resulted in a wave operator which contained a mix of linear and non-linear terms which, following linearisation, resulted in complex source terms. He aimed to avoid this by linearising the equations around an arbitrary base flow at the beginning of the analysis. He split the fluid variables into their base components plus a residual component using the Navier-Stokes equations e.g. $\rho = \overline{\rho} + \rho'$ where $\overline{\rho} = \overline{\rho}(\boldsymbol{y})$ and ρ' is unsteady. It is general in the sense that the base flow can be arbitrarily chosen. He showed that Lilley's solution can be obtained when choosing a parallel base flow, but the true mean flow of the jet can be used to be more accurate, this results in a relation between the mean-square pressure in the far field to the source correlation function. Like Lighthill's equation, Goldstein showed that there is an exact analogy between fluctuations in a real flow and linear inviscid fluctuations in an arbitrary base flow produced by externally imposed stress distribution and energy flux perturbations [22].

Goldstein's analogy has now seen wide spread use. For example, Goldstein & Leib [23] sought to include the instability waves through the use of a weakly non-parallel mean flow (small spread rate). They showed that the instability wave contribution to the acoustic spectrum was only present for $\theta \leq 30°$. Furthermore, in 2008 Goldstein & Leib [18] found that this formulation renders the Green's function solution uniformly valid across the critical layer. To do this, they used asymptotic expansions of the true non parallel flow matching this now weakly nonparallel inner solution to a parallel meanflow based Green's function in the outer region. This renders the Green's function solution uniformly valid.

It is important to note that all acoustic analogies are exact formulations of the Navier Stokes equations. The accuracy of their predictions wholly depend

on the source term that is used. If the source term was known exactly, it would be possible to find the exact far-field sound, as it is, the source term can only be estimated and normally taken from numerical simulations (LES or DNS). Samanta [24] investigated the effect of errors in the source term on the results of the acoustic analogies and found that it was more beneficial to explicitly consider mean flow in the wave operator than in Lighthill's analogy. *Our work in this thesis seeks to resolve this uncertainty* by using LES together with an improved mathematical model of the turbulence statistics.

Identifying the source term

Since the 1990s sound sources have been estimated (through turbulence correlations) mostly using numerical methods. Initially Reynolds-Averaged Navier Stokes (RANS) simulations were used extensively in combination with a turbulent-viscosity model. This was computationally less expensive than unsteady simulations such as large-eddy simulations (LES) and direct numerical simulations (DNS) and still gave relatively good predictions despite empiricism.

The majority of research on jet noise predictions using Goldstein's acoustic analogy have focused on cold jets. Morris and Zaman (2010) [25] used Particle Image Velocimetry (PIV) to measure second and fourth order correlations and length scales of the flow at several locations and frequencies. They found that the length scales varies with Strouhal number, i.e. at low St the length scales are constant and at high St they vary inversely with St. They compared their findings with a RANS simulation, for which the RANS simulation over-predicted the length of the potential core and the rate of decay of the centerline velocity, however the ratio of length scales was found to be similar between the experimental data and the simulation.

As we mentioned, Goldstein and Leib (2008) [18] developed a jet noise model for cold jets which used a RANS meanflow and also contained several empirical constants to model the spectral tensor, that is the space-time Fourier transforms of the Reynolds stress autocovariance tensor. Karabasov et al (2010) [26] aimed to gain better predictions for cold jets, through the use of LES (with sub-grid scale modelling) in addition to RANS modelling. They used the mean flow which was determined from a RANS model, and Goldstein's acoustic analogy using a Gaussian function model to describe the two-point correlation function for the

fourth order velocity fluctuations. Parameters, which describe the turbulence length and time scales, within this Gaussian function model were assumed to be proportional to turbulence information from the RANS model. Notably, in this paper they found the proportionality constants from LES rather than empirically. Based on investigation of correlation amplitude, this paper only considered correlations R_{1111}, R_{2222}, R_{3333}, R_{1212}, R_{2323} in its acoustic predictions. However, since they only considered one jet it is unclear as to whether these assumptions will be valid for other Mach numbers or jet temperature ratios.

In 2011, Afsar et al. [27] showed that the acoustic spectral tensor for heated jets, following several approximations, could be reduced to 11 components. This paper notably included the 'coupling terms' which had never before been included in jet noise analysis. They aimed to obtain an initial understanding of the potential effects of the coupling terms in jet noise predictions, however since there was no space-time data for the correlation functions, it was not possible for them to calculate predictions. They looked at three Mach numbers: $Ma = 0.5, 0.9, 1.48$ at a temperature ratio $TR = 2.7$. The main outcome from this paper was that the coupling term R_{4111} was found to be negative at the small subsonic Mach number and positive for the high subsonic/supersonic cases. Hence, the coupling term was speculated to be important in the reduction of jet noise at large Mach numbers. However, due to a lack of space-time data this result was only obtained at a few points along the shear layer, and other coupling terms were not fully investigated. One of the main aims of this thesis is to further expand on this work by running LES for several cold and heated subsonic jets to obtain the space-time data which can then be used to calculate the spectral tensor using an analytical model informed by the LES data (i.e. amplitude, and length scales taken from LES). This will allow us to carry out a detailed analysis on the spectral tensor components for heated and cold jets, and their importance in the noise predictions. This level of analysis has not previously been done before.

Numerical methods

Over the last decade there have been many advancements made in LES, which has been discussed in a recent review article [13]. One of the most important changes has been the inclusion of the nozzle geometry in the simulations which was previously neglected, instead a RANS mean flow through the nozzle was used

and perturbations created throughout as an attempt to estimate the turbulence. This resulted in numerical artefacts being introduced to the turbulence (and corresponding far-field noise) which made it impossible to study the effects of changing jet parameters (Mach number, jet temperature ratio etc.). Since nozzle geometry was not included explicitly in the LES, the Reynolds number was typically chosen to be in the range $0.1 - 5 \times 10^5$ since there was no high Reynolds number wall-bounded flow to consider.

In computational aerodynamics, several meshing methods have been used with success: structured multi-block, the Chimera (overset grids), Cartesian (cut cell or immersed boundary) and generalised unstructured meshes. The structured meshes were used for several years, however to include nozzle geometry this became more difficult, particularly for more complicated geometries such as those with chevrons. This meant that another technique had to be used, one way to do this was by cartesian adaptive mesh refinement (AMR) on structured grids. The LAVA framework from NASA [28] utilised this, as did the Lattice Boltzmann method (LBM) which has been successfully used for low Mach number flows but is still under investigation for higher Mach numbers [29, 30].

Many other researchers have developed methods using unstructured grids instead. For example, the Navel Research Laboratory developed the 'JENRE' solver [31] which focused mostly on investigating jet noise from military style nozzles, and, Cascade Technologies have developed the compressible flow solver 'CharLES', which recently has implemented a mesh generation technique using Voronoi diagrams which create a mesh based on Euclidean distance [32].

There has been a lot of recent research using the different acoustic analogies mentioned in the previous sections and making use of CFD and experimental data to determine the empirical coefficients which will always be present within these approaches.

2.1.3 Other Hybrid Approaches

Heuristic approach to two-source jet noise models

Before the 1970s it was thought that turbulence was made entirely of eddies from a range of scales distributed randomly throughout the flow. Then in 1971, Crow & Champagne [33] discovered experimentally that there were also large coherent

structures present; Brown & Roshko (1974) [34] also observed this separation of scales and noted that the large scale are seemingly orderly and the small scale are random. Laufer et al (1976) [35] performed experiments for supersonic jets to measure how the noise radiation differs at different locations. They found that the noise radiated to 90° was characteristically different to that radiated to 30°. The pressure signal at 90° was found to be random but smooth, similar to that from a subsonic jet whereas the signal at 30° contained more sharp oscillation. They concluded that there must be two different noise sources which is the cause of this disparity.

Tam and Chen [36] then showed that jet noise is also made up of a (highly directional) large scale component as well as the (more dominant) fine scale component. Later Tam et al (1996) [37] empirically found two similarity spectra when analysing jet noise data from the Jet Noise Laboratory at NASA Langley Research Center. These similarity spectra were applicable for both supersonic and subsonic jets indicating that the characteristics of noise and the mechanisms of its generation are constant across all Mach numbers and jet temperature ratio. They also found that the presence of shock waves did not exhibit any distortion from the two similarity spectra. There has since been many more confirmations of the similarity spectra by comparing with experimental data, for instance Viswanathan [38, 39] compared the spectra with a range of subsonic jets. It has also been confirmed for more complex jets, such as coaxial jets [40] and non-axisymmetric jets [41], and even more recently to a wider range of jets including (non-laboratory) supersonic military jets, rockets and even volcanoes [42] emphasising that the similarity spectra do not depend on Mach number, temperature ratio or jet diameter.

It has been generally known that large scale turbulence produces sound via instability waves and Mach wave radiation [42]. The Mach wave radiation dominates in the downstream region whereas the noise generated from the fine scale turbulence dominates in the upstream and sideline locations. As the Mach number of the jet increases the noise generated from the large scale structures dominates over that of the small scale.

Tam & Aurialt [43] developed a semi-empirical model to predict the noise generated from the fine-scale turbulence. The model is semi-empirical due to the use of the $k - \epsilon$ model which they used to obtain turbulence information, and

the acoustic model also contains three empirical constants. However, the model accurately predicted the fine scale jet noise from all experimental data available at that time. They suggested that the fine-scale turbulence generates noise via the volume sources in the jet mixing layer.

Recently Xu and Li [44] developed anisotropic source models for fine-scale and large-scale turbulence noise using Goldstein's acoustic analogy, determining the mean flow from RANS data and choosing empirical coefficients to match experimental data. Their model was for isothermal jets and assumed a locally parallel mean flow, however did consider both subsonic and supersonic jets.

Wavepacket models for the large scale turbulence

Wavepackets in the jet were first discovered by Mollo-Christensen (1963) [45]. Since then, there have been several wavepacket models (e.g. [46], [47]) which were discussed in a recent review by Jordan and Colonius (2013) [48]. As mentioned, turbulent jets are made up of two scales: fine scale and large scale structures. The large scale structures are coherent whereas the fine-scale structures are random. Wavelet analysis focuses on the large scale coherent structures. They decompose the flow variables into azimuthal modes and insert these into the Navier Stokes equations to obtain:

$$L(\bar{\boldsymbol{q}}) = R_{0,0} \tag{2.1.12}$$

$$L(\tilde{\boldsymbol{q}}_{m,\omega}) = R_{m,\omega} \qquad \omega \neq 0, m \tag{2.1.13}$$

where L is the Navier Stokes operator linearised about the mean flow, and $R_{m,\omega}$ represents a generalised mode-dependent Reynolds stress. The first equation is simply the RANS equation, and (2.1.13) is an exact representation of the Navier Stokes equations, however to simplify the equation it is assumed that the Reynolds stress $R_{m,\omega} = 0$. Since the wave packet model only consider the low modes, this is deemed to be a fine assumption as it does not matter whether or not it is true for the higher modes [49]. This equation has been thoroughly investigated and solved numerically for: a parallel mean flow (which reduces the equation to that of the Orr-Sommerfeld equations)[50] and a weakly non-parallel flow, which was found through extension of the parallel flow using multiple scales analysis [49, 51]. A parabolised stability equation (PSE) framework has also been used which has benefits of being less computationally complex [52].

2.2 Installation Noise Modelling: the 'Edge Effect'

As mentioned in the introduction, edge noise is caused by the turbulent jet interacting with the trailing edge of the wing. Edge noise experiments began in the 1970s by Olsen & Boldman [53]. In the 1980s, Wang [54] showed that the presence of an external surface increased the noise measured on the same side as the jet flow in comparison to the isolated jet, whereas noise measured on the opposite side of the nozzle was reduced. This is shown pictorially in Figure 2.4, where the noise measured on the same side as the nozzle is referred to as the 'reflected' noise and noise measured on the opposite side is referred to as the 'shielded' noise.

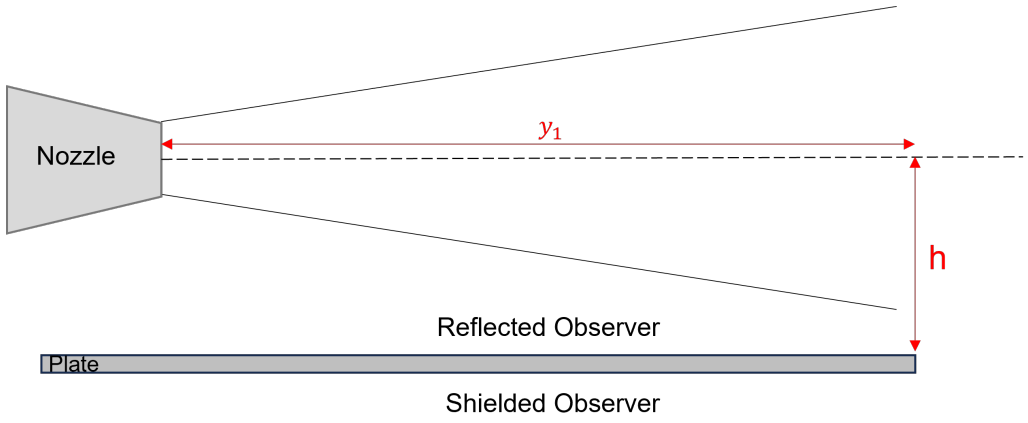

Figure 2.4: Description of the edge noise problem

Wang also found that this effect could increase the sideline noise ($\theta = 90$) on take-off, which was corroborated by [55, 56]. This amplification on sound due to the interaction with the trailing-edge is mainly at low frequencies up to the peak Strouhal number (i.e. the normalised angular frequency, $St = fD_J/U_J$ based on jet exit velocity, U_J and diameter, D_J); typically this is at $St \sim 0.1$.

Brown's recent experiments [57] confirm the work done in the 1970s by Olsen & Boldman [53] and Wang's result showing that the amplification in sound perpendicular to the jet axis (i.e., $\theta = 90°$) is typically of the order of 10dB for a high speed jet at an acoustic Mach number based on the speed of sound at infinity, $Ma = U_J/c_\infty$, of $Ma = 0.9$, shown in Figure 2.5. It is clear to see that as the plate moves further away from the jet, this noise amplification (edge noise)

reduces to become negligible in comparison with the jet noise (isolated noise).

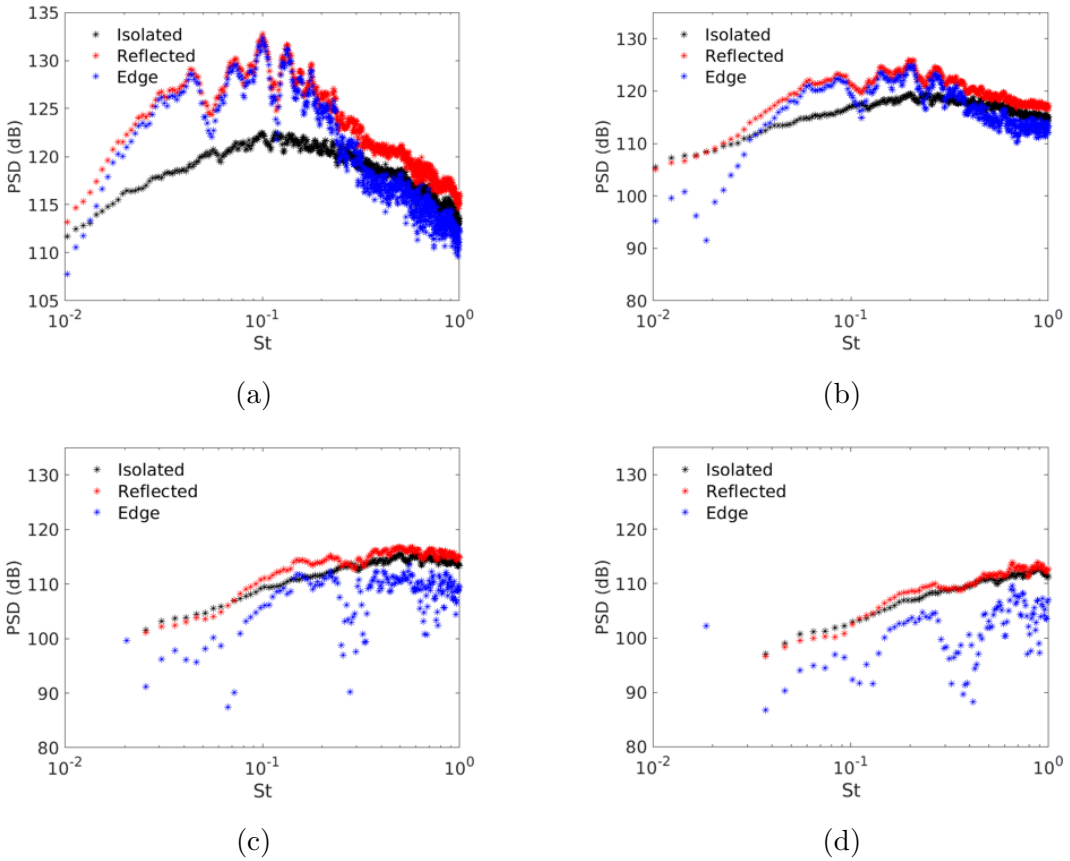

Figure 2.5: Comparison of edge noise and jet noise contributions at $Ma = 0.9$ at (a) $h = 0.5$, (b) $h = 1$, (c) $h = 2.5$, (d) $h = 4.5$ using Brown's [57] data

Additionally, as θ reduces, the jet noise contribution increases until, at shallow angles (e.g., $\theta = 30°$), the jet noise dominates the total noise radiation signature at almost all measured frequencies; typically this covers Strouhal numbers, $St = [0.01, 2.0]$. Bridges also found that the amplification in sound is greater at lower Ma, e.g., at $Ma = 0.5$ cf. 0.9; which is consistent with the 'dipole' directionality of the edge noise source. The streamwise location (y_1) was also found to have an important impact on the magnitude of low frequency noise amplification. Brown's results shows that when the edge is located in the vicinity of where the jet potential core terminates the amplification reaches its greatest magnitude. Lastly, the round jet appeared to result in greater noise amplification than the high-aspect ratio rectangular (i.e. planar) jet flow [57].

2.2.1 Analytical Methods in Installation Noise Modelling

This problem was first studied analytically by Ffowcs Williams and Hall [58] in 1970. They used Lighthill's acoustic analogy, neglected viscous effects and assumed $p = c^2\rho$ to obtain a Green's function equation for the pressure. However since this theory was based on Lighthill's method it neglected meanflow interaction effects, meaning it was only applicable for very low Mach numbers. Goldstein used rapid distortion theory to include mean flow effects in 1979 [59].

Rapid distortion theory can be used when the turbulence intensity is small and the length/time scale for the interaction is much smaller than the length/time scale of the turbulent eddy decay. Asymptotically, this means that it is possible to find a length/time that is infinitely large compared to the interaction but still small compared to the turbulent eddy decay, meaning that the flow is an inviscid and non-heat conducting compressible one which can be described by the linearised Euler equations. See Figure 2.6 for a depiction of this problem.

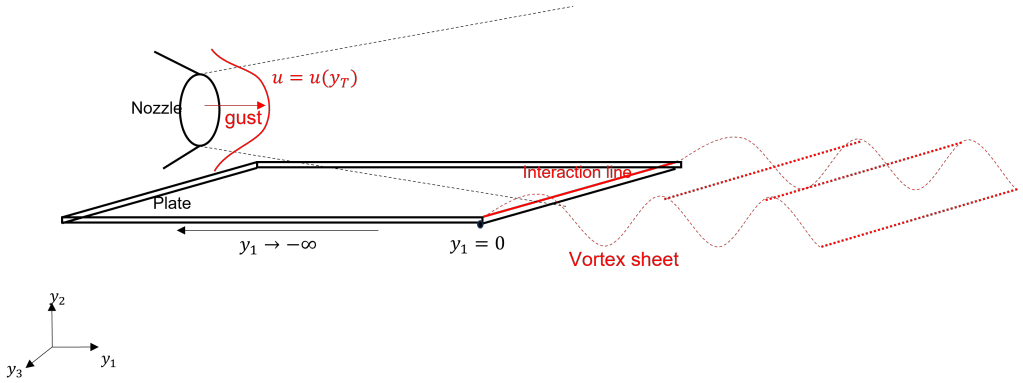

Figure 2.6: Canonical trailing-edge noise problem

The discontinuity in the solid surface boundary condition can be treated formally using the Wiener-Hopf technique for a flat plate that is doubly infinite in the spanwise direction and lies parallel to the level curves of the streamwise mean flow. The so-called 'gust solution' then acts as the input to an inhomogeneous boundary value problem in which the scattered pressure field is determined at the output.

The gust-induced boundary condition and the homogeneous solutions to the Rayleigh equation (which enters the solution to the Wiener-Hopf problem) were found using the method of matched asymptotic expansions at the low frequency limit [60, 61, 62].

Goldstein et al (2013, 2017) [60, 61] showed that the pressure and transverse velocity fluctuations could be expressed as a convolution product of the Rayleigh Green's function and one of the arbitrary convected quantities. This allowed them to formulate an equation for the acoustic spectrum of a planar mean flow. The papers differ in their approach to relating the convected quantities to the physical properties of the flow. Additionally, in 2013 only the low frequency asymptotic limit was considered, whereas in 2017 a high frequency factor was applied, allowing the acoustic spectrum to be found for a wider range of frequencies.

Goldstein, Leib & Afsar [62] (which will now be referred to as GLA19) extended Goldstein et al (2017)[61] to mean flows of arbitrary cross-section. They generated a formula for the acoustic spectrum which is applicable for a wide range of mean flows, and showed that it produced reasonable predictions for the case of an axisymmetric round jet interacting with the trailing edge of a flat plate. However, the formulation involved four nested integrals, which can be computationally expensive on a desktop computer. In addition to this, the acoustic spectrum predictions were only very good for an acoustic Mach number of 0.7.

Hence, in Chapter 8, this thesis extends the acoustic spectrum formulation to find better approximations across the frequency range for a range of subsonic Mach numbers, as well as utilising computer parallelisation techniques (using CPU and GPU) to reduce the time spent in calculating the acoustic spectrum. As in jet noise modelling, the difficulties often are associated with inadequate source models. Most analytical methods have also chosen parameters by hand, this thesis investigates the use of optimisation methods to automate the choosing of parameters in a way where they should be optimal, and investigates the universality across subsonic Mach number, far field angle, and plate location.

2.2.2 Direct Numerical Methods

Numerical methods can also be used to predict trailing edge noise. Bondarenko et al (2012) [63] studied edge interaction noise using an LES solver and calculating the predicted noise via the Ffowcs Williams-Hawkings (FW-H) integral using different surfaces. Semiletov et al (2016) [64] also used their numerical solver CABERET and the FW-H method to predict edge noise.

More recently, Rego et al (2020) [65] investigated the interaction noise using the numerical lattice-Boltzmann method. Notably, they found that the overall trends of installation noise could be predicted using by only considering the near field for an isolated jet.

Machine learning has also been used in recent years [66] using a large database of experimental data from NASA to generate empirical models which can predict edge noise over a range of Mach number, far field angle, and plate location.

2.3 Summary

In this literature review, we have discussed some of the main methods and results of research regarding jet noise and edge noise predictions. As mentioned throughout, this thesis deals with Goldstein's generalised acoustic analogy for jet noise predictions and the rapid distortion theory framework for edge noise predictions.

The main aims of this thesis are to fully analyse the acoustic spectral tensor for all 11 correlations that were found by Afsar et al [27] for four jets. This will enable us to check the effect of heating and increasing the Mach number on the spectral tensor and the predictions. We aim to check the spectral tensor (the space-time Fourier transform of the fluctuating Reynolds stress tensor) and the predictions for universality across Mach number and temperature ratio. Although we have highlighted certain technical difficulties in the computation of the parallel flow Green's function, we use this formulation for the solution to wave propagation problem in this thesis. This is largely because of the focus on subsonic Mach numbers. There will be a reduction in the predicted peak sound at the small angles because of this ([67]) but it will nevertheless indicate the limit of applicability for a parallel flow solution. Finally we can combine the predictions for jet noise and edge noise to find predictions for the installation noise.

Figure 2.7 shows the process for this calculation, which will be tackled in the following chapters.

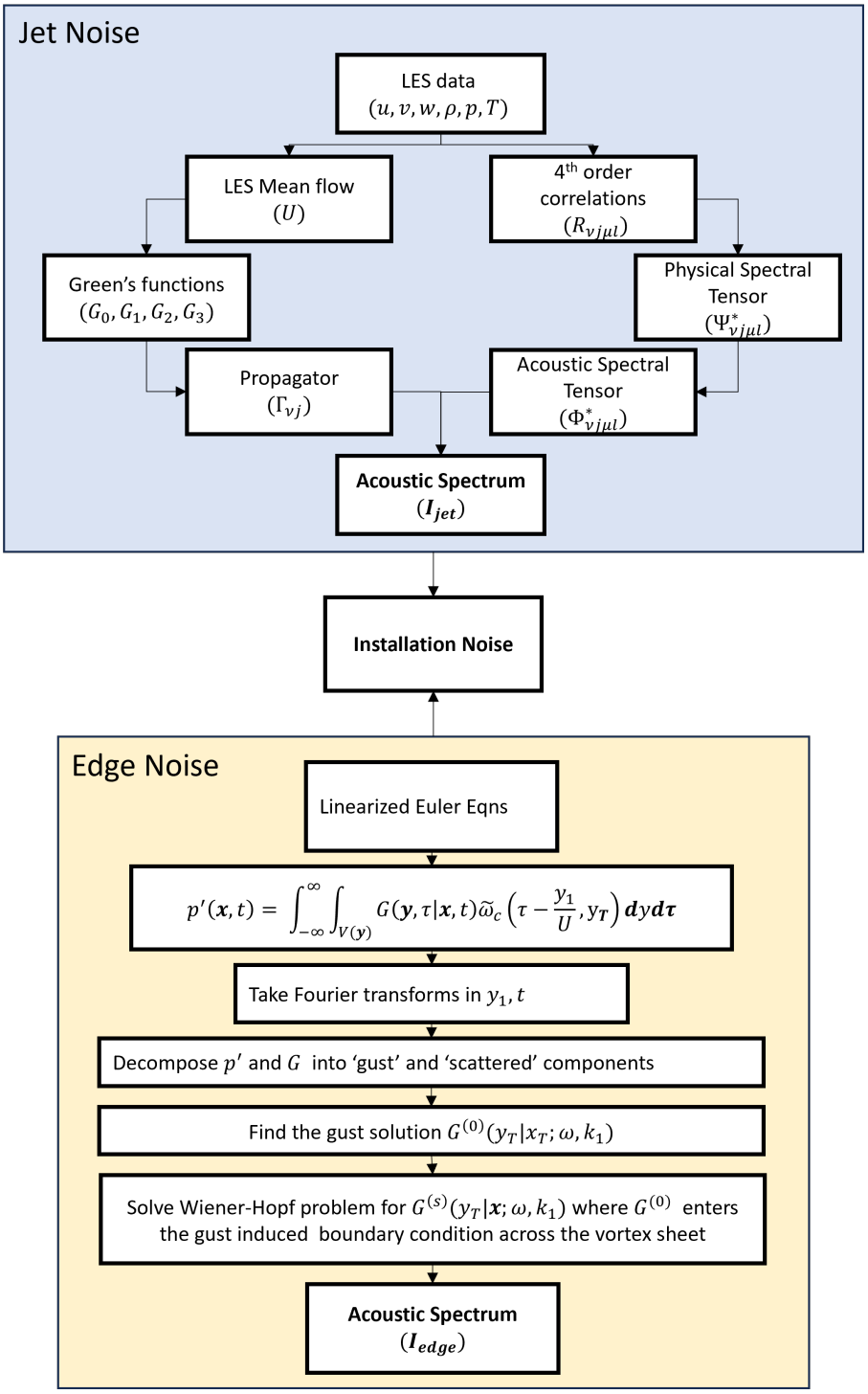

Figure 2.7: Process diagram for installation noise predictions (see Chps. 4 and 8 for definition of terms)

Chapter 3

Computational Simulations: Results and Validation

As mentioned in Chapter 2, in order to use acoustic analogies to predict the acoustic spectrum it is assumed that the turbulence is known. In this thesis, the turbulence structure for the four jets described in Table 3.1 is calculated via LES. Please note, from now on the set point abbreviations will be used when referring to the jets. These jets were chosen from Tanna's [68] experimental dataset as there has been several experimental and computational investigations for these jets in the literature, hence we can validate both our turbulence and acoustic results. In this chapter the LES is described and our turbulence results are validated against experimental data. To the best knowledge of the author, parametric LES study of these jets has not appeared in the literature.

Table 3.1: LES database (from hereon the set point abbreviations will be used when referring to each jet)

Set Point	Ma	TR	Re
$SP03$	0.5	1.0	$584,000$
$SP07$	0.9	0.84	$1,051,200$
$SP42$	0.5	2.7	$584,000$
$SP46$	0.9	2.7	$1,051,200$

These simulations were carried out when the author was visiting Mississippi

State University, using the in-house implicit LES code developed by Dr. Sescu, which has been validated for other problems, such as in [69, 70, 71]. In the following section we discuss the equations solved.

3.1 LES Equations

The program uses generalised curvilinear coordinates with the transformations: $\xi = \xi(x_1, x_2, x_3, t)$, $\eta = \eta(x_1, x_2, x_3, t)$, $\zeta = \zeta(x_1, x_2, x_3, t)$ corresponding to the computational streamwise, wall-normal and spanwise directions respectively, and (x_1, x_2, x_3) are the equivalent physical Cartesian coordinates which are normalised by the jet diameter D_j. Similarly, the fluid velocity (v_1, v_2, v_3) is normalised by the jet velocity U_j, pressure is normalised by the dynamic pressure $\rho_\infty U_j^2$, and temperature is normalised by the farstream temperature T_∞. Hence the Reynolds number, Prandtl number and Mach number are defined as:

$$Re = \frac{\rho_\infty U_j D_j}{\mu_\infty}, \qquad Pr = \frac{\mu_\infty C_p}{k_\infty}, \qquad Ma = \frac{U_j}{c_\infty} \tag{3.1.1}$$

where μ_∞ is the dynamic viscosity, c_∞ is the speed of sound and k_∞ is the thermal conductivity, all measured in the farstream.

The Navier-Stokes equations are:

$$\frac{\partial \rho}{\partial \tau} + \frac{\partial}{\partial y_j}\rho v_j = 0 \tag{3.1.2}$$

$$\frac{\partial}{\partial \tau}(\rho v_i) + \frac{\partial}{\partial y_j}(\rho v_i v_j) + \frac{\partial p}{\partial y_i} - \frac{\partial}{\partial y_j}\tau_{ij} = 0 \qquad i = 1, 2, 3 \tag{3.1.3}$$

$$\frac{\partial E}{\partial \tau} + \frac{\partial}{\partial y_j}(v_j E) + \frac{\partial}{\partial y_j}(p v_j) + \frac{\partial}{\partial y_j} q_j - \frac{\partial}{\partial y_j}(v_i \tau_{ij}) = 0 \tag{3.1.4}$$

Es-Sahli et al [69] showed that the Navier Stokes equations can be written as a vector equation:

$$\mathbf{Q}_t + \mathbf{F}_\xi + \mathbf{G}_\eta + \mathbf{H}_\zeta = \mathbf{S}. \tag{3.1.5}$$

where the subscript denotes differentiation. The vector of conservative variables $(\boldsymbol{Q})$ is given by

$$\mathbf{Q} = \frac{1}{J}\{\ \rho, \quad \rho v_i, \quad E\ \}^T, i = 1, 2, 3 \tag{3.1.6}$$

ρ is the non-dimensional density of the fluid, and E is the total energy. The flux vectors, $\mathbf{F}$, $\mathbf{G}$ and $\mathbf{H}$, are given by

$$\mathbf{F} = \frac{1}{J}\left\{ \rho V_1, \quad \rho v_i V_1 + \xi_{x_i}(p + \tau_{i1}), \quad EV_1 + p\tilde{V_1} + \xi_{x_i}\Theta_i \right\}^T, \tag{3.1.7}$$

$$\mathbf{G} = \frac{1}{J}\left\{ \rho V_2, \quad \rho v_i V_2 + \eta_{x_i}(p + \tau_{i2}), \quad EV_2 + p\tilde{V_2} + \eta_{x_i}\Theta_i \right\}^T, \tag{3.1.8}$$

$$\mathbf{H} = \frac{1}{J}\left\{ \rho V_3, \quad \rho v_i V_3 + \zeta_{x_i}(p + \tau_{i3}), \quad EV_3 + p\tilde{V_3} + \zeta_{x_i}\Theta_i \right\}^T \tag{3.1.9}$$

where the contravariant velocity components are given by

$$V_1 = \xi_{x_i} v_i, \quad V_2 = \eta_{x_i} v_i, \quad V_3 = \zeta_{x_i} v_i \tag{3.1.10}$$

with the Einstein summation convention applied over $i = 1, 2, 3$. The Jacobian of the curvilinear transformation from the physical space to computational space is denoted by J, and the derivatives ξ_{x_i}, η_{x_i}, ζ_{x_i} represent grid metrics.

The shear stress tensor and the heat flux are given as

$$\tau_{ij} = \frac{\mu}{Re}\left[\left(\frac{\partial \xi_k}{\partial x_j}\frac{\partial v_i}{\partial \xi_k} + \frac{\partial \xi_k}{\partial x_i}\frac{\partial v_j}{\partial \xi_k}\right) - \frac{2}{3}\delta_{ij}\frac{\partial \xi_l}{\partial x_k}\frac{\partial v_k}{\partial \xi_l}\right] \tag{3.1.11}$$

$$\Theta_i = v_j \tau_{ij} + \frac{\mu}{(\gamma - 1)M_\infty^2 RePr}\frac{\partial \xi_l}{\partial x_i}\frac{\partial T}{\partial \xi_l} \tag{3.1.12}$$

respectively, and $\mathbf{S}$ is the source vector term. The dynamic viscosity (μ) is linked to the temperature using the dimensionless Sutherland's equation:

$$\mu = T^{3/2}\frac{1 + C_2/T_\infty}{T + C_2/T_\infty} \tag{3.1.13}$$

where for air at sea level, $C_2 = 110.4K$. There are no subgrid scale terms in (3.1.5) since an implicit large eddy simulation framework is considered here.

The time marching uses the 2nd order Adams-Bashforth method:

$$\boldsymbol{Q}^{n+1} = \boldsymbol{Q}^n + k\Big[\sum_{\nu=0}^{K} \beta_\nu L(\boldsymbol{Q}^{n-\nu})\Big] \tag{3.1.14}$$

and the spatial derivatives are calculated using the dispersion relation preserving (DRP) of Tam and Webb [72] or the high-resolution 9-point DRP optimised scheme of Bogey and Bailly [73]. For further details on the numerical method see [69, 70].

3.2 Mesh

The mesh was generated using GridPro which takes in topology and a wireframe and then iterates to obtain a smooth grid. It is a structured Cartesian grid which spans from $3D_j$ upstream to $55D_j$ downstream of the nozzle exit. In the radial direction the outer radius of the domain ranges from $16D_j$ at the nozzle to $22D_j$ at the end of the domain.

Best practices in LES were described in a review paper by Brès and Lele (2019)[13] and they emphasised the importance of including nozzle geometry in simulations to achieve the correct nozzle exit conditions. We also show this importance in Figure 3.1, which compares meanflow results for SP07 using two nozzle geometries (where the ARN2 nozzle is the nozzle used in most experiment/LES cases we validate against). The other nozzle did not capture the potential core. Note that we assume that the boundary layer is laminar inside the nozzle for all grids. Table 3.2 compares the three grids.

Table 3.2: Comparison of grids

Grid	Number of cells
Old	$11,778,624$
ARN2 fine	$13,244,832$
ARN2 extrafine	$23,078,528$

Figure 3.1 also shows that the fine grid provides enough resolution to capture the meanflow and turbulent kinetic energy (which lies within experimental uncertainty at most locations), therefore this fine mesh (shown in Figure 3.2 and detailed in Table 3.3) is used for all LES cases.

The computational unsteady data was obtained after an initial transient of $400 - 500$ convective time units for the $Ma = 0.9$ jets, and $250 - 300$ convective time units for the $Ma = 0.5$ jets was discarded. The statistics were then calculated over 230 convective time units.

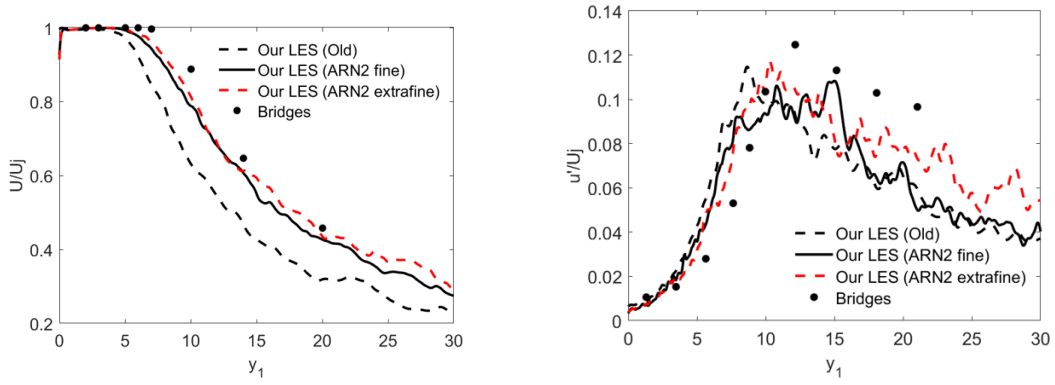

(a) (b)

Figure 3.1: SP07: LES results checking different grids for (a) U/Uj (b) u'/Uj

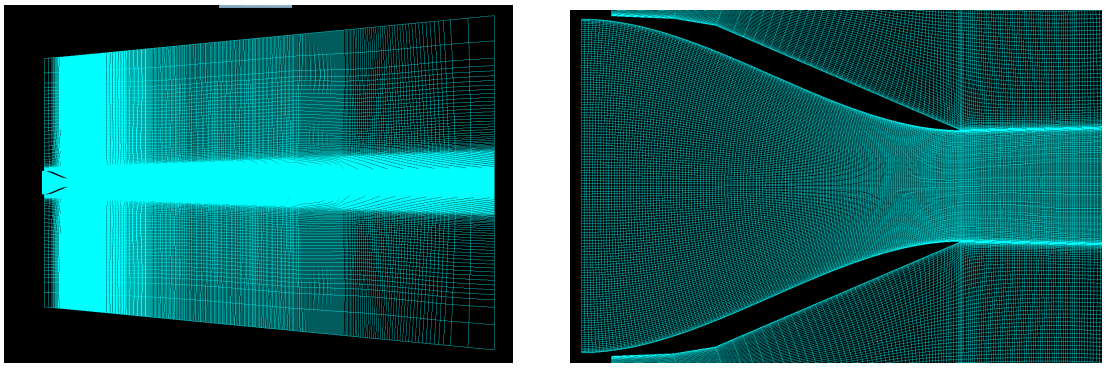

(a) (b)

Figure 3.2: Fine mesh for LES (a) whole domain (b) nozzle area

Table 3.3: Mesh details for ARN2 fine (length normalised by D_j, and time normalised by D_j/U_j)

	ARN2 fine
Outer block size ($N_x \times N_r \times N_\phi$)	$578 \times 158 \times 144$
Total cells count	13.2 M
Δx at nozzle exit	0.009
Average Δx for $0 < x < 4$	0.03
Average Δx for $4 < x < 10$	0.07
Min Δr in shear layer	0.003
$r\Delta\phi$ in shear layer	0.02
Time step, Δt	0.000326

3.3 Results

Figure 3.3 shows the meanflow results from the LES cases, where the velocity is normalised by the jet velocity U_j. We see that heating reduces the potential core, as expected. In this thesis, most analysis will be done at the end of the potential core since this is the maximum sound producing region. We define start and end points of the end of the potential core, where the start point is the y_1 where $U(y_1, r = 0) = 0.95$ and the end point is the y_1 where $U(y_1, r = 0) = 0.9$. These locations for each jet are defined in Table 3.4.

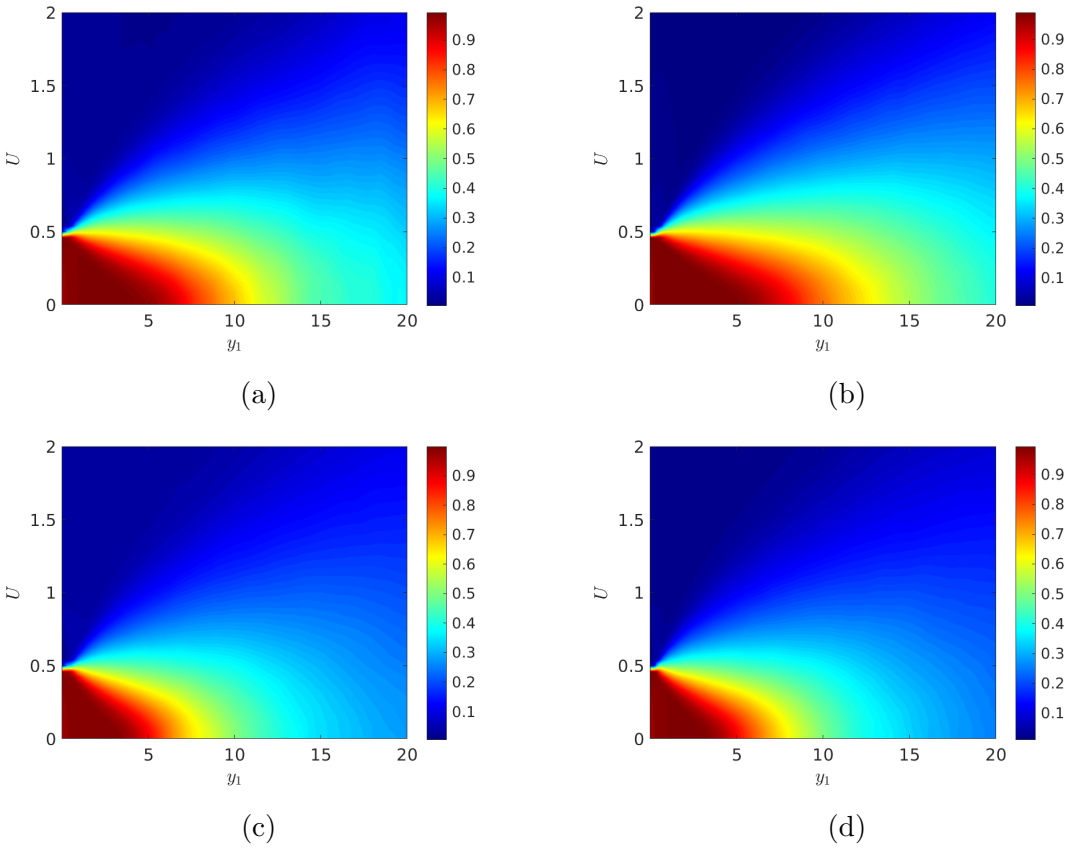

Figure 3.3: LES meanflow contours for (a) SP03 (b) SP07 (c) SP42 (d) SP46

3.3.1 Validation

Figures 3.4, 3.5 compare the meanflow and turbulent kinetic energy (tke) that we obtain through our LES with data from literature. Since SP07 is most often used as a test point in the literature, we validate the LES and grid by comparing our

Table 3.4: Initial and terminal points of the end of potential core

Case	End of potential core: initial point (y_1 = start)	End of potential core: terminal point (y_1 = end)
SP03	5.8	6.8
SP07	6.5	7.6
SP42	4.3	4.9
SP46	4.25	4.9

results with various experimental [74, 75, 76, 77] and LES data [78, 79]. SP03 and SP46 are compared with Bridges data [74] alone, and SP42 is compared with Mielke et al [80, 81]. We see from these comparisons that the potential core is well captured by the LES. The streamwise meanflow is predicted very well across all jets. However the turbulent kinetic energy is under predicted at the peak, but the initial ascent is captured. This is likely due to either the lack of a turbulent boundary layer inside the nozzle or the grid resolution. Note, that experimental data for the turbulent kinetic energy for SP42 was not available, therefore only our LES result is shown here.

Further validation of the streamwise meanflow velocity and turbulent kinetic energy is shown in Figure 3.6 which compares the radial profile of SP07 with Bridges [82] at several y_1 locations. We see the LES under predicts slightly outside the potential core region, but the spatial shape is captured well. Then, Figure 3.7 compares the axial profile of the meanflow and turbulent kinetic energy on the shear layer, where the error bars for the experimental data show that for the majority of locations the LES agrees with experiment.

The spread rate (S) and velocity decay constant (B) (defined in (3.3.1) and (3.3.2) respectively), were also calculated for each jet. The jet half-width $r_{1/2}(y_1)$ is defined as the r where $U(y_1, r_{1/2}) = U(y_1)/2$. The velocity decay constant is found by the equation of a straight line (3.3.2) where y_1^0 is the intercept with the y_1 axis.

$$S = \frac{dr_{1/2}(y_1)}{dy_1} \tag{3.3.1}$$

$$\frac{U(y_1, r = 0)}{U_j} = \frac{B}{(y_1 - y_1^0)/D_j} \tag{3.3.2}$$

Our results are compared with experimental values in Table 3.5. We get good agreement with the hot jets, but not with the cold jets. This is likely due to the

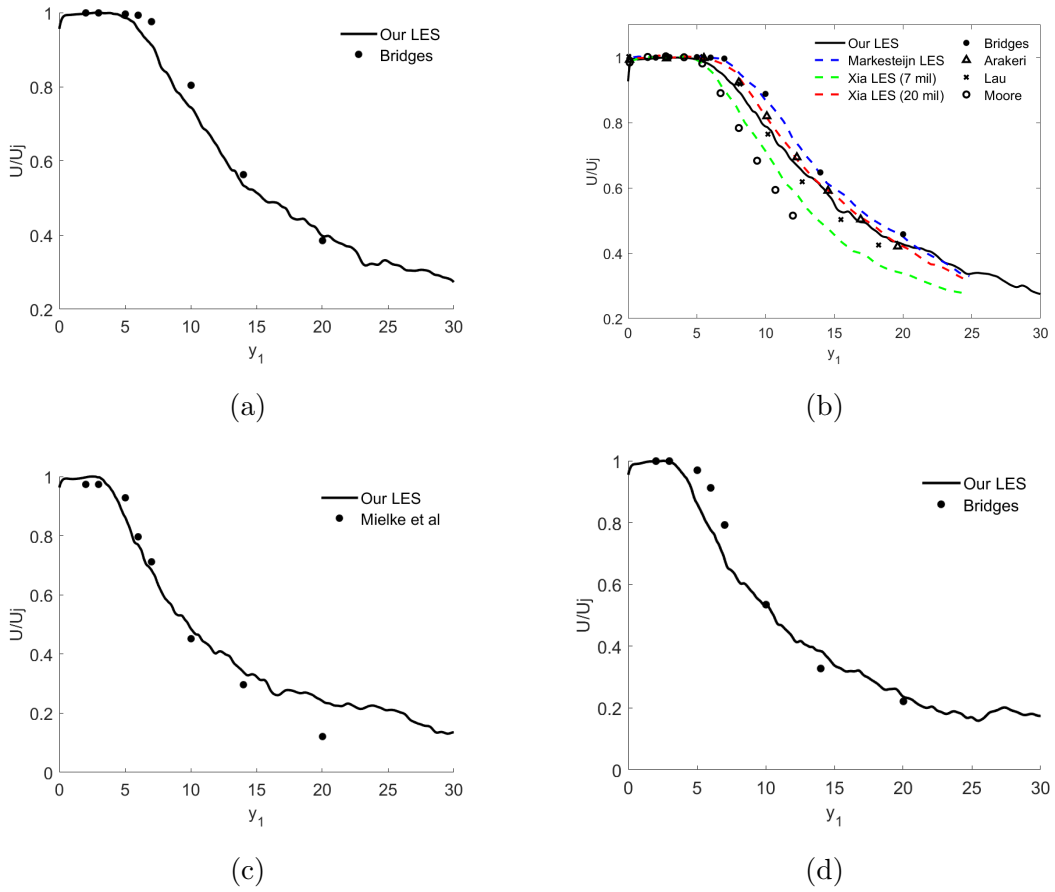

Figure 3.4: LES meanflow centerline ($r = 0$) results for (a) SP03 (b) SP07 (c) SP42 (d) SP46

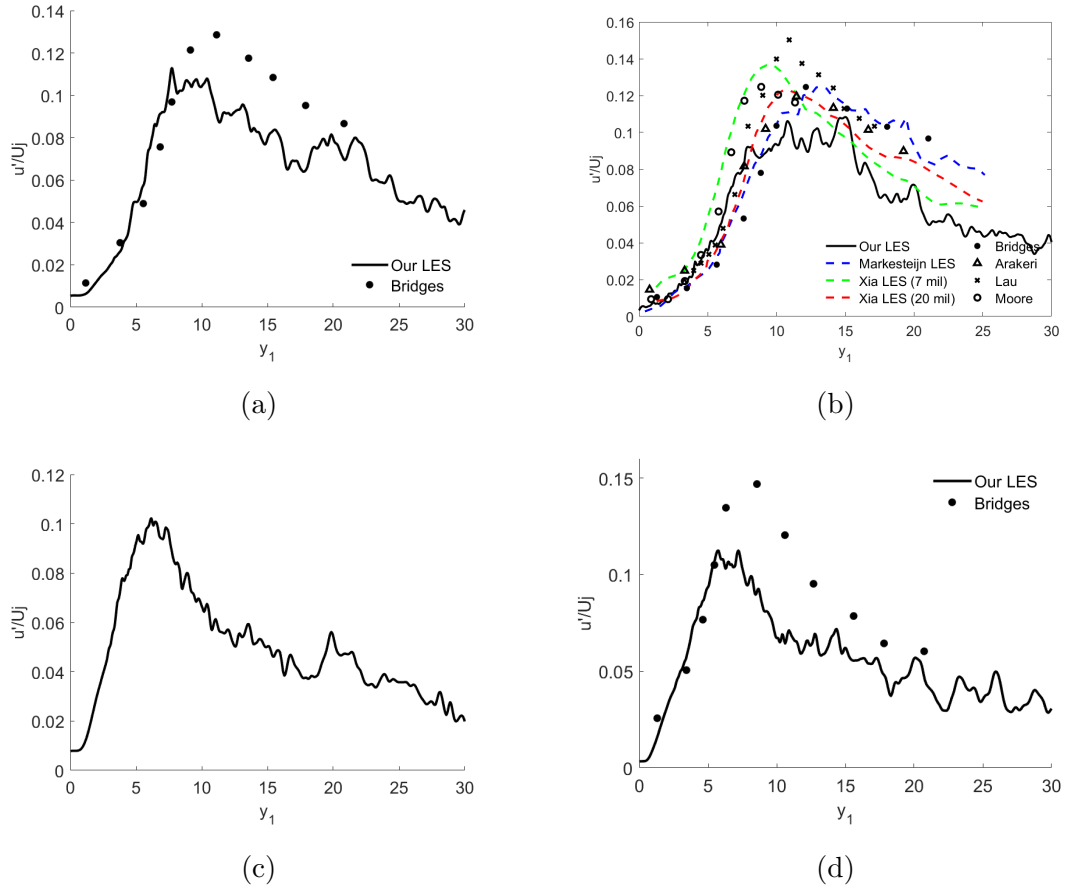

Figure 3.5: LES tke centerline ($r = 0$) results for (a) SP03 (b) SP07 (c) SP42 (d) SP46

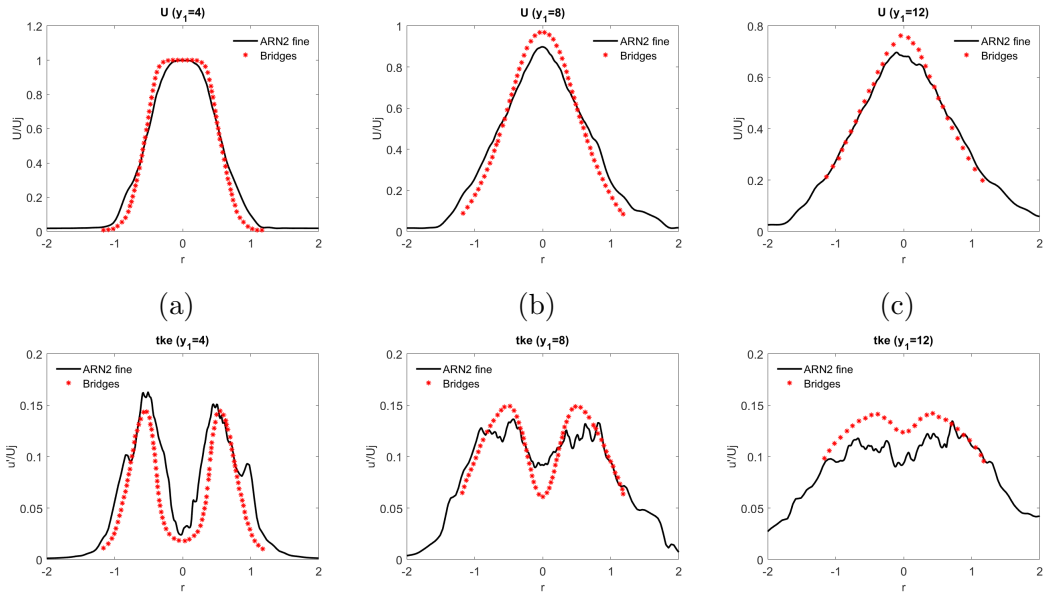

(a) (b) (c)

(d) (e) (f)

Figure 3.6: SP07: compare radial profile with Bridges for: (a) $U(y_1 = 4)$ (b) $U(y_1 = 8)$ (c) $U(y_1 = 12)$ (d) $tke(y_1 = 4)$ (e) $tke(y_1 = 8)$ (f) $tke(y_1 = 12)$

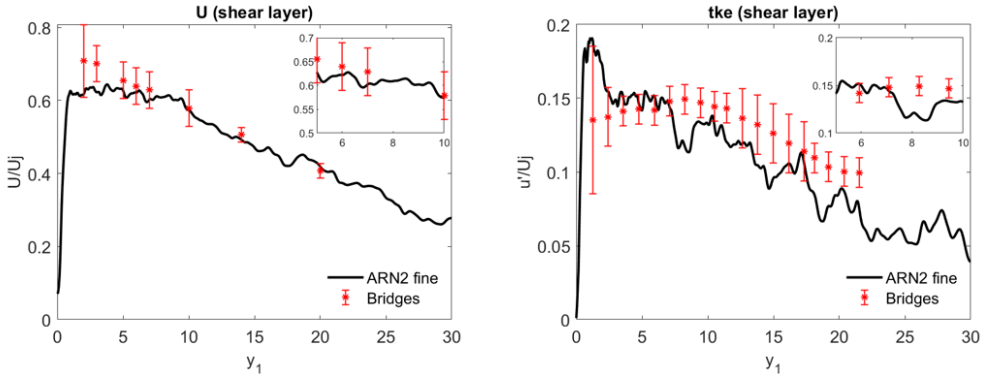

(a) (b)

Figure 3.7: SP07: compare axial profile with Bridges on the shear layer ($r = 0.5$) for: (a) U (b) tke

calculations taking place too close the the potential core for the cold cases, since their potential core is longer and we do not have data for large y_1.

Table 3.5: Comparison of spread rate and velocity decay constant with experiment

Case	S	B
SP03 ($Ma = 0.5$, $TR = 1.0$)	0.067	7.14
SP07 ($Ma = 0.9$, $TR = 0.84$)	0.067	8.3
SP42 ($Ma = 0.5$, $TR = 2.7$)	0.084	5.88
SP46 ($Ma = 0.9$, $TR = 2.7$)	0.084	5.0
Panchapakesan and Lumley[83]	0.096	6.06
Hussein et al (hot wire)[84]	0.102	5.9
Hussein et al (laser-Doppler)[84]	0.094	5.8

3.3.2 Q Criterion

The Q criterion allows us to visualise the vortical structures within the jets, where positive values correspond to areas of the flow field where the vorticity magnitude is greater than the magnitude of the rate of strain.

The Q criterion was calculated for the $Ma = 0.9$ jets and a slice is shown in Figures 3.8,3.9 for SP07 and SP46 respectively. This allows us to visualise the vorticity of the jets and shows quite clearly that the heated case breaks down faster than the cold case.

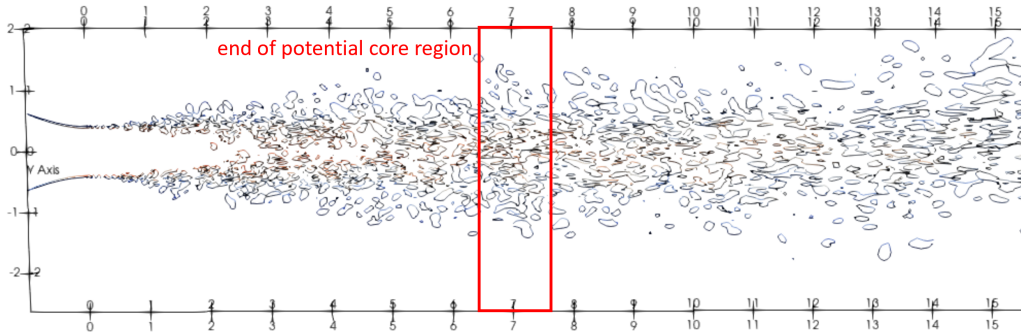

Figure 3.8: SP07: Q criterion

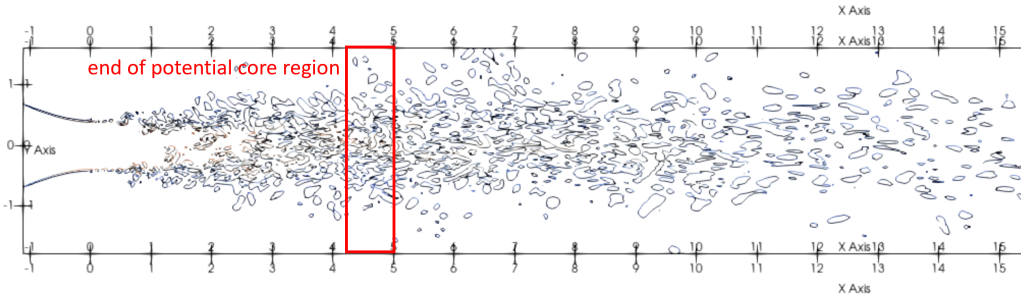

Figure 3.9: SP46: Q criterion

3.4 Summary

In this chapter we have calculated turbulence data using LES for four jets and validated the meanflow velocity and turbulence kinetic energy against experimental and computational simulations from the literature. This has completed the first stage of the jet noise calculation and Figure 3.10 shows that using this data we can now calculate the propagator and the turbulence statistics. Chapter 4 will focus on the Green's functions and propagator calculation and Chapters 5-6 will focus on the turbulence statistics and spectral tensor calculation.

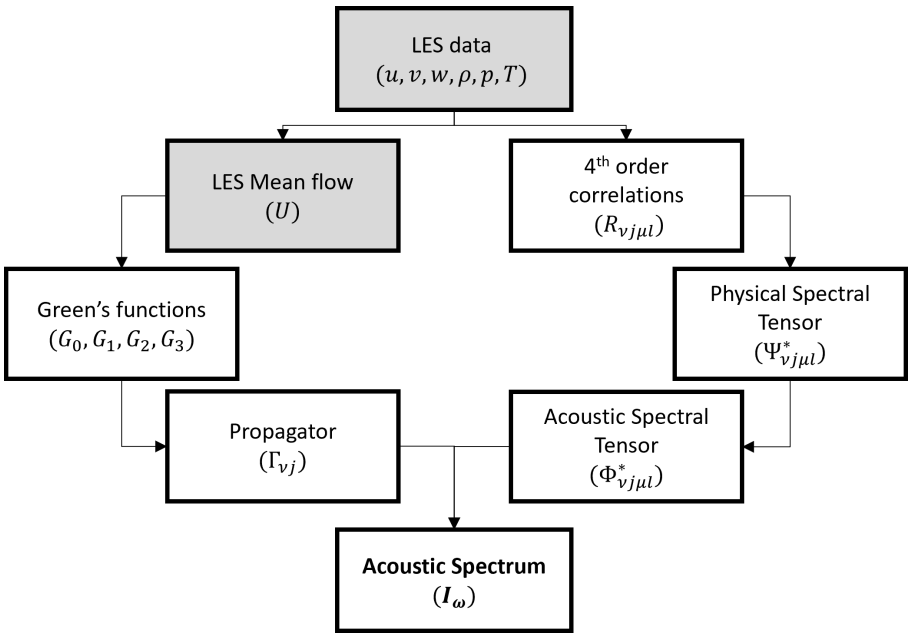

Figure 3.10: Chapter 3: Summary of process so far

Chapter 4

Jet Noise Modelling: Theory

As mentioned in the literature review, the acoustic analogy can be used to predict jet noise. In this thesis we use Goldstein's generalised acoustic analogy which rewrites the Navier Stokes equations as a wave equation where the wave operator is linear and acts upon non-linear variables. Since the operator is linear, Green's functions can be used to solve the equations.

This chapter goes over the mathematical derivation of Goldstein's acoustic analogy and its solution. Additionally, computational results of the propagator are discussed.

4.1 Goldstein's Acoustic Analogy

Goldstein's generalised acoustic analogy rearranges the Euler equations (i.e. setting viscous terms in (3.1.2)-(3.1.4) to zero), since viscosity and the heat flux vector were shown to not have a noticeable effect on the sound pressure level (SPL). The main feature of this analogy is the subtraction of a 'base' flow, from the equations, i.e. the evolution of the fluctuating fluid variables can be found by subtracting the time-averaged Euler equations from the full Euler equations, see Appendix A.1 for details. This results in the system of equations:

$$\frac{\partial \rho'}{\partial \tau} + \frac{\partial}{\partial y_j}(\rho' \tilde{v}_j + u_j) = 0 \tag{4.1.1}$$

$$\frac{\partial u_i}{\partial \tau} + \frac{\partial}{\partial y_j}(\tilde{v}_j u_j) + \frac{\partial p'}{\partial y_j} + \tilde{v}_j \frac{\partial \tilde{v}_i}{\partial y_j} + \rho' \tilde{v}_k \frac{\partial \tilde{v}_i}{\partial y_k} = \frac{\partial e_{ij}}{\partial y_j} \qquad i = 1, ..3. \tag{4.1.2}$$

$$\frac{1}{(\gamma - 1)} \frac{\partial p'}{\partial \tau} + \frac{1}{(\gamma - 1)} \frac{\partial}{\partial y_j}(p' \tilde{v}_j) + p' \frac{\partial \tilde{v}_j}{\partial y_j} + \frac{\partial}{\partial\ y_j}(u_j \tilde{h}) + u_i \tilde{v}_k \frac{\partial \tilde{v}_i}{\partial y_k} = Q \tag{4.1.3}$$

where the source terms are on the right hand side and are given by:

$$e_{ij} = -\left[\rho v_i' v_j' - \bar{\rho}\widetilde{v_i' v_j'}\right] \tag{4.1.4}$$

$$Q = -\tilde{v}_j \frac{\partial e_{ij}}{\partial y_i} + \frac{1}{2}\delta_{ij}\left[\frac{De_{ij}}{D\tau} + \frac{\partial \tilde{v}_k}{\partial y_k} e_{ij}\right] - \frac{\partial}{\partial y_i}\left[\rho v_j' h_0' - \bar{\rho}\widetilde{v_j' h_0'}\right] \tag{4.1.5}$$

and the stagnation enthalpy is $h_0 = h + v^2/2$, where its mean and perturbation are defined in Appendix A.1.3.

These equations can be written in terms of a linear operator L_{wave} acting on the fluid variables and another L_{source} acting on the source terms, which allows a solution to be found using Green's theorem. Since we are interested in finding the noise at an observer location $\boldsymbol{x}$ far away from the jet, it makes sense to use the adjoint Green's function (which has incoming wave behaviour at $(\boldsymbol{y}, \tau)$) rather than the direct Green's function (which has outgoing wave behaviour at $(\boldsymbol{y}, \tau)$). Therefore the adjoint Green's function decays at large τ.

We then take the inner product of the (4.1.1)-(4.1.3) with the adjoint Green's function $G_\mu(\boldsymbol{y}, \tau | x, t)$ where $\mu = 1, 2, 3, 4, 5$, and $G_i, i = 1, 2, 3$ are multiplied with the momentum equations, G_4 is multiplied with the energy equation and G_5 is multiplied with the mass equation. Taking the integral (over $\tau, V_\infty(\boldsymbol{y})$) of the sum of these equations, and using representation theory, allows us to obtain the linearised adjoint Green's function equations: (for full details refer to [85]).

$$\frac{\partial G_i}{\partial \tau} + \tilde{v}_j \frac{\partial G_i}{\partial y_j} + \frac{\partial G_5}{\partial y_i} - G_k \frac{\partial \tilde{v}_k}{\partial y_i} + \tilde{h}\frac{\partial G_4}{\partial y_i} - G_4 \tilde{v}_k \frac{\partial \tilde{v}_i}{\partial y_k} = 0 \qquad i = 1, ..3. \tag{4.1.6}$$

$$\frac{1}{\gamma - 1}\frac{\partial G_4}{\partial \tau} + \frac{\tilde{v}_j}{\gamma - 1}\frac{\partial G_4}{\partial y_j} - G_4 \frac{\partial \tilde{v}_j}{\partial y_j} + \frac{\partial G_j}{\partial y_j} = -\delta(\boldsymbol{x} - \boldsymbol{y})\delta(t - \tau) \tag{4.1.7}$$

$$\frac{\partial G_5}{\partial \tau} + \tilde{v}_j \frac{\partial G_5}{\partial y_j} - G_i \tilde{v}_k \frac{\partial \tilde{v}_i}{\partial y_k} = 0 \tag{4.1.8}$$

4.2 Parallel Flow Green's Function

4.2.1 Derivation

Now, for a parallel mean flow where $\tilde{v}_i = \delta_{i1} U(y_2, y_3), \bar{p} = const = p_\infty, \rho = \rho(y_2, y_3), \tilde{h} = \tilde{h}(y_2, y_3)$, (4.1.6)-(4.1.8) reduce to:

$$\frac{DG_i}{D\tau} + \frac{\partial G_5}{\partial y_i} - G_1\frac{\partial U}{\partial y_i} + \tilde{h}\frac{\partial G_4}{\partial y_i} = 0 \qquad i = 1, ..3. \tag{4.2.1}$$

$$\frac{1}{\gamma - 1}\frac{DG_4}{D\tau} + \frac{\partial G_j}{\partial y_j} = -\delta(\boldsymbol{x} - \boldsymbol{y})\delta(t - \tau) \tag{4.2.2}$$

$$\frac{DG_5}{D\tau} = 0 \tag{4.2.3}$$

where $D/D\tau = \partial/\partial\tau + U(y_2, y_3)\partial/\partial y_1$. As shown in Afsar (2009) [85], (4.2.1) can be further simplified by taking the material derivative:

$$\frac{D^2G_i}{D\tau^2} + \frac{D}{D\tau}\frac{\partial G_5}{\partial y_i} - \frac{DG_1}{D\tau}\frac{\partial U}{\partial y_i} - G_1\frac{D}{D\tau}\frac{\partial U}{\partial y_i} + \frac{D\tilde{h}}{D\tau}\frac{\partial G_4}{\partial y_i} + \tilde{h}\frac{D}{D\tau}\frac{\partial G_4}{\partial y_i} = 0 \tag{4.2.4}$$

Since $\tilde{h} = \tilde{h}(y_2, y_3)$, $D\tilde{h}/D\tau = 0$. Using (4.2.1) with $i = 1$ gives $DG_1/D\tau = -\partial G_5/\partial y_1 - \tilde{h}\partial G_4/\partial y_1$. and the commutative relation

$$\frac{D}{D\tau}\frac{\partial G}{\partial y_i} = \frac{\partial}{\partial y_i}\frac{DG}{D\tau} - \frac{\partial U}{\partial y_i}\frac{\partial G}{\partial y_1}$$

can be used to simplify (4.2.4):

$$\begin{aligned}\frac{D^2G_i}{D\tau^2} + \Big[\frac{\partial}{\partial y_i}\frac{DG_5}{D\tau} - \frac{\partial U}{\partial y_i}\frac{\partial G_5}{\partial y_1}\Big] - \Big[-\frac{\partial G_5}{\partial y_1} - \tilde{h}\frac{\partial G_4}{\partial y_1}\Big]\frac{\partial U}{\partial y_i} \\ - G_1\Big[\frac{\partial}{\partial y_i}\frac{DU}{D\tau} - \frac{\partial U}{\partial y_i}\frac{\partial U}{\partial y_1}\Big] + \tilde{h}\Big[\frac{\partial}{\partial y_i}\frac{DG_4}{D\tau} - \frac{\partial U}{\partial y_i}\frac{\partial G_4}{\partial y_1}\Big] = 0\end{aligned} \tag{4.2.5}$$

Cancelling terms and using (4.2.3), this reduces to,

$$\frac{D^2G_i}{D\tau^2} + \tilde{h}\frac{\partial}{\partial y_i}\frac{DG_4}{D\tau} = 0 \tag{4.2.6}$$

dividing through by $\tilde{c}^2 = \tilde{h}(\gamma - 1)$ gives,

$$\frac{1}{\tilde{c}^2}\frac{D^2G_i}{D\tau^2} + \frac{1}{\gamma - 1}\frac{\partial}{\partial y_i}\frac{DG_4}{D\tau} = 0 \tag{4.2.7}$$

then, by introducing a new variable $G_0 = \frac{1}{\gamma - 1}DG_4/D\tau$ in (4.2.2) and (4.2.7) we obtain what will henceforth be referred to as Afsar's conservation equations:

$$\frac{D^2G_i}{D\tau^2} + \tilde{c}^2\frac{\partial G_0}{\partial y_i} = 0 \qquad i = 1, ..3. \tag{4.2.8}$$

$$G_0 + \frac{\partial G_i}{\partial y_i} = -\delta(\boldsymbol{x} - \boldsymbol{y})\delta(t - \tau) \tag{4.2.9}$$

Note that these equations do not require the gradient of the mean flow which simplifies the process of finding the solution for a computational mean flow which may not be smooth.

Taking the Fourier transform in time of these equations gives:

$$(i\omega + U(y_2, y_3)\frac{\partial}{\partial y_1})^2\tilde{G}_i + \tilde{c}^2\frac{\partial}{\partial y_1}\tilde{G}_0 = 0 \tag{4.2.10}$$

$$\tilde{G}_0 + \frac{\partial}{\partial y_i}\tilde{G}_i = \frac{-\delta(\boldsymbol{x}-\boldsymbol{y})}{2\pi} \tag{4.2.11}$$

where

$$\tilde{G}_\sigma(\boldsymbol{y}|\boldsymbol{x};\omega) = \frac{1}{2\pi}\int_{-\infty}^{\infty} e^{i\omega(t-\tau)}G_\sigma(\boldsymbol{y}|\boldsymbol{x}, t-\tau)d(t-\tau) \tag{4.2.12}$$

$(\sigma = 0, 1, 2, 3, 4)$.

Now taking the Fourier transform in the streamwise direction:

$$\hat{G}_\sigma(\boldsymbol{y}_T|\boldsymbol{x}_T;\omega,k_1) = \frac{1}{2\pi}\int_{-\infty}^{\infty} e^{-ik_1(x_1-y_1)}\tilde{G}_\sigma(x_1-y_1,\boldsymbol{y}_T|\boldsymbol{x}_T;\omega)d(x_1-y_1) \tag{4.2.13}$$

$$\frac{\partial}{\partial y_i} = \delta_{i1}(-ik_1) + \frac{\partial}{\partial y_T}\delta_{iT} \tag{4.2.14}$$

gives

$$\hat{D}_0^2\hat{G}_i - \tilde{c}^2\frac{\partial\hat{G}_0}{\partial y_i} = 0 \tag{4.2.15}$$

$$\hat{G}_0 + \frac{\partial}{\partial y_i}\hat{G}_i = -\frac{\delta(\boldsymbol{x}_T-\boldsymbol{y}_T)}{(2\pi)^2} \tag{4.2.16}$$

where $\hat{D}_0 = (Uk_1-\omega)$. Rearranging (4.2.15) for $\hat{G}_i$ and inserting this into (4.2.16) gives:

$$\hat{G}_0 + \frac{\partial}{\partial y_i}\Big[\frac{\tilde{c}^2}{\hat{D}_0^2}\frac{\partial}{\partial y_i}\hat{G}_0\Big] = -\frac{\delta(\boldsymbol{x}_T-\boldsymbol{y}_T)}{(2\pi)^2} \tag{4.2.17}$$

Expanding the gradient operator using cylindrical coordinates and defining $A(r;k_1,\omega) = \tilde{c}^2/\hat{D}_0^2$ gives:

$$\begin{aligned}\hat{G}_0 + &\Big[-ik_1e_{1i} + \frac{\partial}{\partial r}e_{ri} + \frac{1}{r}\frac{\partial}{\partial\psi}e_{\psi i}\Big] \\ &\Big[A(r;k_1,\omega)\Big(-ik_1e_{1i} + \frac{\partial}{\partial r}e_{ri} + \frac{1}{r}\frac{\partial}{\partial\psi}e_{\psi i}\Big)\hat{G}_0\Big] = -\frac{1}{(2\pi)^2}\frac{\delta(R-r)\delta(\Psi-\psi)}{r}\end{aligned} \tag{4.2.18}$$

Using orthogonality conditions where $e_{mi}e_{mj} = 1$ (no sum on m) when $i = j$ and zero otherwise, and noting that $\partial e_{ri}/\partial\psi = e_{\psi i}$ and $\partial e_{\psi i}/\partial\psi = -e_{ri}$ reduces the left hand side of this equation to:

$$\begin{aligned}\hat{G}_0 + \Big[(-ik_1)^2 A(r;k_1,\omega) + \frac{\partial}{\partial r}\Big(A(r;k_1,\omega)\frac{\partial}{\partial r}\Big)\Big]\hat{G}_0 \\ + \frac{e_{\psi i}}{r}\frac{\partial}{\partial\psi}\Big[A(r;k_1,\omega)e_{ri}\frac{\partial}{\partial r}\Big]\hat{G}_0 + \frac{e_{\psi i}}{r}\frac{\partial}{\partial\psi}\Big[A(r;k_1,\omega)\frac{e_{\psi i}}{r}\frac{\partial}{\partial\psi}\Big]\hat{G}_0\end{aligned} \tag{4.2.19}$$

then, expanding the second line simplifies the equation and we can define the Rayleigh operator $\hat{L}_R$:

$$\underbrace{\Big[\Big(1 - k_1^2 A(r;k_1,\omega)\Big) + \frac{\partial}{\partial r}\Big(A(r;k_1,\omega)\frac{\partial}{\partial r}\Big) + \frac{A(r;k_1,\omega)}{r}\frac{\partial}{\partial r} + \frac{A(r;k_1,\omega)}{r^2}\frac{\partial^2}{\partial\psi^2}\Big]}_{\hat{L}_R}\hat{G}_0 \tag{4.2.20}$$

we can show that $\hat{L}_R$ is dimensionless, remember $A = \tilde{c}^2/\hat{D}_0^2 = \tilde{c}^2/(Uk_1 - \omega)^2 = [L^2]/[T^2]1/[T^{-2}] = [L^2]$, therefore:

$$[\hat{L}_R] = [1] - [L^{-2}][L^2] + [L^{-1}][L^2][L^{-1}] + [L^2][L^{-1}][L^{-1}] + [L^2][L^{-2}] = O(1)$$

Now, looking only at the terms in (4.2.20) with derivatives in r:

$$\begin{aligned}\frac{\partial A}{\partial r}\frac{\partial\hat{G}_0}{\partial r} + A\frac{\partial^2\hat{G}_0}{\partial r^2} + \frac{A}{r}\frac{\partial\hat{G}_0}{\partial r} &= \frac{1}{r}\Big[r\frac{\partial A}{\partial r}\frac{\partial\hat{G}_0}{\partial r} + A\frac{\partial\hat{G}_0}{\partial r}\Big] + A\frac{\partial^2\hat{G}_0}{\partial r^2} \\ &= \frac{1}{r}\Big[\frac{\partial}{\partial r}\Big(rA\frac{\partial\hat{G}_0}{\partial r}\Big) - A\frac{\partial}{\partial r}\Big(r\frac{\partial\hat{G}_0}{\partial r}\Big) + A\frac{\partial\hat{G}_0}{\partial r}\Big] + A\frac{\partial^2\hat{G}_0}{\partial r^2} \\ &= \frac{1}{r}\frac{\partial}{\partial r}\Big(rA\frac{\partial\hat{G}_0}{\partial r}\Big)\end{aligned} \tag{4.2.21}$$

Therefore we obtain the equation:

$$\Big(1 - k_1^2 A + \frac{A}{r^2}\frac{\partial^2}{\partial\psi^2}\Big)\hat{G}_0 + \frac{1}{r}\frac{\partial}{\partial r}\Big(rA\frac{\partial\hat{G}_0}{\partial r}\Big) = -\frac{1}{(2\pi)^2}\frac{\delta(R-r)\delta(\Psi-\psi)}{r} \tag{4.2.22}$$

We can take Fourier transforms in the azimuthal direction, noting that $\hat{G}_0$ only depends on ψ, Ψ through their difference $(\Psi - \psi)$:

$$\overline{G}_0^{(m)}(r|R;k_1,\omega,|\boldsymbol{x}|,\theta) = \frac{1}{2\pi}\int_{-\infty}^{\infty} e^{-im(\Psi-\psi)}\hat{G}_0(r|R,\Psi-\psi;k_1,\omega,|\boldsymbol{x}|,\theta)d(\Psi-\psi) \tag{4.2.23}$$

and

$$\frac{1}{2\pi}\int_{-\infty}^{\infty} e^{-im(\Psi-\psi)}\hat{L}_R(r,\psi;k_1,\omega)\Big[\hat{G}_0(r|R,\Psi-\psi;k_1,\omega)\Big]d(\Psi-\psi) = -\frac{1}{(2\pi)^3}\frac{\delta(R-r)}{r} \tag{4.2.24}$$

which can be written in terms of the m^{th} mode Rayleigh operator:

$$\overline{L}_R^{(m)}(r;k_1,\omega)\Big[\overline{G}_0^{(m)}(r|R;k_1,\omega,|\boldsymbol{x}|,\theta)\Big] = -\frac{1}{(2\pi)^3}\frac{\delta(R-r)}{r} \tag{4.2.25}$$

where

$$\overline{L}_R^{(m)}(r;k_1,\omega) = 1-(k_1^2+\frac{m^2}{r^2})A + \frac{1}{r}\frac{\partial}{\partial r}\Big(rA\frac{\partial}{\partial r}\Big) \tag{4.2.26}$$

Remember $A(r;k_1,\omega) = \tilde{c}^2/\hat{D}_0^2$ and

$$\begin{aligned}
\hat{D}_0 = Uk_1-\omega &= \omega\Big[\frac{Uk_1}{\omega}-1\Big] \\
&= \omega\Big[\frac{U}{c_\infty}\frac{c_\infty k_1}{\omega}-1\Big] \\
&= \omega\Big[M(r)\frac{k_1}{k_\infty}-1\Big] \\
&= c_\infty k_\infty\Big[M(r)\hat{k}_1-1\Big] \\
&= c_\infty k_\infty \overline{D}_0
\end{aligned} \tag{4.2.27}$$

where $\hat{k}_1 = k_1/k_\infty$. Then we can define $\tilde{c} = c_\infty/a_r$ where $a_r = c_\infty/\tilde{c}$. Therefore,

$$A(r;k_1,\omega) = \frac{\tilde{c}^2}{\hat{D}_0^2} = \frac{1}{a_r^2k_\infty^2\overline{D}_0^2} \tag{4.2.28}$$

So we can write (4.2.26) as:

$$\begin{aligned}
\overline{L}_R^{(m)}(r;k_1,\omega) &= \Big[1-\Big(k_1^2+\frac{m^2}{r^2}\Big)\frac{1}{a_r^2k_\infty^2\overline{D}_0^2}+\frac{1}{r}\frac{\partial}{\partial r}\Big(\frac{r}{a_r^2k_\infty^2\overline{D}_0^2}\frac{\partial}{\partial r}\Big)\Big] \\
&= \frac{1}{k_\infty^2}\overline{\overline{L}}_R^{(m)}(r;k_1,\omega)
\end{aligned} \tag{4.2.29}$$

where we define $\overline{\overline{L}}_R^{(m)}(r;k_1,\omega)$:

$$\overline{\overline{L}}_R^{(m)}(r;k_1,\omega) = \Big[k_\infty^2-\Big(k_1^2+\frac{m^2}{r^2}\Big)\frac{1}{a_r^2\overline{D}_0^2}+\frac{1}{r}\frac{\partial}{\partial r}\Big(\frac{r}{a_r^2\overline{D}_0^2}\frac{\partial}{\partial r}\Big)\Big] \tag{4.2.30}$$

Hence, (4.2.25) becomes:

$$\overline{\overline{L}}_R^{(m)}(r;k_1,\omega)\Big[\overline{G}_0^{(m)}(r|R;k_1,\omega,|\boldsymbol{x}|,\theta)\Big] = -\frac{k_\infty^2}{(2\pi)^3}\frac{\delta(R-r)}{r} \tag{4.2.31}$$

Note that this equation can be written in standard Sturm-Liouville form:

$$\Big[rQ(r;k_1,\omega)+\frac{d}{dr}\Big(rP(r;k_1,\omega)\frac{d}{dr}\Big)\Big]\overline{\overline{G}}_0^{(m)}(r|R;k_1,\omega,|\boldsymbol{x}|,\theta) = -\delta(R-r) \tag{4.2.32}$$

where

$$Q(r;k_1,\omega)=k_\infty^2-(k_1^2+\frac{m^2}{r^2})\frac{1}{a_r^2\overline{D}_0^2} \tag{4.2.33}$$

$$P(r;k_1,\omega)=\frac{1}{a_r^2\overline{D}_0^2} \tag{4.2.34}$$

and

$$\overline{\overline{G}}_0^{(m)}(r|R;k_1,\omega,|\boldsymbol{x}|,\theta)=\Big[\frac{(2\pi)^3}{k_\infty^2}\Big]\overline{G}_0^{(m)}(r|R;k_1,\omega,|\boldsymbol{x}|,\theta) \tag{4.2.35}$$

Note that $a_r\neq 0$ and $\overline{D}_0\neq 0$ since we restrict our analysis to subsonic jets. If $\overline{D}_0=0$ this is termed the 'critical layer' as it introduces a singularity.

4.2.2 Green's Function Solution to (4.2.32)

Since this is a standard Sturm-Liouville equation we can use the standard result given by (A.2.8) (see Appendix. A.2 for details):

$$\begin{aligned}\overline{\overline{G}}_0^{(m)}(r|R;k_1,\omega,|\boldsymbol{x}|,\theta)=&\frac{w_1^{(m)}(r;k_1,\omega,|\boldsymbol{x}|,\theta)w_2^{(m)}(R;k_1,\omega,|\boldsymbol{x}|,\theta)H(R-r)}{J^{(m)}(w_1,w_2)}\\&+\frac{w_2^{(m)}(r;k_1,\omega,|\boldsymbol{x}|,\theta)w_1^{(m)}(R;k_1,\omega,|\boldsymbol{x}|,\theta)H(r-R)}{J^{(m)}(w_1,w_2)}\end{aligned} \tag{4.2.36}$$

where w_1,w_2 are two linearly independent homogeneous solutions, H is the step function and J is the invariant. Therefore, inside the jet where $r<R$ we have the solution for $\overline{G}_0^{(m)}$:

$$\overline{G}_0^{(m)}(r|R;k_1,\omega,|\boldsymbol{x}|,\theta)=\frac{k_\infty^2}{(2\pi)^3}\frac{w_1^{(m)}(r;k_1,\omega,|\boldsymbol{x}|,\theta)w_2^{(m)}(R;k_1,\omega,|\boldsymbol{x}|,\theta)}{J^{(m)}(w_1,w_2)} \tag{4.2.37}$$

where we show in Appendix. A.2:

$$J^{(m)}(w_1,w_2)=J^{(m)}(k_1,\omega,|\boldsymbol{x}|,\theta)=-P(r_{end})r_{end}\Delta^{(m)}(k_1,\omega,|\boldsymbol{x}|,\theta) \tag{4.2.38}$$

where $\Delta^{(m)}(k_1,\omega,|\boldsymbol{x}|,\theta)=W(w_1^{(m)},w_2^{(m)})|_{r_{end}}$ is the dispersion relation and W is the Wronskian. Therefore:

$$\overline{G}_0^{(m)}(r|R;k_1,\omega,|\boldsymbol{x}|,\theta)=\frac{k_\infty^2}{(2\pi)^3}\frac{w_1^{(m)}(r;k_1,\omega,|\boldsymbol{x}|,\theta)w_2^{(m)}(R;k_1,\omega,|\boldsymbol{x}|,\theta)}{-P(r_{end})r_{end}\Delta^{(m)}(k_1,\omega,|\boldsymbol{x}|,\theta)} \tag{4.2.39}$$

Note that at r_{end}, since $M(r_{end})=0, a_r(r_{end})=1$ $P(r_{end})=1$.So

$$\overline{G}_0^{(m)}(r|R;k_1,\omega,|\boldsymbol{x}|,\theta)=\frac{k_\infty^2}{(2\pi)^3}\frac{w_1^{(m)}(r;k_1,\omega,|\boldsymbol{x}|,\theta)w_2^{(m)}(R;k_1,\omega,|\boldsymbol{x}|,\theta)}{-r_{end}\Delta^{(m)}(k_1,\omega,|\boldsymbol{x}|,\theta)} \tag{4.2.40}$$

Acoustic field equations for (w_1, w_2)

As mentioned (w_1, w_2) are homogeneous solutions which satisfy the conditions of the Green's function:

- continuity at $r = R$
- Jump in its derivative of $1/P(r)r$

which are proven in Appendix. A.2. The first solution, w_1, is the solution to:

$$\overline{\overline{L}}_R^{(m)}(r; k_1, \omega)\Big[w_1^{(m)}(r; k_1, \omega, |\boldsymbol{x}|, \theta)\Big] = 0 \tag{4.2.41}$$

where the operator is radially inhomogeneous, as are the P, Q coefficients:

$$\overline{\overline{L}}_R^{(m)}(r; k_1, \omega) = Q(r; k_1, \omega) + \frac{1}{r}\frac{d}{dr}\Big(rP(r; k_1, \omega)\frac{d}{dr}\Big) \tag{4.2.42}$$

This $w_1^{(m)}$ is found numerically as was done in [86] ($\tilde{G}_0^{(m)}$ in that paper).

The other solution $w_2^{(m)}(R; k_1, \omega, |\boldsymbol{x}|, \theta)$ where $R = r_{end}$ is then found by solving:

$$\overline{\overline{L}}_R^{(m)}(R; k_1, \omega)\Big[w_2^{(m)}(R; k_1, \omega, |\boldsymbol{x}|, \theta)\Big] = 0 \tag{4.2.43}$$

where

$$\overline{\overline{L}}_R^{(m)}(R; k_1, \omega) = Q(R; k_1, \omega) + \frac{1}{R}\frac{d}{dR}\Big(RP(r; k_1, \omega)\frac{d}{dR}\Big) \tag{4.2.44}$$

We have already shown that $P(R; k_1, \omega) = 1$, therefore $Q(R; k_1, \omega) = k_\infty^2 - k_1^2 - m^2/R^2$ and the operator is given by:

$$\begin{aligned}\overline{\overline{L}}_R^{(m)} &= \Big[(k_\infty^2 - k_1^2) - \frac{m^2}{R^2} + \frac{1}{R}\frac{d}{dR} + \frac{d^2}{dR^2}\Big] \\ &= \Big[\frac{d^2}{dR^2} + \frac{1}{R}\frac{d}{dR} + (\gamma_R^2(k_1; k_\infty) - \frac{m^2}{R^2})\Big]\end{aligned} \tag{4.2.45}$$

where $\gamma_R^2(k_1; k_\infty) = k_\infty^2 - k_1^2$. This operator is outgoing in $(\boldsymbol{x}, t)$/incoming in $(\boldsymbol{y}, \tau)$. The standard solution to this equation is the Hankel transform:

$$w_2^{(m)}(R; k_1, \omega) = H_m^{(1)}(\gamma_R R) = H_m^{(1)}\big(\sqrt{k_\infty^2 - k_1^2}R\big) \tag{4.2.46}$$

Therefore, the Green's function solution inside the jet is given by:

$$\boxed{\overline{G}_0^{(m)}(r|R; k_1, \omega, |\boldsymbol{x}|, \theta) = -\frac{k_\infty^2}{(2\pi)^3}A_m(k_1, \omega, \theta)w_1^{(m)}(r; k_1, \omega, |\boldsymbol{x}|, \theta)H_m^{(1)}(\gamma_R R)} \tag{4.2.47}$$

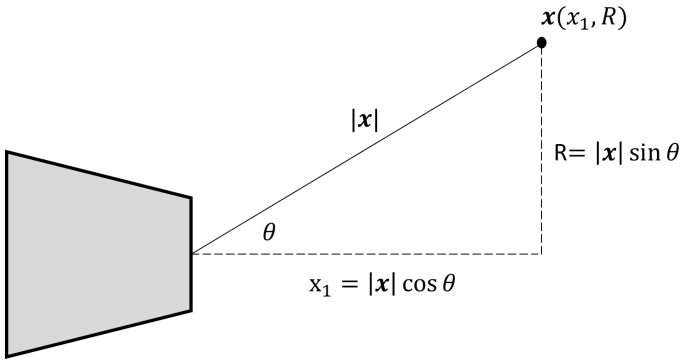

Figure 4.1: Geometry of the problem

where

$$A_m(k_1, \omega, \theta) = \frac{1}{r_{end}\Delta^{(m)}(k_1, \omega, \theta)|_{r_{end}}} \tag{4.2.48}$$

Now since $w_2^{(m)}(R; k_1, \omega, |\boldsymbol{x}|, \theta)$ is found at the maximum radius R, which using the geometry of the problem shown in Figure 4.1 we can rewrite in terms of the distance $|\boldsymbol{x}|$:

$$w_2^{(m)}(R; k_1, \omega, |\boldsymbol{x}|, \theta) = H_m^{(1)}(\gamma_R |\boldsymbol{x}| \sin\theta)$$

Then when we take the asymptotic limit at $|\boldsymbol{x}| \to \infty$, this is given by:

$$w_2^{(m)}(R; k_1, \omega, |\boldsymbol{x}|, \theta) = \sqrt{\frac{2}{\pi\gamma_R R}} \exp\left[i\Big(\gamma_R R - \frac{m\pi}{2} - \frac{\pi}{4}\Big)\right] \tag{4.2.49}$$

We can write the Green's function solution simply as:

$$\overline{G}_0^{(m)}(r|R; k_1, \omega, |\boldsymbol{x}|, \theta) = \Phi^{(m)}(k_1, \omega, \theta) w_2^{(m)}(R; k_1, \omega, |\boldsymbol{x}|, \theta) \tag{4.2.50}$$

where

$$\Phi^{(m)}(k_1, \omega, \theta) = -\frac{k_\infty^2}{(2\pi)^3} A_m(k_1, \omega, \theta) w_1^{(m)}(r; k_1, \omega, |\boldsymbol{x}|, \theta) \tag{4.2.51}$$

which in the limit $|\boldsymbol{x}| \to \infty$ is:

$$\overline{G}_0^{(m)}(r|R; k_1, \omega, |\boldsymbol{x}|, \theta) = \sqrt{\frac{2}{\pi\gamma_R R}} \Phi^{(m)}(k_1, \omega, \theta) \exp\left[i\Big(\gamma_R R - \frac{m\pi}{2} - \frac{\pi}{4}\Big)\right] \tag{4.2.52}$$

Now, to return back to spatial coordinates we begin by taking the inverse Fourier transform in k_1 which gives:

$$\tilde{G}_0^{(m)}(y_1, r|R; \omega, |\boldsymbol{x}|, \theta) = \int_{-\infty}^{\infty} e^{ik_1(x_1 - y_1)} \overline{G}_0^{(m)}(r|R; k_1, \omega, |\boldsymbol{x}|, \theta) dk_1 \tag{4.2.53}$$

and under the limit $|\boldsymbol{x}| \to \infty$:

$$\lim_{|\boldsymbol{x}|\to\infty} \tilde{G}_0^{(m)} = \lim_{|\boldsymbol{x}|\to\infty} \int_{-\infty}^{\infty} e^{ik_1 x_1} \underbrace{\left[e^{-ik_1 y_1}\Phi^{(m)}(k_1,\omega,\theta)\sqrt{\frac{2}{\pi\gamma_R R}}e^{-i(m\pi/2+\pi/4)}\right]}_{\tilde{\Phi}^{(m)}} e^{i\gamma_R R} dk_1 \tag{4.2.54}$$

Using $x_1 = |\boldsymbol{x}|\cos\theta$ and $R = |\boldsymbol{x}|sin\theta$, the equation can be written as:

$$\lim_{|\boldsymbol{x}|\to\infty} \tilde{G}_0^{(m)}(y_1, r|R;\omega,|\boldsymbol{x}|,\theta) = \lim_{|\boldsymbol{x}|\to\infty} \int_{-\infty}^{\infty} e^{ik_1|\boldsymbol{x}|\cos\theta + i\gamma_R|\boldsymbol{x}|\sin\theta}\tilde{\Phi}^{(m)}(k_1,\omega,|\boldsymbol{x}|,\theta)dk_1 \tag{4.2.55}$$

Finally, we can define $h(k_1, k_\infty) = k_1\cos\theta + \gamma_R \sin\theta$ which results in the standard form:

$$\boxed{\lim_{|\boldsymbol{x}|\to\infty} \tilde{G}_0^{(m)}(y_1, r|R;\omega,|\boldsymbol{x}|,\theta) = \lim_{|\boldsymbol{x}|\to\infty} \int_{-\infty}^{\infty} e^{i|\boldsymbol{x}|h(k_1,k_\infty)}\tilde{\Phi}^{(m)}(k_1,\omega,|\boldsymbol{x}|,\theta)dk_1} \tag{4.2.56}$$

Evaluation of integral (4.2.56) via Complexification

This integral can be solved in the Complex plane, where we represent the Cauchy principal value using $⨍$ indicating the integral limits going to ∞, and removing any singularities on our contour C:

$$\lim_{|\boldsymbol{x}|\to\infty} \tilde{G}_0^{(m)}(y_1, r|R;\omega,|\boldsymbol{x}|,\theta) = \lim_{|\boldsymbol{x}|\to\infty} ⨍_C e^{i|\boldsymbol{x}|h(k_1,k_\infty)}\tilde{\Phi}^{(m)}(k_1,\omega,|\boldsymbol{x}|,\theta)dk_1 \tag{4.2.57}$$

where $k_1 = \xi + i\eta$ is now complex. This means γ_R^2 can now be written as $\gamma_R^2 = \overline{\gamma}_R = k_\infty^2 - k_1^2 = k_\infty^2 - \xi^2 + \eta^2 - 2\xi\eta i$. Which can also be written in terms of magnitude and angle as:

$$\begin{aligned}\overline{\gamma}_R &= |\overline{\gamma}_R|e^{i\arg\overline{\gamma}_R} \\ &= |\overline{\gamma}_R|e^{i(\arg\overline{\gamma}_R + 2n\pi)}\end{aligned} \tag{4.2.58}$$

where $\arg\overline{\gamma}_R = Im(\overline{\gamma}_R)/Re(\overline{\gamma}_R)$ and $2n\pi$ can be added to the angle since by Euler's formula $e^{2n\pi i} = \cos(2n\pi) + i\sin(2n\pi) = 1$, therefore we can revolve $2n\pi$ around the complex plane and there is no change to $\overline{\gamma}_R$.

Since $\gamma_R^2 = (k_\infty^2 - k_1^2)$ we can introduce two new variables:

$$k_1^a = (k_\infty + k_1) = |k_\infty + k_1|e^{i\arg(k_\infty + k_1)} = |k_1^a|e^{i(\arg|k_1^a| + 2n_a\pi)} \tag{4.2.59}$$

$$k_1^b = (k_\infty - k_1) = |k_\infty - k_1|e^{i\arg(k_\infty - k_1)} = |k_1^b|e^{i(\arg|k_1^b| + 2n_b\pi)} \tag{4.2.60}$$

where n_a, n_b are two integers. Then γ_R^2 can be written as:

$$\gamma_R^2 = k_1^a k_1^b = |k_1^a||k_1^b| e^{i(\arg k_1^a + \arg k_1^b + 2N\pi)} \tag{4.2.61}$$

where $N = n_a + n_b$ is still an integer, and therefore $e^{i2N\pi}$ still has no impact on γ_R^2. The problem enters when we take the square root to find γ_R, since this gives:

$$\gamma_R^{(N)} = |\overline{\gamma}_R|^{1/2} e^{i(1/2 \arg \overline{\gamma}_R + N\pi)} \tag{4.2.62}$$

Now the $e^{iN\pi}$ will change γ_R depending on whether the N chosen is even or odd:

$$\gamma_R^{(0)} = |\overline{\gamma}_R|^{1/2} e^{i(1/2 \arg \overline{\gamma}_R)}$$

$$\gamma_R^{(1)} = |\overline{\gamma}_R|^{1/2} e^{i(1/2 \arg \overline{\gamma}_R + \pi)} = -\gamma_R^{(0)}$$
$$\gamma_R^{(2)} = |\overline{\gamma}_R|^{1/2} e^{i(1/2 \arg \overline{\gamma}_R + 2\pi)} = \gamma_R^{(0)}$$

Therefore if we circulate the origin of $\overline{\gamma}_R$ by 2π then $\gamma_R = \overline{\gamma}_R^{1/2}$ changes sign. However if we circulate twice about the origin the sign returns to the original $\gamma_R^{(0)}$. Since there are infinitely many branches of γ_R since $N \to \infty$ there is arbitrariness over which branch we choose in order to define γ_R.

We have shown that in order to maintain sign parity in γ_R (which appears in h) we have to circulate the origin twice. However, we cannot do this if we wish to apply Cauchy's residue theorem which only applies within one circulation of the Complex plane (i.e. for $0 < arg(k_1) < 2\pi$). Therefore, if we want to maintain $0 < \arg \gamma_R < 2\pi$ we must remove a line (branch cut) of fixed arg from the complex plane. This means we cannot cross the real axis as this gives a change in sign and the branch cut is an interval of length 2π where $\arg \gamma_R = (\theta_0, \theta_0 + 2\pi)$.

The branch cut connects the branch points which are defined as the points where $\gamma_R = 0$:

$$\gamma_R = (k_1^a k_1^b)^{1/2} \tag{4.2.63}$$

Therefore, the branch points are $k_1^a = k_\infty + k_1 = 0 \to k_1 = -k_\infty$, and $k_1^b = k_\infty - k_1 = 0 \to k_1 = k_\infty$.

Alternatively, we can define $k_1^a = 1/\xi^a$, $k_1^b = 1/\xi^b$ and the corresponding branch points are $\xi^a = \xi^b = 0$. This means $k_1^a = k_1^b = \infty$ are also branch points. Therefore in terms of k_1, these branch points are: $k_1 \to \pm\infty$. Therefore the branch cuts are indicated in red in Figure 4.2(a). Then the indented contour that will be taken to exclude the branch cut is shown in the dashed black line

in Figure 4.2(b), this includes taking a small radius around the branch points. However, when this indented contour is deformed it will cross the real axis. Therefore, we rotate the branch cut around the branch points by 90 degrees, which is shown in Figure 4.2(c). Note that this does not impact the indented contour.

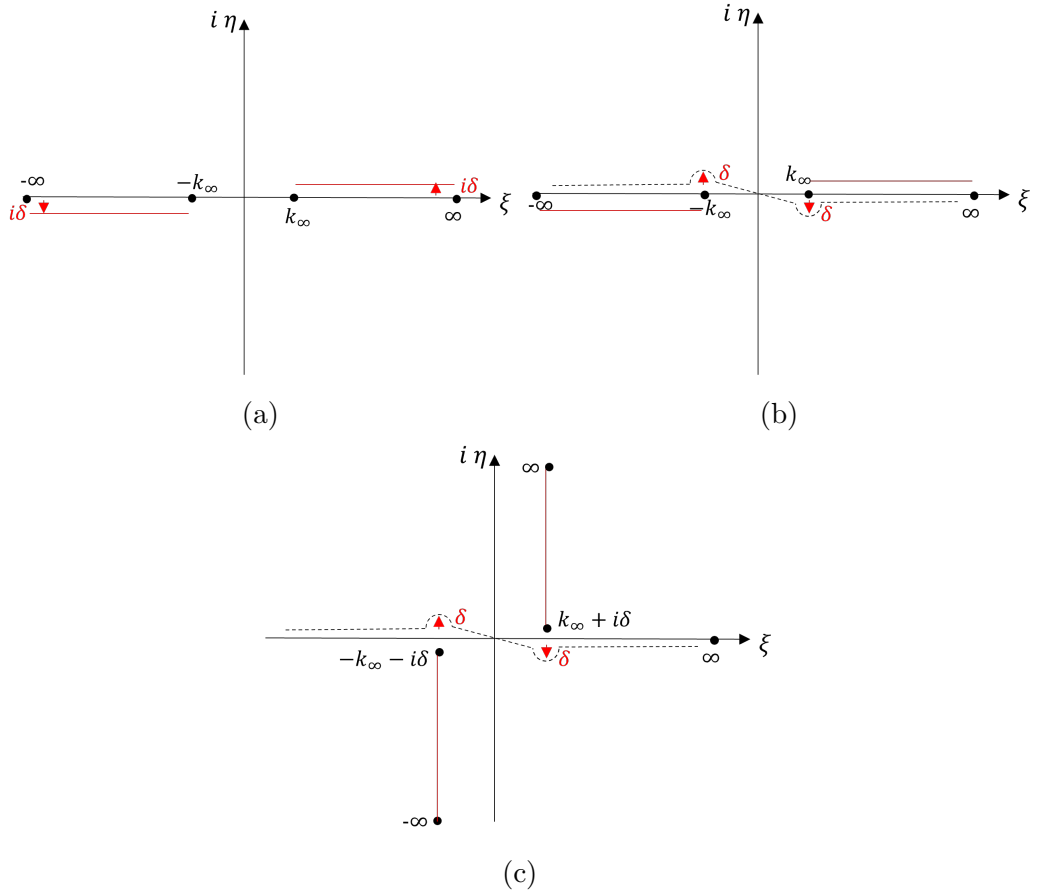

Figure 4.2: Visualisation of the branch cut on the complex plane needed for calculating the inverse Fourier transform in k_1 for $\overline{G}_0^{(m)}$ (a) chosen branch cut, (b) corresponding indented contour, (c) rotated branch cut

Asymptotic Expansion of (4.2.57)

We have shown that $\gamma_R = \pm\sqrt{k_\infty^2 - k_1^2}$, so we need to choose a value for γ_R that satisfies wave behaviour. If γ_R is real, then $k_1 < k_\infty$ and we choose the positive root which gives the correct behaviour of an outgoing wave at the observation point (t, R). If γ_R is complex, then $k_1 > k_\infty$ and for outgoing wave behaviour we choose the positive root so $\gamma_R = i\sqrt{k_1^2 - k_\infty^2}$.

Looking at the inverse Fourier Transform in ω shows why the positive root was chosen:

$$\begin{aligned} g^{(m)}(t-\tau,|x|,\theta) &= \int_{-\infty}^{\infty} G_0^{(m)}(\omega,|x|,\theta)e^{-i\omega(t-\tau)}d\omega \\ &= \int_{-R}^{R}\int_{-\infty}^{\infty} \tilde{\Phi}^{(m)}(k_1,\omega,|x|,\theta)e^{i\omega\tau}e^{ik_1|x|\cos\theta}e^{-i\omega t}e^{i\gamma_R R}d\omega dk_1 \\ &= \int_{-R}^{R}\int_{-\infty}^{\infty} A[e^{-i(\omega t-\gamma_R R)}]d\omega dk_1 \end{aligned} \tag{4.2.64}$$

where $A = \tilde{\Phi}^{(m)}(k_1,\omega,|x|,\theta)e^{i\omega\tau}e^{ik_1x_1}$, then, differentiating implicitly we see this becomes $-iA(\omega dt - \gamma_R dR) = 0$, which can be rearranged to give the phase speed of waves going to (R,t), i.e. $dR/dt = \omega/\gamma_R > 0$ is outwardly propagating when $\gamma_R > 0$. Hence, the positive branch of the single values square root for γ_R is chosen.

The integral starts off on the indented real axis which avoids the branch points:

$$\int_{-N}^{N} \tilde{\Phi}^{(m)}(k_1,\omega,|\boldsymbol{x}|,\theta)e^{i|\boldsymbol{x}|h(k_1,k_\infty)}dk_1 \qquad k_1 \in \mathbb{R} \tag{4.2.65}$$

moving this integral to the complex plane gives:

$$J^{(m)}(\omega,|x|,\theta) = \int_C \tilde{\Phi}^{(m)}(k_1,\omega,|\boldsymbol{x}|,\theta)e^{i|\boldsymbol{x}|h(k_1,k_\infty)}dk_1 \qquad k_1 \in \mathbb{C} \tag{4.2.66}$$

where we define the contour C as the path of steepest descent where

$$h'(k_1^*,k_\infty) = 0$$

and the prime denotes differentiation with respect to k_1, and k_1^* is the stationary point. A pictorial representation of the deformed contour is shown in Figure 4.3 which shows the contour split into four (L_1, L_2, Γ_N, C') and how it avoids crossing the branch cuts.

Then the integral can be split into four corresponding to the different regions of the contour:

$$\begin{aligned} J^{(m)} = &\int_{\Gamma_N} \tilde{\Phi}^{(m)}(k_1,\omega,|\boldsymbol{x}|,\theta)e^{i|\boldsymbol{x}|h(k_1,k_\infty)}dk_1 - \int_{L_1} \tilde{\Phi}^{(m)}(k_1,\omega,|\boldsymbol{x}|,\theta)e^{i|\boldsymbol{x}|h(k_1,k_\infty)}dk_1 \\ &- \int_{L_2} \tilde{\Phi}^{(m)}(k_1,\omega,|\boldsymbol{x}|,\theta)e^{i|\boldsymbol{x}|h(k_1,k_\infty)}dk_1 - \int_{C'} \tilde{\Phi}^{(m)}(k_1,\omega,|\boldsymbol{x}|,\theta)e^{i|\boldsymbol{x}|h(k_1,k_\infty)}dk_1 \end{aligned} \tag{4.2.67}$$

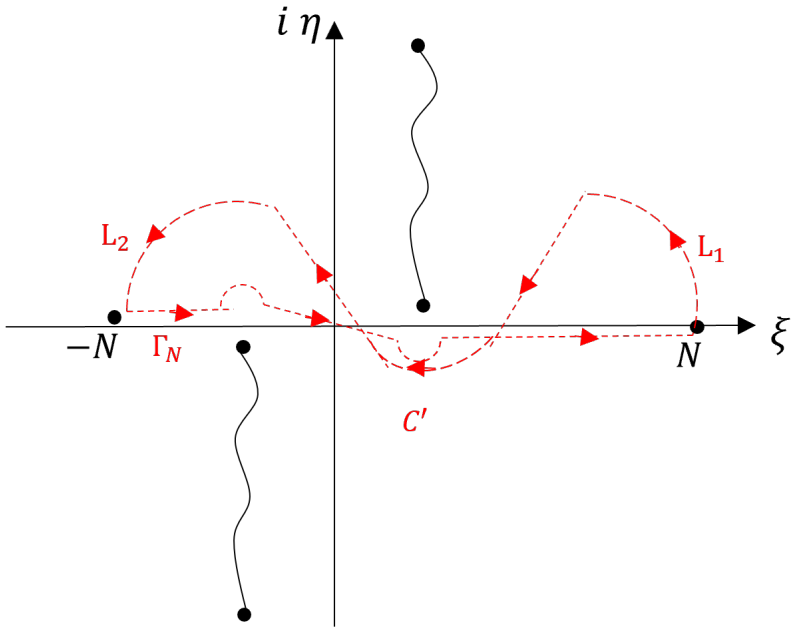

Figure 4.3: Deformed contour consisting of four sections L_1, L_2, Γ_N, C'.

Now, the integral over Γ_N is neglected since it is equal to the residues from the branch points but we do not know what they are. Then we can bound the integrals over L_1, L_2 by looking at an integral over a wedge using Jordan's Lemma. Later, we show the angle of the wedge can be estimated as $\pi/4$, then if we define $k_1 = Ke^{i\alpha}$, where $K = |k_1|$, $\alpha = arg(k_1)$, changing variables to α, the integral is given by:

$$\int_{L_1} \tilde{\Phi}^{(m)}(k_1) e^{i|\boldsymbol{x}|\gamma_R(k_1)\sin\theta} e^{iK|x|\cos\theta\cos\alpha} e^{-K|x|\cos\theta\sin\alpha} Kie^{i\alpha} d\alpha \tag{4.2.68}$$

using Jordan's Lemma for a wedge, this integral can be bounded:

$$\begin{aligned}\int_{L_1} \tilde{\Phi}^{(m)}(k_1) e^{i|\boldsymbol{x}|h(k_1,k_\infty)} dk_1 &\leq \int_0^{\pi/4} |\overline{\Phi}^{(m)}(k_1) e^{-K|x|\cos\theta\sin\alpha} K| d\alpha \\ &\leq \overline{\Phi}^{(m)}(k_1) K e^{-K|x|\cos\theta\sin\alpha} \frac{\pi}{4} \\ &\leq O(K^n e^{-K|x|\cos\theta\sin\alpha}) = o(1)\end{aligned} \tag{4.2.69}$$

since $K \to \infty$ and the exponential will go to zero. Here we have included the modulation terms into $\overline{\Phi}^{(m)}(k_1)$. The integral of L_2 will be identical since the parabola is symmetric and the transformation of a circle on the origin along the real axis has no effect on bounds. Hence, in the limit $N \to \infty$ the integrals over L_1, L_2 are neglected. Therefore the contour integral becomes:

$$I^{(m)}(\omega, |x|, \theta) = \lim_{|x|\to\infty} \int_{C'} \tilde{\Phi}^{(m)}(k_1, \omega, |\boldsymbol{x}|, \theta) e^{i|\boldsymbol{x}|h(k_1,k_\infty)} dk_1 \tag{4.2.70}$$

Remember that C' is the contour where $h'(k_1^*) = 0$, so we can use Laplace's method to rewrite this integral as a Taylor expansion:

$$I^{(m)}(\omega, |x|, \theta) = \int_{C'} \Big[\tilde{\Phi}^{(m)}(k_1^*) + O(k_1 - k_1^*)\Big] \exp\Big[i|x|\big(h(k_1^*) + 0.5(k_1 - k_1^*)^2 h''(k_1^*) + O(k_1 - k_1^*)^3\big)\Big] dk_1 \tag{4.2.71}$$

which is

$$I^{(m)}(\omega, |x|, \theta) = \tilde{\Phi}^{(m)}(k_1^*) e^{i|x|h(k_1^*)} \int_{C'} e^{i|x|/2(k_1 - k_1^*)^2 h''(k_1^*)} dk_1 \tag{4.2.72}$$

The integral over C' was chosen to be dominated by the stationary point, therefore we can increase the limits to ∞, then defining $s = k_1 - k_1^*$ and $\alpha = -h''(k_1^*)$ simplifies the integral to:

$$I^{(m)}(\omega, |x|, \theta) = \tilde{\Phi}^{(m)}(k_1^*) e^{i|x|h(k_1^*)} \int_{-\infty}^{\infty} \exp\Big[-\frac{i|x|}{2} s^2 \alpha\Big] ds \tag{4.2.73}$$

Currently, s is in the complex plane but we are integrating along the real axis from $-\infty$ to ∞. We can rotate s by $\pi/4$ by introducing $s' = se^{i\pi/4}$, then $s^2 = s'^2 e^{-i\pi/2} = -is'^2$, and $ds = ds' e^{i\pi/4}$, so the integral becomes:

$$I^{(m)}(\omega, |x|, \theta) = \tilde{\Phi}^{(m)}(k_1^*) e^{i|x|h(k_1^*)} e^{-i\pi/4} \int_{-\infty}^{\infty} \exp\Big[-As'^2\Big] ds' \tag{4.2.74}$$

where $A = |x|/2\alpha$. Lastly introducing $\overline{s} = \sqrt{A}s'$ converts the integral into the well known Gaussian integral:

$$I^{(m)}(\omega, |x|, \theta) = \tilde{\Phi}^{(m)}(k_1^*) e^{i|x|h(k_1^*)} e^{-i\pi/4} \frac{1}{\sqrt{A}} \int_{-\infty}^{\infty} e^{-\overline{s}^2} d\overline{s} \tag{4.2.75}$$

which has the solution $\sqrt{\pi}$, therefore the Green's function becomes:

$$G^{(m)}(\omega, |x|, \theta) = \tilde{\Phi}^{(m)}(k_1^*, \omega, \theta) e^{i|x|h(k_1^*)} e^{-i\pi/4} \sqrt{\frac{\pi}{|x|/2\alpha}} \tag{4.2.76}$$

Now we find the stationary point k_1^* by looking at $h'(k_1^*) = 0$

$$h'(k_1^*) = \cos\theta - \frac{k_1^* \sin\theta}{\sqrt{k_\infty^2 - k_1^{*2}}} = 0 \rightarrow \boxed{k_1^* = k_\infty \cos\theta} \tag{4.2.77}$$

where $k_1^* = +k_\infty \cos\theta$ since this is the physically admissible wave number which gives the correct outgoing wave in (R, t) coordinates, i.e. it propagates from the jet to the observer.

We find α by calculating the second derivative and evaluating it at the stationary point:

$$\alpha = \frac{k_\infty^2 \sin\theta}{(k_\infty^2 - k_\infty^2 \cos^2\theta)^{3/2}} = \frac{k_\infty^2 \sin\theta}{k_\infty^3 \sin^3\theta} = \frac{1}{k_\infty \sin^2\theta} \tag{4.2.78}$$

Then we find $h(k_1^*)$:

$$h(k_1^*) = k_\infty \cos^2\theta + \sqrt{k_\infty^2 - k_\infty^2 \cos^2\theta}\sin\theta = k_\infty \tag{4.2.79}$$

substituting these results back into (4.2.76) gives:

$$G_0^{(m)}(\omega, |x|, \theta) = \tilde{\Phi}^{(m)}(k_1^*, \omega, \theta) e^{i(|x|k_\infty - i\pi/4)} \sqrt{\frac{2k_\infty \pi}{|x|}} \sin\theta \tag{4.2.80}$$

Remember that $\tilde{\Phi}^{(m)}$ can be expanded using (4.2.54), and note that $\gamma_R = \sqrt{k_\infty^2 - k_1^{*^2}} = k_\infty \sin\theta$, therefore:

$$\tilde{\Phi}^{(m)}(y_1, R, k_1^*, \omega, \theta) = e^{ik_1^* y_1} \Phi^{(m)}(k_1^*, \omega, \theta) \sqrt{\frac{2}{\pi k_\infty \sin\theta R}} e^{-im\pi/2 - i\pi/4} \tag{4.2.81}$$

Then using (4.2.51) for $\Phi^{(m)}(k_1^*, \omega, \theta)$:

$$\boxed{G_0^{(m)}(y_1, r, \omega, |x|, \theta) = \frac{k_\infty^2}{(2\pi)^3 |x|} e^{ik_\infty(|x| - y_1\cos\theta)} A_m(k_\infty \cos\theta, \omega, \theta) w_1^{(m)}(r) e^{-im\pi/2}} \tag{4.2.82}$$

where we have absorbed a factor of $2i$ into A_m, so now:

$$A_m(k_1, \omega, \theta) = \frac{2i}{r_{end} \Delta^{(m)}(k_1, \omega, \theta)|_{r_{end}}} \tag{4.2.83}$$

Now during this analysis we found the stationary point $k_1^* = \xi = k_\infty \cos\theta$ and we assumed that using the path of steepest descent meant that the integral was dominated by the result at this stationary point. To find the exact path of stationary phase we define a new variable: $\Lambda_S(k_1) = |\boldsymbol{x}| h(k_1, k_\infty)$. Then we can look at the real and imaginary parts, where we take the real part to be a constant which is fixed as $h(k_1^*) = k_\infty$. Then we only have to find the imaginary part of $\Lambda_S(k_1)$. Then we can write:

$$\frac{1}{|\boldsymbol{x}|}\Lambda_S(k_1) = k_\infty + iIm(h) = k_1 \cos\theta + \sqrt{k_\infty^2 - k_1^2}\sin\theta \tag{4.2.84}$$

Setting $k_1 = \xi + i\eta$ and equating real and imaginary parts gives us an expression for the imaginary part of h: $Im(h) = \eta\cos\theta - \xi\eta\sin^2\theta/\overline{k}_\infty$. Where $\overline{k}_\infty = k_\infty - \xi\cos\theta$. This can then be used to obtain the exact path of stationary phase:

$$\eta(\xi) = -\frac{(k_\infty - \xi\cos\theta)(\xi - k_\infty\cos\theta)}{\sin\theta\sqrt{(\xi - k_\infty\cos\theta)^2 + k_\infty^2 \sin\theta^2}} \tag{4.2.85}$$

which is shown in Figure 4.4 at $\theta = 30, St = 0.2, M_\infty = 0.9$ where we can see it crosses the real axis twice, the first crossing is when $k_1 = k_\infty \cos\theta = k_1^*$ and the second is when $k_1 = k_\infty / \cos\theta$. Now, if we approximate the parabola with a straight line where it crosses the ξ-axis, it can be estimated that the angle is given by θ, as shown in the Figure. Then if we consider large $|\xi| >> 0$ and $|\eta| >> 0$ $\eta/\xi \to 1$ then from (4.2.85) $\eta/\xi \approx \cos\theta/|\sin\theta| \approx 1$, therefore $\cos\theta = \sin\theta = 1$, and $\theta = \pi/4$.

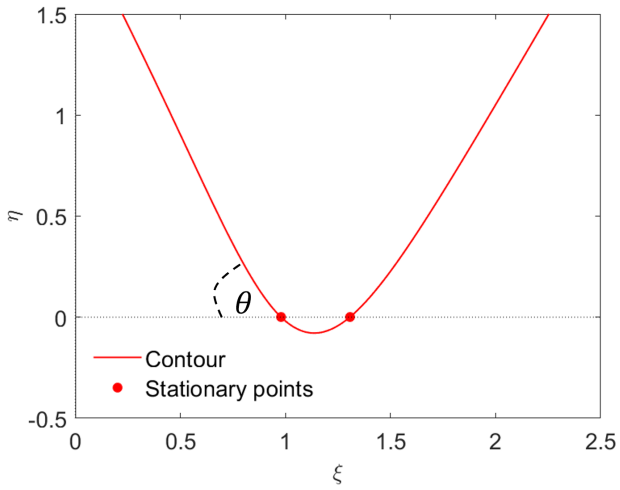

Figure 4.4: Contour of stationary phase

Inverse Fourier transform in m

Now, lastly to obtain the Green's function as a function of azimuthal angle $(\Psi - \psi)$, we need to take the inverse Fourier transform in m. This can be written as a Fourier series:

$$\begin{aligned} G_0(r, y_1, \Psi - \psi, \omega, |x|, \theta) &= \int_{-\infty}^{\infty} G_0^{(m)}(r, y_1, \omega, |x|, \theta) e^{-im(\Psi-\psi)} dm \\ &= \sum_{m=-\infty}^{\infty} G_0^{(m)}(r, y_1, \omega, |x|, \theta) e^{-im(\Psi-\psi)} \end{aligned} \tag{4.2.86}$$

Therefore, the Green's function can be written succinctly as:

$$G_0(r, y_1, \Psi - \psi, \omega, |x|, \theta) = \frac{k_\infty^2}{(2\pi)^3 |x|} e^{ik_\infty(|x| - y_1\cos\theta)} \sum_{m=-\infty}^{\infty} \overline{Q}_m(r, k_\infty \cos\theta, \Psi - \psi) \tag{4.2.87}$$

where $\overline{Q}_m(r, k_\infty \cos\theta, \Psi - \psi) = A_m(k_\infty \cos\theta, \omega, \theta) w_1^{(m)}(r) e^{-im\pi/2} e^{-im(\Psi-\psi)}$. Then we can split the sum into three parts: negative m, positive m, and $m = 0$.

$$\sum_{m=-\infty}^{\infty} \overline{Q}_m(r, k_\infty \cos\theta, \Psi - \psi) = \sum_{m=-\infty}^{-1} \overline{Q}_m + \overline{Q}_0 + \sum_{m=1}^{\infty} \overline{Q}_m \tag{4.2.88}$$

Then defining $n = -m$, brings the first term to $\sum_{n=\infty}^{1} \overline{Q}_{-n}$, then, since n is a dummy variable we can go back to m, giving the sum:

$$\sum_{m=-\infty}^{\infty} \overline{Q}_m(r, k_\infty \cos\theta, \Psi - \psi) = \sum_{m=1}^{\infty} (\overline{Q}_{-m} + \overline{Q}_m) + \overline{Q}_0 \tag{4.2.89}$$

Now we need to look at the symmetry of the $\overline{Q}$ term. Firstly, looking at the $w_1^{(m)}$ term, remember that this was defined as the solution to (4.2.41), where $Q(r, k_\infty, \omega) = k_\infty^2 - (k_1^2 + m^2/r^2) P(r, k_1, \omega)$, and $P(r) = 1/(a_r^2 \overline{D}_0^2)$. When $P = 1$, $w_1^{(m)}$ can be written as a power series using the method of Frobenius, whereas when $P \neq 1$, $w_1^{(m)}$ can be found numerically. This means there are two cases to investigate.

Azimuthal mode symmetry: $P(r) = 1/(a_r^2 \overline{D}_0^2) \neq 1$

When $P(r) \neq 1$, the operator $\overline{\overline{L}}_R^{(m)}$ depends on mode through m^2. Therefore:

$$w_1^{(-m)}(r) = w_1^{(m)}(r) \tag{4.2.90}$$

This implies that the derivatives are also symmetric.

Now the amplitude factor A_m was defined in (4.2.83) and depends on mode through the Wronskian $\Delta^{(m)}$, which is rewritten here:

$$\Delta^{(m)}(k_\infty \cos\theta, r_e) = w_1^{(m)}(r_e) k_\infty \sin\theta H_m^{(1)'}(R k_\infty \sin\theta) - H_m^{(1)}(R k_\infty \sin\theta) w_1^{(m)'}(r_e) \tag{4.2.91}$$

where the prime refers to the derivative with respect to the argument. Then using the definition of Hankel transforms:

$$\begin{aligned} H_{-m}^{(1)}(z) &= (-1)^m H_m^{(1)}(z) \\ H_{-m}^{(1)'}(z) &= (-1)^m H_m^{(1)'}(z) \end{aligned} \tag{4.2.92}$$

and the fact that $w_1^{(m)}$ is symmetrical, this gives:

$$\begin{aligned} \Delta^{(-m)}(k_\infty \cos\theta, r_e) &= (-1)^m [w_1^{(m)}(r_e) k_\infty \sin\theta H_m^{(1)'} - H_m^{(1)} w_1^{(m)'}(r_e)] \\ &= (-1)^m \Delta^{(m)}(k_\infty \cos\theta, r_e) \end{aligned} \tag{4.2.93}$$

Therefore, the amplitude factor is $A_{-m} = (-1)^m A_m$. Then if we write $\overline{Q}_m = Q_m(r, k_\infty \cos\theta) e^{-im[(\Psi-\psi)+\pi/2]}$ where $Q_m(r, k_\infty \cos\theta) = A_m(k_\infty \cos\theta) w_1^{(m)}(r, k_\infty \cos\theta)$, and note that $Q_{-m} = (-1)^m Q_m$, then for negative modes:

$$\overline{Q}_{-m} = (-1)^m Q_m(r, k_\infty \cos\theta) e^{im[(\Psi-\psi)+\pi/2]} \tag{4.2.94}$$

Then, note that $(-1)^m = e^{\pm im\pi}$, therefore

$$(-1)^m e^{im\pi/2} = \begin{cases} e^{3im\pi/2} \\ e^{-im\pi/2} \end{cases} = (-i)^m$$

Therefore,

$$\overline{Q}_{-m}(r, k_\infty \cos\theta, \Psi - \psi) = (-i)^m Q_m(r, k_\infty \cos\theta) e^{im(\Psi-\psi)} \tag{4.2.95}$$

$$\overline{Q}_m(r, k_\infty \cos\theta, \Psi - \psi) = (-i)^m Q_m(r, k_\infty \cos\theta) e^{-im(\Psi-\psi)} \tag{4.2.96}$$

$$\overline{Q}_0(r, k_\infty \cos\theta, \Psi - \psi) = Q_0(r, k_\infty \cos\theta) \tag{4.2.97}$$

Azimuthal mode symmetry: $P(r) = 1/(a_r^2 \overline{D}_0^2) = 1$

Now, as mentioned above, if $P = 1$ then $w_1^{(m)}$ can be written as a power series which is equivalent to the Bessel function $J_m(k_\infty \sin\theta)$. Again, using the properties of Bessel functions:

$$\begin{aligned} J_{-m}(z) &= (-1)^m J_m(z) \\ J'_{-m}(z) &= (-1)^m J'_m(z) \end{aligned} \tag{4.2.98}$$

Therefore,

$$w_1^{(-m)} = (-1)^m w_1^{(m)} \tag{4.2.99}$$

Then, using these results, we find the Wronskian:

$$\begin{aligned} \Delta^{(-m)}(k_\infty \cos\theta) = (-1)^m (-1)^m [&J_m(Rk_\infty \sin\theta) k_\infty \sin\theta H_m^{(1)'}(Rk_\infty \sin\theta) \\ &- H_m^{(1)}(Rk_\infty \sin\theta) k_\infty \sin\theta J'_m(Rk_\infty \sin\theta)] \\ = \Delta^{(m)}(k_\infty \cos\theta, r_e) \end{aligned} \tag{4.2.100}$$

and, the amplitude factor is $A_{-m} = (-1)^m A_m$, which is identical to the $P(r) \neq 1$ case. Hence, the solution for $\overline{Q}_m(r, k_\infty \cos\theta, \Psi - \psi)$ is also identical for all $P(r)$.

Solution

Hence, using (4.2.95)-(4.2.97) the Fourier series becomes:

$$\begin{aligned}\sum_{m=-\infty}^{\infty} \overline{Q}_m &= \sum_{m=1}^{\infty}(-i)^m Q_m(r, k_\infty \cos\theta)\Big[e^{-im(\Psi-\psi)} + e^{im(\Psi-\psi)}\Big] + Q_0(r, k_\infty \cos\theta) \\ &= \sum_{m=1}^{\infty}(-i)^m Q_m(r, k_\infty \cos\theta) 2\cos m(\Psi-\psi) + Q_0(r, k_\infty \cos\theta) \\ &= \sum_{m=0}^{\infty}(-i)^m \epsilon_m Q_m(r, k_\infty \cos\theta)\cos m(\Psi-\psi)\end{aligned} \tag{4.2.101}$$

where $\epsilon_m = 1$ when $m = 0$, and $\epsilon_m = 2$ when $m \geq 1$.

Therefore, we get the final solution for the Green's function:

$$\boxed{G_0 = \frac{k_\infty^2}{(2\pi)^3|x|} e^{ik_\infty(|x|-y_1\cos\theta)} \sum_{m=0}^{\infty}(-i)^m \epsilon_m A_m(k_\infty\cos\theta) w_1^{(m)}(r, k_\infty\cos\theta)\cos m(\Psi-\psi)} \tag{4.2.102}$$

4.3 Acoustic Spectrum Formulation

Afsar et al (2011) [27] (referred to as AGF from now on) showed that by using an axisymmetric approximation the acoustic spectrum could be reduced to 11 independent terms. This thesis follows the work done in this paper, therefore the relevant equations are rewritten here for convenience.

AGF used the Goldstein (2003) [22] formulation of generalism, which introduces the non-linear pressure variable $p'_e = p' + (\gamma-1)(\rho v'^2 - \bar{\rho}\tilde{v'^2})/2$ so that the right hand side source terms of (4.1.2) and (4.1.3) can be combined into the single tensor $e''_{\nu j}$ defined below in (4.3.5). This also requires using the full form of h'_0 (A.1.3). The operator acting on the $e''_{\nu j}$ source term can be transferred to the Green's function. Doing this, the acoustic spectrum is given by the Fourier transform of the far field pressure autocovariance

$$I_e(\boldsymbol{x};\omega) = \frac{1}{2\pi}\int_{-\infty}^{\infty} e^{i\omega\tau}\overline{p_e^2}(\boldsymbol{x},\tau)d\tau \tag{4.3.1}$$

where

$$\overline{p_e^2}(\boldsymbol{x},\tau) = \frac{1}{2T}\int_{-T}^{T} p_e(\boldsymbol{x},t)p_e(\boldsymbol{x},t+\tau)dt \tag{4.3.2}$$

and

$$p'_e(\boldsymbol{x},t) = -\int_{-\infty}^{\infty}\int_{V(y)} \gamma_{\nu j}(\boldsymbol{x}|\boldsymbol{y},t-\tau)e''_{\nu j}(\boldsymbol{y},\tau)d\boldsymbol{y}d\tau \tag{4.3.3}$$

where the negative sign comes from the integration by parts when the operator on $e''_{\nu j}$ is transferred to the Green's function [18]. Then $\gamma_{\nu j}$ is given by:

$$\gamma_{\nu j}(\boldsymbol{y},\tau|\boldsymbol{x},t) = \frac{\partial G_\nu(\boldsymbol{y},\tau|\boldsymbol{x},t)}{\partial y_j} - (\gamma-1)\delta_{\nu k}\frac{\partial \tilde{v}_k}{\partial y_j}G_4(\boldsymbol{y},\tau|\boldsymbol{x},t) \tag{4.3.4}$$

where G_ν is calculated from G_0 which was found in (4.2.102) and

$$e''_{\nu j}(\boldsymbol{y},\tau) = \Big[-(\rho v'_\nu v'_j - \overline{\rho v'_\nu v'_j})\Big] - \frac{\delta_{\nu j}(\gamma-1)}{2}\Big[-(\rho v'^2 - \overline{\rho v'^2})\Big] \tag{4.3.5}$$

Note that $e''_{\nu j}$ can also be written as: $e''_{\nu j}(\boldsymbol{y},\tau) = \epsilon_{\nu j\sigma m}e^{(0)}_{\sigma m}(\boldsymbol{y},\tau)$ where

$$\epsilon_{\nu j\sigma m} = \delta_{\nu\sigma}\delta_{jm} - \frac{\gamma-1}{2}\delta_{\nu j}\delta_{\sigma m} \tag{4.3.6}$$

and

$$e^{(0)}_{\sigma m}(\boldsymbol{y},\tau) = -\Big[\rho v'_\sigma v'_m - \overline{\rho v_{\sigma'} v'_m}\Big] \tag{4.3.7}$$

Note that $e^{(0)}_{\sigma m}$ is the generalised Reynolds stress tensor (i.e. if σm reduce to ij it reduces to (4.1.4)). It is important to note the differential operator in the Goldstein 2002 and Goldstein 2003 formulations are identical, therefore the Green's function theory that we have developed in the previous section is unchanged and can still be used.

Inserting the equation for $\overline{p_e^2}$ into the Fourier transform gives:

$$I_e(\boldsymbol{x};\omega) = \frac{1}{2\pi}\int_{-\infty}^{\infty} e^{i\omega\tau}\frac{1}{2T}\int_{-T}^{T} p_e(\boldsymbol{x},t)p_e(\boldsymbol{x},t+\tau)dtd\tau \tag{4.3.8}$$

Multiplying by $e^{i\omega t - i\omega t}$ allows the integral to be written as:

$$I_e(\boldsymbol{x};\omega) = \frac{1}{2T}\frac{1}{2\pi}\int_{-T}^{T}\Big[\int_{\infty}^{\infty} e^{i\omega(t+\tau)}p_e(\boldsymbol{x},t+\tau)d(t+\tau)\Big]e^{-i\omega t}p_e(\boldsymbol{x},t)dt \tag{4.3.9}$$

Note for the inner integral in square brackets t is constant, therefore $d\tau = d(t+\tau)$. Notably, these integrals are Fourier transforms for which we define by integrals:

$$\hat{p}_e(\boldsymbol{x};\omega) = \frac{1}{2\pi}\int_{-\infty}^{\infty} e^{-i\omega z}p_e(\boldsymbol{x},z)dz \tag{4.3.10}$$

$$\hat{p}^*_e(\boldsymbol{x};\omega) = \frac{1}{2\pi}\int_{-\infty}^{\infty} e^{i\omega z}p_e(\boldsymbol{x},z)dz \tag{4.3.11}$$

Hence the acoustic spectrum becomes:

$$\frac{2T}{2\pi}I_e(\boldsymbol{x};\omega) = \hat{p}_e^*(\boldsymbol{x};\omega)\frac{1}{2\pi}\int_{-T}^{T} e^{-i\omega t}p_e(\boldsymbol{x},t)dt \tag{4.3.12}$$

which can also be written as:

$$I_e(\boldsymbol{x};\omega) = \lim_{T\to\infty}\frac{\pi}{T}\hat{p}_e^*(\boldsymbol{x};\omega)\hat{p}_e(\boldsymbol{x};\omega,T) \tag{4.3.13}$$

Since the pressure is given by (4.3.3) and $\gamma_{\nu j}(\boldsymbol{x},t,\boldsymbol{y},\tau) = \gamma_{\nu j}(\boldsymbol{x}|\boldsymbol{y},t-\tau)$, we find:

$$\hat{p}_e(\boldsymbol{x};\omega,T) = -(2\pi)\int_{V(\boldsymbol{y})}\hat{\Gamma}_{\nu j}(\boldsymbol{x}|\boldsymbol{y};\omega)\hat{e}_{\nu j}(\boldsymbol{y};\omega,T)d\boldsymbol{y} \tag{4.3.14}$$

and

$$\hat{p}_e^*(\boldsymbol{x};\omega,T) = -(2\pi)\int_{V(\boldsymbol{z})}\hat{\Gamma}_{\nu j}^*(\boldsymbol{x}|\boldsymbol{z};\omega)\hat{e}_{\nu j}^*(\boldsymbol{y};\omega,T)d\boldsymbol{z} \tag{4.3.15}$$

Note that T is only in the argument of $\hat{e}_{\nu j}$ since this is a random variable and required averaging, whereas $\hat{\Gamma}_{\nu j}$ is deterministic and does not require averaging and is the time Fourier transform of $\gamma_{\nu j}$:

$$\hat{\Gamma}_{\nu j}(\boldsymbol{x}|\boldsymbol{y};\omega) = \int_{-\infty}^{\infty} e^{i\omega(t-\tau)}\gamma_{\nu j}(\boldsymbol{x}|\boldsymbol{y},t-\tau)d(t-\tau) \tag{4.3.16}$$

Therefore the acoustic spectrum is given by:

$$\begin{aligned} I_e(\boldsymbol{x};\omega) = (2\pi)^2\int_{V(\boldsymbol{y})}\int_{V(\boldsymbol{z})}&\hat{\Gamma}_{\nu j}(\boldsymbol{x}|\boldsymbol{y};\omega)\hat{\Gamma}_{\mu l}^*(\boldsymbol{x}|\boldsymbol{z};\omega) \\ &\lim_{T\to\infty}\Big(\frac{2\pi}{2T}\Big)\hat{e}_{\nu j}(\boldsymbol{y};\omega,T)\hat{e}_{\mu l}^*(\boldsymbol{z};\omega,T)d\boldsymbol{y}d\boldsymbol{z} \end{aligned} \tag{4.3.17}$$

Looking at the the product of $\hat{e}_{\nu j}, \hat{e}_{\mu l}^*$:

$$\hat{e}_{\nu j}(\boldsymbol{y};\omega,T)\hat{e}_{\mu l}^*(\boldsymbol{z};\omega,T) = \frac{1}{(2\pi)^2}\int_{-T}^{T} e^{-i\omega\tau}e''_{\nu j}(\boldsymbol{y},\tau)d\tau\int_{-T}^{T} e^{i\omega\bar{\tau}}e''_{\mu l}(\boldsymbol{z},\bar{\tau})d\bar{\tau} \tag{4.3.18}$$

Replacing τ in the first integral by $\bar{\tau}-\tau_0$:

$$\hat{e}_{\nu j}(\boldsymbol{y};\omega,T)\hat{e}_{\mu l}^*(\boldsymbol{z};\omega,T) = \frac{1}{(2\pi)^2}\int_{-T}^{T} e^{-i\omega(\bar{\tau}-\tau_0)}e''_{\nu j}(\boldsymbol{y},\bar{\tau}-\tau_0)d\bar{\tau}\int_{-T}^{T} e^{i\omega\bar{\tau}}e''_{\mu l}(\boldsymbol{z},\bar{\tau})d\bar{\tau} \tag{4.3.19}$$

Using the convolution theorem this gives:

$$\begin{aligned} \frac{2\pi}{2T}\hat{e}_{\nu j}(\boldsymbol{y};\omega,T)\hat{e}_{\mu l}^*(\boldsymbol{y}+\boldsymbol{\eta};\omega,T) &= \frac{1}{2\pi}\int d\tau_0 e^{-i\omega\tau_0}\frac{1}{2T}\Big[\int_{-T}^{T} e''_{\nu j}(\boldsymbol{y},\tau)e''_{\mu l}(\boldsymbol{y}+\boldsymbol{\eta},\tau+\tau_0)d\tau\Big] \\ &= \frac{1}{2\pi}\int e^{-i\omega\tau_0}\mathcal{R}_{\nu j\mu l}(\boldsymbol{y},\boldsymbol{\eta},\tau_0)d\tau_0 \\ &= \mathcal{H}_{\nu j\mu l}(\boldsymbol{y},\boldsymbol{\eta};\omega) \end{aligned} \tag{4.3.20}$$

where we have replaced $\boldsymbol{z} = \boldsymbol{y} + \boldsymbol{\eta}$ and defined

$$\mathcal{H}_{\nu j \mu l} = \epsilon_{\nu j \sigma m} H_{\sigma m \lambda n} \epsilon_{\mu l \lambda n} \tag{4.3.21}$$

where

$$H_{\nu j \mu l}(\boldsymbol{y}, \boldsymbol{\eta}; \omega) = \frac{1}{2\pi} \int_{-\infty}^{\infty} e^{-i\omega\tau} R_{\nu j \mu l}(\boldsymbol{y}, \boldsymbol{\eta}, \tau) d\tau \tag{4.3.22}$$

and

$$R_{\nu j \mu l}(\boldsymbol{y}, \boldsymbol{\eta}, \tau) = \frac{1}{2T} \int_{-T}^{T} [\rho v'_\nu v'_j - \overline{\rho v'_\nu v'_j}](\boldsymbol{y}, t)[\rho v'_\mu v'_l - \overline{\rho v'_\mu v'_l}](\boldsymbol{y}+\boldsymbol{\eta}, t+\tau) dt \tag{4.3.23}$$

where $v'_\mu(\boldsymbol{y}, t) = v_\mu(\boldsymbol{y}, t) - \tilde{v}_\mu(\boldsymbol{y})$, where the tilde represents the Favre average. The fourth component of the velocity is related to the enthalpy h and is defined as:

$$v'_4 = (\gamma - 1)\Big[h' + \frac{1}{2} v'^2\Big](\boldsymbol{y}, t) = c'^2 + \frac{\gamma - 1}{2} v'^2 \tag{4.3.24}$$

Therefore, the acoustic spectrum is:

$$I_e(\boldsymbol{x}; \omega) = (2\pi)^2 \int_{V(\boldsymbol{y})} \Gamma_{\nu j}(\boldsymbol{x}|\boldsymbol{y}; \omega) \int_{V_\infty(\boldsymbol{\eta})} \Gamma^*_{\mu l}(\boldsymbol{x}|\boldsymbol{y} + \boldsymbol{\eta}; \omega) \mathcal{H}_{\nu j \mu l}(\boldsymbol{y}, \boldsymbol{\eta}; \omega) d\boldsymbol{\eta} d\boldsymbol{y} \tag{4.3.25}$$

where $\Gamma^*_{\mu l}(\boldsymbol{x}|\boldsymbol{y} + \boldsymbol{\eta}; \omega) = \Gamma^*_{\mu l}(\boldsymbol{x}|\boldsymbol{y}; \omega) e^{i\boldsymbol{k}\cdot\boldsymbol{\eta}}$ using the WKBJ approximation (shown in Appendix B of [27]), this allows (4.3.25) to be written as

$$I_e(\boldsymbol{x}; \omega) = (2\pi)^2 \int_{V(\boldsymbol{y})} \Gamma_{\nu j}(\boldsymbol{x}|\boldsymbol{y}; \omega) \Gamma^*_{\mu l}(\boldsymbol{x}|\boldsymbol{y}; \omega) \Phi^*_{\nu j \mu l}(\boldsymbol{y}; \omega, \boldsymbol{k}) d\boldsymbol{y} \tag{4.3.26}$$

where $\Phi^*_{\nu j \mu l}$ is defined in (4.3.32). Then

$$I(\boldsymbol{x}; \omega) = \lim_{|\boldsymbol{x}| \to \infty} I_e(\boldsymbol{x}; \omega) \tag{4.3.27}$$

AGF [27] also showed that the acoustic spectrum could be written as a summation of three terms, representing the momentum-flux, coupling term, and enthalpy-flux respectively:

$$\frac{I(\boldsymbol{x}; \omega)}{(2\pi)^2} = \int_{V(\boldsymbol{y})} \Big\{ I^{[1]}(\boldsymbol{x}|\boldsymbol{y}; \omega) + I^{[2]}(\boldsymbol{x}|\boldsymbol{y}; \omega) + I^{[3]}(\boldsymbol{x}|\boldsymbol{y}; \omega) \Big\} d\boldsymbol{y} \tag{4.3.28}$$

following axisymmetry approximations these terms were found to be:

$$\begin{aligned} I^{[1]}(\boldsymbol{x}|\boldsymbol{y}; \omega) = {} & [|G_{22}|^2 + |G_{33}|^2 + 2|G_{23}|^2] \Phi^*_{2222} \\ & + Re[G_{11}(G^*_{22} + G^*_{33})](\Phi^*_{1122} + \Phi^*_{2211}) \\ & + |G_{11}|^2 \Phi^*_{1111} + 2[Re(G_{22} G^*_{33}) - |G_{23}|^2] \Phi^*_{2233} \\ & + 4[|G_{12}|^2 + |G_{13}|^2] \Phi^*_{1212} \end{aligned} \tag{4.3.29}$$

$$I^{[2]}(\boldsymbol{x}|\boldsymbol{y};\omega) = 2Re\Big[\Gamma_{41}(G^*_{22}+G^*_{33})\Phi^*_{4122}+\Gamma_{41}G^*_{11}\Phi^*_{4111} + 2[\Gamma_{42}G^*_{12}+\Gamma_{43}G^*_{13}]\Phi^*_{4221}\Big] \tag{4.3.30}$$

$$I^{[3]}(\boldsymbol{x}|\boldsymbol{y};\omega) = [|\Gamma_{42}|^2+|\Gamma_{43}|^2]\Phi^*_{4242}+|\Gamma_{41}|^2\Phi^*_{4141} \tag{4.3.31}$$

where $G_{ij} = 1/2(\Gamma_{ij}+\Gamma_{ji})$, * represents the complex conjugate, and the acoustic spectral tensor was defined as the Fourier transform in spatial separation of $\mathcal{H}_{\nu j\mu l}$:

$$\Phi^*_{\nu j\mu l}(\boldsymbol{y};\omega,k_1,\boldsymbol{k}_\perp) = \int_{\boldsymbol{\eta}} \mathcal{H}_{\nu j\mu l}(\boldsymbol{y},\boldsymbol{\eta};\omega)e^{\boldsymbol{k}\cdot\boldsymbol{\eta}}d\boldsymbol{\eta} \tag{4.3.32}$$

The remainder of this chapter will find the propagator terms (i.e. the Green's function terms) using the numerical meanflow data obtained from the LES. Then in chapters 5 and 6 the fourth order correlations will be found numerically from the LES, and post-processed to find the spectral tensor $\Phi^*_{\nu j\mu l}$. Then in Chapter 7 the acoustic spectrum will be calculated using these equations and integrating over $\boldsymbol{y}$.

4.4 Green's Function: Numerical Results

4.4.1 Code Validation

The first stage of the propagator calculation was to obtain $\tilde{G}^{(m)}_0 = w^{(m)}_1(r, k_\infty\cos\theta)$. This was found by numerically solving the system of equations:

$$\frac{d\tilde{G}^{(m)}_0}{dr} = \frac{k^2_\infty}{a^2_r}(1-M(r)\cos\theta)^2\tilde{G}^{(m)}_r \tag{4.4.1}$$

$$\frac{d\tilde{G}^{(m)}_r}{dr} = \Big[\frac{a^2_r\cos^2\theta}{(1-M(r)\cos\theta)^2}+\frac{a^2_r(m/r)^2}{k^2_\infty(1-M(r)\cos\theta)^2}-1\Big]\tilde{G}^{(m)}_0-\frac{\tilde{G}^{(m)}_r}{r} \tag{4.4.2}$$

The Green's function code that was used to solve these equations was first validated using several numerical routines, for an analytical meanflow based on Tam & Burton [87]. This comparison is shown in Figure 4.5 for several Strouhal numbers.

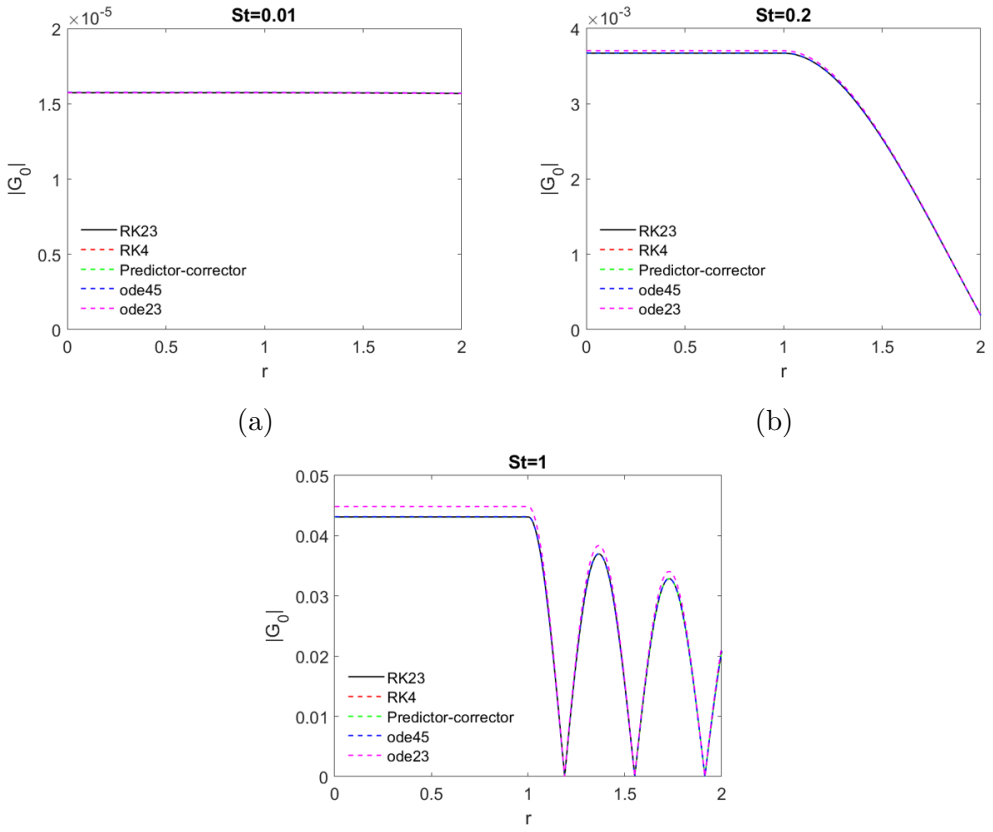

(a) (b)

(c)

Figure 4.5: Green's function numerical solution using different numerical algorithms (a) $St = 0.01$ (b) $St = 0.2$ (c) $St = 1.0$

We see that all routines give similar results at low St, and only ode23 gives different results at high St, therefore for the remaining calculations we use the 4th order Runge Kutta routine. Note that for this comparison $b = 0.001$ was chosen for the meanflow profile, i.e. a very sharp meanflow, which implies the numerical calculation will also be converged for a smoother meanflow.

4.4.2 Properties of the Doppler Factor

This section looks at the properties of the Doppler factor which is present in the propagator calculations. The Doppler factor is defined as $(1 - M(r)cos\theta)^n$, we look at the effect of n for different meanflow profiles (relating to different y_1 locations) in Figure 4.6.

There are two main observations;

- inverse Doppler factors are largest inside the jet, whereas positive Doppler factors are largest in the upstream region; and
- as the flow becomes more developed the factor is smeared over a larger angular and radial extent.

4.4.3 Resolution Checks

Since the Green's function calculation requires derivatives it is important to check convergence. This section checks convergence for SP03 at $\theta = 30$. Figure 4.7 shows convergence for G_0, Figure 4.8 shows convergence for $G_r \sim dG_0/dr$, and Figure 4.9 shows convergence for $dG_r/dr \sim d^2G_0/dr^2$. All figures show that using a grid of $nr = 401$ points in the radial direction is sufficient for convergence.

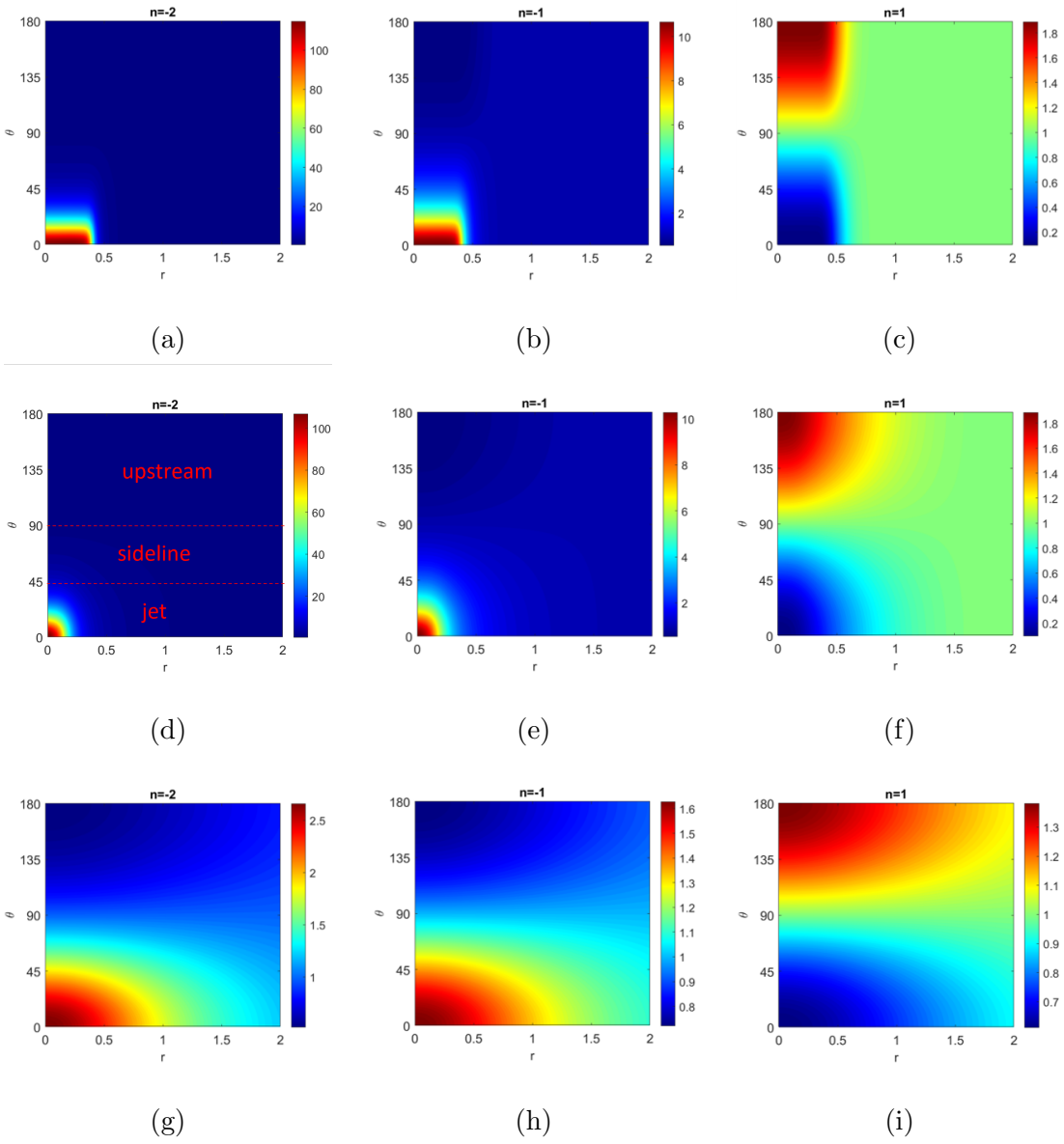

Figure 4.6: Spatial properties of Doppler factor for different meanflow profiles at several powers of n: (a) Top hat ($n = -2$) (b) Top hat ($n = -1$) (c) Top hat ($n = 1$) (d) Gaussian ($n = -2$) (e) Gaussian ($n = -1$) (f) Gaussian ($n = 1$) (g) Fully developed ($n = -2$) (h) Fully developed ($n = -1$) (i) Fully developed ($n = 1$)

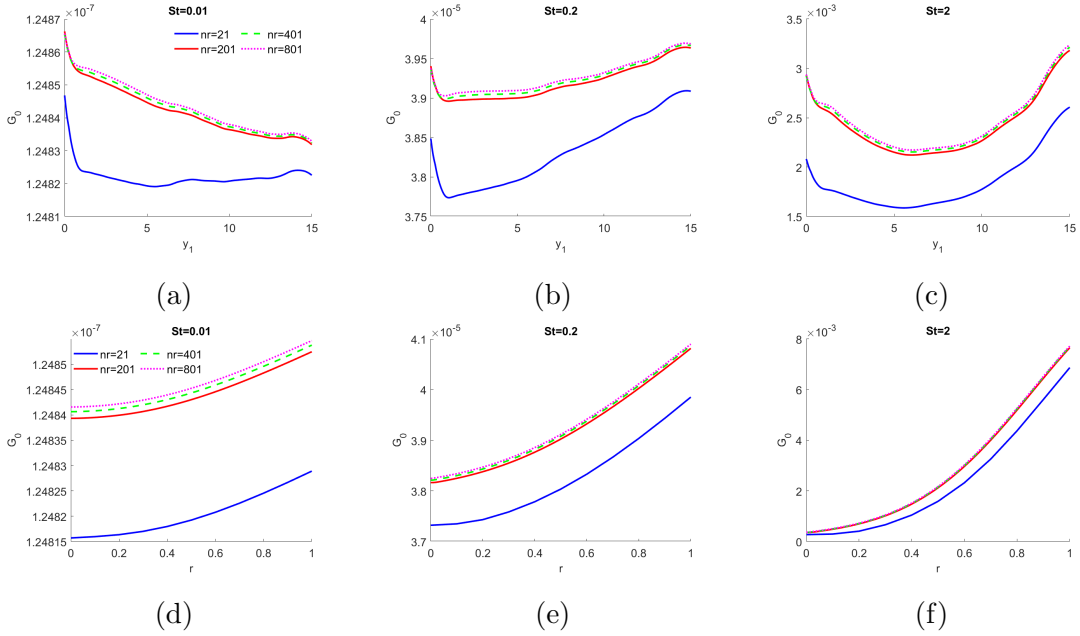

Figure 4.7: SP03: Resolution check for G_0 at $r = 0.5$ for (a) $St = 0.01$ (b) $St = 0.2$ (c) $St = 2.0$, and at y_1 =start for (d) $St = 0.01$ (e) $St = 0.2$ (f) $St = 2.0$

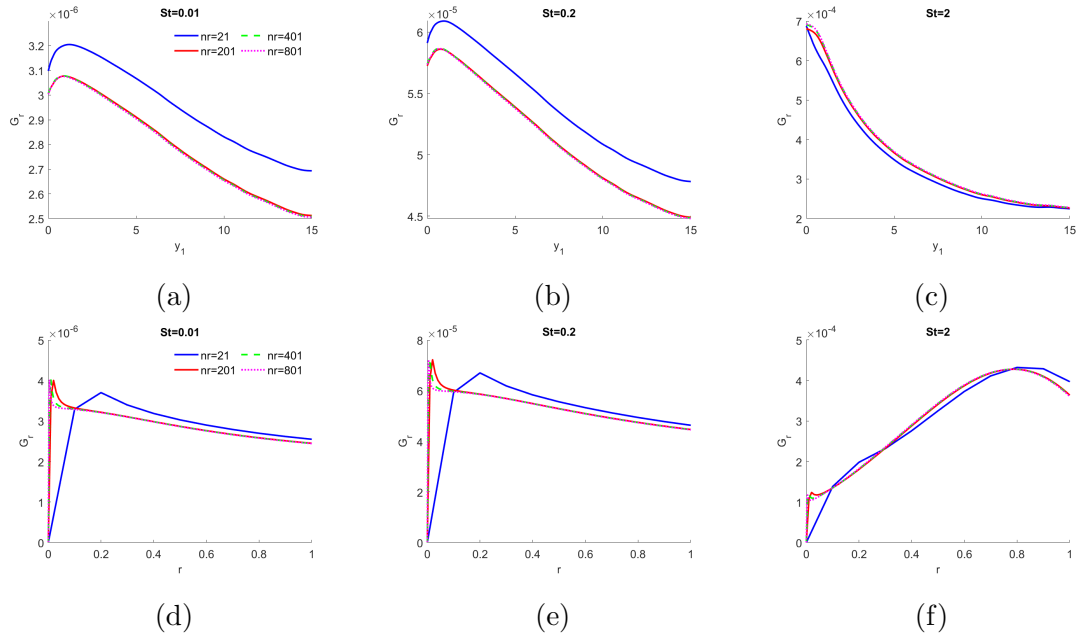

Figure 4.8: SP03: Resolution check for G_r at $r = 0.5$ for (a) $St = 0.01$ (b) $St = 0.2$ (c) $St = 2.0$, and at y_1 =start for (d) $St = 0.01$ (e) $St = 0.2$ (f) $St = 2.0$

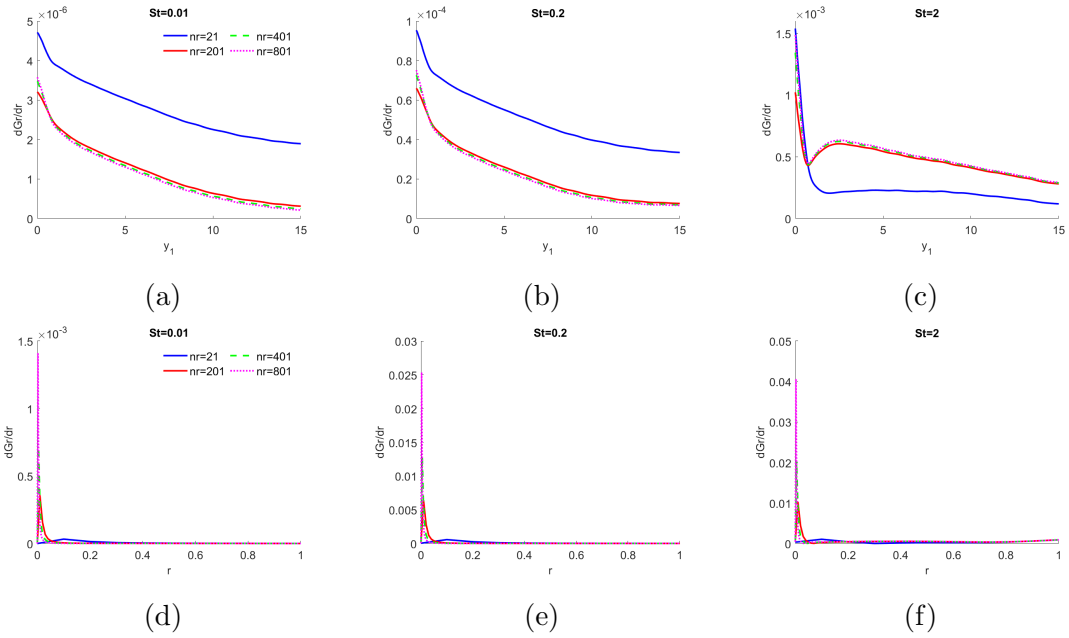

Figure 4.9: SP03: Resolution check for dG_r/dr at $r = 0.5$ for (a) $St = 0.01$ (b) $St = 0.2$ (c) $St = 2.0$, and at y_1 =start for (d) $St = 0.01$ (e) $St = 0.2$ (f) $St = 2.0$

4.5 Propagator

Now we can calculate the propagator components that are present in the acoustic spectrum formulation. For cold jets this reduces to five components, and for heated jets this reduces to ten components. The numerical calculation follows the process shown in Figure 4.10.

This section aims to show the propagator components at several θ,St, and spatial location for the four jets. We wish to look at the magnitude of components to see which components have the potential to have the most significant impact on the acoustic spectrum. Then in the next chapters we will look at the spectral tensors and finally in Chapter 7 we will see the total acoustic predictions.

Figures 4.11-4.14 show the momentum-flux propagator components for SP03, SP07, SP42 and SP46 respectively at $\theta = 30, 90$. These show that for the majority of locations on the shear layer and St at $\theta = 30$ the propagator component that multiplies Φ^*_{1212} has the greatest magnitude and therefore at this angle it is most likely that Φ^*_{1212} will be the main contributor to the noise. Note that for the $Ma = 0.5$ jets, at high frequency ($St = 2$) other propagator components become relatively large, especially the one which multiplies Φ^*_{1111}, meaning they may have

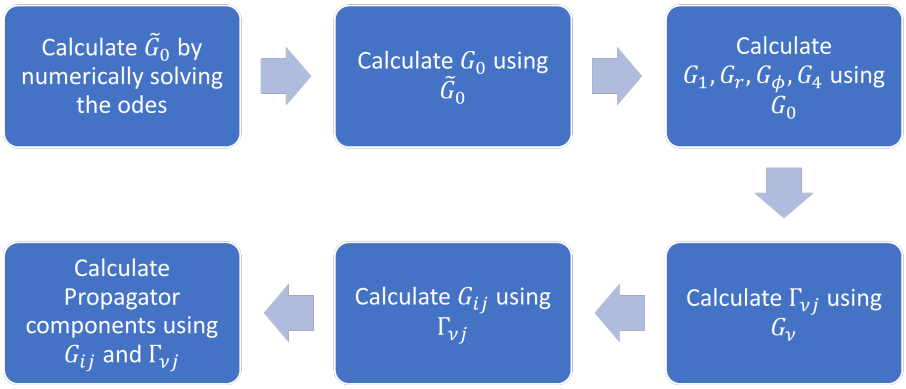

Figure 4.10: Process of obtaining the propagator components

an impact on the high frequency noise. Another key observation is that at $\theta = 90$ there is a difference between the cold and heated jets, cold jets are still dominated by the terms which multiplies Φ^*_{1212} inside the potential core region for small/peak frequencies, whereas for heated jets the largest component everywhere is the one that multiplies Φ^*_{2222}.

Figures 4.15 and 4.16 compare the coupling propagator terms for SP42 and SP46, these show that the term that multiplies the spectral tensor Φ^*_{4221} has the greatest magnitude for most locations and both angles. However, again note that for the $Ma = 0.5$ jet at high frequency ($St = 2$) the other terms become significantly large, especially Φ^*_{4111}.

Finally, Figures 4.17 and 4.18 compare the enthalpy-flux propagator components for SP42 and SP46. Similarly to the coupling term case, it is clear that the term multiplying Φ^*_{4242} has the greatest magnitude at all locations on the shear layer, both angles and most St. The main difference between jets lies in the high frequencies, where for SP42 at $\theta = 30, St = 2$ both terms have similar magnitudes.

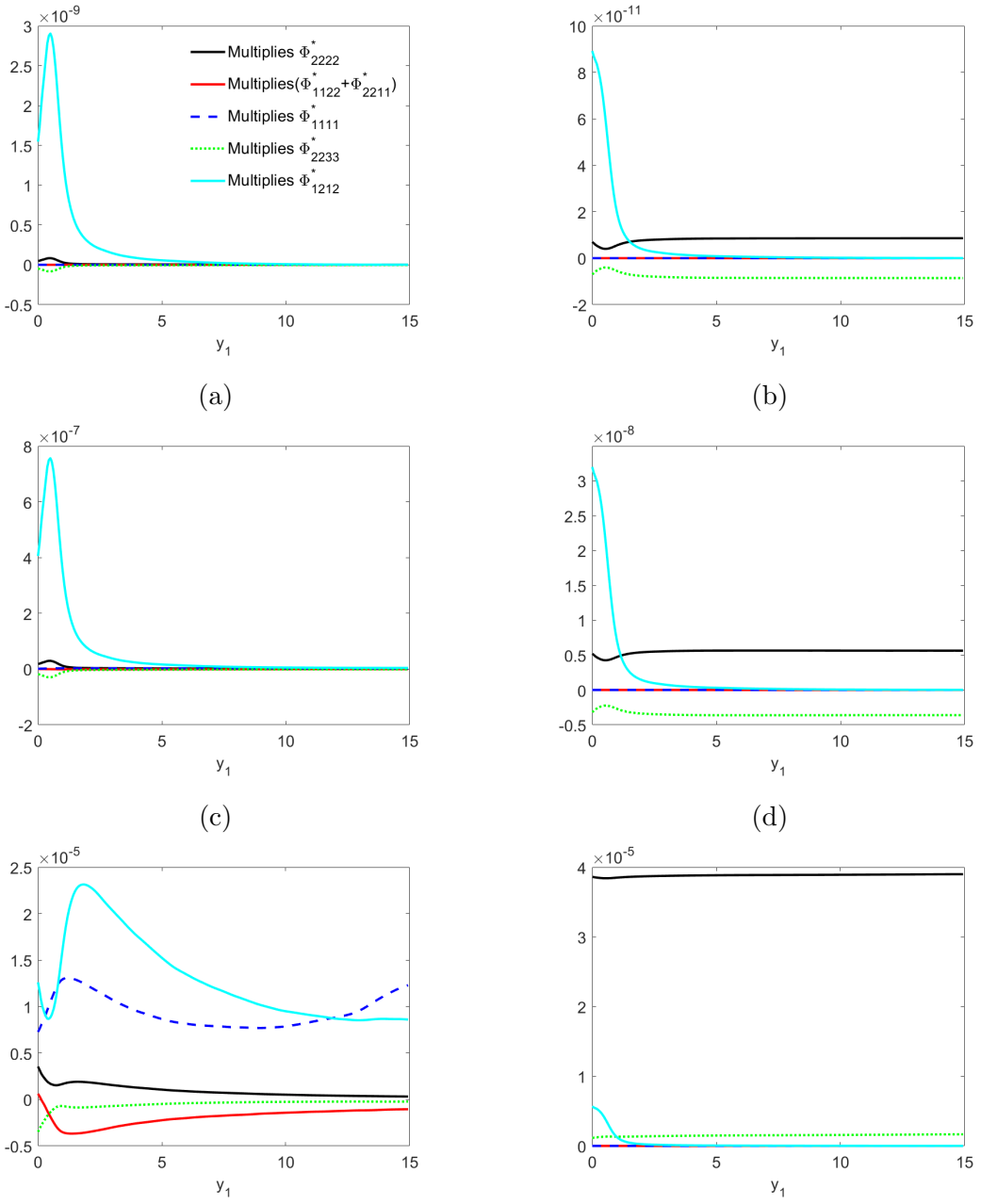

Figure 4.11: SP03: Comparison of momentum-flux propagator components on the shear layer for (a) $St = 0.01, \theta = 30$ (b) $St = 0.01, \theta = 90$ (c) $St = 0.2, \theta = 30$ (d) $St = 0.2, \theta = 90$ (e) $St = 2.0, \theta = 30$ (f) $St = 2.0, \theta = 90$

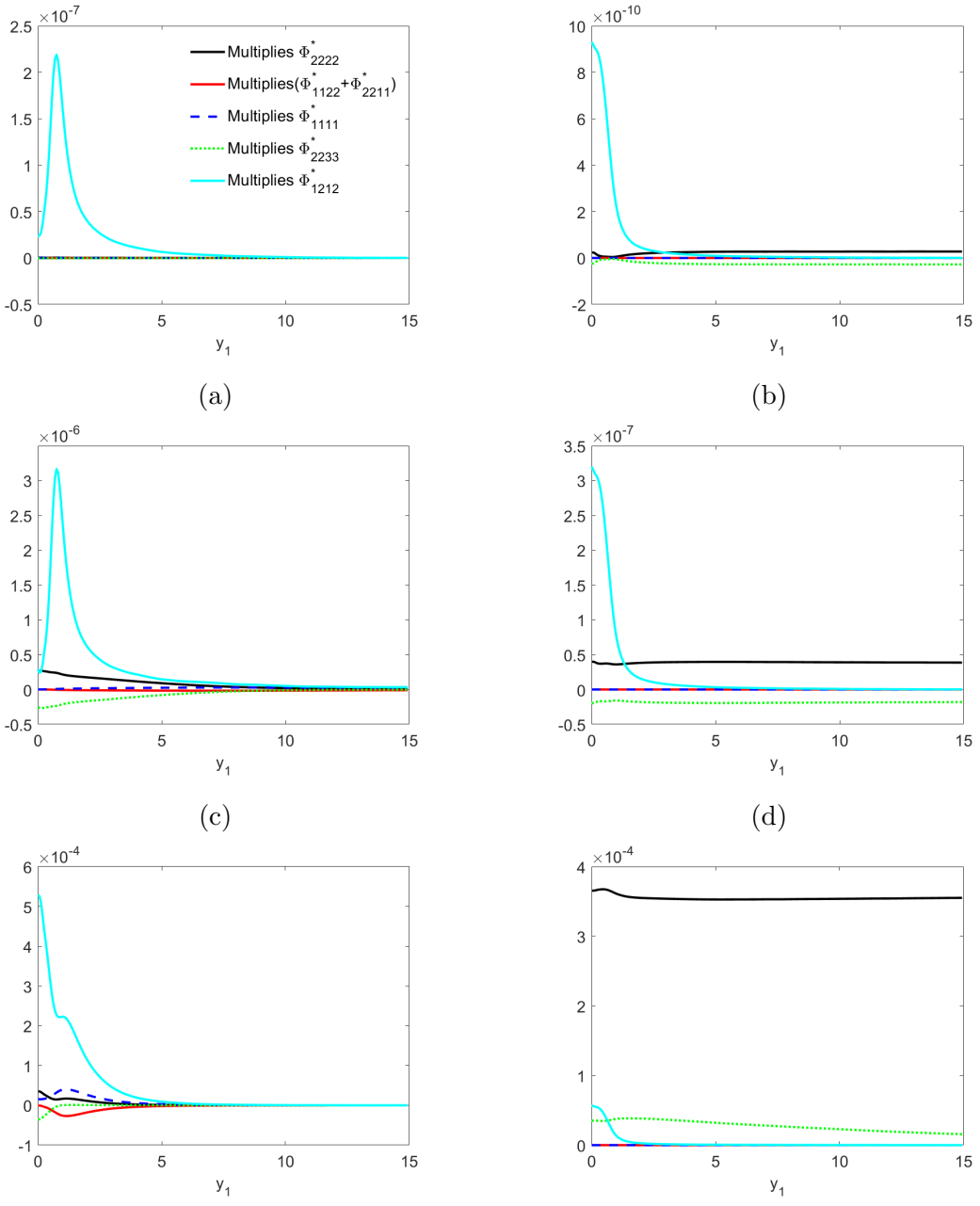

Figure 4.12: SP07: Comparison of momentum-flux propagator components on the shear layer for (a) $St = 0.01, \theta = 30$ (b) $St = 0.01, \theta = 90$ (c) $St = 0.2, \theta = 30$ (d) $St = 0.2, \theta = 90$ (e) $St = 2.0, \theta = 30$ (f) $St = 2.0, \theta = 90$

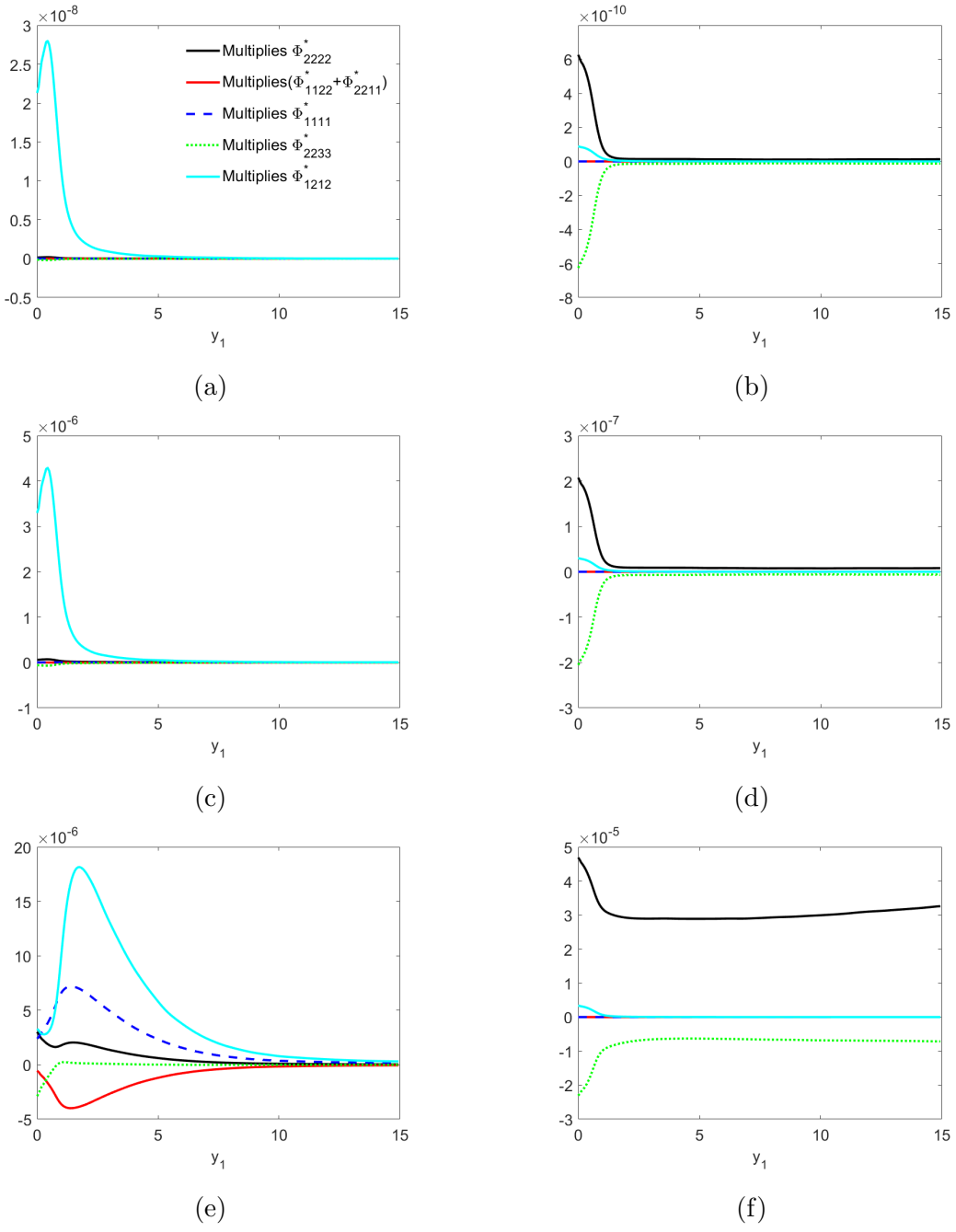

Figure 4.13: SP42: Comparison of momentum-flux propagator components on the shear layer for (a) $St = 0.01, \theta = 30$ (b) $St = 0.01, \theta = 90$ (c) $St = 0.2, \theta = 30$ (d) $St = 0.2, \theta = 90$ (e) $St = 2.0, \theta = 30$ (f) $St = 2.0, \theta = 90$

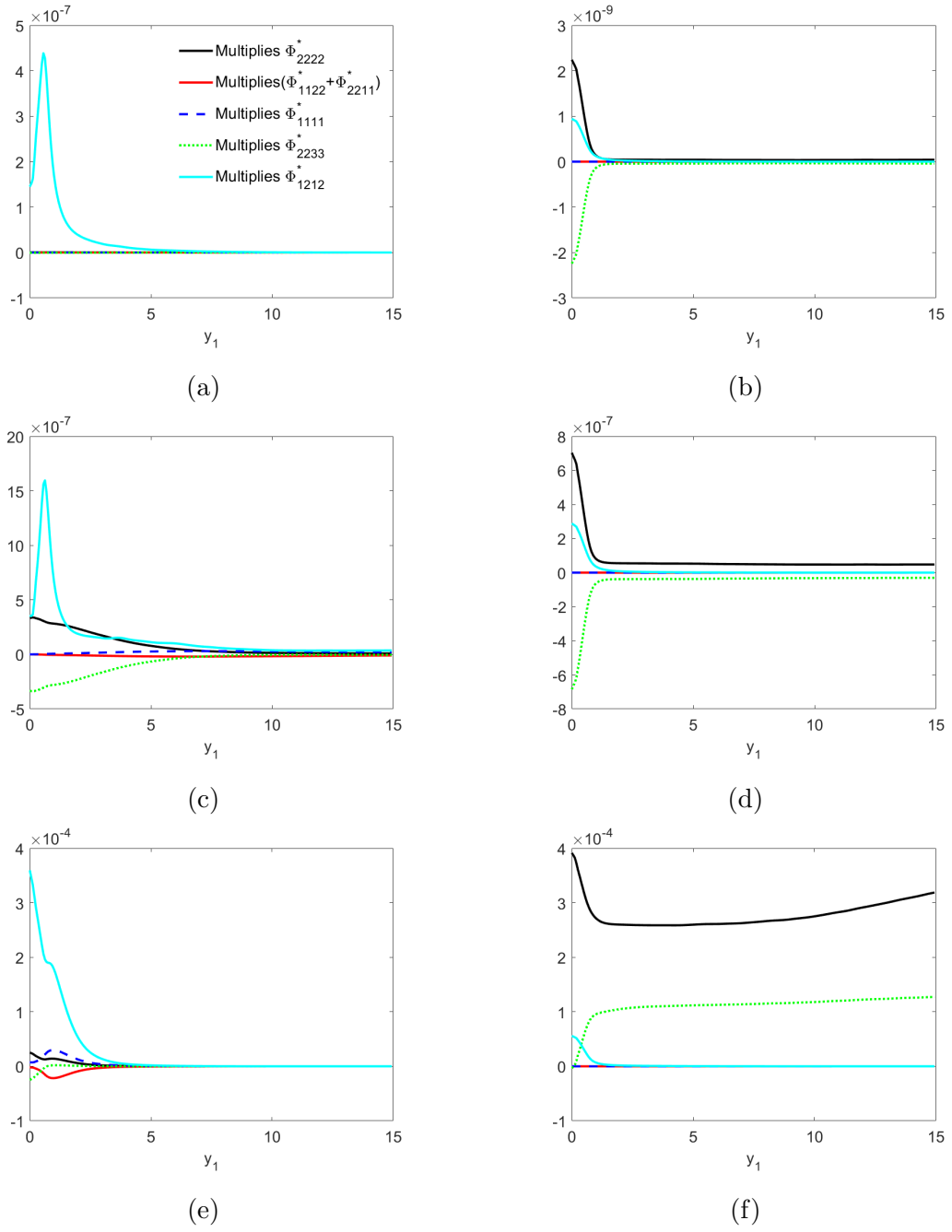

Figure 4.14: SP46: Comparison of momentum-flux propagator components on the shear layer for (a) $St = 0.01, \theta = 30$ (b) $St = 0.01, \theta = 90$ (c) $St = 0.2, \theta = 30$ (d) $St = 0.2, \theta = 90$ (e) $St = 2.0, \theta = 30$ (f) $St = 2.0, \theta = 90$

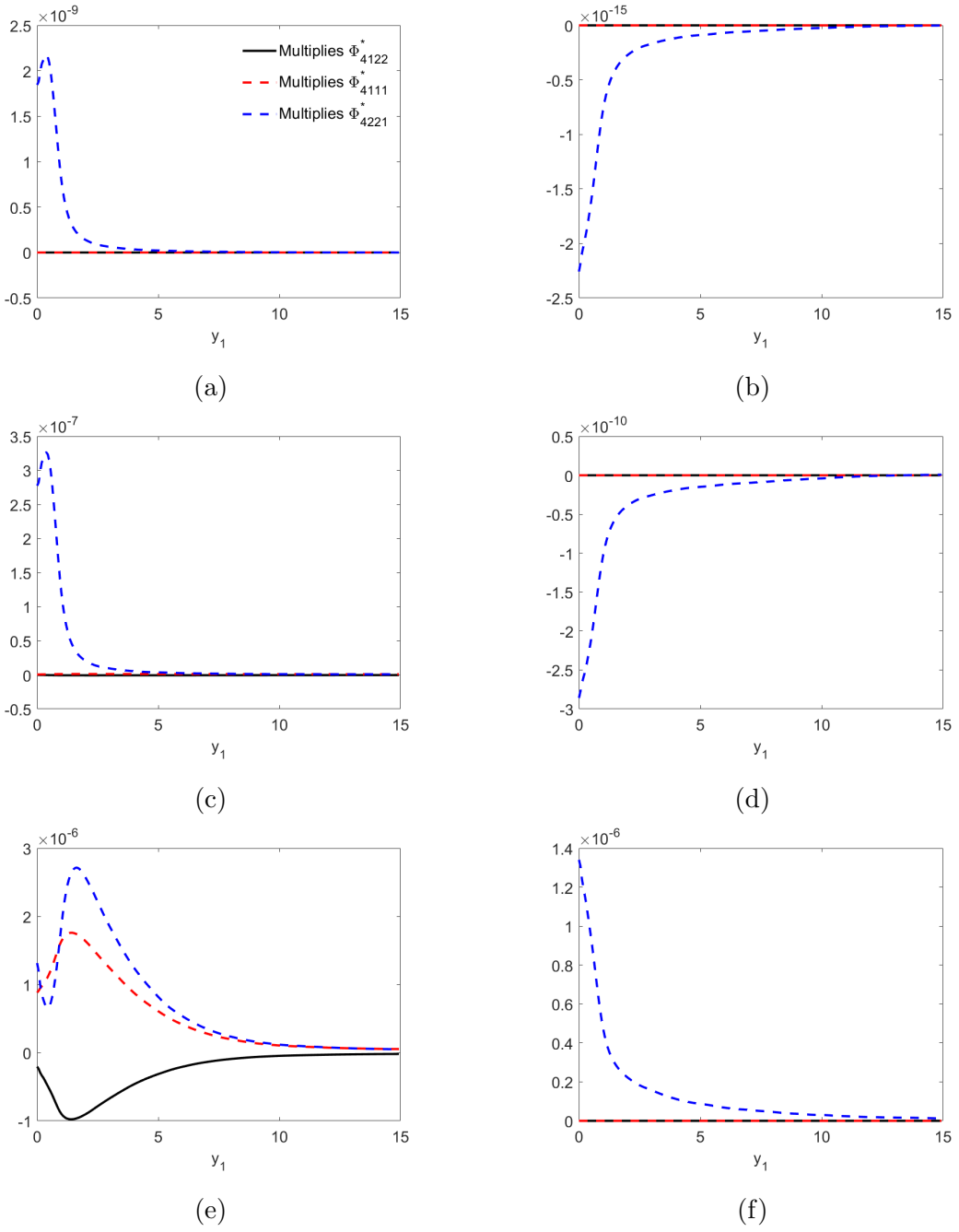

Figure 4.15: SP42: Comparison of coupling propagator components on the shear layer for (a) $St = 0.01, \theta = 30$ (b) $St = 0.01, \theta = 90$ (c) $St = 0.2, \theta = 30$ (d) $St = 0.2, \theta = 90$ (e) $St = 2.0, \theta = 30$ (f) $St = 2.0, \theta = 90$

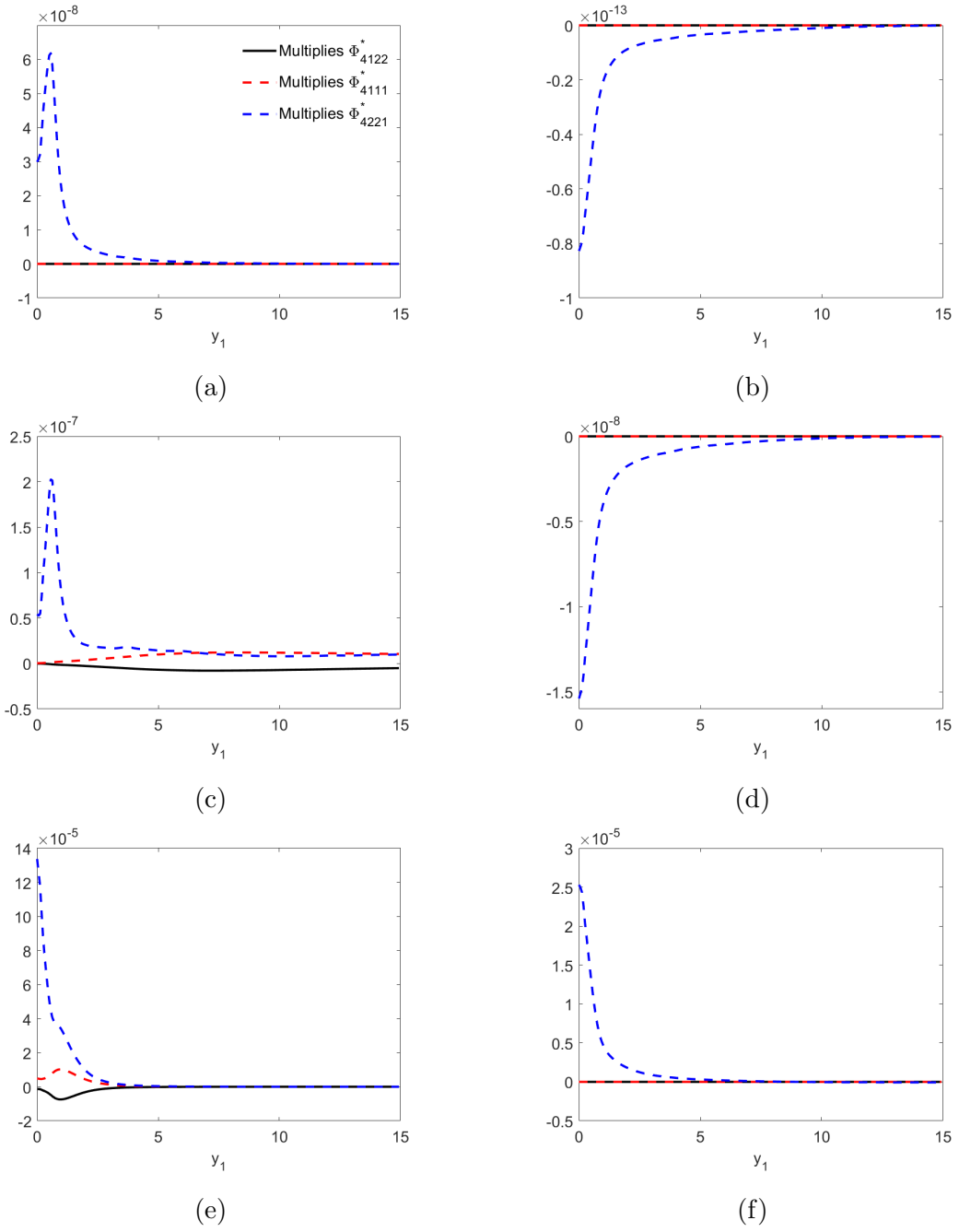

Figure 4.16: SP46: Comparison of coupling propagator components on the shear layer for (a) $St = 0.01, \theta = 30$ (b) $St = 0.01, \theta = 90$ (c) $St = 0.2, \theta = 30$ (d) $St = 0.2, \theta = 90$ (e) $St = 2.0, \theta = 30$ (f) $St = 2.0, \theta = 90$

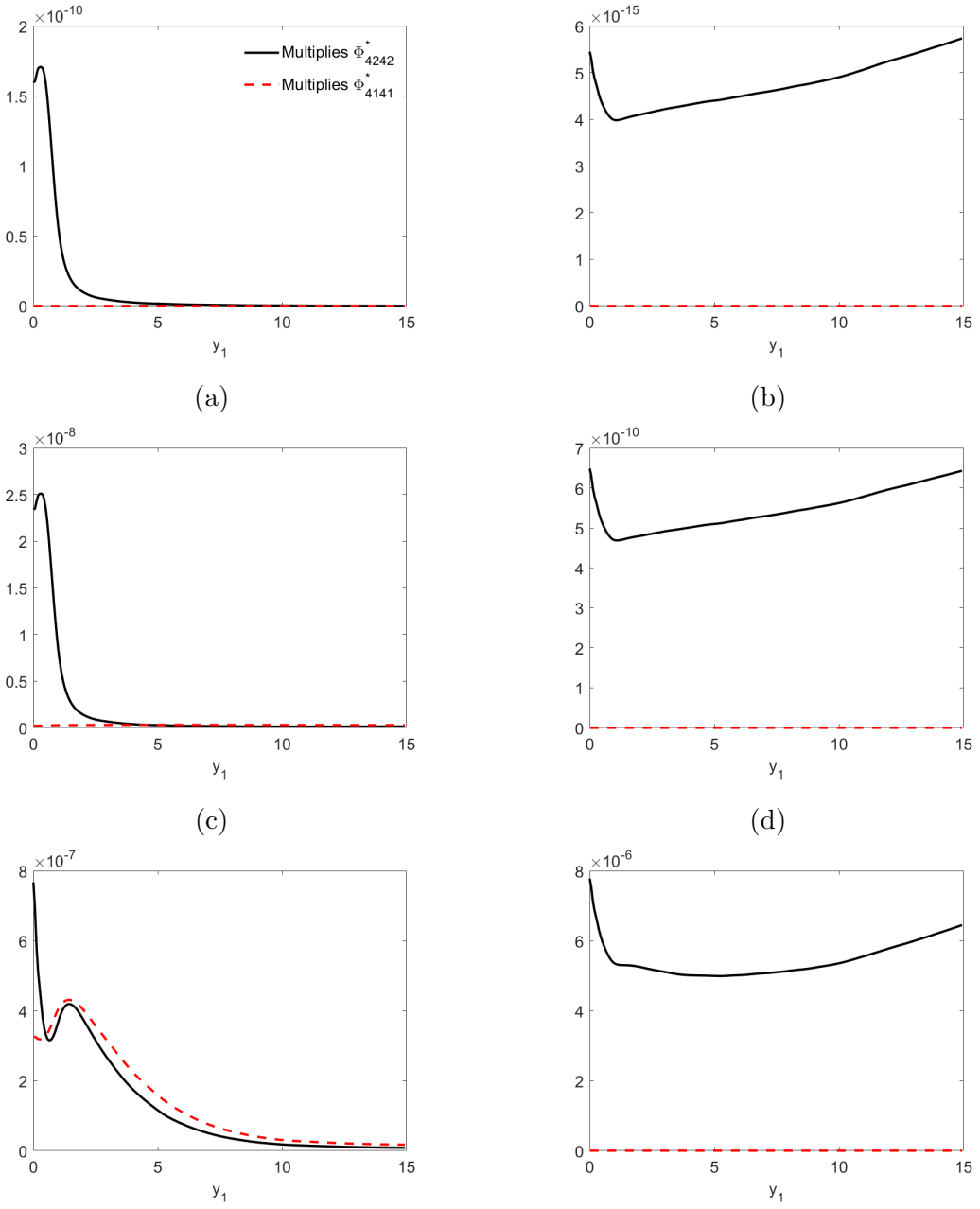

Figure 4.17: SP42: Comparison of enthalpy-flux propagator components on the shear layer for (a) $St = 0.01, \theta = 30$ (b) $St = 0.01, \theta = 90$ (c) $St = 0.2, \theta = 30$ (d) $St = 0.2, \theta = 90$ (e) $St = 2.0, \theta = 30$ (f) $St = 2.0, \theta = 90$

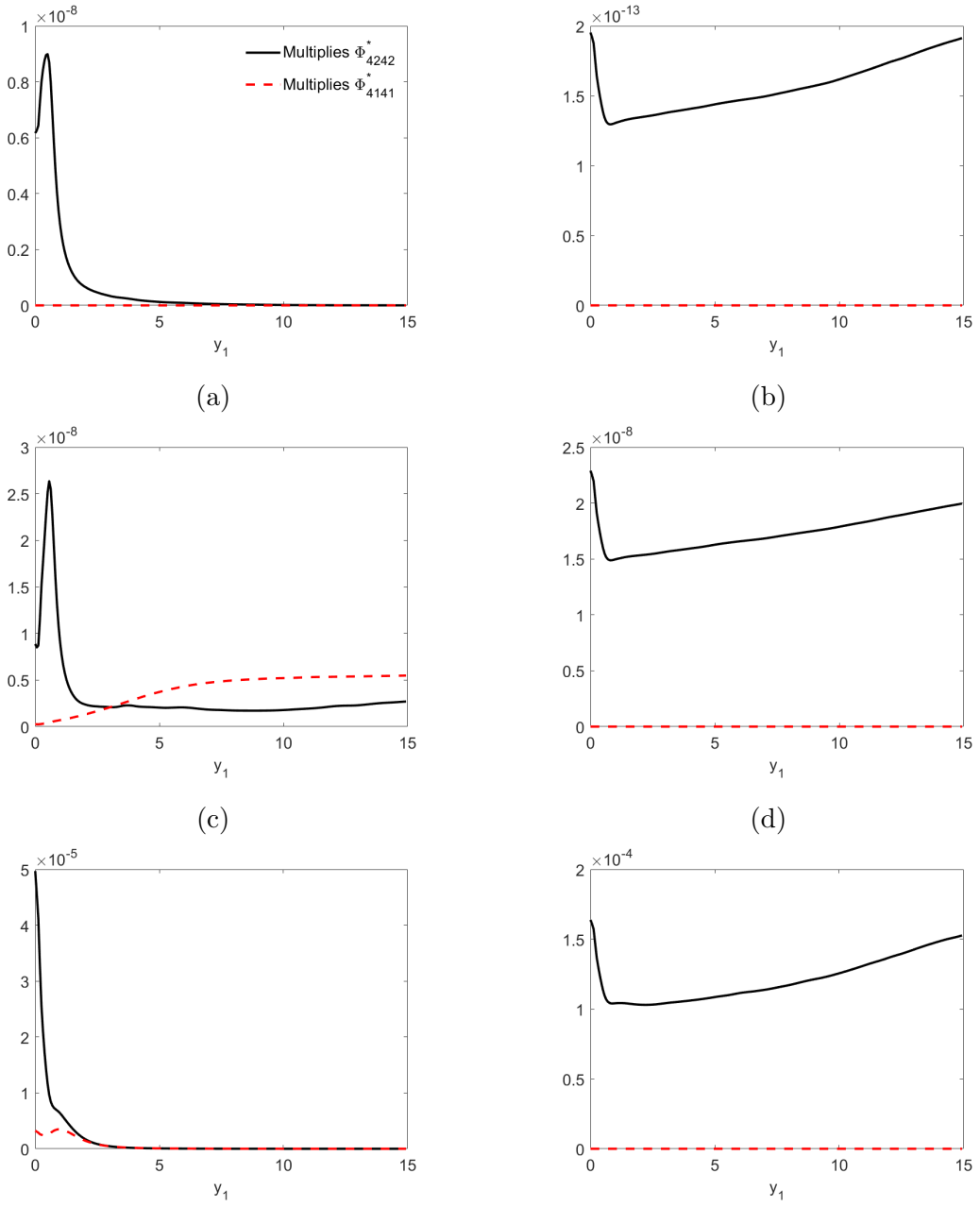

Figure 4.18: SP46: Comparison of enthalpy-flux propagator components on the shear layer for (a) $St = 0.01, \theta = 30$ (b) $St = 0.01, \theta = 90$ (c) $St = 0.2, \theta = 30$ (d) $St = 0.2, \theta = 90$ (e) $St = 2.0, \theta = 30$ (f) $St = 2.0, \theta = 90$

4.6 Summary

In this chapter we have re-derived the Green's function solution G_0 and calculated the propagator components that enter the acoustic spectrum formulation.

The process diagram in Figure 4.19 summarises our progress so far and shows that the next step in the calculation is to calculate the 4th order correlation functions.

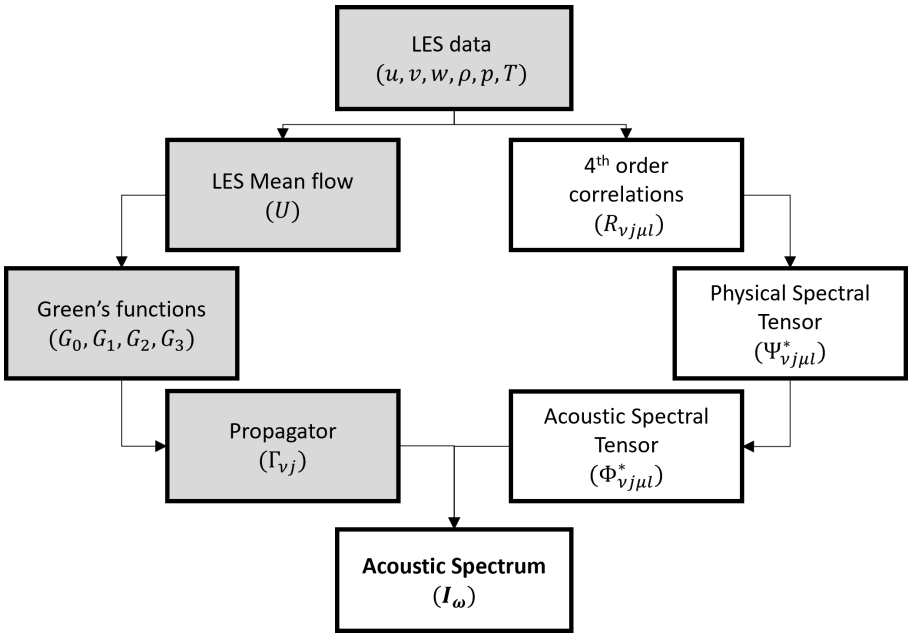

Figure 4.19: Chapter 4: Summary of process so far

Chapter 5

Jet Noise: Space-time Structure of Turbulence

In the previous chapter, Goldstein's acoustic analogy was summarised, and we saw it can be broken down into two parts: the spectral tensor which contains the turbulence information, and the propagator. We have found the propagator components in the previous chapter, and now chapters 5 and 6 focus on the spectral tensor.

The first step in the spectral tensor calculation is to calculate the 4th order correlations from the turbulence data. AGF [27] showed that the acoustic spectrum could be written as a summation of the three basic sound production components. That is, sound generated by momentum flux (i.e. Reynolds stress only), enthalpy flux (temperature fluctuations) and coupling terms involving the interaction between these two. This formula is shown below:

$$I_\omega(\boldsymbol{x}|\boldsymbol{y};\boldsymbol{k}^a) = \sum_{n=1}^{3} I_\omega^{[n]}(\boldsymbol{x}|\boldsymbol{y};\boldsymbol{k}^a) \tag{5.0.1}$$

where $\boldsymbol{k}^a$ is the acoustic wavenumber that is defined later in Chapter 6, and:

$$I_\omega^{[1]}(\boldsymbol{x}|\boldsymbol{y};\boldsymbol{k}^a) = G_{ij}(\boldsymbol{x}|\boldsymbol{y};\omega)G_{kl}^*(\boldsymbol{x}|\boldsymbol{y};\omega)\Phi_{ij,kl}^*(\boldsymbol{y};\boldsymbol{k}^a,\omega) \tag{5.0.2a}$$

$$I_\omega^{[2]}(\boldsymbol{x}|\boldsymbol{y};\boldsymbol{k}^a) = 2Re\Gamma_{4j}(\boldsymbol{x}|\boldsymbol{y};\omega)G_{kl}^*(\boldsymbol{x}|\boldsymbol{y};\omega)\Phi_{4j,kl}^*(\boldsymbol{y};\boldsymbol{k}^a,\omega) \tag{5.0.2b}$$

$$I_\omega^{[3]}(\boldsymbol{x}|\boldsymbol{y};\boldsymbol{k}^a) = \Gamma_{4j}(\boldsymbol{x}|\boldsymbol{y};\omega)\Gamma_{4l}^*(\boldsymbol{x}|\boldsymbol{y};\omega)\Phi_{4j,4l}^*(\boldsymbol{y};\boldsymbol{k}^a,\omega) \tag{5.0.2c}$$

and G_{ij} is the propagator related to the vector Green's function of the adjoint linearised Euler equations given by Eq.(6) in [27].

The spectral function $\Phi^*_{\nu j\mu l}$ enters the acoustic spectrum by the following components in Table 5.1 when an appropriate axisymmetric approximation is made. These are directly linked to the fourth order correlations of the turbulence data via Fourier transforms. Hence, this chapter focuses on the space-time structure of the turbulence (via the correlation functions), which will then be used in Chapter 6 to calculate the spectral tensor. This full analysis of the turbulence structure for heated and cold jets has not yet been done fully in the literature.

Table 5.1: Spectral Tensor Components.

	Spectral Tensor Components	Independent Components
Momentum flux term	Φ^*_{ijkl}	Φ^*_{1111}, Φ^*_{2222}, Φ^*_{1212}, Φ^*_{2233}, Φ^*_{1122}, Φ^*_{2211}
Enthalpy flux/momentum flux coupling term	Φ^*_{4jkl}	Φ^*_{4111}, Φ^*_{4122}, Φ^*_{4221}
Enthalpy flux term	Φ^*_{4j4l}	Φ^*_{4141}, Φ^*_{4242}

5.1 Amplitudes

Fourth order correlations for two points in space are calculated using the equation:

$$R_{\mu j\nu l}(\boldsymbol{x},\boldsymbol{\eta},\tau) = \overline{[v'_\mu v'_j - \overline{v'_\mu v'_j}](\boldsymbol{x},t)[v'_\nu v'_l - \overline{v'_\nu v'_l}](\boldsymbol{x}+\boldsymbol{\eta},t+\tau)} \tag{5.1.1}$$

Where we define the point $\boldsymbol{x}$ as the probe location (y_1, r), and $\boldsymbol{\eta}, \tau$ are the spatial and temporal separations respectively. The overbar indicates Reynolds time averaging $\frac{1}{2T}\int_{-T}^{T}(...)dt$, and the Greek indices range from $1-4$ whereas the Latin indices range from $1-3$. Then, (v'_1, v'_2, v'_3) are the velocity perturbations and v'_4 is related to the enthalpy fluctuation and is given by:

$$v'_4 = (\gamma-1)\Big[h' + \frac{1}{2}v'^2\Big] \tag{5.1.2}$$

There are 63 independent components of $R_{\mu j\nu l}$, which reduces to 45 components when looking at their initial amplitude (i.e when $\tau = \boldsymbol{\eta} = 0$). The

amplitudes for the momentum correlations are compared in Figure 5.1 for all four jets, where the red bars indicate correlation functions that are present within the AGF acoustic spectrum.

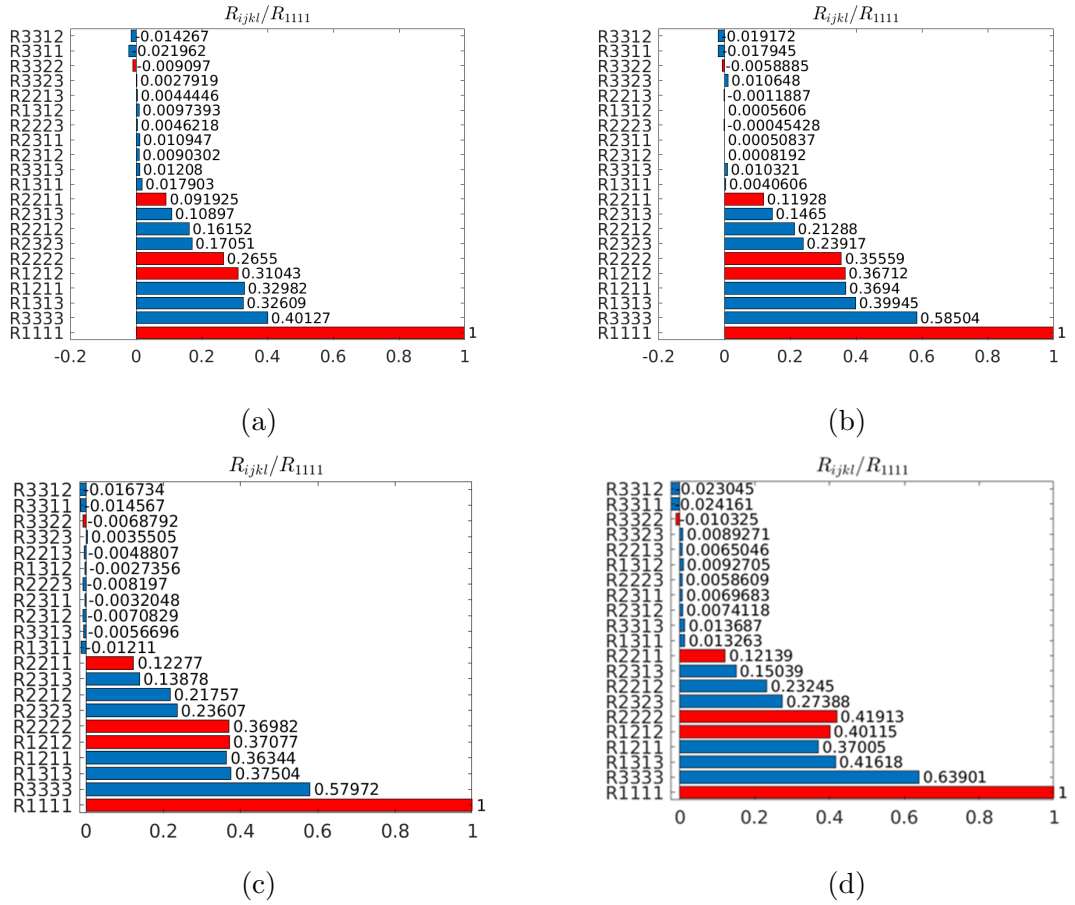

Figure 5.1: Comparison of amplitudes for the momentum flux correlations for (a) SP03 (b) SP07 (c) SP42 (d) SP46 (red bar indicates correlation functions present within the AGF formulation of the acoustic spectrum).

From this comparison it is clear that we can neglect R_{2233} from our following calculations since its magnitude is negligible in comparison to R_{1111}. We also see from this figure that heating the jet does not significantly affect the level of contribution from any of the momentum flux terms. Additionally, we see that the acoustic Mach number of jet also does not have a significant impact on the contribution of terms.

On the other hand, Figure 5.2 compares the coupling terms R_{4jkl} for both Mach numbers and we see the contribution of these coupling terms (in comparison to R_{1111}) increases for the lower Mach number, where for $Ma = 0.5$ the coupling

terms are almost double that of the $Ma = 0.9$ terms.

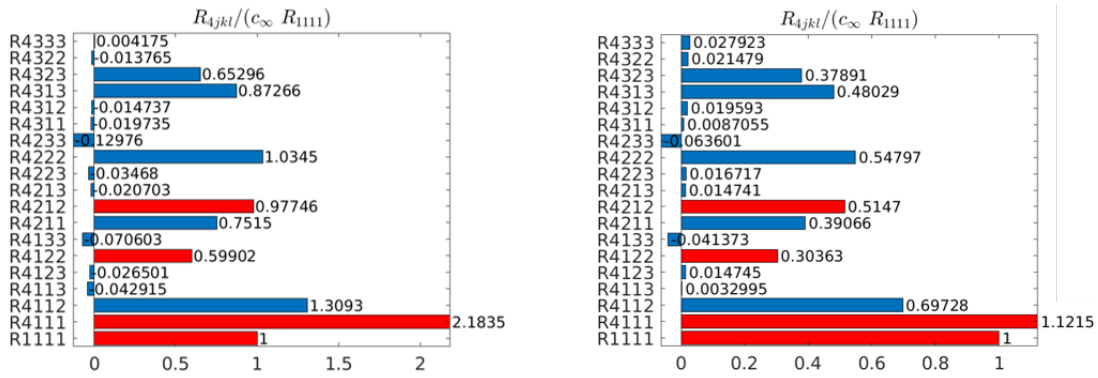

(a) (b)

Figure 5.2: Comparison of amplitudes for the coupling correlations for (a) SP42 (b) SP46 (red bar indicates correlation functions present within the AGF formulation of the acoustic spectrum).

This difference in contribution is further magnified in the temperature flux terms R_{4j4l} shown in Figure 5.3, where for $Ma = 0.5$ the enthalpy-flux terms are almost quadruple that of the $Ma = 0.9$ terms.

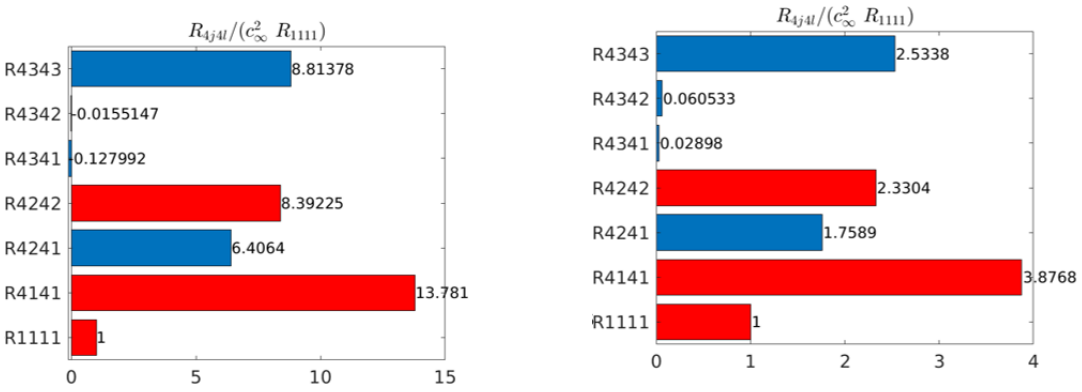

(a) (b)

Figure 5.3: Comparison of amplitudes for the coupling correlations for (a) SP42 (b) SP46 (red bar indicates correlation functions present within the AGF formulation of the acoustic spectrum).

This increase in contribution is intuitive since the momentum correlation R_{1111} will be smaller in amplitude for the smaller Mach number since the velocity perturbation v_1' will be smaller. However v_4' does not vary as much with Mach

number since it is dominated by the temperature fluctuations. Since both jets are heated at the same temperature ratio, the $R_{4j\mu l}$ terms will remain more or less constant across jets.

Therefore, based on comparing the amplitudes to R_{1111} we can only neglect one term in the AGF formulation of the acoustic spectrum. Therefore, we have 10 terms which will be required for the acoustic spectrum calculations. Five terms for the unheated jets, and ten terms for the heated jets.

5.2 Axisymmetric Turbulence

It should also be noted that the AGF formulation of the acoustic spectrum assumed axisymmetric turbulence, however it was not confirmed. Therefore in this section we check that this assumption holds using our LES data using formulations derived in Koshuriyan et al (2024) [88]. We check both, the diagonal quadratic form:

$$I_1 = \frac{R_{iikk}}{R_{1111}} = \frac{R_{1111} + R_{1122} + R_{1133} + R_{2211} + R_{2222} + R_{2233} + R_{3311} + R_{3322} + R_{3333}}{R_{1111}} \tag{5.2.1}$$

where isotropic turbulence would approximate this to

$$I_1^{iso} = 9 - 12\frac{R_{1212}}{R_{1111}}$$

and axisymmetric turbulence would approximate it to

$$I_1^{axi} = 1 + \frac{4}{R_{1111}}(R_{2222} - R_{2323} + R_{1122})$$

and the Hermitian quadratic form:

$$I_2 = \frac{R_{ikik}}{R_{1111}} = \frac{R_{1111} + 2R_{1212} + 2R_{1313} + 2R_{2323} + R_{2222} + R_{3333}}{R_{1111}} \tag{5.2.2}$$

where isotropic turbulence would approximate this to

$$I_2^{iso} = 3 + 6\frac{R_{1212}}{R_{1111}}$$

and axisymmetric turbulence would approximate it to

$$I_2^{axi} = 1 + \frac{2}{R_{1111}}(R_{2222} + 2R_{1212} + R_{2323})$$

Figure 5.4 compares the spatial structure of the diagonal and hermitian forms of the correlations using the isotropic approximation and the axisymmetric

approximation for SP03. It shows that the axisymmetric approximation appears to be good at most spatial locations, whereas the isotropic approximation is poor as expected. Figure 5.5 compares the approximations for both forms on the shear layer for SP03 confirming that the turbulence can be approximated as being axisymmetric. This is also true for the other jets, which can be seen in Appendix B.1.

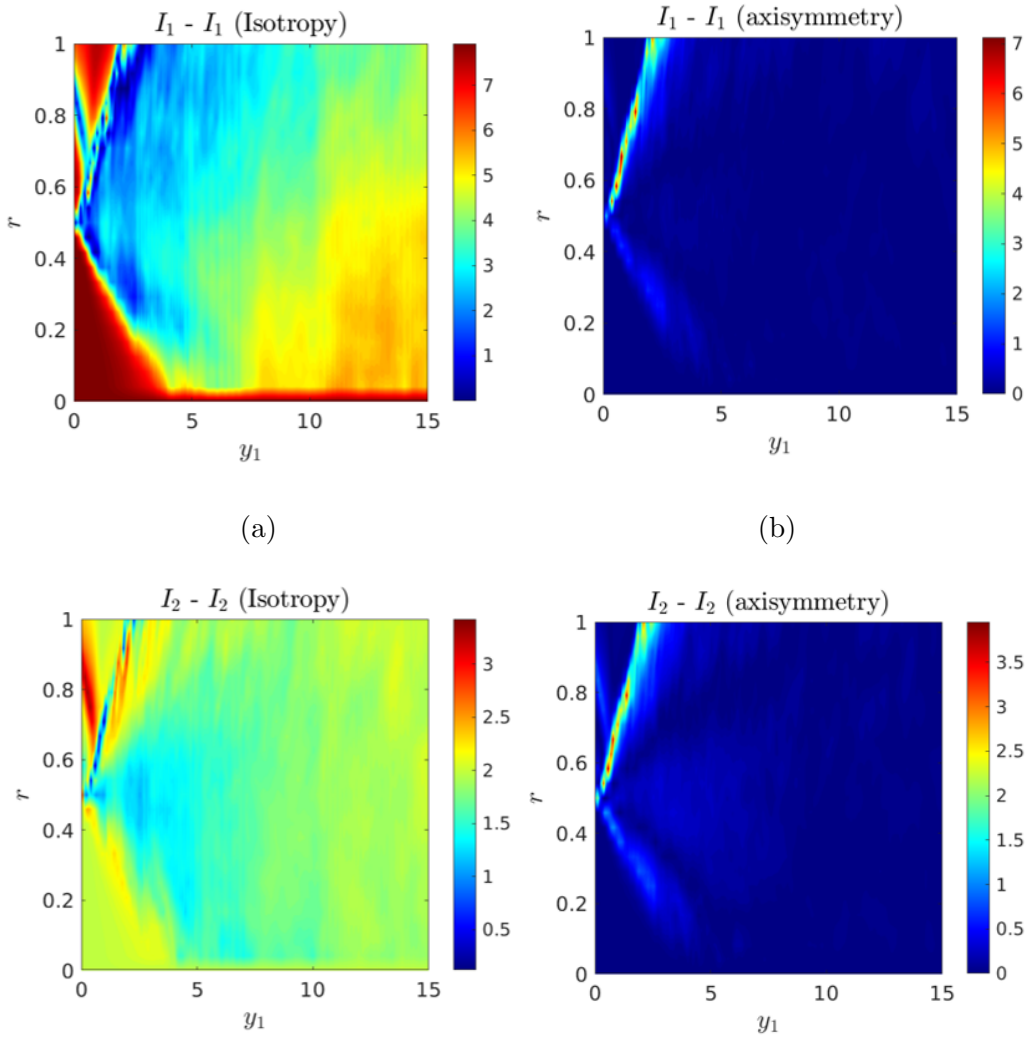

(a) (b)

(c) (d)

Figure 5.4: SP03: Compare diagonal quadratic form using (a) isotropic and (b) axisymmetric approximations, and compare Hermitian form using (c) isotropic and (d) axisymmetric approximations

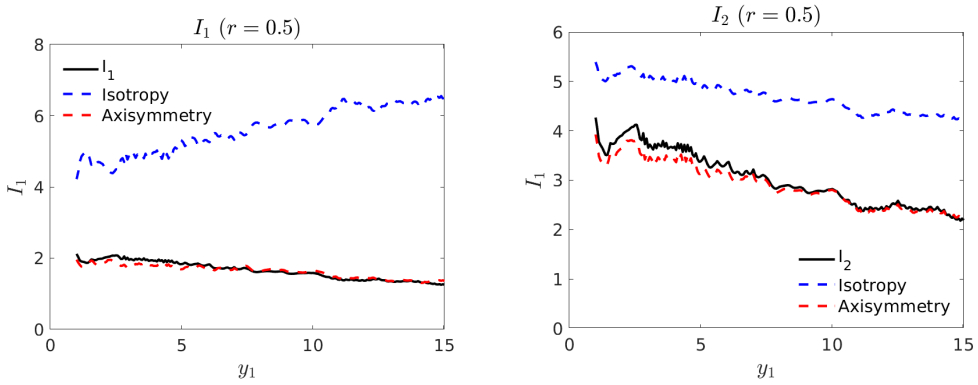

(a) (b)

Figure 5.5: SP03: Check the axisymmetry approximation on the shear layer using (a) the diagonal form (b) the Hermitian form.

5.3 Convective Velocity

The convection velocity was calculated following the methodology from Liu and Lai (2021) [89]. This method looks at the correlation data and for each streamwise separation (η_1) finds the time separation τ where the correlation is maximum. Then by plotting this τ against η_1 the gradient can be found which is the convective velocity in the streamwise direction. Similarly, this can be done for η_2 to find the transverse convection velocity.

It is known that the convection velocity varies depending on location in the jet. Figure 5.6 shows the spatial variation of R_{1111} and R_{1212} for SP03 and SP07. This figure shows that U_c is relatively constant along y_1, particularly at the potential core region ($5 < y_1 < 8$) on the shear layer ($r = 0.5$). It experiences more variation in the radial direction, however it should be noted that the LES mesh resolution is also reduced outside of the jet shear layer.

Figure 5.7 compares the space time structure of the correlations using our U_c ($U_c = 0.6$) with correlations from the literature [90] and we show good agreement for R_{1111} and R_{1212}. Our R_{2222} does not decay as fast in space as theirs does, however the auto-correlation and $\eta_1 = 0.1$ matches well.

The streamwise convection velocity was calculated for each of the ten correlations within the AGF formulation and values along the shear layer are compared in Figure 5.8. It is found that for all correlations in the cold jets the convection velocity can be taken as $U_c = 0.6$. However, for heated jets, $U_c = 0.6$

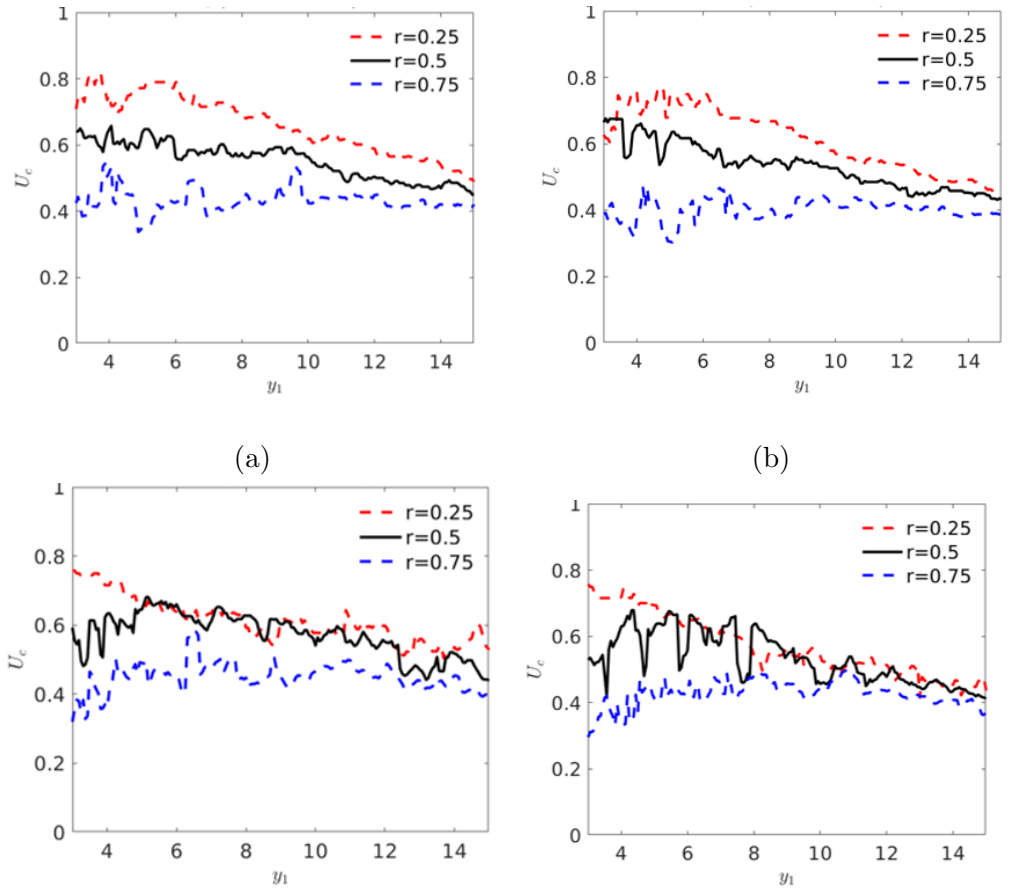

Figure 5.6: Spatial variation of the streamwise convective velocity, U_c, for (a) SP03 R_{1111} (b) SP03 R_{1212} (c) SP07 R_{1111} (d) SP07 R_{1212}

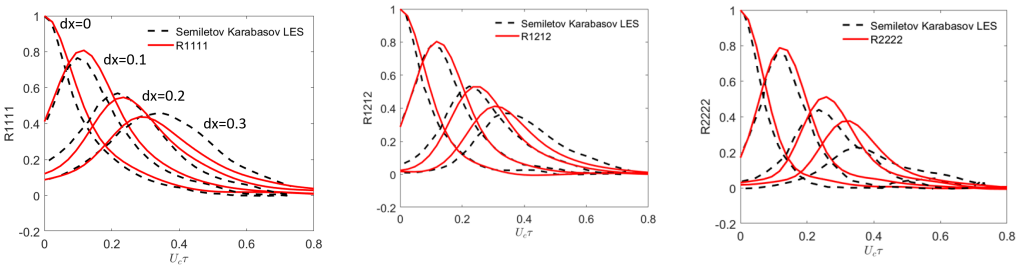

Figure 5.7: SP07: Comparison of space-time correlations using LES data and $U_c = 0.6$ with Semiletov and Karabasov (2016) [90] for (a) R_{1111} (b) R_{1212} (c) R_{2222}

is only true for R_{1111} and R_{1212}, for all other correlations $U_c = 0.4$ is a better estimation for the shear layer. This difference in convective velocity for heated correlations has, to my knowledge, not been found before.

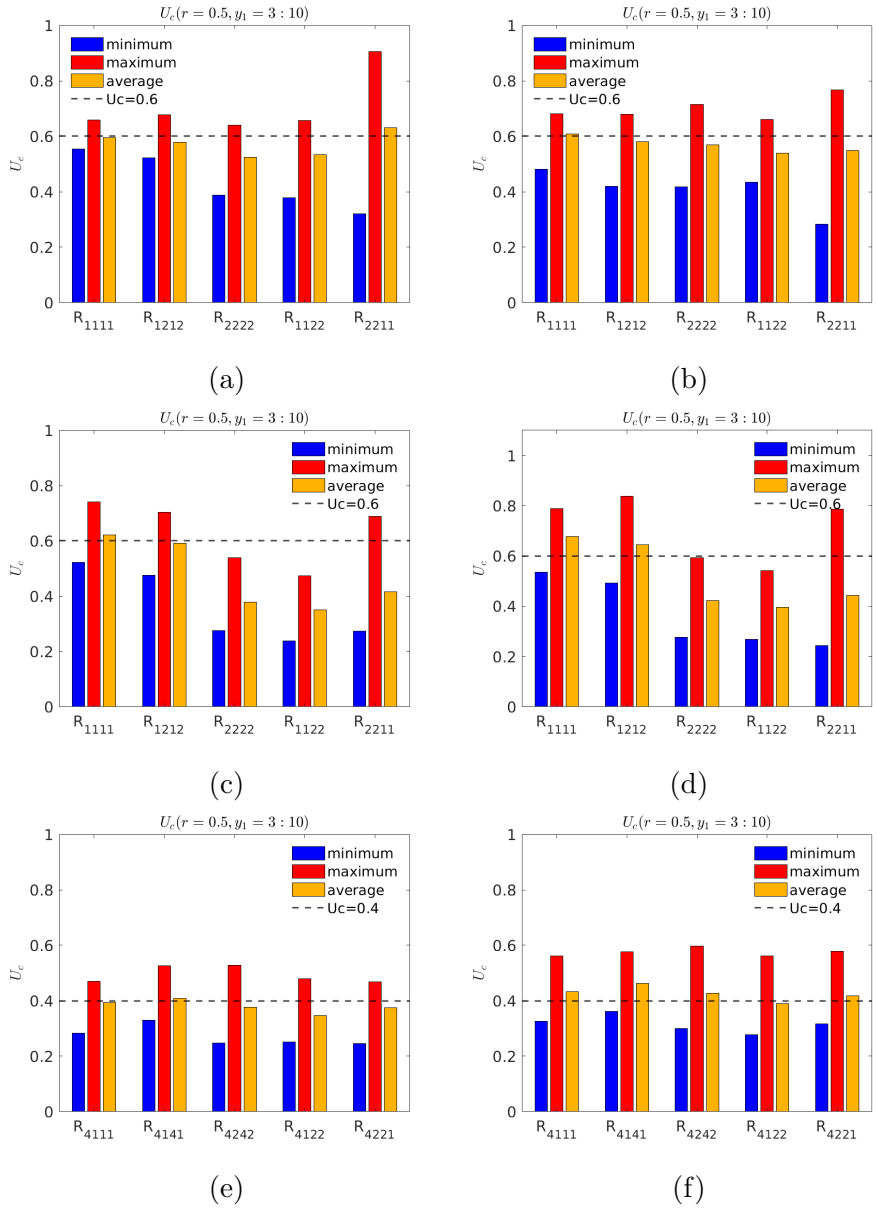

Figure 5.8: Values of U_c along shear layer ($r = 0.5$) for each correlation for (a) SP03 (b) SP07 (c) SP42 R_{ijkl} (d) SP46 R_{ijkl} (e) SP42 $R_{4j\nu l}$ (f) SP46 $R_{4j\nu l}$

5.3.1 Taylor's Hypothesis

Taylor's hypothesis states that a turbulence field will remain relatively 'frozen' within a flow, and as such evolve with respect to a convected variable. Taylor's basic assumption was that if the turbulence intensity is sufficiently small, then flow disturbances (eddies of a lengthscale smaller than an $O(1)$ body dimension) are convected, or transported, with the local mean flow without change to their spatial structure.

Since spatial correlations are always more difficult to obtain due to probe displacement effects in real experiments and/or increased streamwise resolution needed in computational simulations, the principal advantage of using Taylor's hypothesis is the conversion of an Eulerian spatial function to a temporal correlation function meaning:

$$R_{11}(\eta_1, 0; \boldsymbol{x}_T) \equiv R_{11}(0, U_c\tau; \boldsymbol{x}_T). \tag{5.3.1}$$

as was shown in [91, 92]. In other words, a streamwise spatial correlation function at zero time separation is identical to an Eulerian time correlation at zero spatial separation when the time co-ordinate is re-scaled via 'convected time unit', $U_c\tau$.

There are two approximations underlying Taylor's hypothesis: first that the convection velocity is constant, and second, that the flow is incompressible. The interesting extension then arises of whether the hypothesis in the form of (5.3.1) is applicable to shear flow turbulence[93, 94] at high Mach numbers and for high-order correlations.

Figure 5.9 checks Taylor's hypothesis for our four jets, using the fourth order turbulence correlations (R_{1111}, R_{1212}), where we used $U_c = 0.6$. Although Taylor's hypothesis appears to be remarkably accurate at the start of the potential core and along the jet shear layer, remember we have shown that there is spatial variation in U_c. Therefore, these results only indicate that at least in the location where convection velocity is constant, Taylor's hypothesis remains very accurate. In other words, there is a direct correspondence between the (Eulerian) temporal correlation function and the zero-time delay streamwise spatial correlation. For further details on this investigation see [95].

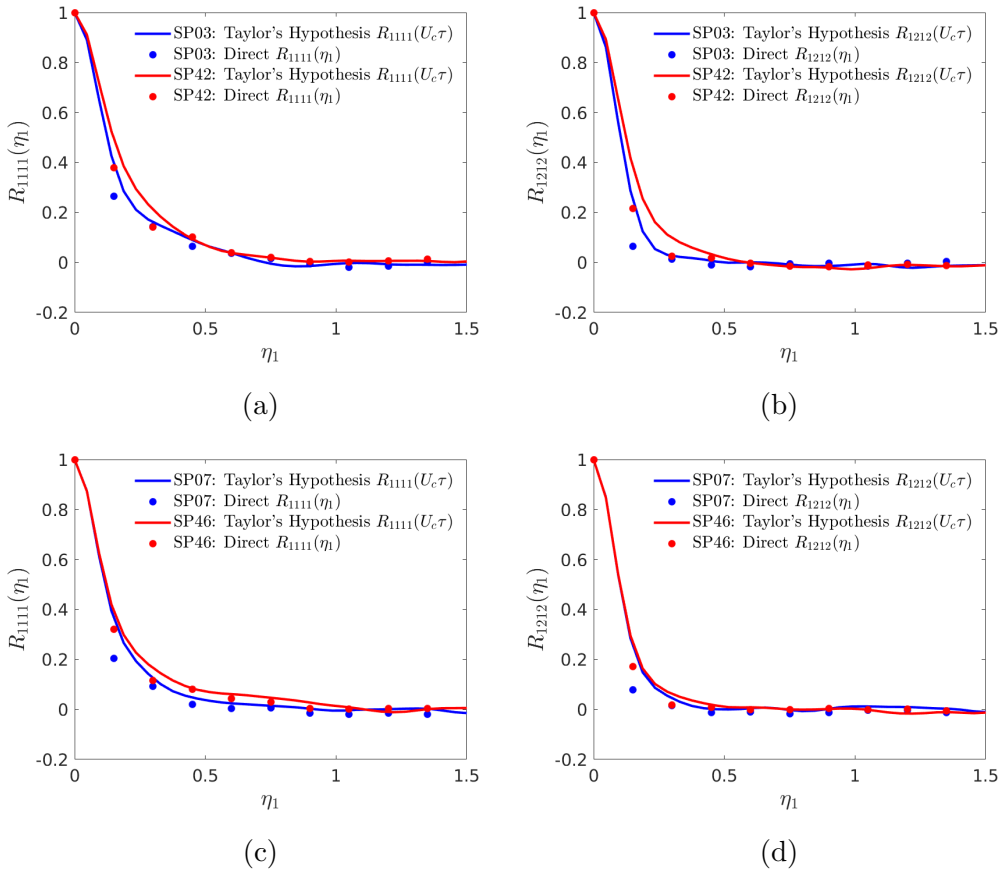

Figure 5.9: Check Taylor's Hypothesis on shear layer ($r = 0.5$) at start of potential core for (a) $Ma = 0.5, R_{1111}$ (b) $Ma = 0.5, R_{1212}$ (c) $Ma = 0.9, R_{1111}$ (d) $Ma = 0.9, R_{1212}$.

5.4 Space-time Correlations

The fourth order correlations were calculated from the LES data using (5.1.1) for a range of spatial (η_1, η_2) and temporal (τ) separations. In the next chapter we use this data to calculate the spectral tensor in two ways: analytically and numerically. To calculate the spectral tensor analytically we fit an analytical function to the data, this function is based on that from Afsar et al (2019)[67] and is given by:

$$\begin{aligned}\frac{R_{\nu j\mu l}(\boldsymbol{y},\boldsymbol{\eta},\tau)}{R_{\nu j\mu l}(\boldsymbol{y},\boldsymbol{0},0)} &= \Big[1 + a_1\tau\frac{\partial}{\partial\tau}\Big]e^{-X(\boldsymbol{y},\boldsymbol{\eta},\tau)} \\ &= \Big[1 + \frac{a_1 U_c\tau}{l_0^2 X}(\eta_1 - U_c\tau)\Big]e^{-X(\boldsymbol{y},\boldsymbol{\eta},\tau)}\end{aligned} \tag{5.4.1}$$

where

$$X(\boldsymbol{y},\boldsymbol{\eta},\tau) = \sqrt{\frac{\eta_1^2}{l_1(\boldsymbol{y})^2} + \frac{(\eta_1 - U_c\tau)^2}{l_0(\boldsymbol{y})^2} + \Big(\frac{\eta_2}{l_2(\boldsymbol{y})}\Big)^m} \tag{5.4.2}$$

and there is no sum on ν, j, μ, l. This section discusses the fourth order correlations, uses optimisation to find the optimal length scales (l_0, l_1, l_2) for the analytical model to fit the LES data, and checks for universality across acoustic Mach number and jet temperature ratio.

5.4.1 Optimised Turbulence Length Scales

The length scales were found on the shear layer at the start of the potential core, a_1, l_0, l_1 were optimised when setting $\eta_2 = 0$, and then l_2 was optimised when setting $\eta_1 = 0$, m (the power of the transverse separation) was optimised for R_{1111} and found to be 1, this was then fixed for all correlations. The objective function was defined as the root mean squared error of the model compared to the numerical data for all available temporal and spatial separations. The optimisation routine MP-AIDEA [96] was used for the optimisation and is discussed in more detail in Chapter 8.

Figures 5.10 and 5.11 compare the optimised model with the numerical data for SP03 when $\eta_2 = 0$, and $\eta_1 = 0$ respectively. These show that in general the model fits the data very well, particularly for R_{1111}, R_{1212} and R_{2222}, however since R_{1122} and R_{2211} have some oscillations in the numerical data the model cannot capture these, this is a larger problem for the l_2 optimisation where only the auto-correlation has good representation for these correlations. This

is similar for all the jets which can be seen in Appendix. B.2. Figures 5.12 and 5.13 similarly compares the optimised model against the numerical data for the coupling/enthalpy flux correlations for SP42.

This shows that the model works well for all correlations, however, like R_{1122}, R_{2211} oscillations are present in the numerical data for R_{4122} which cannot be captured by the model. Also, note that since the convection velocity is smaller for the coupling/enthalpy flux correlations the x-axis does not extend as far as the SP03 figures. Coupling/enthalpy flux correlations for SP46 are also well represented by the model, which can be seen in Appendix. B.2.

Since these optimisations were performed separately for each correlation and jet we define the lengthscales which were found as the individually optimised lengthscales. These are then shown in Tables 5.2-5.5 for SP03, SP07, SP42 ad SP46 respectively.

Table 5.2: SP03: Individual optimised lengthscales

	Momentum-flux				
	R_{1111}	R_{1212}	R_{2222}	R_{1122}	R_{2211}
a_1	-0.02	-0.11	-0.20	-0.42	0.23
l_0	0.17	0.10	0.09	0.15	0.15
l_1	0.55	0.37	0.26	0.48	0.38
l_2	0.05	0.06	0.04	0.20	0.10

Table 5.3: SP07: Individual optimised lengthscales

	Momentum-flux				
	R_{1111}	R_{1212}	R_{2222}	R_{1122}	R_{2211}
a_1	-0.04	-0.12	-0.14	-0.23	-0.03
l_0	0.15	0.10	0.09	0.15	0.15
l_1	0.42	0.32	0.28	0.64	0.32
l_2	0.04	0.05	0.04	0.12	0.09

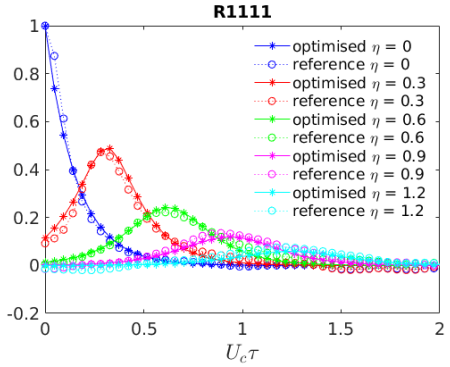

(a)

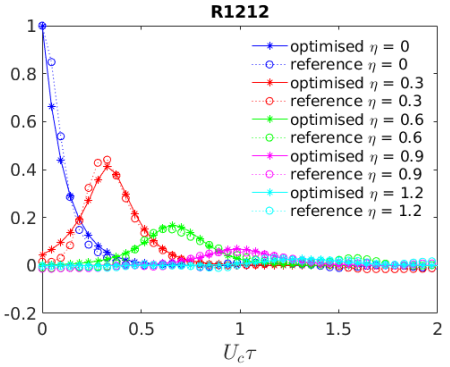

(b)

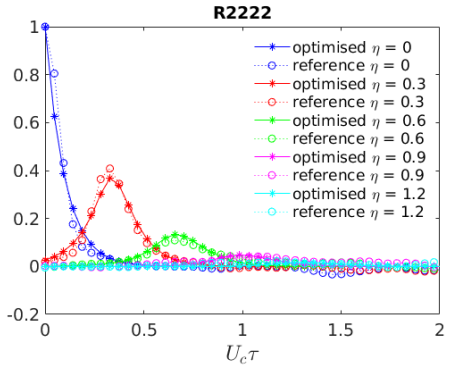

(c)

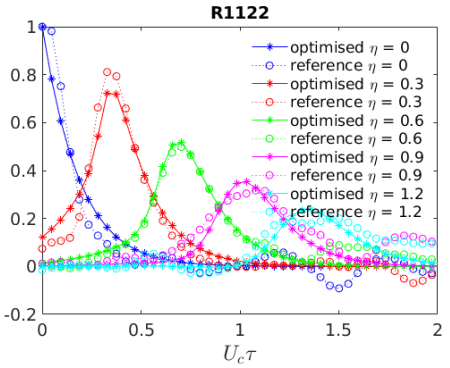

(d)

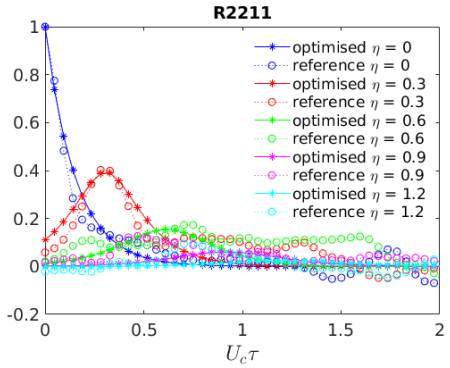

(e)

Figure 5.10: SP03: comparison of the optimised model with the numerical data (when $\eta_2 = 0$) for (a) R_{1111} (b) R_{1212} (c) R_{2222} (d) R_{1122} (e) R_{2211}

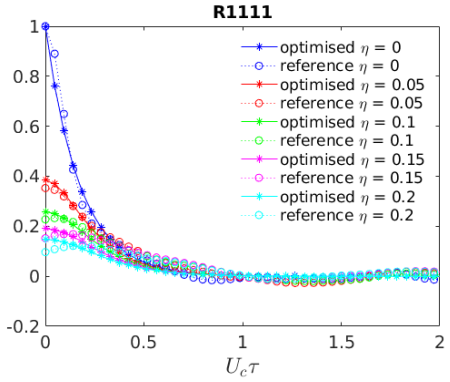

(a)

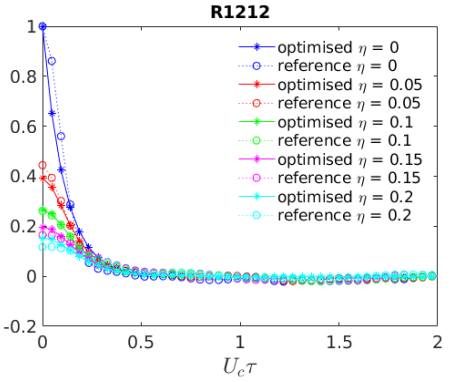

(b)

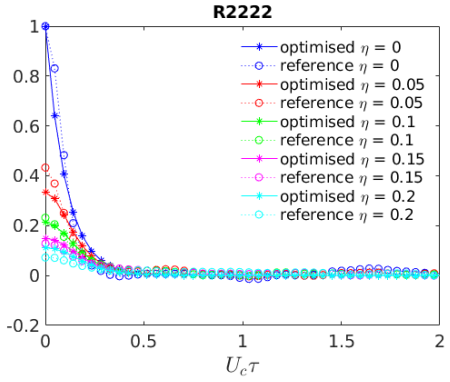

(c)

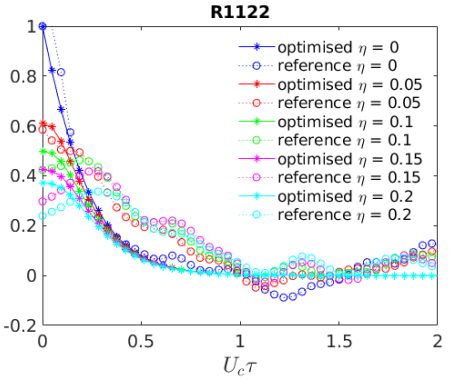

(d)

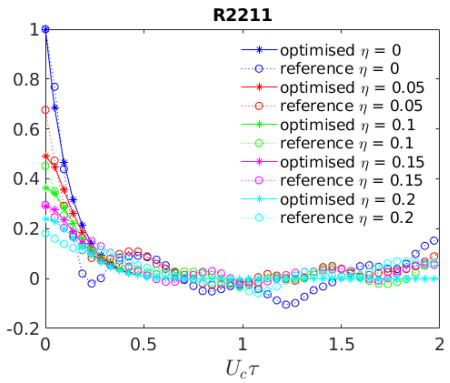

(e)

Figure 5.11: SP03: comparison of the optimised model with the numerical data (when $\eta_1 = 0$) for (a) R_{1111} (b) R_{1212} (c) R_{2222} (d) R_{1122} (e) R_{2211}

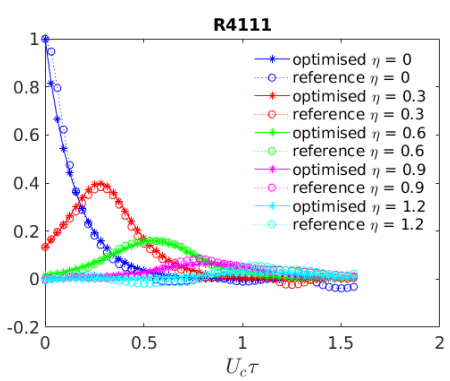

(a)

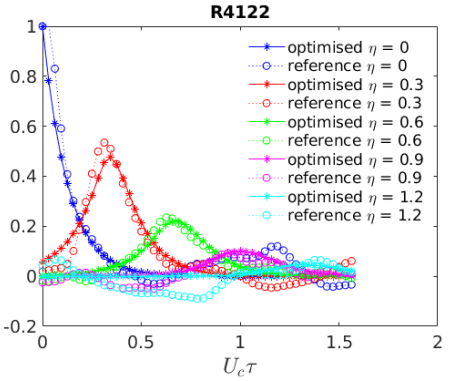

(b)

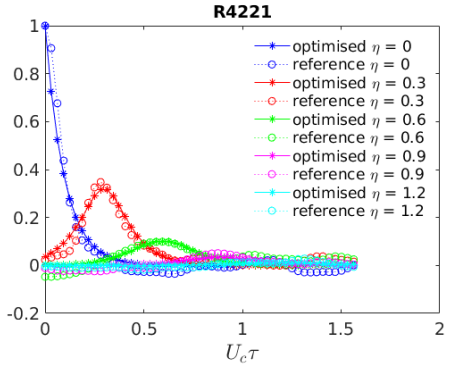

(c)

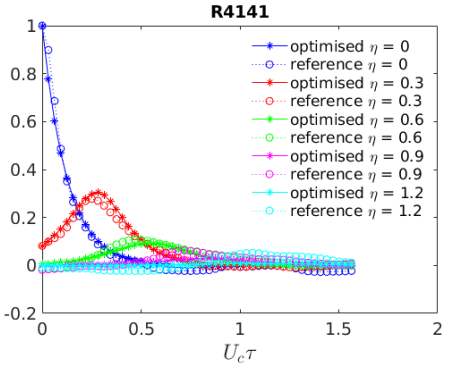

(d)

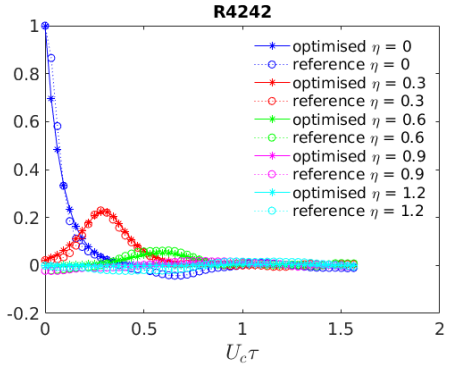

(e)

Figure 5.12: SP42: comparison of the optimised model with the numerical data (when $\eta_2 = 0$) for coupling and enthalpy flux correlations (a) R_{4111} (b) R_{4122} (c) R_{4221} (d) R_{4141} (e) R_{4242}

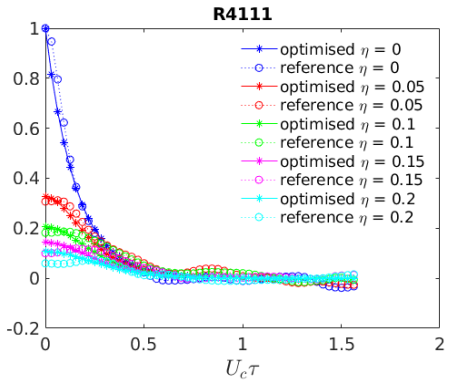

(a)

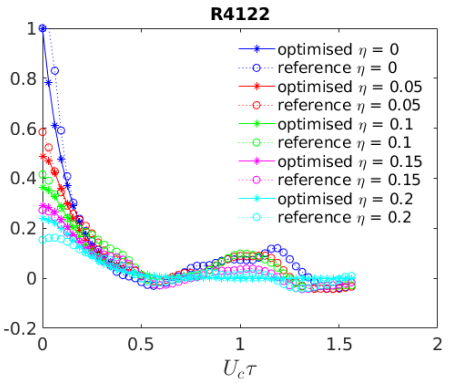

(b)

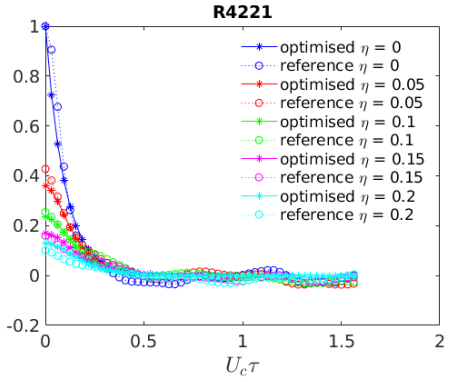

(c)

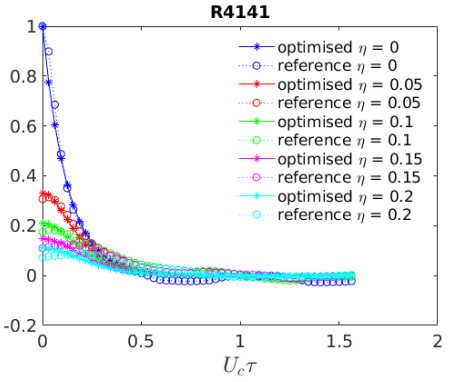

(d)

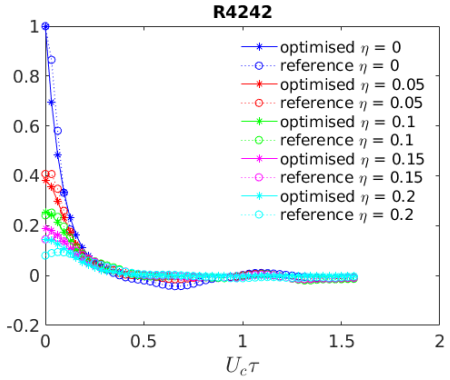

(e)

Figure 5.13: SP42: comparison of the optimised model with the numerical data (when $\eta_1 = 0$) for coupling and enthalpy flux correlations (a) R_{4111} (b) R_{4122} (c) R_{4221} (d) R_{4141} (e) R_{4242}

Table 5.4: SP42: Individual optimised lengthscales

	Momentum-flux					Coupling			Enthalpy-flux	
	R_{1111}	R_{1212}	R_{2222}	R_{1122}	R_{2211}	R_{4111}	R_{4122}	R_{4221}	R_{4141}	R_{4242}
a_1	0.00	-0.15	-0.01	-0.18	0.14	0.10	-0.15	0.01	0.10	0.01
l_0	0.20	0.12	0.09	0.15	0.17	0.17	0.11	0.10	0.14	0.09
l_1	0.42	0.32	0.19	0.48	0.37	0.32	0.36	0.26	0.25	0.20
l_2	0.04	0.04	0.04	0.10	0.09	0.04	0.10	0.05	0.04	0.05

Table 5.5: SP46: Individual optimised lengthscales

	Momentum-flux					Coupling			Enthalpy-flux	
	R_{1111}	R_{1212}	R_{2222}	R_{1122}	R_{2211}	R_{4111}	R_{4122}	R_{4221}	R_{4141}	R_{4242}
a_1	0.05	-0.06	0.09	-0.07	0.26	0.11	-0.02	0.12	0.10	0.11
l_0	0.18	0.12	0.08	0.13	0.18	0.16	0.10	0.09	0.12	0.08
l_1	0.38	0.31	0.19	0.40	0.27	0.31	0.36	0.25	0.22	0.19
l_2	0.03	0.04	0.03	0.08	0.08	0.03	0.10	0.04	0.03	0.05

5.4.2 Universality

By visual inspection of the correlation functions it appears that they might be universal across acoustic Mach number and jet temperature ratio. Therefore, in this section we compare three methods of optimisation:

1. Individual optimum (e.g. SP03 R_{1111})
2. Temperature optimum (e.g. cold jet R_{1111})
3. Component optimum (e.g. R_{1111})

Note that a universal correlation function that would represent all correlation functions is not possible since we can clearly see from Figures 5.10-5.13 that the rate of decay of the amplitude changes depending on function. Therefore the most general function we can investigate is the component optimum.

The individual optimum was found in the previous section, so in Figures 5.14 and 5.15 we compare these with the temperature optimum (which checks universality across Ma) and the component optimum (which checks universality of the temperature ratio) for R_{1111}, R_{1212}, R_{2222} for the isothermal jets and heated jets respectively.

This figure shows that the temperature optimum gives a good representation of the data, implying that there is universality across Mach number. The

component optimum on the other hand, only works well for some correlations and is noticeably poor for R_{2222} since the heated jets decay faster in η_1. However, since R_{2222} is not the largest contributor to the acoustic spectrum, it is possible that using the component optimum will still result in good acoustic predictions. This will be investigated in Chapter 7.

Figure 5.16 similarly compares $R_{4111}, R_{4141}, R_{4242}$ for SP42 and SP46. This also confirms universality of parameters across Mach number.

Tables 5.6, 5.7 show the optimised lengthscales for a cold jet and a hot jet respectively. Then Table 5.8 shows the optimised lengthscales for the component optimum (i.e. assuming universality across Ma and TR).

Table 5.6: Optimised lengthscales for a cold jet

	Momentum-flux				
	R_{1111}	R_{1212}	R_{2222}	R_{1122}	R_{2211}
a_1	-0.03	-0.11	-0.17	-0.32	0.08
l_0	0.16	0.10	0.09	0.14	0.14
l_1	0.47	0.34	0.27	0.56	0.35
l_2	0.05	0.06	0.04	0.19	0.12

Table 5.7: Optimised lengthscales for a hot jet

	Momentum-flux					Coupling			Enthalpy-flux	
	R_{1111}	R_{1212}	R_{2222}	R_{1122}	R_{2211}	R_{4111}	R_{4122}	R_{4221}	R_{4141}	R_{4242}
a_1	0.02	-0.11	0.04	-0.13	0.18	0.11	-0.08	0.06	0.10	0.06
l_0	0.19	0.12	0.08	0.14	0.17	0.17	0.11	0.10	0.13	0.08
l_1	0.39	0.31	0.19	0.44	0.31	0.31	0.36	0.26	0.23	0.19
l_2	0.04	0.04	0.04	0.11	0.09	0.04	0.11	0.05	0.04	0.05

Table 5.8: Component optimised lengthscales

	Momentum-flux					Coupling			Enthalpy-flux	
	R_{1111}	R_{1212}	R_{2222}	R_{1122}	R_{2211}	R_{4111}	R_{4122}	R_{4221}	R_{4141}	R_{4242}
a_1	-0.01	-0.11	-0.06	-0.22	0.15	0.11	-0.08	0.06	0.10	0.06
l_0	0.17	0.11	0.08	0.14	0.16	0.17	0.11	0.10	0.13	0.08
l_1	0.43	0.32	0.22	0.49	0.32	0.31	0.36	0.26	0.23	0.19
l_2	0.04	0.05	0.04	0.14	0.10	0.04	0.11	0.05	0.04	0.05

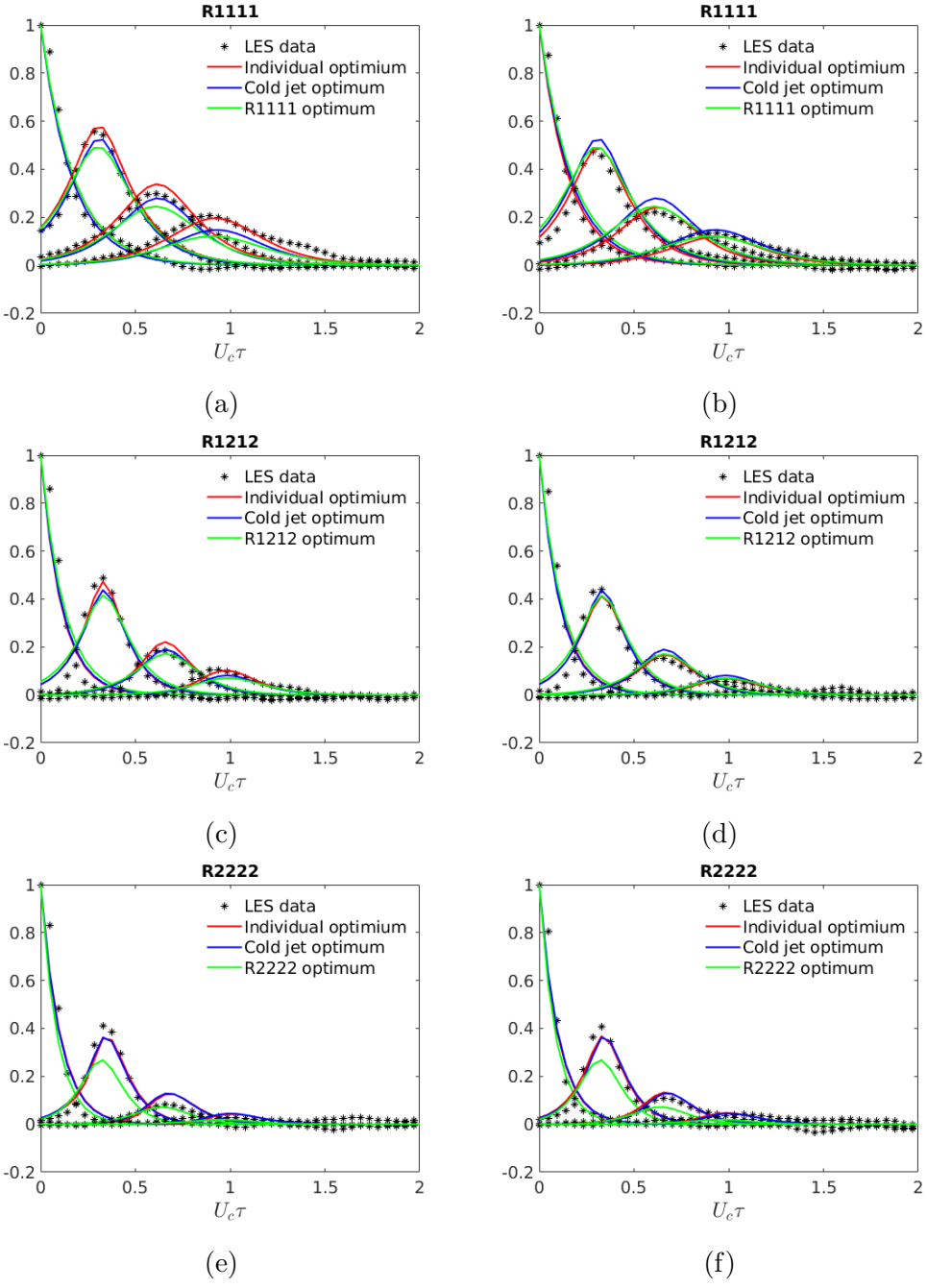

Figure 5.14: Universality of length scales for momentum-flux correlations (a,c,e) SP03, (b,d,f) SP07

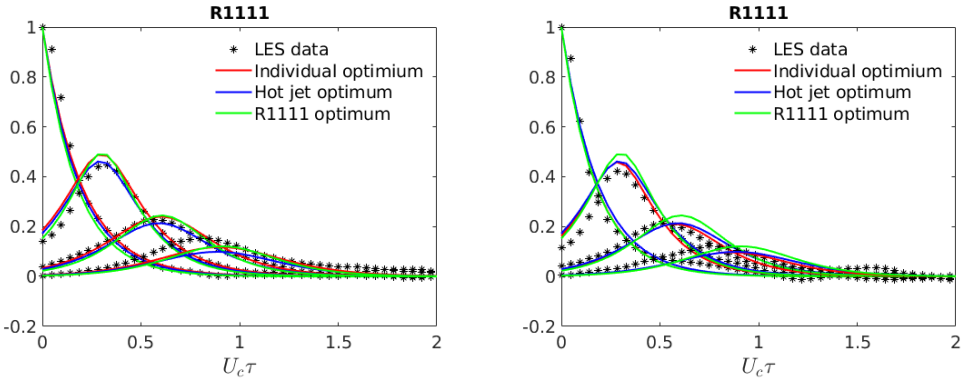

(a)

(b)

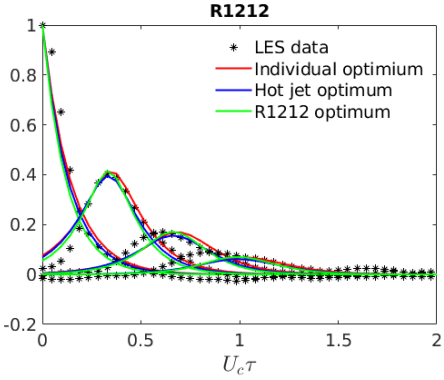

(c)

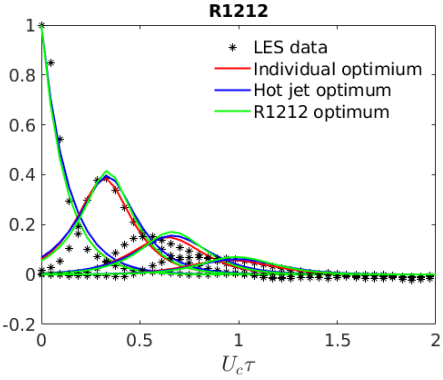

(d)

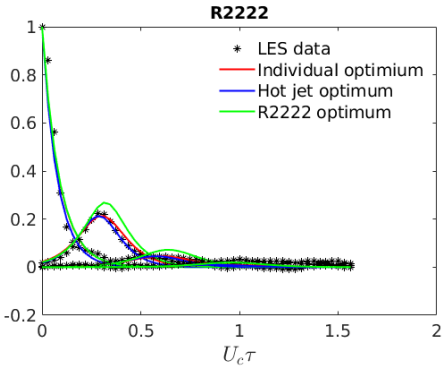

(e)

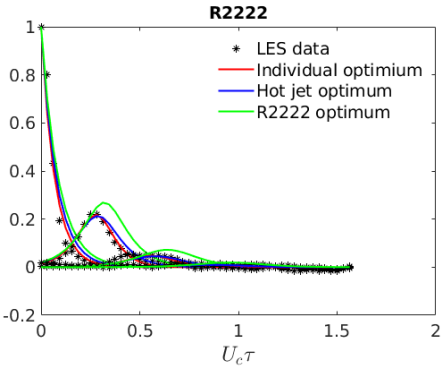

(f)

Figure 5.15: Universality of length scales for momentum-flux correlations (a,c,e) SP42, (b,d,f) SP46

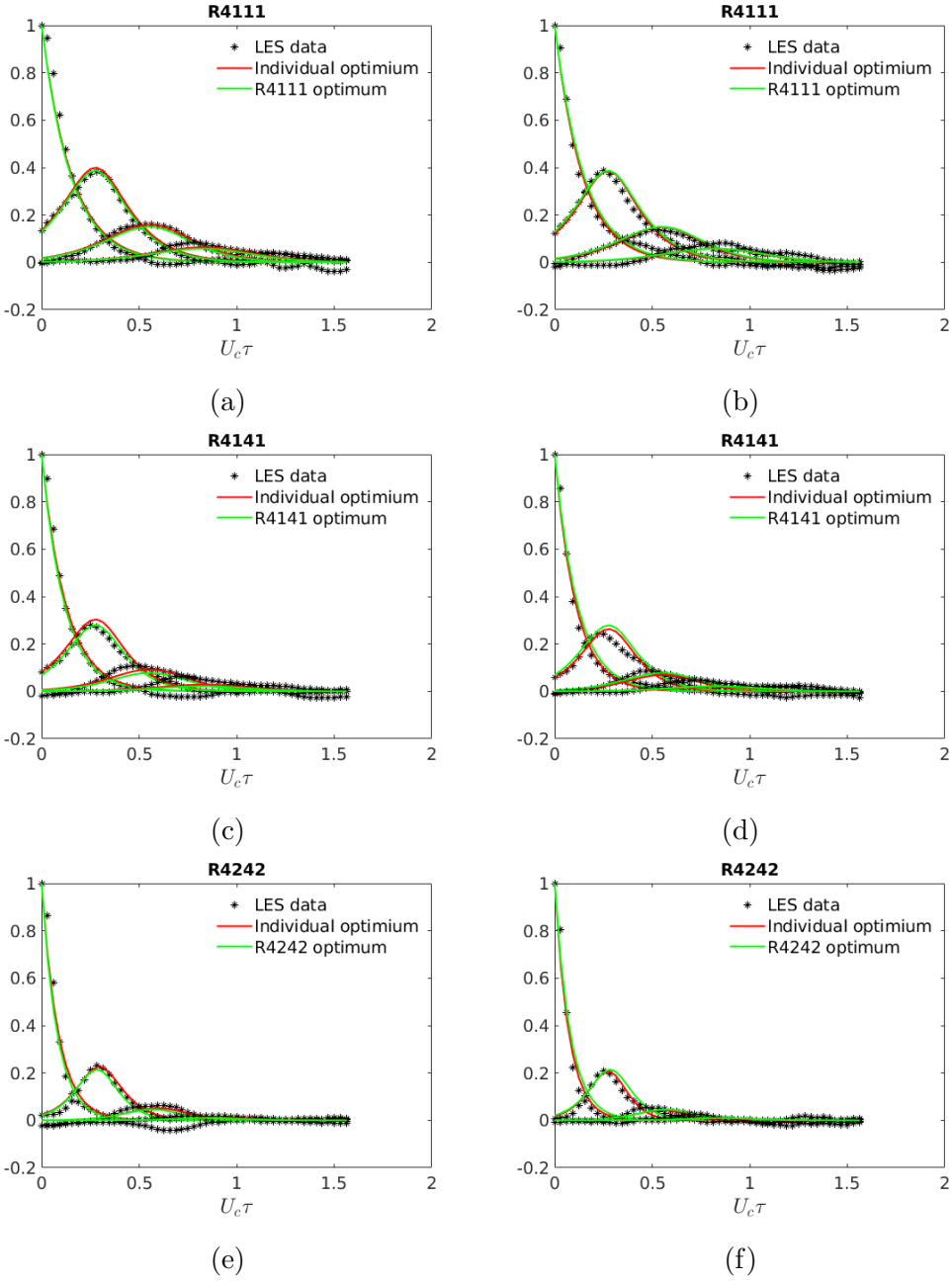

Figure 5.16: Universality of length scales for coupling and enthalpy-flux correlations, (a,c,e) SP42, (b,d,f) SP46

5.4.3 Quasi-Normality Approximation

Quasi-normality approximates the fourth order correlations using second order correlations:

$$R_{\nu j \mu l} = R_{\nu \mu} R_{jl} + R_{\nu l} R_{j \mu} \tag{5.4.3}$$

where

$$R_{\mu\nu}(\boldsymbol{y}, \boldsymbol{\eta}, \tau) = \overline{\sqrt{\rho(\boldsymbol{y}, t)} v'_\mu(\boldsymbol{y}, t) \sqrt{\rho(\boldsymbol{y} + \boldsymbol{\eta}, t + \tau)} v'_\nu(\boldsymbol{y} + \boldsymbol{\eta}, t + \tau)} \tag{5.4.4}$$

Figure 5.17 compares the fourth order correlation calculated directly from the LES data with the quasi-normality approximation for SP03 on the shear layer at the start of the potential core. We see that the approximation holds well for most of the correlations and only R_{1122} is not well represented. Similar results were found for SP07, which are shown in Appendix B.3.

However, Figures 5.18 and 5.19 compare the approximation for the heated jet SP42. Figure 5.19 shows that the approximation works well for most of coupling and enthalpy flux correlations, however, Figure 5.18 shows that it does not work well for most momentum flux correlations. Similar results were found for SP46, which are shown in Appendix B.3.

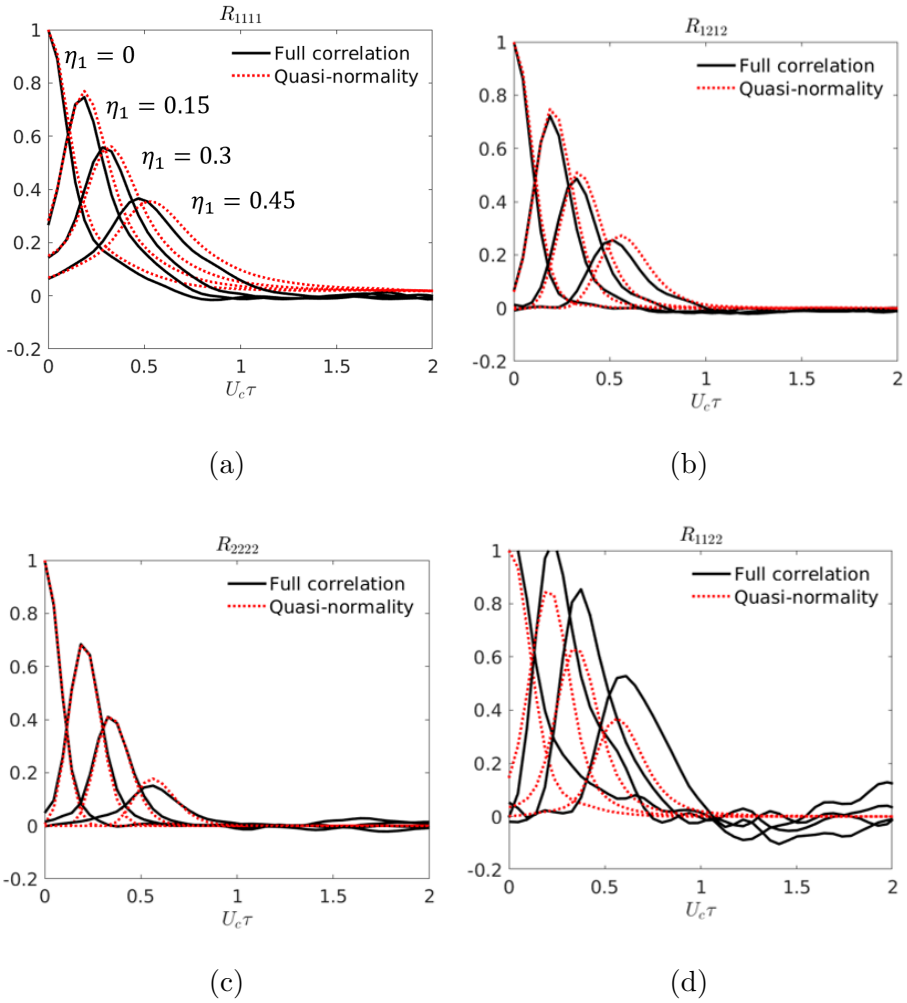

Figure 5.17: SP03: comparison of the quasi-normality approximation at $(y_1, r) = (y_1^{start}, 0.5)$ for (a) R_{1111} (b) R_{1212} (c) R_{2222} (d) R_{1122}

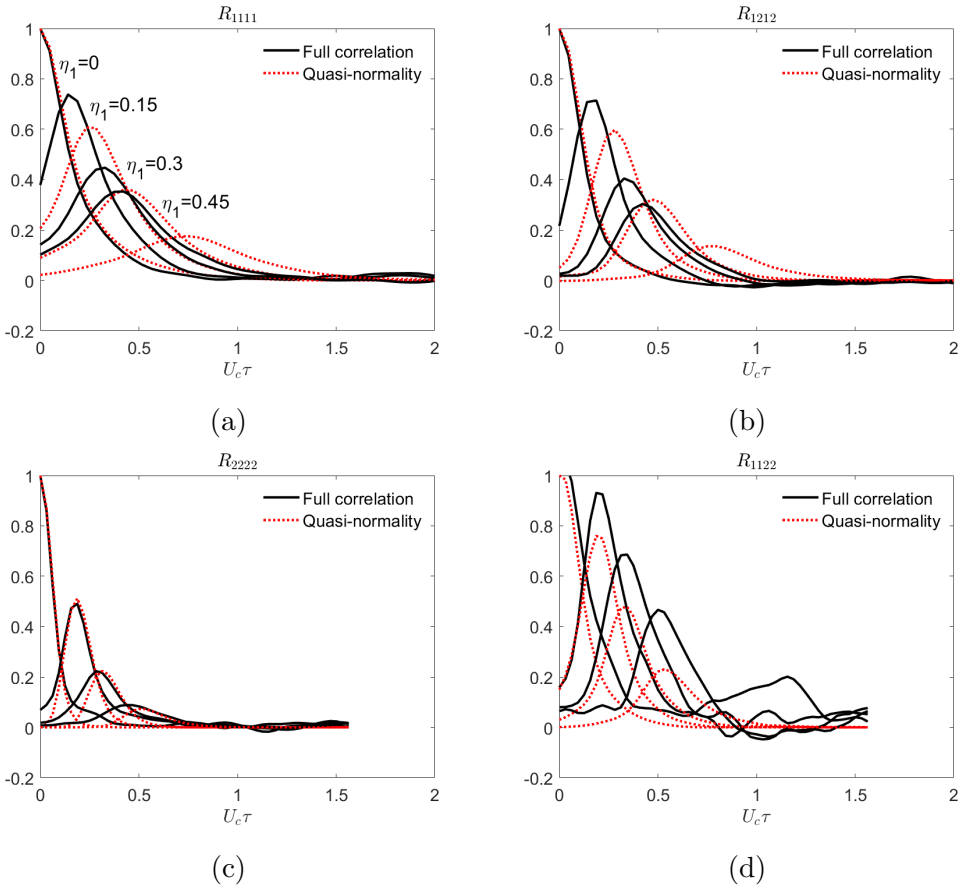

Figure 5.18: SP42: comparison of the quasi-normality approximation at $(y_1, r) = (y_1^{start}, 0.5)$ for (a) R_{1111} (b) R_{1212} (c) R_{2222} (d) R_{1122}

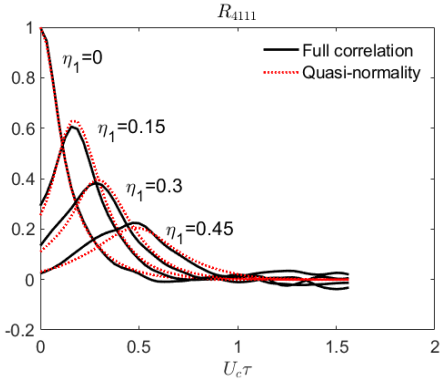

(a)

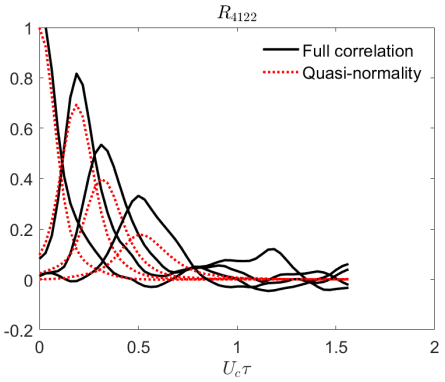

(b)

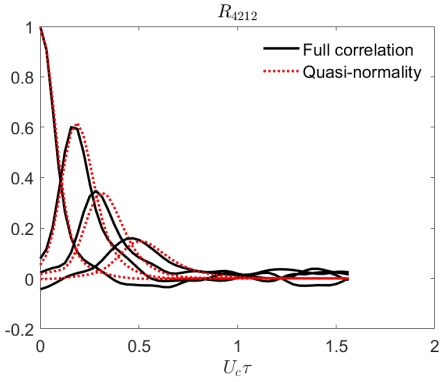

(c)

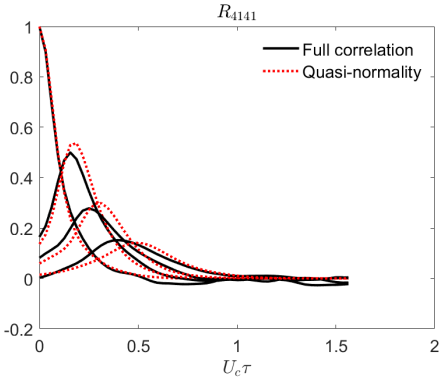

(d)

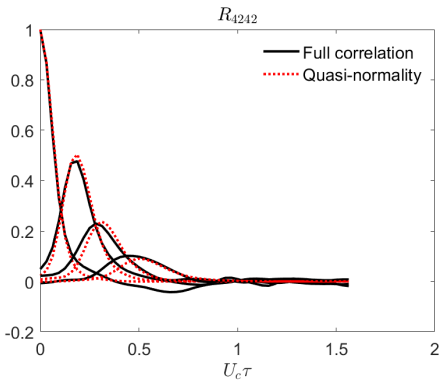

(e)

Figure 5.19: SP42: comparison of the quasi-normality approximation at $(y_1, r) = (y_1^{start}, 0.5)$ for (a) R_{4111} (b) R_{4122} (c) R_{4221} (d) R_{4141} (e) R_{4242}

5.5 Summary

In this section we have post-processed the LES data to obtain 4th order correlations which will be utilised in the spectral tensor calculation. We confirmed that the LES data is axisymmetric, and that the R_{2233} component can be neglected due to its negligible amplitude in comparison to R_{1111}. We also optimised length scales for each correlation and investigated their universality, finding that universality across Mach number is a good representation of the data, and universality across Mach number and temperature ratio is a good representation for some correlations but not all, R_{2222} becomes underrepresented for the cold jets at some spatial separations.

The process diagram in Figure 5.20 summarises our progress so far and shows the next step in the calculation is to find the physical spectral tensor which will be done in the next chapter. In this chapter we will also check universality for the spectral tensor since then we will gain a better understanding of the impact of the potential under-representation of the correlation functions.

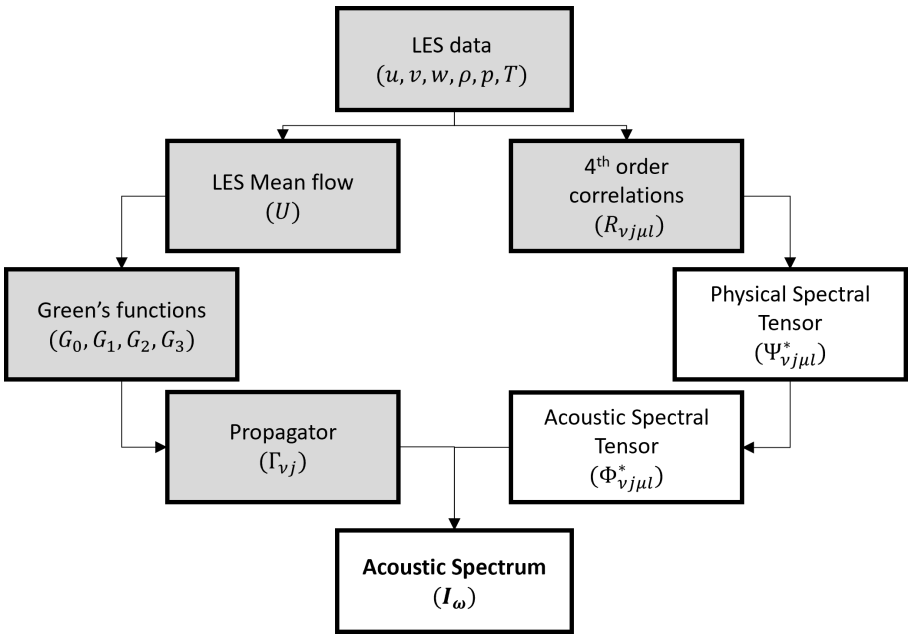

Figure 5.20: Chapter 5: Summary of process so far

Chapter 6

Jet Noise: Spectral Turbulence Analysis

This chapter calculates the spectral tensor in two ways: semi-analytically by using the length scales which were found by optimising against the correlation data in Chapter 5 as an input into an analytical formula, and fully numerically by calculating the numerical Fourier transforms of the correlations. Note the numerical spectral tensor is only found at one location to validate the analytical solution, this location is where the turbulent kinetic energy is the largest.

The spectral tensor was defined in (4.3.32) as the Fourier transform of $\mathcal{H}_{\nu j\mu l}$, where $\mathcal{H}_{\nu j\mu l}$ is linearly related to $H_{\nu j\mu l}$, the Fourier transform in time of the physical 4th order turbulence correlation. Hence, we can define a new variable $\Psi_{\nu j\mu l}$ as the *physical* spectral tensor (i.e. it is physically related to the turbulence):

$$\begin{aligned}\Psi^*_{\nu j\mu l}(\boldsymbol{y};\omega,k_1,k_T) &= \int_{\boldsymbol{\eta}} H_{\nu j\mu l}(\boldsymbol{y},\boldsymbol{\eta};\omega)e^{i\boldsymbol{k}\cdot\boldsymbol{\eta}}d\boldsymbol{\eta} \\ &= \frac{1}{2\pi}\int_{\boldsymbol{\eta}}\int_{-\infty}^{\infty} e^{i(\boldsymbol{k}\cdot\boldsymbol{\eta}-\omega\tau)}R_{\nu j\mu l}(\boldsymbol{y},\boldsymbol{\eta},\tau)d\tau d\boldsymbol{\eta}\end{aligned} \tag{6.0.1}$$

Then the acoustic spectral tensor $\Phi^*_{\nu j\mu l}$ is found through the linear relation:

$$\Phi^*_{\nu j\mu l} = \epsilon_{\nu j\sigma m}\Psi^*_{\nu j\mu l}\epsilon_{\mu l\lambda n} \tag{6.0.2}$$

where $\epsilon_{\nu j\sigma m}$ was defined in (4.3.6).

6.1 Analytical Spectral Tensor: Derivation

6.1.1 Physical Spectral Tensor

We assume the turbulence correlation functions $R_{\nu j \mu l}$ are represented by the analytical model from [67]:

$$\frac{R_{\nu j \mu l}(\boldsymbol{y}, \boldsymbol{\eta}, \tau)}{R_{\nu j \mu l}(\boldsymbol{y}, \mathbf{0}, 0)} = \Big(1 + a_1 \tau \frac{\partial}{\partial \tau}\Big) R_0(\boldsymbol{y}, \boldsymbol{\eta}, \tau) \tag{6.1.1}$$

where there is no sum on ν, j, μ, l and

$$R_0(\boldsymbol{y}, \boldsymbol{\eta}, \tau) = e^{-X(\boldsymbol{y}, \boldsymbol{\eta}, \tau)} \tag{6.1.2}$$

and

$$X(\boldsymbol{y}, \boldsymbol{\eta}, \tau) = \sqrt{\frac{\eta_1^2}{l_1(\boldsymbol{y})^2} + \frac{(\eta_1 - U_c\tau)^2}{l_0(\boldsymbol{y})^2} + f(\boldsymbol{\eta_T}; l_2(\boldsymbol{y}))} \tag{6.1.3}$$

where $l_i(y_1, r) = c_i L_T(y_1, r)$ are length scales related to the turbulence since $L_T(y_1, r) = k(y_1, r)^{3/2}/\epsilon(y_1, r)$ from the LES data. In the previous chapter we optimised l_i at one spatial location (start of potential core and on the shear layer), this allows us to calculate c_i at that location. We make the assumption that c_i is a constant since it would be impossible to calculate at every spatial location (since the optimisation at a single location for one correlation takes roughly 2 minutes, across all spatial locations $(nx, nr) = (321, 49)$ this would be 22 days per correlation per jet!), therefore the spatial nature of the length scales comes from $L_T(y_1, r)$ alone.

The spectral tensor is the 3D Fourier transform:

$$\frac{\Psi^*_{\nu j \mu l}(\boldsymbol{y}; \omega, k_1, k_T)}{R_{\nu j \mu l}(\boldsymbol{y}, \mathbf{0}, 0)} = \int_{\boldsymbol{\eta}} e^{i(\boldsymbol{k}\cdot\boldsymbol{\eta})} \frac{1}{2\pi} \int_{-\infty}^{\infty} e^{-i\omega\tau} \Big(1 + a_1 \tau \frac{\partial}{\partial \tau}\Big) R_0 \, d\tau \, d\boldsymbol{\eta} \tag{6.1.4}$$

We define new variables: $\tilde{\tau} = U_c\tau/l_0$, $\tilde{\eta_i} = \eta_i/l_i$ where $i = 1, 2, 3$, and $\tilde{\xi} = (\eta_1 - U_c\tau)/l_0 = \tilde{\eta_1} l_r - \tilde{\tau}$ where $l_r = l_1/l_0$. Since we are assuming axisymmetry ($l_2 = l_3 = l_T$). Note that $\tau\partial/\partial\tau = \tilde{\tau}\partial/\partial\tilde{\tau}$, and $i\omega\tau = i\omega l_0\tilde{\tau}/U_c = i\tilde{\omega}\tilde{\tau}$ when we define $\tilde{\omega} = \omega l_0/U_c$, likewise $i(\boldsymbol{k}\cdot\boldsymbol{\eta}) = i(\tilde{\boldsymbol{k}}\cdot\tilde{\boldsymbol{\eta}})$ when we define $\tilde{k}_i = k_i l_i$.

Rewriting the integral using these scaled variables gives:

$$\frac{\Psi^*_{\nu j \mu l}(\boldsymbol{y}; \tilde{\omega}, \tilde{k}_1, \tilde{k}_T)}{R_{\nu j \mu l}(\boldsymbol{y}, \mathbf{0}, 0)} = \Big(\frac{l_T^2 l_1 l_0}{U_c}\Big) \int_{\tilde{\boldsymbol{\eta}}} e^{i(\tilde{\boldsymbol{k}}\cdot\tilde{\boldsymbol{\eta}})} \frac{1}{2\pi} \int_{-\infty}^{\infty} e^{-i\tilde{\omega}\tilde{\tau}} \Big(1 + a_1 \tilde{\tau} \frac{\partial}{\partial \tilde{\tau}}\Big) R_0 \, d\tilde{\tau} \, d\tilde{\boldsymbol{\eta}} \tag{6.1.5}$$

In the a_1 term of the integral we can replace $\tilde{\tau}$ using

$$\frac{\partial}{\partial\tilde{\omega}}e^{-i\tilde{\omega}\tilde{\tau}} = -i\tilde{\tau}e^{-i\tilde{\omega}\tilde{\tau}}$$

Therefore the time integral becomes

$$\frac{l_0}{U_c}\frac{1}{2\pi}\int_{-\infty}^{\infty}\left\{e^{-i\tilde{\omega}\tilde{\tau}}R_0 + \Big[-\frac{a_1}{i}\frac{\partial}{\partial\tilde{\omega}}e^{-i\tilde{\omega}\tilde{\tau}}\frac{\partial}{\partial\tilde{\tau}}R_0\Big]\right\}d\tilde{\tau} \tag{6.1.6}$$

where the term in square brackets can be integrated by parts:

$$= -\frac{a_1 l_0}{U_c}\frac{1}{2\pi}\int_{-\infty}^{\infty}\left[\frac{\partial}{\partial\tilde{\tau}}\Big(R_0\frac{\partial}{\partial\tilde{\omega}}e^{-i\tilde{\omega}\tilde{\tau}}\Big) - R_0\frac{\partial^2}{\partial\tilde{\tau}\partial\tilde{\omega}}e^{-i\tilde{\omega}\tilde{\tau}}\right]d\tilde{\tau}$$

The first term integrates to zero, and using

$$\frac{\partial^2}{\partial\tilde{\tau}\partial\tilde{\omega}}e^{-i\tilde{\omega}\tilde{\tau}} = \frac{\partial}{\partial\tilde{\omega}}\Big(-i\tilde{\omega}e^{-i\tilde{\omega}\tilde{\tau}}\Big) = -i\Big(1+\tilde{\omega}\frac{\partial}{\partial\tilde{\omega}}\Big)e^{-i\tilde{\omega}\tilde{\tau}}$$

the integral is reduced to:

$$= -\frac{a_1 l_0}{U_c}\frac{1}{2\pi}\int_{-\infty}^{\infty}R_0\Big[1+\tilde{\omega}\frac{\partial}{\partial\tilde{\omega}}\Big]e^{-i\tilde{\omega}\tilde{\tau}}d\tilde{\tau} \tag{6.1.7}$$

Inserting this back into (6.1.6) gives

$$\frac{l_0}{U_c}L_{\tilde{\omega}}\frac{1}{2\pi}\int_{-\infty}^{\infty}R_0(\tilde{\boldsymbol{\eta}},\tilde{\tau},l(\boldsymbol{y}))e^{-i\tilde{\omega}\tilde{\tau}}d\tilde{\tau} \tag{6.1.8}$$

where we define

$$L_{\tilde{\omega}} = (1-a_1) - a_1\tilde{\omega}\frac{\partial}{\partial\tilde{\omega}}$$

Inserting this time integral back into the full spectral tensor gives:

$$\frac{\Psi^*_{\nu j\mu l}(\boldsymbol{y};\tilde{\omega},\tilde{k}_1,\tilde{k}_T)}{A_0(\boldsymbol{y})R_{\nu j\mu l}(\boldsymbol{y},\boldsymbol{0},0)} = L_{\tilde{\omega}}\int_{\tilde{\boldsymbol{\eta}}}e^{i(\tilde{\boldsymbol{k}}\cdot\tilde{\boldsymbol{\eta}})}\frac{1}{2\pi}\int_{-\infty}^{\infty}e^{-i\tilde{\omega}\tilde{\tau}}e^{-\sqrt{\tilde{\eta}_1^2+(\tilde{\eta}_1 l_r-\tilde{\tau})^2+f(\tilde{\boldsymbol{\eta}}_{\boldsymbol{T}})}}d\tilde{\tau}d\tilde{\boldsymbol{\eta}} \tag{6.1.9}$$

where $A_0(\boldsymbol{y}) = (l_T(\boldsymbol{y})^2 l_0(\boldsymbol{y})l_1(\boldsymbol{y}))/U_c$ is an amplitude. Then if we introduce $\tilde{\xi} = \tilde{\eta}_1 l_r - \tilde{\tau}$, then the integrals can be rewritten as:

$$\frac{\Psi^*_{\nu j\mu l}(\boldsymbol{y};\tilde{\omega},\tilde{k}_1,\tilde{k}_T)}{A_0(\boldsymbol{y})R_{\nu j\mu l}(\boldsymbol{y},\boldsymbol{0},0)} = L_{\tilde{\omega}}\int_{\tilde{\boldsymbol{\eta}}_{\boldsymbol{T}}}e^{i(\tilde{\boldsymbol{k}}_{\boldsymbol{T}}\cdot\tilde{\boldsymbol{\eta}}_{\boldsymbol{T}})}\int_{\tilde{\eta}_1}e^{i\overline{k}_1\tilde{\eta}_1}\frac{1}{2\pi}\int_{-\infty}^{\infty}e^{i\tilde{\omega}\tilde{\xi}}e^{-\sqrt{\tilde{\eta}_1^2+\tilde{\xi}^2+f(\tilde{\boldsymbol{\eta}}_{\boldsymbol{T}})}}d\tilde{\xi}d\tilde{\eta}_1 d\tilde{\boldsymbol{\eta}}_{\boldsymbol{T}} \tag{6.1.10}$$

where we define $\overline{k}_1 = \tilde{k}_1 - \tilde{\omega}l_r$. This enables us to use the result (#867) from Campbell and Foster [97], which reduces the right hand side of the equation to:

$$L_{\tilde{\omega}}\int_{\tilde{\boldsymbol{\eta}}_{\boldsymbol{T}}}e^{i(\tilde{\boldsymbol{k}}_{\boldsymbol{T}}\cdot\tilde{\boldsymbol{\eta}}_{\boldsymbol{T}})}\int_{\tilde{\eta}_1}e^{i\overline{k}_1\tilde{\eta}_1}\frac{\sqrt{\tilde{\eta}_1^2+f(\tilde{\boldsymbol{\eta}}_T)}}{\pi\sqrt{\tilde{\omega}^2+1}}K_1\Big((\tilde{\omega}^2+1)^{1/2}\sqrt{\tilde{\eta}_1+f(\tilde{\boldsymbol{\eta}}_{\boldsymbol{T}})}\Big)d\tilde{\eta}_1 d\tilde{\boldsymbol{\eta}}_{\boldsymbol{T}} \tag{6.1.11}$$

Then, using another result (#917.8) from Campbell and Foster [97], this becomes:

$$\frac{\Psi^*_{\nu j\mu l}(\boldsymbol{y};\tilde{\omega},\tilde{k}_1,\tilde{k}_T)}{A_0(\boldsymbol{y})R_{\nu j\mu l}(\boldsymbol{y},\boldsymbol{0},0)} = L_{\tilde{\omega}}\int_{\tilde{\boldsymbol{\eta}}_{\boldsymbol{T}}} e^{i(\tilde{\boldsymbol{k}}_{\boldsymbol{T}}\cdot\tilde{\boldsymbol{\eta}}_{\boldsymbol{T}})}\Big[\frac{1+\chi^{1/2}\sqrt{f(\tilde{\boldsymbol{\eta}}_T)}}{\chi^{3/2}}\Big]e^{-\chi^{1/2}\sqrt{f(\tilde{\boldsymbol{\eta}}_T)}}d\tilde{\boldsymbol{\eta}}_{\boldsymbol{T}} \tag{6.1.12}$$

where $\chi = (\tilde{k}_1 - \tilde{\omega}l_r)^2 + \tilde{\omega}^2 + 1 = \bar{k_1}^2 + \tilde{\omega}^2 + 1$.

We can write this succinctly as:

$$\frac{\Psi^*_{\nu j\mu l}(\boldsymbol{y};\tilde{\omega},\tilde{k}_1,\tilde{k}_T)}{A_0(\boldsymbol{y})R_{\nu j\mu l}(\boldsymbol{y},\boldsymbol{0},0)} = L_{\tilde{\omega}}\int_{\tilde{\boldsymbol{\eta}}_{\boldsymbol{T}}} e^{i(\tilde{\boldsymbol{k}}_{\boldsymbol{T}}\cdot\tilde{\boldsymbol{\eta}}_{\boldsymbol{T}})}F_a(\tilde{\boldsymbol{\eta}}_T;\chi)d\tilde{\boldsymbol{\eta}}_{\boldsymbol{T}} \tag{6.1.13}$$

where

$$F_a(\tilde{\boldsymbol{\eta}}_T;\chi) = \Big[\frac{1+\chi^{1/2}\sqrt{f(\tilde{\boldsymbol{\eta}}_T)}}{\chi^{3/2}}\Big]e^{-\chi^{1/2}\sqrt{f(\tilde{\boldsymbol{\eta}}_T)}} \tag{6.1.14}$$

Then, in the cylindrical coordinate system we write $\tilde{\boldsymbol{\eta}}_T = (\tilde{\eta}_T\cos\psi, \tilde{\eta}_T\sin\psi)$, and $\tilde{\boldsymbol{k}}_T = (\tilde{k}_T\cos\Psi, \tilde{k}_T\sin\Psi)$ where $\tilde{\eta}_T = |\tilde{\eta}_T|$, $\tilde{k}_T = |\tilde{k}_T|$. This means the dot product is $\tilde{\boldsymbol{k}}_{\boldsymbol{T}}\cdot\tilde{\boldsymbol{\eta}}_{\boldsymbol{T}} = \tilde{\eta}_T\tilde{k}_T\cos\theta$ where $\theta = \psi - \Psi$, and the integral becomes:

$$\frac{\Psi^*_{\nu j\mu l}(\boldsymbol{y};\tilde{\omega},\tilde{k}_1,\tilde{k}_T)}{A_0(\boldsymbol{y})R_{\nu j\mu l}(\boldsymbol{y},\boldsymbol{0},0)} = L_{\tilde{\omega}}\int_{\tilde{\eta}_T}\int_0^{2\pi} e^{i\tilde{\eta}_T\tilde{k}_T\cos\theta}F_a(\tilde{\eta}_T;\chi)\tilde{\eta}_T d\theta d\tilde{\eta}_T \tag{6.1.15}$$

where we assume F_a only depends on the magnitude of $\tilde{\eta}_T$. Then, since $2\pi J_0(\tilde{k}_T\tilde{\eta}_T) = \int_0^{2\pi} e^{i\tilde{\eta}_T\tilde{k}_T\cos\theta}d\theta$ this becomes:

$$\frac{\Psi^*_{\nu j\mu l}(\boldsymbol{y};\tilde{\omega},\tilde{k}_1,\tilde{k}_T)}{A_0(\boldsymbol{y})R_{\nu j\mu l}(\boldsymbol{y},\boldsymbol{0},0)} = L_{\tilde{\omega}}2\pi\int_{\tilde{\eta}_T} F_a(\tilde{\eta}_T;\chi)\tilde{\eta}_T J_0(\tilde{k}_T\tilde{\eta}_T)d\tilde{\eta}_T \tag{6.1.16}$$

which is simply the Hankel transform of F_a:

$$\frac{\Psi^*_{\nu j\mu l}(\boldsymbol{y};\tilde{\omega},\tilde{k}_1,\tilde{k}_T)}{A_0(\boldsymbol{y})R_{\nu j\mu l}(\boldsymbol{y},\boldsymbol{0},0)} = L_{\tilde{\omega}}2\pi\bar{H}(\chi) \tag{6.1.17}$$

The derivative of the Hankel transform with respect to omega can be found via the chain rule:

$$\frac{\partial\bar{H}}{\partial\tilde{\omega}} = \frac{\partial\bar{H}}{\partial\chi}\frac{\partial\chi}{\partial\tilde{\omega}} = \frac{\partial\bar{H}}{\partial\chi}\Big[\frac{\partial\chi}{\partial\tilde{\omega}}\frac{\partial\tilde{\omega}}{\partial\tilde{\omega}} + \frac{\partial\chi}{\partial\bar{k}_1}\frac{\partial\bar{k}_1}{\partial\tilde{\omega}}\Big] = \frac{\partial\bar{H}}{\partial\chi}\Big[2\tilde{\omega} - 2l_r\bar{k}_1\Big] \tag{6.1.18}$$

Therefore, the physical spectral tensor is analytically given by:

$$\boxed{\frac{\Psi^*_{\nu j\mu l}(\boldsymbol{y};\tilde{\omega},\tilde{k}_1,\tilde{k}_T)}{2\pi A_0(\boldsymbol{y})R_{\nu j\mu l}(\boldsymbol{y},\boldsymbol{0},0)} = (1-a_1)\bar{H}(\chi) - 2a_1\tilde{\omega}(\tilde{\omega} - \bar{k}_1 l_r)\bar{H}'(\chi)} \tag{6.1.19}$$

where,

$$\bar{H}(\chi) = \int_{\tilde{\eta}_T} F_a(\tilde{\eta}_T;\chi)\tilde{\eta}_T J_0(\tilde{k}_T\tilde{\eta}_T)d\tilde{\eta}_T \tag{6.1.20}$$

$$\bar{H}'(\chi) = \frac{\partial \bar{H}}{\partial \chi} = \int_{\tilde{\eta}_T} F'_a(\tilde{\eta}_T;\chi)\tilde{\eta}_T J_0(\tilde{k}_T\tilde{\eta}_T)d\tilde{\eta}_T \tag{6.1.21}$$

and

$$F_a(\tilde{\eta}_T;\chi) = \Big[\frac{1+\chi^{1/2}A}{\chi^{3/2}}\Big]e^{-\chi^{1/2}A} \tag{6.1.22}$$

$$F'_a(\tilde{\eta}_T;\chi) = \frac{\partial F_a}{\partial \chi} = \Big(-\frac{3}{2}\chi^{-5/2} - \frac{A}{\chi^2}\Big)e^{-\chi^{1/2}A} - \frac{A}{2}\Big(\frac{1}{\chi^2} + \frac{A}{\chi^{3/2}}\Big)e^{-\chi^{1/2}A} \tag{6.1.23}$$

where $A = \sqrt{f(\tilde{\eta}_T)}$

6.1.2 Acoustic Spectral Tensor

The acoustic spectral tensor which enters the acoustic spectrum formula is a linear combination of the physical spectral tensor found above. Using (6.0.2), assuming axisymmetry (i.e. $\Psi^*_{1133} = \Psi^*_{1122}, \Psi^*_{3311} = \Psi^*_{2211}, \Psi^*_{3333} = \Psi^*_{2222}$) and neglecting $\Psi^*_{2233}, \Psi^*_{3322}$, this gives:

$$\Phi^*_{1111} = (2-\gamma)\Psi^*_{1111} - \frac{\gamma-1}{2}(2\Psi^*_{1122} + 2\Psi^*_{2211}) + \frac{(\gamma-1)^2}{4}\Psi^*_{mmnn} \tag{6.1.24a}$$

$$\Phi^*_{2222} = (2-\gamma)\Psi^*_{2222} - \frac{\gamma-1}{2}(\Psi^*_{1122} + \Psi^*_{2211}) + \frac{(\gamma-1)^2}{4}\Psi^*_{mmnn} \tag{6.1.24b}$$

$$\Phi^*_{1212} = \Psi^*_{1212} \tag{6.1.24c}$$

$$\Phi^*_{1122} = (2-\gamma)\Psi^*_{1122} - \frac{\gamma-1}{2}(\Psi^*_{1111} + \Psi^*_{2222} + \Psi^*_{1122}) + \frac{(\gamma-1)^2}{4}\Psi^*_{mmnn} \tag{6.1.24d}$$

$$\Phi^*_{2211} = (2-\gamma)\Psi^*_{2211} - \frac{\gamma-1}{2}(\Psi^*_{1111} + \Psi^*_{2222} + \Psi^*_{2211}) + \frac{(\gamma-1)^2}{4}\Psi^*_{mmnn} \tag{6.1.24e}$$

$$\Phi^*_{4111} = \frac{(3-\gamma)}{2}\Psi^*_{4111} - \frac{\gamma-1}{2}(2\Psi^*_{4122}) \tag{6.1.24f}$$

$$\Phi^*_{4122} = \Psi^*_{4122} - \frac{\gamma-1}{2}(\Psi^*_{4111} + 2\Psi^*_{4122}) \tag{6.1.24g}$$

$$\Phi^*_{4221} = \Psi^*_{4221} \tag{6.1.24h}$$

$$\Phi^*_{4141} = \Psi^*_{4141} \tag{6.1.24i}$$

$$\Phi^*_{4242} = \Psi^*_{4242} \tag{6.1.24j}$$

where the invariant $\Psi^*_{mmnn} = \Psi^*_{1111} + 2(\Psi^*_{2222} + \Psi^*_{1122} + \Psi^*_{2211})$.

6.2 Analytical Spectral Tensor: Results

This section will analyse some of the results of the physical spectral tensor. It is well known (and was shown in Chapter 4) that the spectral tensor Φ^*_{1212} (which is equivalent to Ψ^*_{1212}) is responsible for the peak noise (i.e. at $\theta = 30$), so Figure 6.1 shows its contours for SP07 at different St for $\theta = 30, 90$. This shows that the spectral tensor is dominant downstream for very low Strouhal numbers, and at the nozzle exit on the shear layer for high St. For the peak frequencies it dominates close to the end of the potential core region (particularly at $\theta = 90$). Additionally the magnitude of the spectral tensor is maximum at low St and decays as frequency increases which is expected. Figure 6.2 similarly shows Φ^*_{1212} for the heated jet SP46 and we see similar trends. It is clear that heating the jet reduces the magnitude of the spectral tensor and re-positions the peak (still to the end of the potential core), this is in agreement with data from the literature (Fig.7 in [67]), although note this paper only looked at the peak St and $\theta = 30$, and focused on supersonic jets.

These trends for far field angle and Strouhal number are present for all spectral tensors ($\Psi^*_{\nu j \mu l}$), and also the $Ma = 0.5$ jets (SP03, SP42). Figure 6.3 compares all spectral tensors for SP07 at $St = 0.1, \theta = 30$. The spatial structure is very similar across most of the spectral tensors, with the only exception being R_{1122} which experiences a negative region downstream and outside the jet ($r > 1$). The other notable observation is the magnitude of the spectral tensors: Ψ^*_{1111} is largest as expected, however Ψ^*_{2211} and Ψ^*_{1122} also have large magnitudes in comparison to our observation from the correlation amplitudes in Chapter 5. This is likely due to the l_2 length scale which was optimised in Chapter 5 and found to be large in comparison to the other correlations. This optimised length scale is difficult to trust due to the oscillatory nature of the numerical data. Therefore, from this point on we use $l_2 = 0.04$ for all R_{1122}, R_{2211} correlations. Figure 6.4 shows Ψ^*_{1122} and Ψ^*_{2211} using this approximation for SP07. We also make this assumption for the coupling tensor Ψ^*_{4122} in the heated jets since it also experienced oscillations in the numerical data which led to a large l_2 being optimised.

Figures 6.5 and 6.6 show the momentum-flux, and coupling/enthalpy-flux spectral tensors respectively for SP46 at $St = 0.1, \theta = 30$. Note that the assumption $l_2 = 0.04$ is used for R_{1122}, R_{2211} and R_{4122}. These figures show that the enthalpy flux terms are the strongest in magnitude, which agrees with

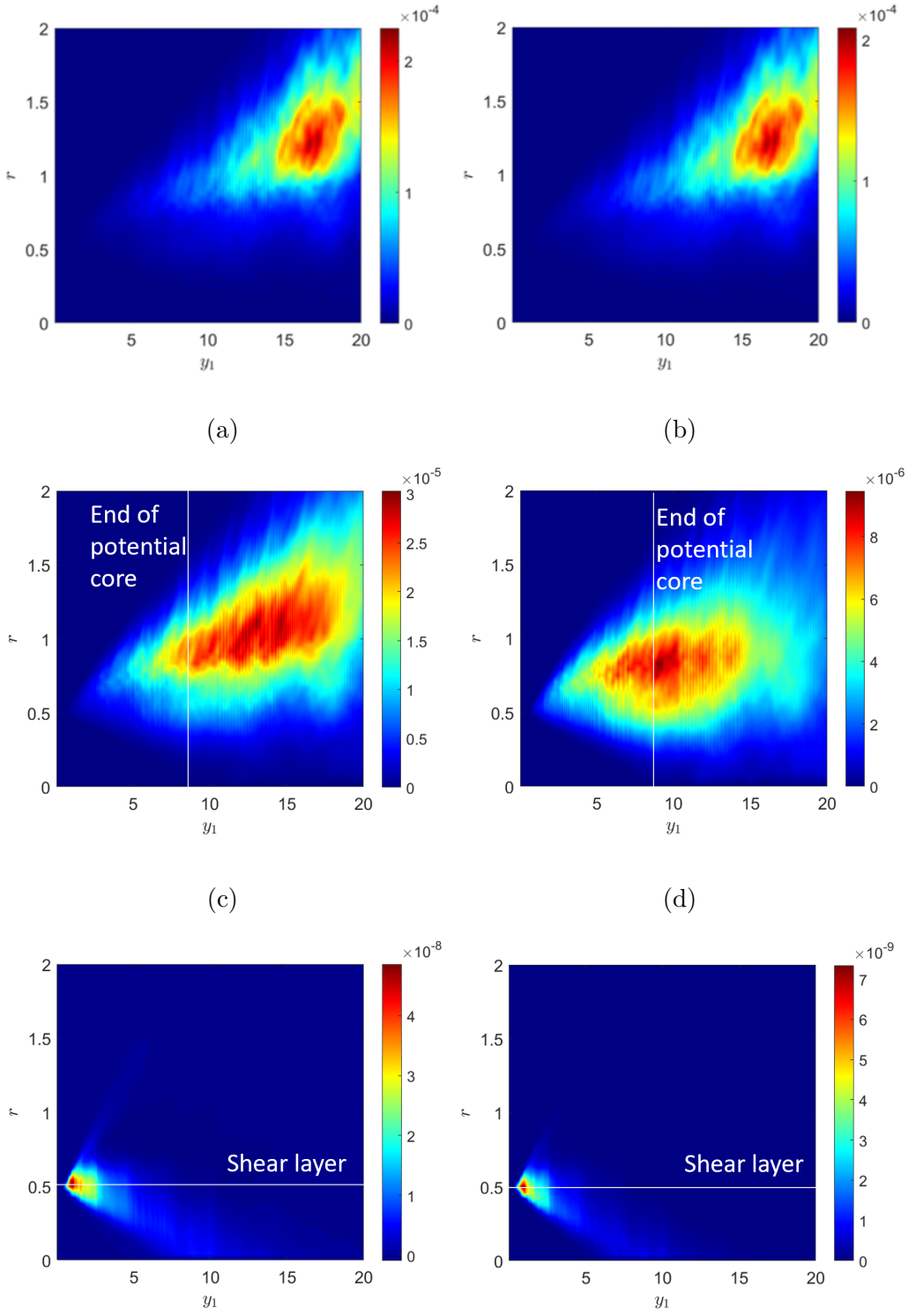

(a) (b) (c) (d) (e) (f)

Figure 6.1: SP07: contour plots of Φ^*_{1212} for (a) $St = 0.01, \theta = 30$ (b) $St = 0.01, \theta = 90$ (c) $St = 0.1, \theta = 30$ (d) $St = 0.1, \theta = 90$ (e) $St = 1.0, \theta = 30$ (f) $St = 1.0, \theta = 90$

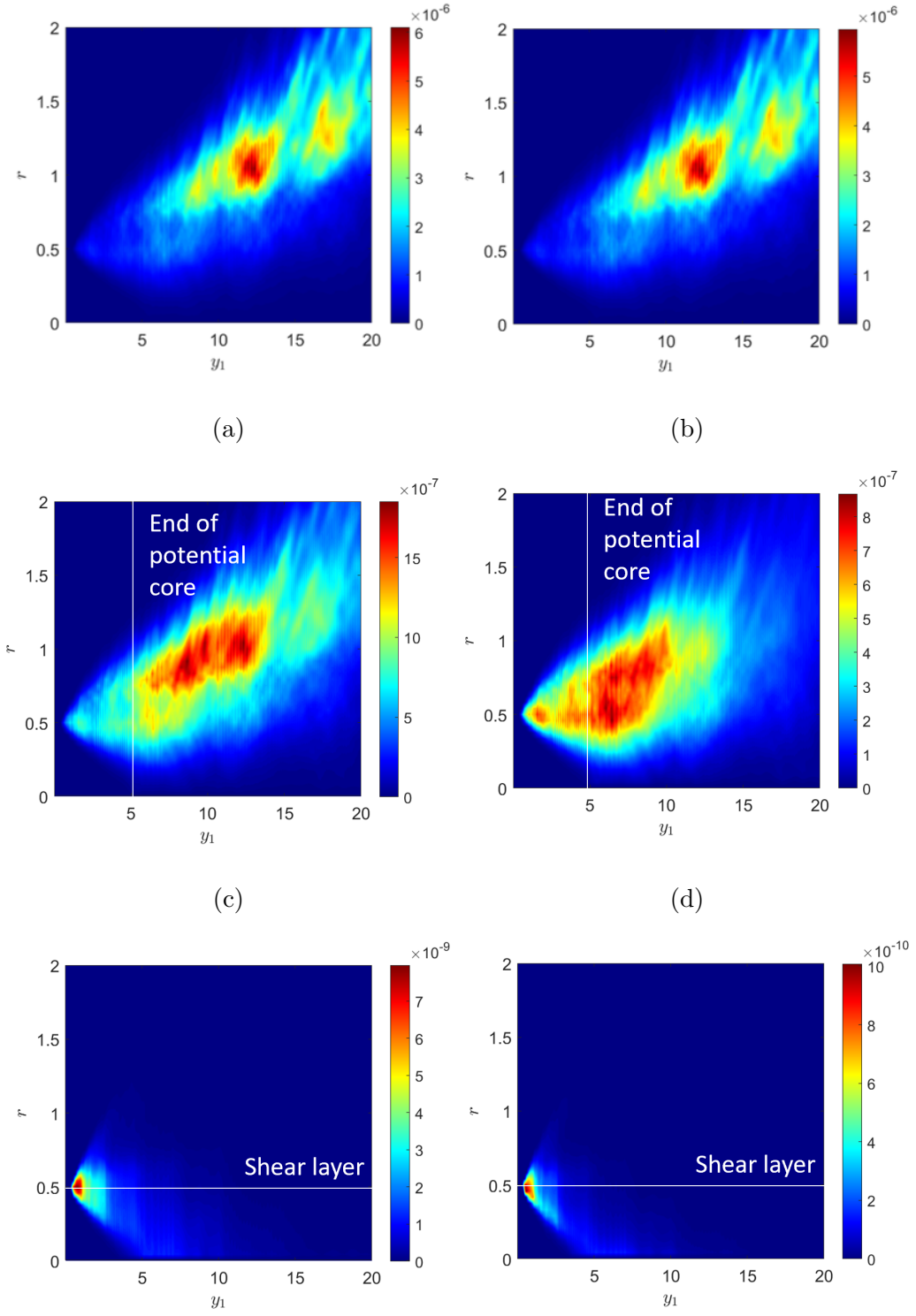

(a) (b)

(c) (d)

(e) (f)

Figure 6.2: SP46: contour plots of Φ^*_{1212} for (a) $St = 0.01, \theta = 30$ (b) $St = 0.01, \theta = 90$ (c) $St = 0.1, \theta = 30$ (d) $St = 0.1, \theta = 90$ (e) $St = 1.0, \theta = 30$ (f) $St = 1.0, \theta = 90$

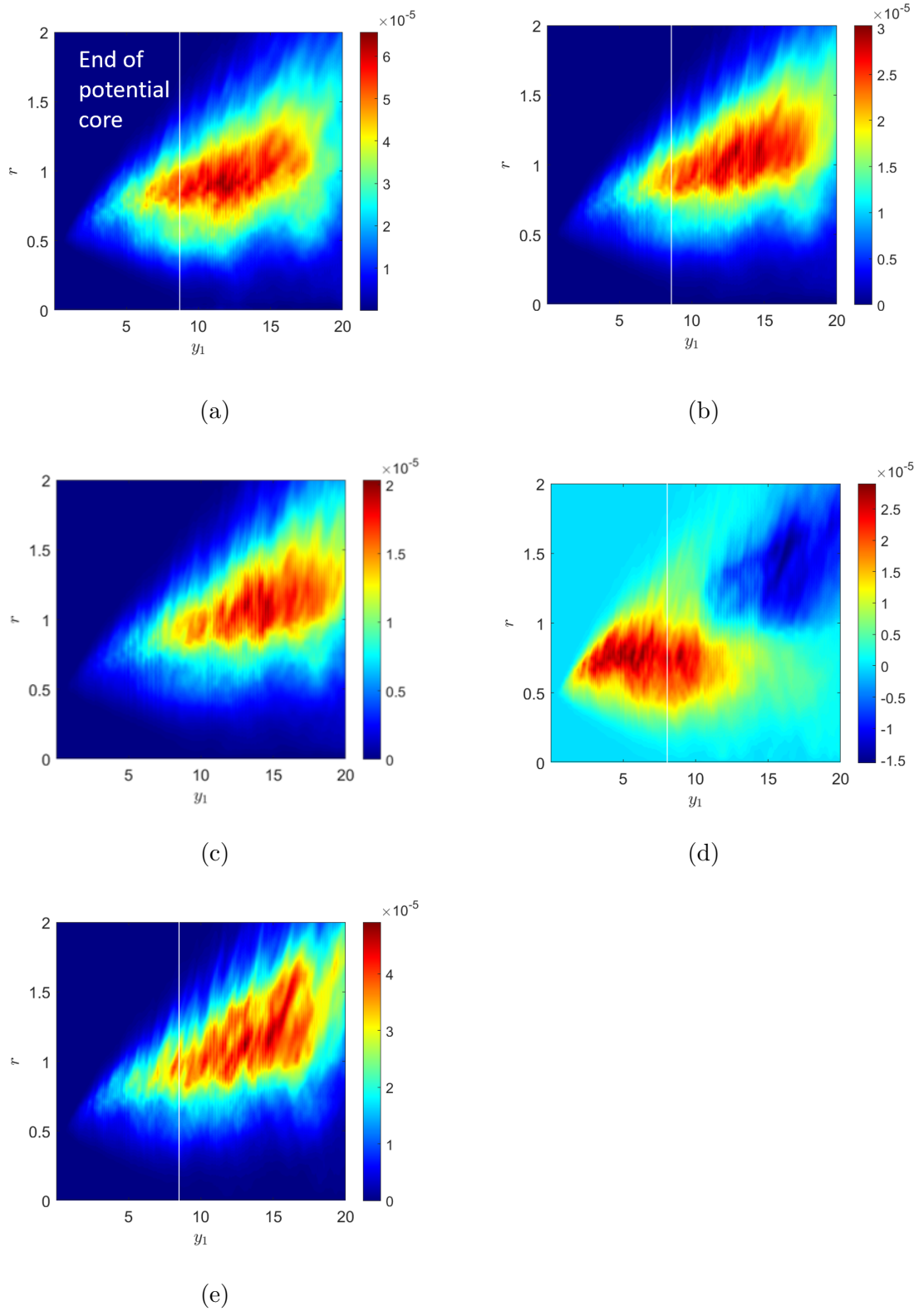

(a) (b)

(c) (d)

(e)

Figure 6.3: SP07: contour plots at $St = 0.1, \theta = 30$ for (a) Ψ^*_{1111} (b) Ψ^*_{1212} (c) Ψ^*_{2222} (d) Ψ^*_{1122} (e) Ψ^*_{2211}

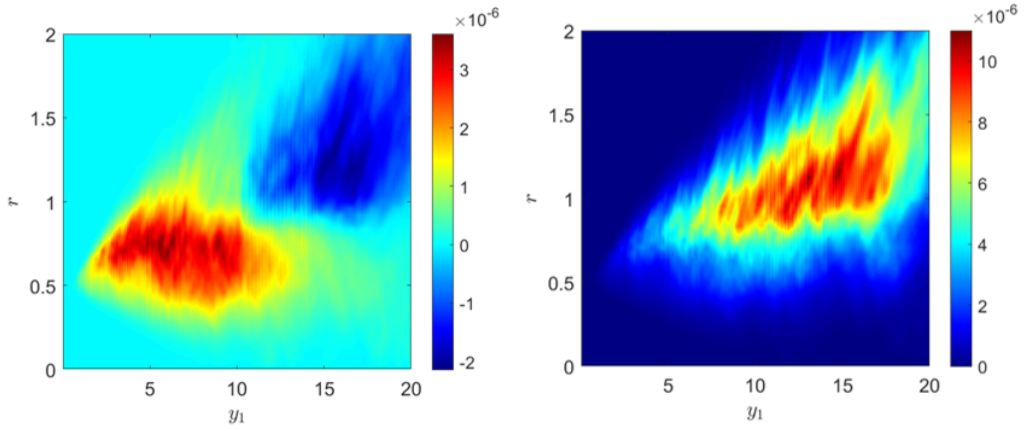

(a) (b)

Figure 6.4: SP07: contour plots at $St = 0.1, \theta = 30$ (assuming $l_2 = 0.04$) for (a) Ψ^*_{1122} (b) Ψ^*_{2211}

the initial assessment of the amplitudes of the correlations in Chapter 5. Similar figures for SP03 and SP42 can be found in Appendix. C.1.

6.2.1 Universality of $\Psi^*_{\nu j \mu l}$

To assess universality of the spectral tensor we look at $\Psi^*_{\nu j \mu l}/R_{ijkl}(\boldsymbol{y}, \boldsymbol{0}, 0)$ since the amplitudes of the correlation functions themselves depend on Ma and temperature ratio. Figure 6.7 compares the momentum-flux spectral tensors for the four jets and Figure 6.8 compares the coupling/enthalpy-flux tensors for the heated jets. Note that these figures are comparing the spectral tensors which were found using the individually optimised lengthscales.

Both figures interestingly show that the amplitude of the spectral tensors are greatly affected by jet and are therefore not universal, this difference must be due to the optimised lengthscales. This shows that the spectral tensor is very sensitive to the lengthscales chosen. However, we showed in Chapter 5 that universal lengthscales, such as those in Table 5.8, could be chosen to obtain a more general spectral tensor. These universal spectral tensors are shown in Figures 6.9, 6.10. Note that the small differences between jets in these figures is caused by $\tilde{k}_T$ which depends on the Mach number and temperature profile. However, if we use these universal spectral tensors we will potentially lose information from the turbulence as the amplitude difference between the individual spectral tensors

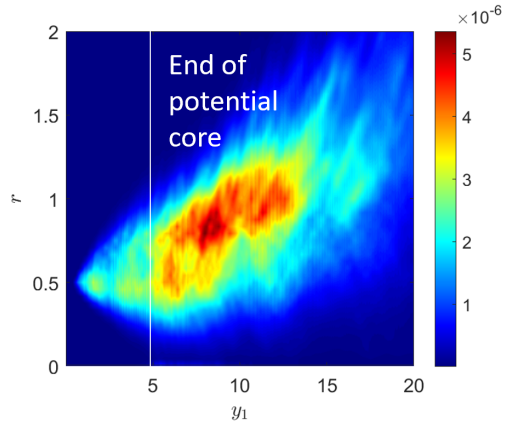

(a)

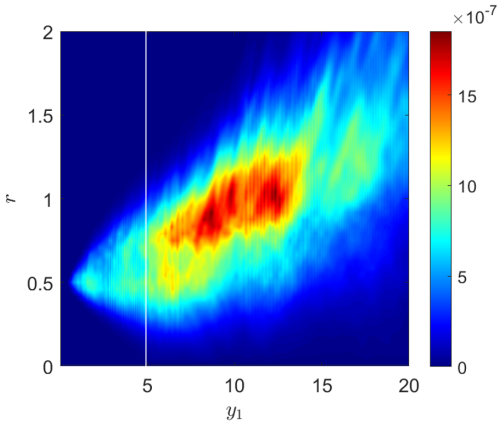

(b)

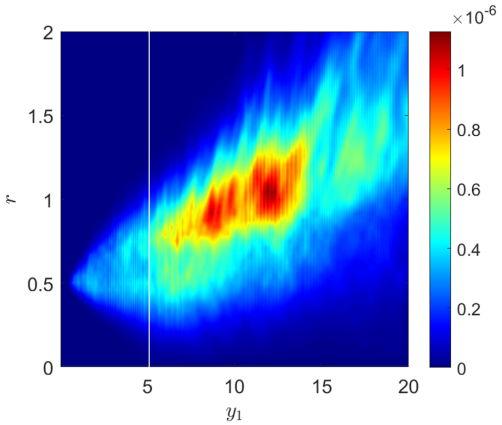

(c)

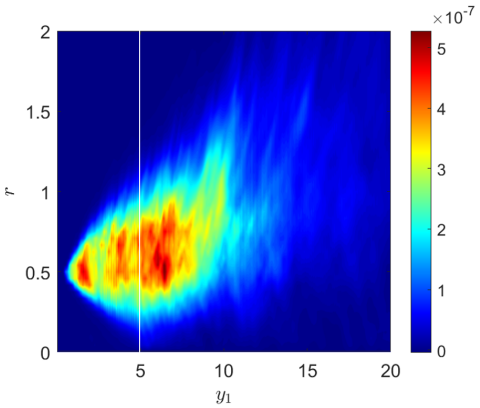

(d)

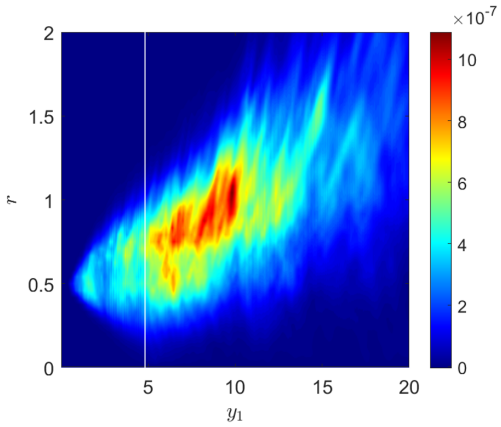

(e)

Figure 6.5: SP46: contour plots at $St = 0.1, \theta = 30$ for (a) Ψ^*_{1111} (b) Ψ^*_{1212} (c) Ψ^*_{2222} (d) Ψ^*_{1122} (e) Ψ^*_{2211}

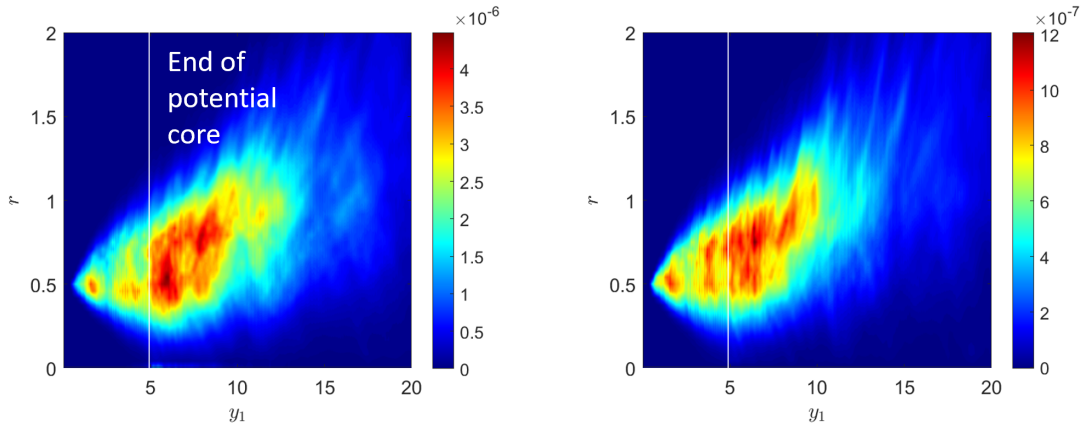

(a) (b)

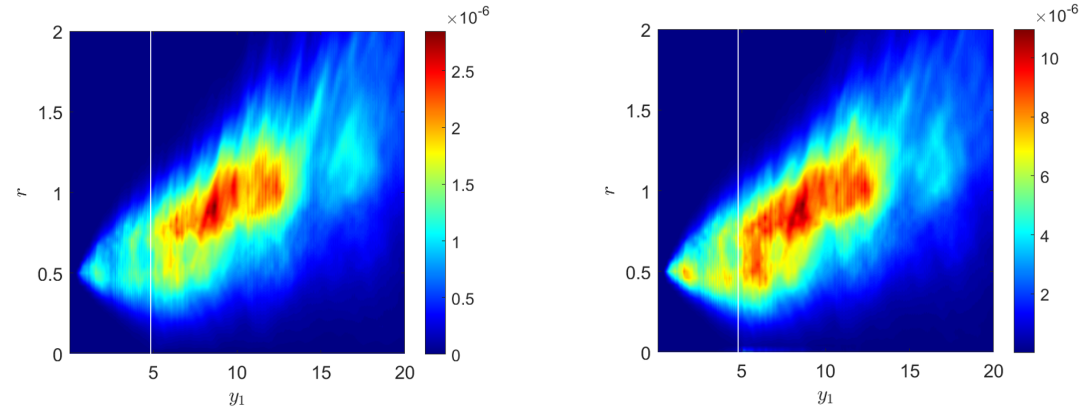

(c) (d)

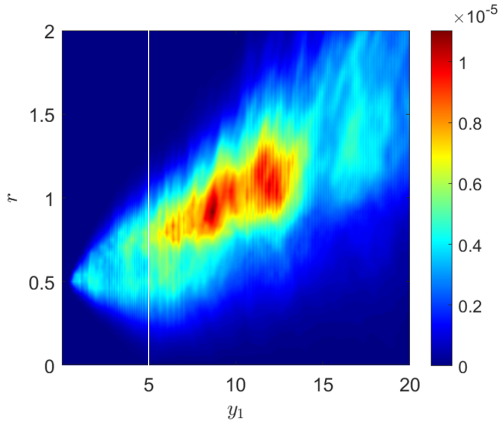

(e)

Figure 6.6: SP46: contour plots at $St = 0.1, \theta = 30$ for (a) Ψ^*_{4111} (b) Ψ^*_{4122} (c) Ψ^*_{4221} (d) Ψ^*_{4141} (e) Ψ^*_{4242}

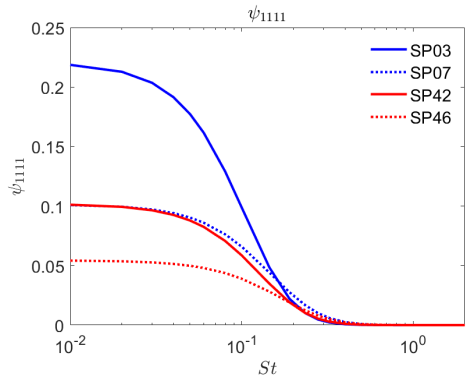

(a)

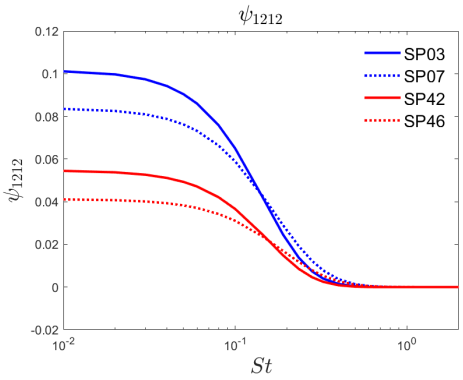

(b)

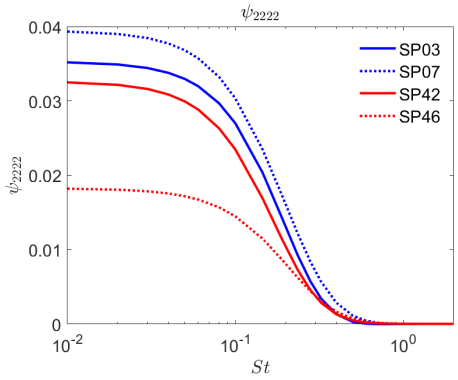

(c)

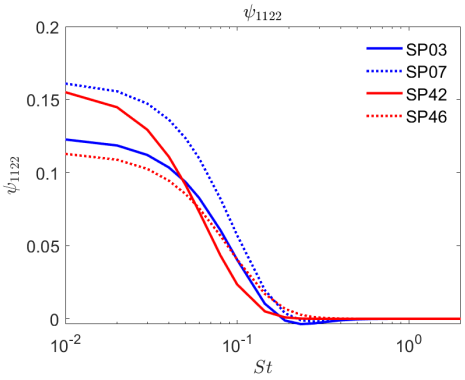

(d)

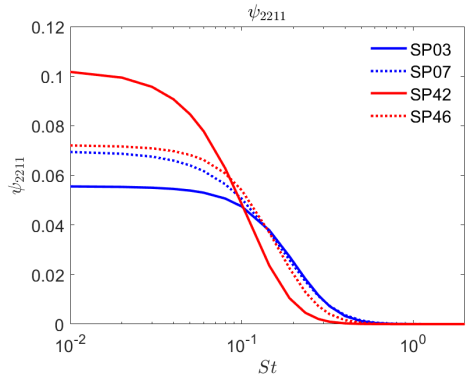

(e)

Figure 6.7: Compare $\Psi^*_{ijkl}/R_{ijkl}(\tau = 0)$ at the start of the potential core and on the shear layer for $\theta = 30$ for all four jets. (a) Ψ^*_{1111} (b) Ψ^*_{1212} (c) Ψ^*_{2222} (d) Ψ^*_{1122} (e) Ψ^*_{2211}

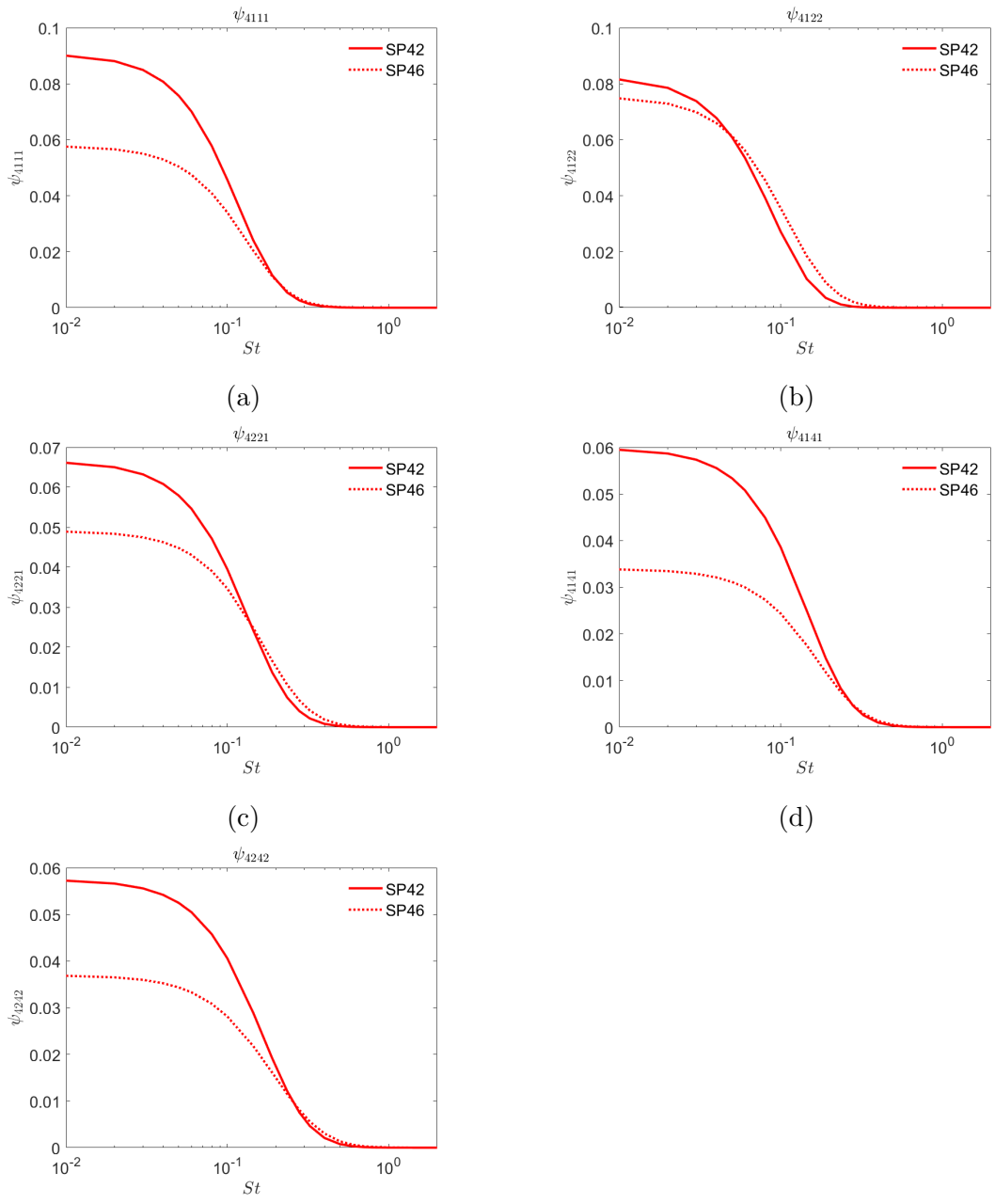

Figure 6.8: Compare $\Psi^*_{4j\mu l}/R_{4j\mu l}(\tau = 0)$ at the start of the potential core and on the shear layer for $\theta = 30$ for all four jets. (a) Ψ^*_{4111} (b) Ψ^*_{4122} (c) Ψ^*_{4221} (d) Ψ^*_{4141} (e) Ψ^*_{4242}

and the universal ones are quite large.

However, note that this universality is only applicable at the start of the potential core where the lengthscales were optimised. Since the length scales also depend on space through $L_T = k^{3/2}/\epsilon$, unless this L_T is also universal across jets, the spectral tensor will not be universal. Figure 6.11 compares Ψ^*_{ijkl} for the four jets at the end of the potential core using the universal lengthscales and shows that there are slight amplitude differences between the jets. In chapter 7 we will assess the impact of using universal length scales on the acoustic predictions.

6.2.2 Effect of Spatially Dependent Length Scales

So far in our analysis we have used spatially dependent length scales where we assume they vary spatially identically to how $L_T = k^{3/2}/\epsilon$ varies. This section assumes that the length scales are in fact constant, and are equal to those scales we optimised in Chapter 5.

Figure 6.12 shows Φ^*_{1212} for SP07 while using the constant lengthscales. Similar to Figure 6.1 it compares the spectral tensor at $\theta = 30, 90$ and $St = 0.01, 0.1, 1.0$. Notably, we see that the spatial structure of the contours remains constant, showing that the spatial variation of the spectral tensor with respect to angle and frequency is only dependent on the spatial variation of the lengthscales. When we approximate the lengthscales to be constant the peak turbulence is located on the shear layer close to the nozzle exit which is equivalent to the correlation function. Additionally the amplitude is smaller than that of Φ^*_{1212} when using spatially varying lengthscales.

Figure 6.13 compares Φ^*_{1212} using spatially varying lengthscales and using constant lengthscales for all four jets, at the end of the potential core on the shear layer at $\theta = 30$. This clearly shows the reduced magnitude when using constant lengthscales is present for all jets, particularly for the $Ma = 0.9$ cases. Figure 6.14 then compares this magnitude difference at the peak frequency $St = 0.2$ for $\Psi^*_{1111}, \Psi^*_{1212}$ and Ψ^*_{2222} for all four jets at $\theta = 30, 90$. This shows that at $\theta = 90$ the peak frequency is roughly captured by the constant lengthscales.

However, since the spatial variation of the spectral tensor is largely different for constant lengthscales, it is likely that once multiplied by the propagator and integrated the acoustic spectrum predictions will not be accurate, particularly the variation with frequency.

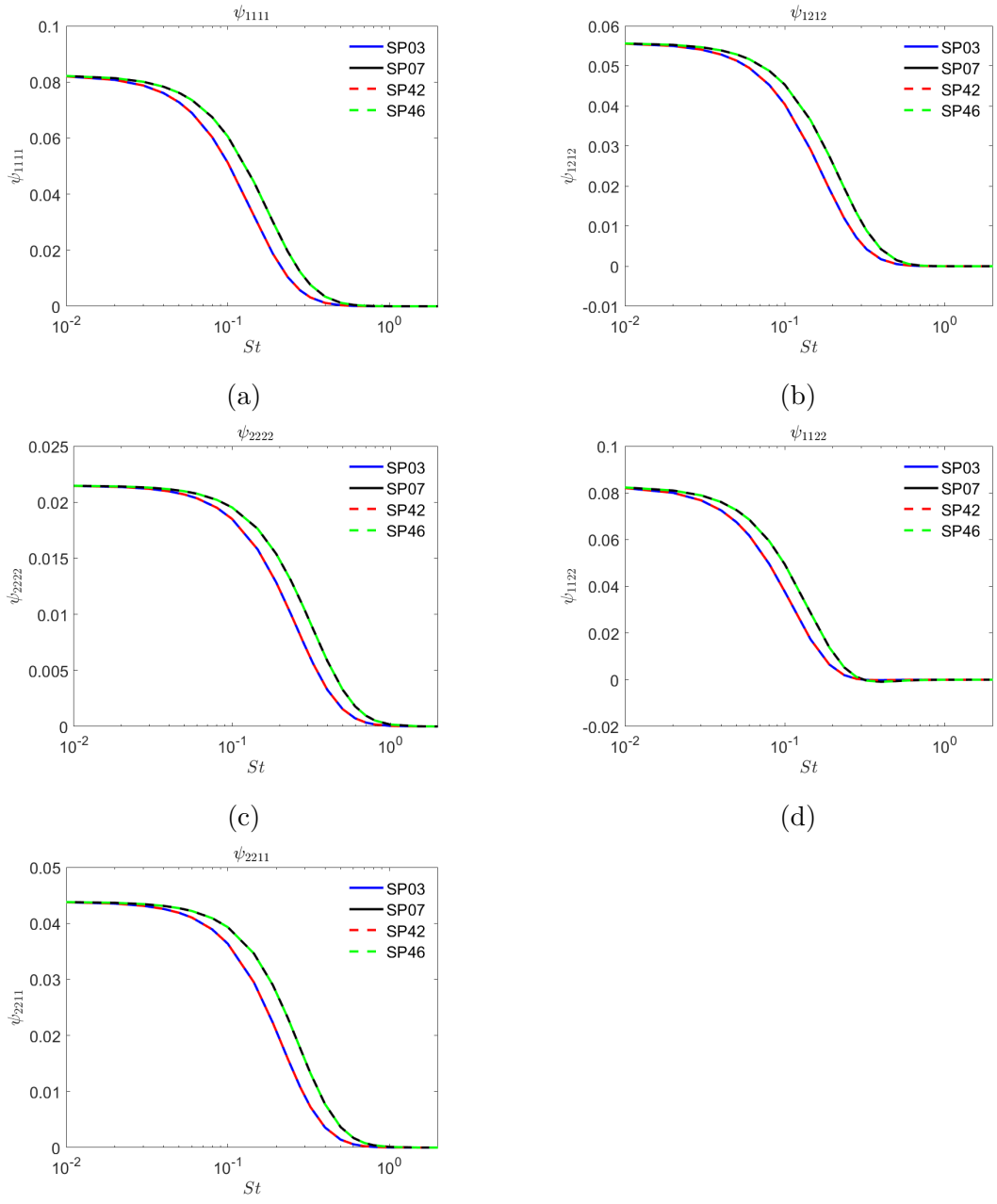

Figure 6.9: Compare $\Psi^*_{ijkl}/R_{ijkl}(\tau = 0)$ at the start of the potential core and on the shear layer for $\theta = 30$ for all four jets, assuming universal lengthscales. (a) Ψ^*_{1111} (b) Ψ^*_{1212} (c) Ψ^*_{2222} (d) Ψ^*_{1122} (e) Ψ^*_{2211}

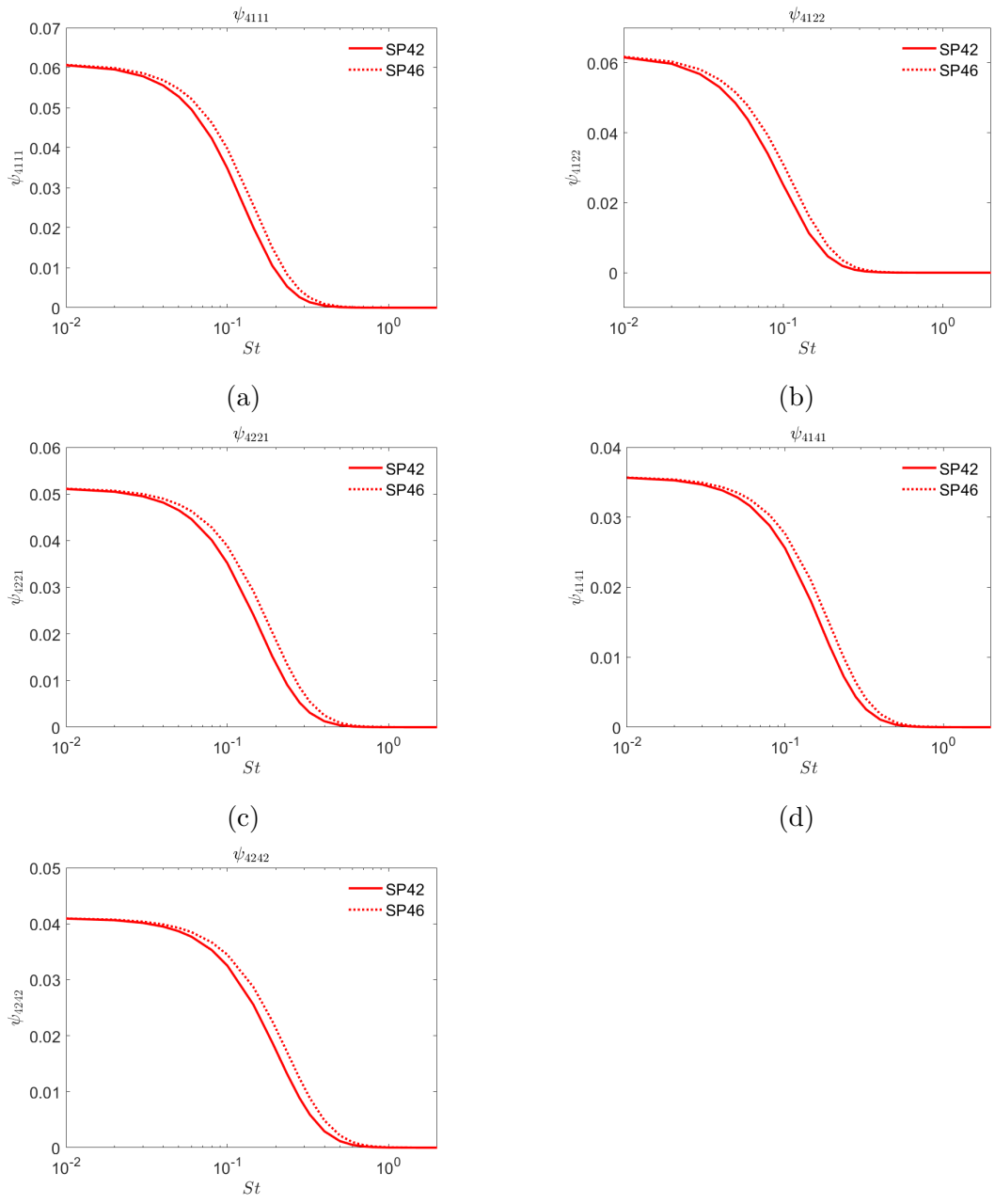

Figure 6.10: Compare $\Psi^*_{4j\mu l}/R_{4j\mu l}(\tau = 0)$ at the start of the potential core and on the shear layer for $\theta = 30$ for all four jets, assuming universal lengthscales. (a) Ψ^*_{4111} (b) Ψ^*_{4122} (c) Ψ^*_{4221} (d) Ψ^*_{4141} (e) Ψ^*_{4242}

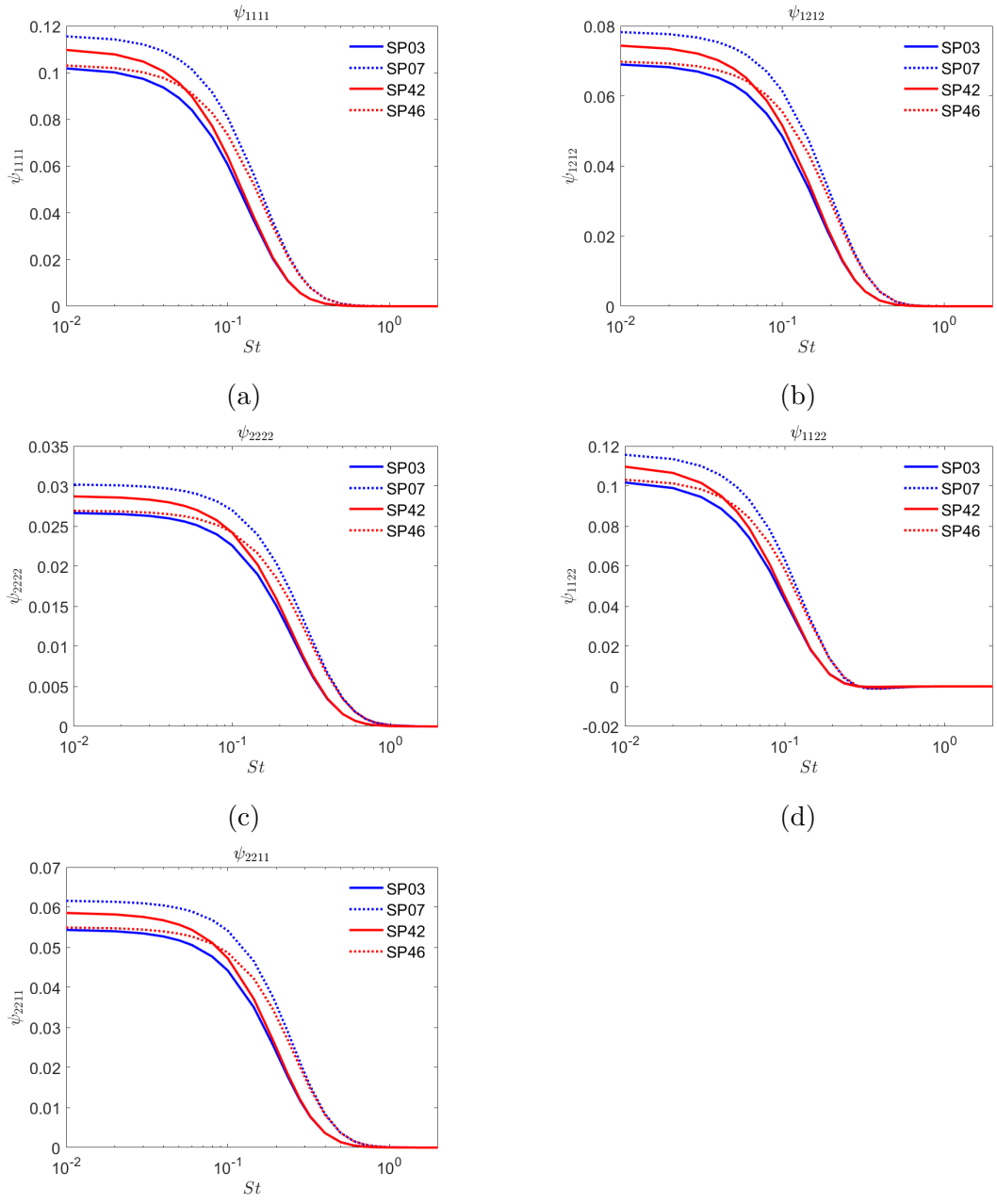

Figure 6.11: Compare $\Psi^*_{ijkl}/R_{ijkl}(\tau = 0)$ at the end of the potential core and on the shear layer for $\theta = 30$ for all four jets, assuming universal lengthscales. (a) Ψ^*_{1111} (b) Ψ^*_{1212} (c) Ψ^*_{2222} (d) Ψ^*_{1122} (e) Ψ^*_{2211}

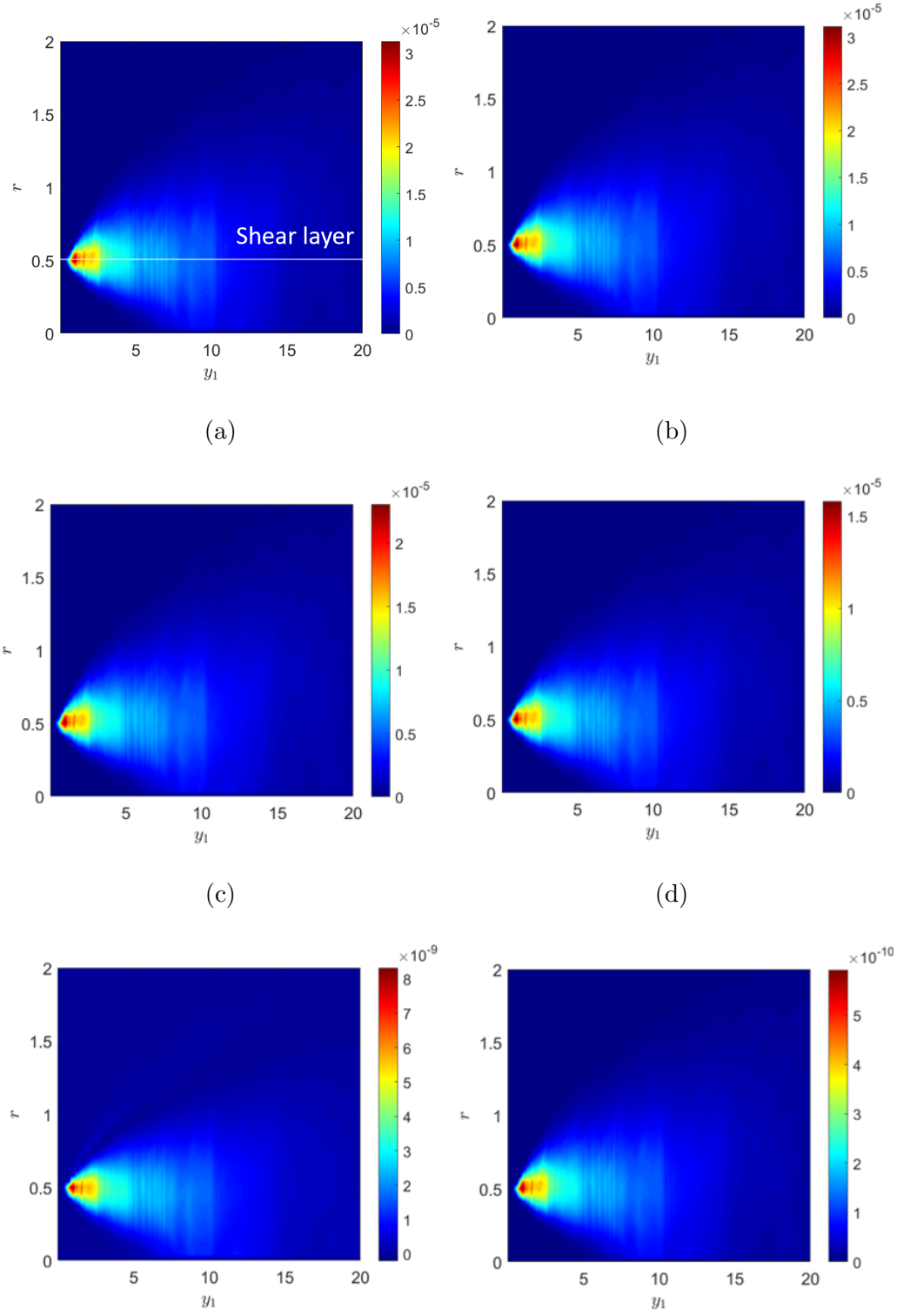

Figure 6.12: SP07: Φ^*_{1212} when approximating constant lengthscales for (a) $St = 0.01, \theta = 30$ (b) $St = 0.01, \theta = 90$ (c) $St = 0.1, \theta = 30$ (d) $St = 0.1, \theta = 90$ (e) $St = 1.0, \theta = 30$ (f) $St = 1.0, \theta = 90$

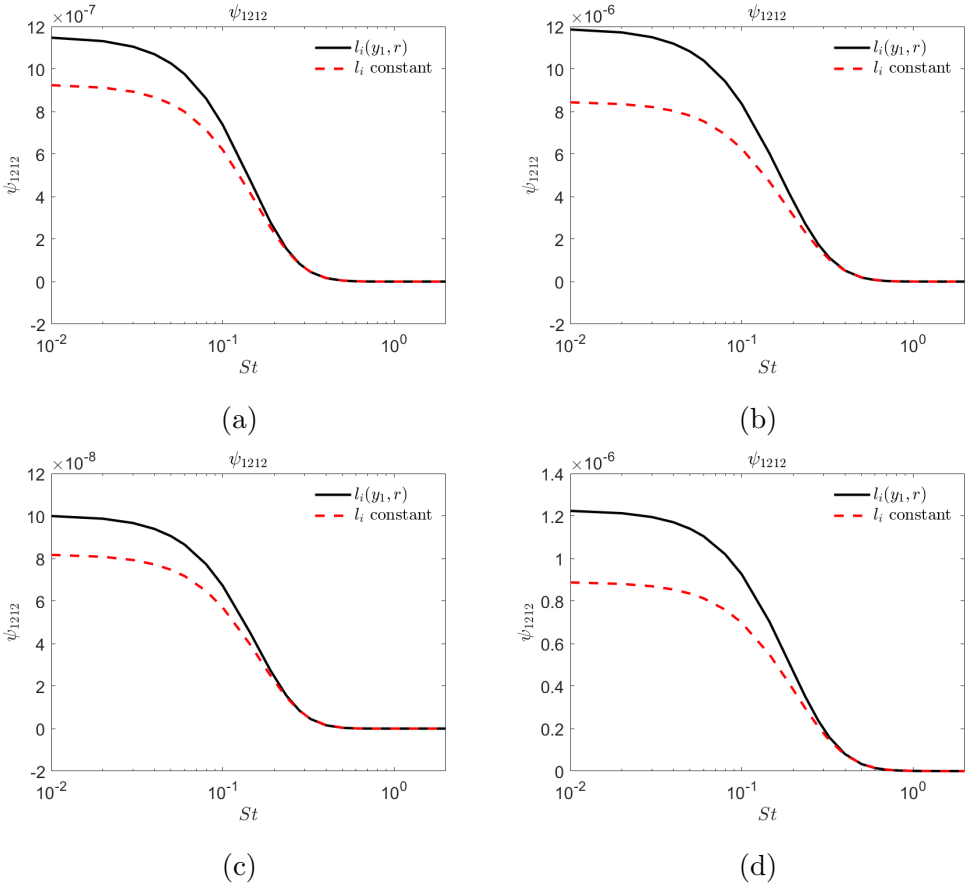

Figure 6.13: Effect of using spatially constant lengthscales on Φ^*_{1212} at the end of the potential core on the shear layer at $\theta = 30$ for (a) SP03 (b) SP07 (c) SP42 (d) SP46

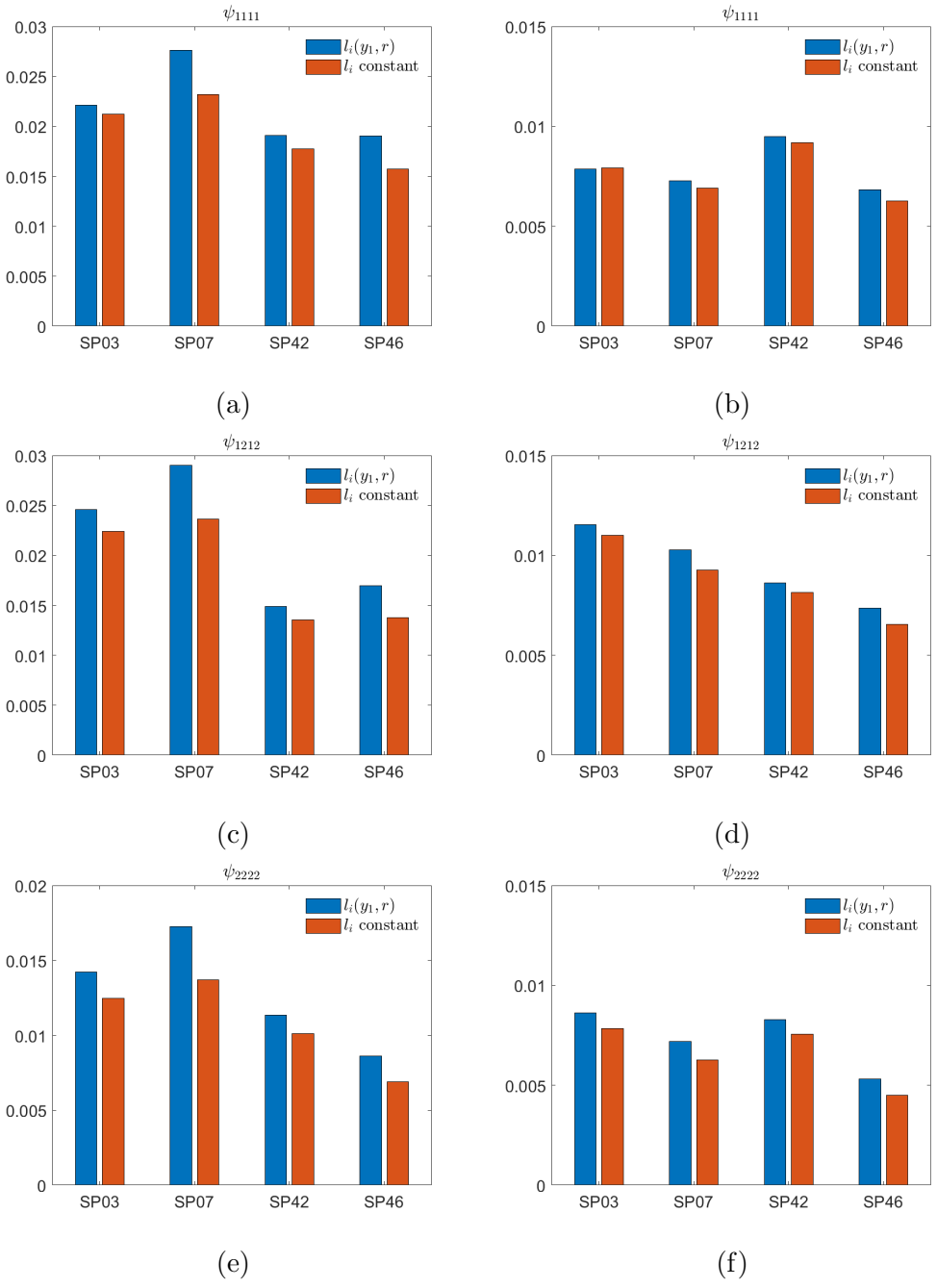

Figure 6.14: Effect of using spatially constant lengthscales on $\Psi^*_{ijkl}/R_{ijkl}(\tau = 0)$ for the peak frequency $St = 0.2$ at the end of the potential core on the shear layer for (a,c,e) $\theta = 30$ and (b,d,f) $\theta = 90$

6.2.3 Effect of Approximations

There are several approximations that we can use to simplify the analytical spectral tensor further. In this section we look at three approximations:

1. Set $a_1 = 0$
2. Set $a_1 = 0, \tilde{k}_T = 0$
3. Set $\tilde{k}_T = 0, \bar{H}'(\chi) = 0$ (Approx)

Figures 6.15 and 6.16 compare these approximations with the full analytical formulation at the end of the potential core on the shear layer at $\theta = 30$ for the isothermal jets and heated jets respectively. From this figure we see that Ψ^*_{1111} is well represented by all approximations, which is intuitive since the optimised a_1 for this tensor was already very small, therefore these approximations mostly check the effect of $\tilde{k}_T$. Therefore we can conclude that $\tilde{k}_T$ can be taken to be zero which agrees with the findings of Afsar et al [67].

From the other tensors we see that only the third approximation is close to the full analytical form at most St. Figure 6.17 then compares this approximation at $St = 0.2$ for angles $\theta = (30, 90)$. This figure better shows the difference in amplitude at this frequency, and shows that for Ψ^*_{1111} it is a very close approximation for all jets, however the other tensors do show a greater difference. However, it is unlikely that this difference will have a large effect on the acoustic predictions and this will be assessed in Chapter 7.

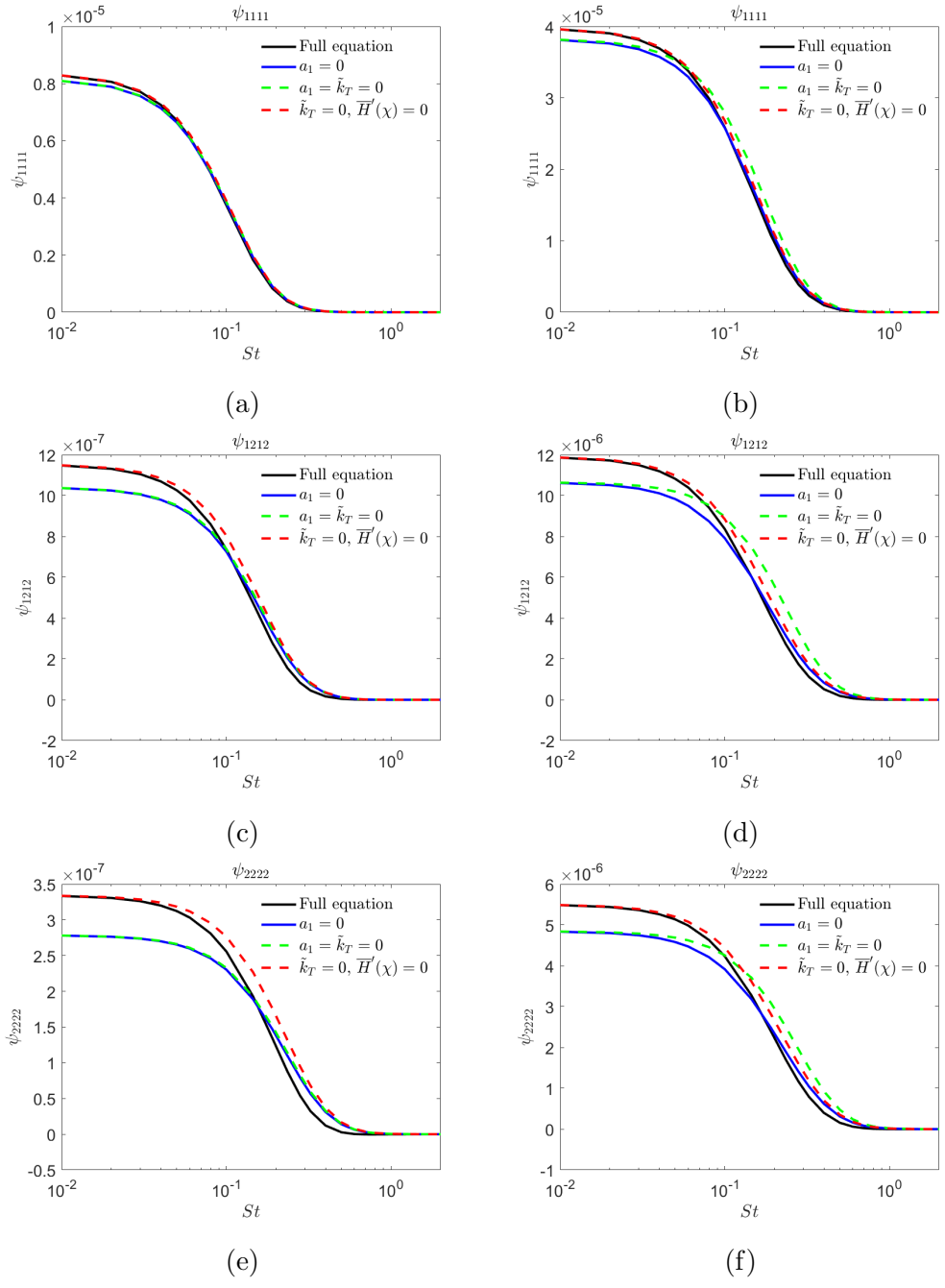

Figure 6.15: Impact of approximations on the analytical spectral tensor at the end of the potential core on the shear layer for (a,c,e) SP03, (b,d,f) SP07

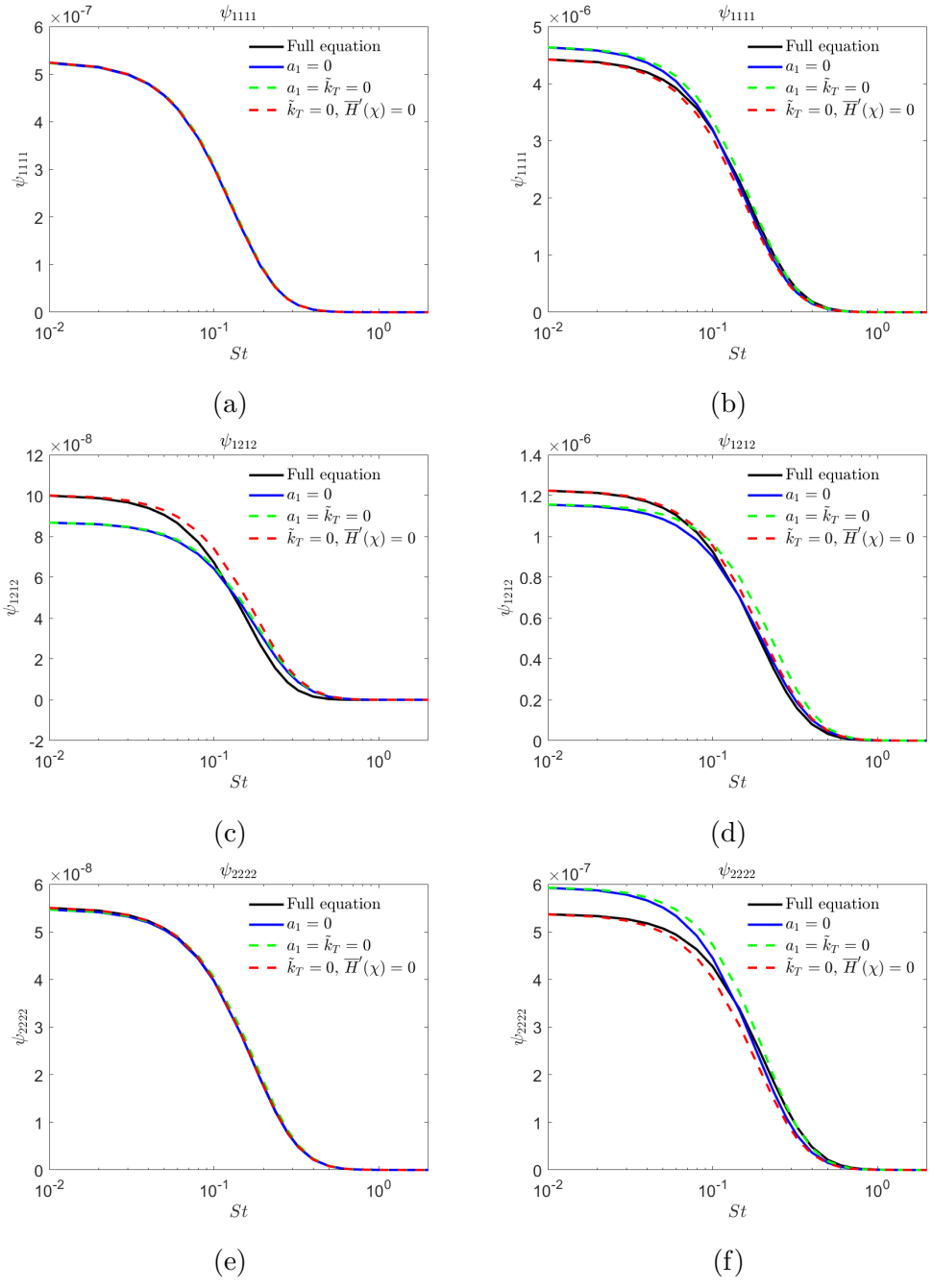

Figure 6.16: Impact of approximations on the analytical spectral tensor at the end of the potential core on the shear layer for (a,c,e) SP42, (b,d,f) SP46

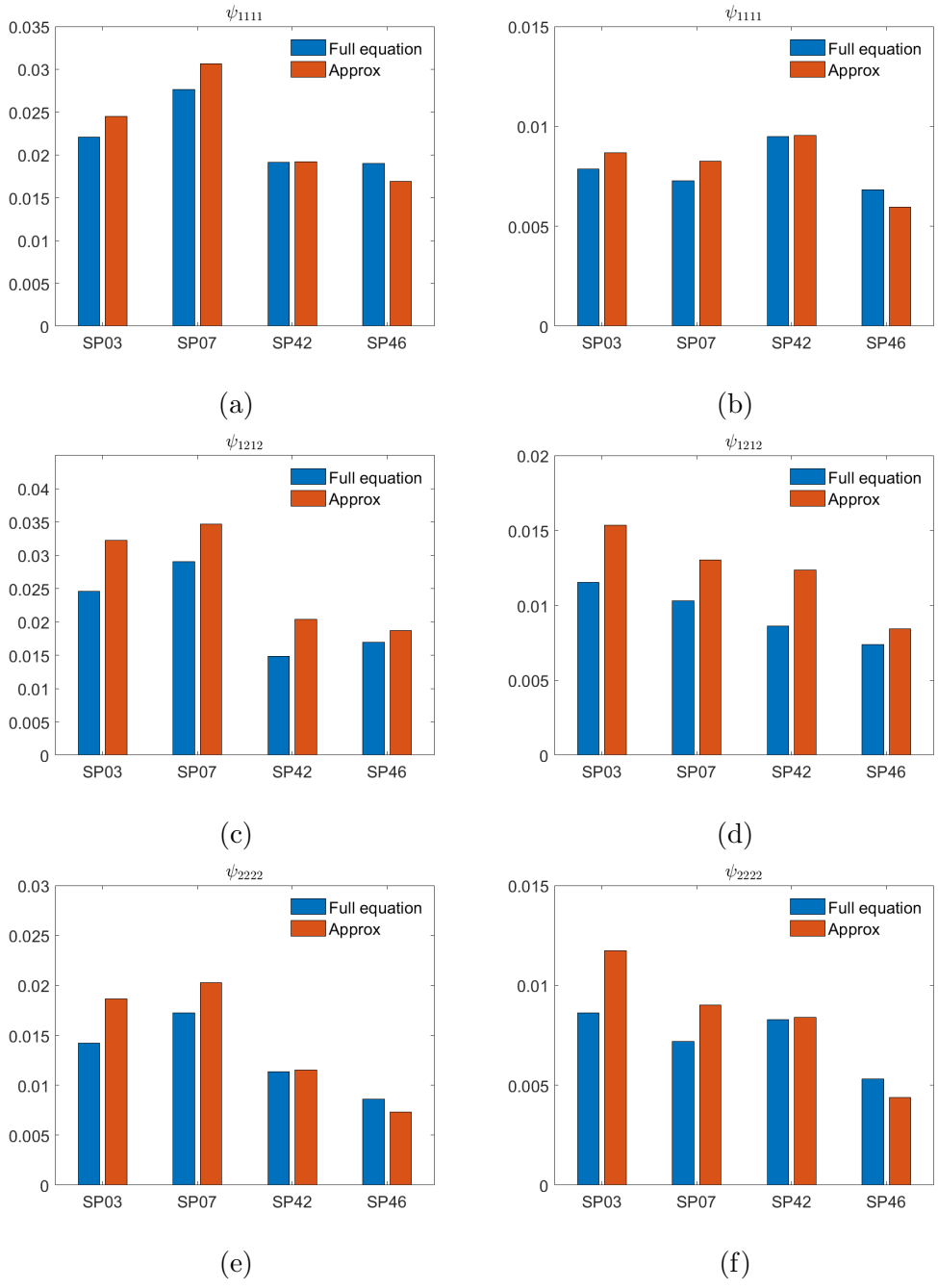

Figure 6.17: Effect of using Approx ($\tilde{k}_T = 0, \bar{H}' = 0$) on $\Psi^*_{ijkl}/R_{ijkl}(\tau = 0)$ for the peak frequency $St = 0.2$ at the end of the potential core on the shear layer for (a,c,e) $\theta = 30$ and (b,d,f) $\theta = 90$

6.3 Numerical Spectral Tensor

So far we have only considered the analytical reconstruction of the spectral tensor which is informed by LES. This section will aim to validate the analytical model by comparing each stage of the calculation against the equivalent numerical Fourier transforms. Only one location is chosen to carry out this check due to time constraints and spatial resolution in $\boldsymbol{\eta}$ at locations outside the shear layer of the jet. Therefore we look at the start of the potential core where the length scales were optimised, this should be the location that has the best fit against the numerical data.

Since the analytical calculation changed variables to $\tilde{\xi} = (\tilde{\eta}_1 l_1/l_0 - \tilde{\tau})$ in (6.1.10) to enable the use of an analytical solution to the Fourier transforms, we can only compare the 2D Fourier transform of $(\tilde{\eta}_1, \tilde{\tau})$ with the numerical calculation and not the individual ones. This comparison is shown in Figure 6.18 for SP07, this shows that the analytical reconstruction gives a reasonable approximation to the direct numerical Fourier transform. An exact replication is not expected since clearly the model will not represent the numerical data exactly for all η_1, τ.

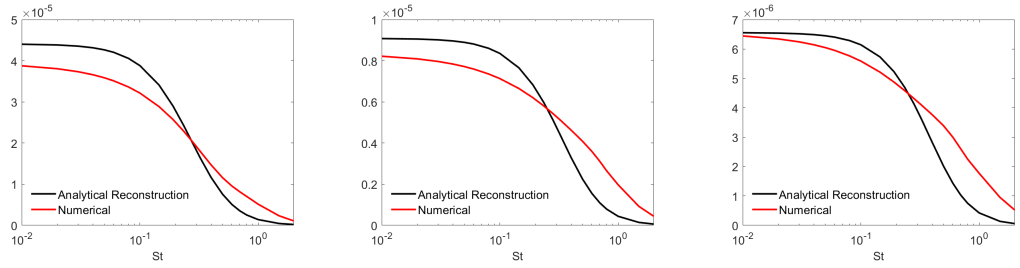

(a) (b) (c)

Figure 6.18: SP07: Comparison of the 2D $(\tilde{\eta}_1, \tilde{\tau})$ Fourier transform of the analytical reconstruction with the Numerical Fourier transform on the shear layer at the start of the potential core for (a) R_{1111} (b) R_{1212} (c) R_{2222}

Similarly, Figure 6.19 compares the full 3D Fourier transform of the analytical reconstruction and the numerical data. Evidently, the η_2 Fourier transform is not as well represented by the analytical reconstruction. This is due to the numerical data going to zero at $\eta_2 = 0.3$, whereas the analytical model takes longer. Figure 6.20 compares the Fourier transforms when the analytical function is set to zero for $\eta_2 > 0.3$, and we see much better agreement. It should be noted

however, that at different locations in the jet, the turbulence does not decay at $\eta_2 = 0.3$, therefore to allow this structure to be captured we choose to retain the analytical η_2 model.

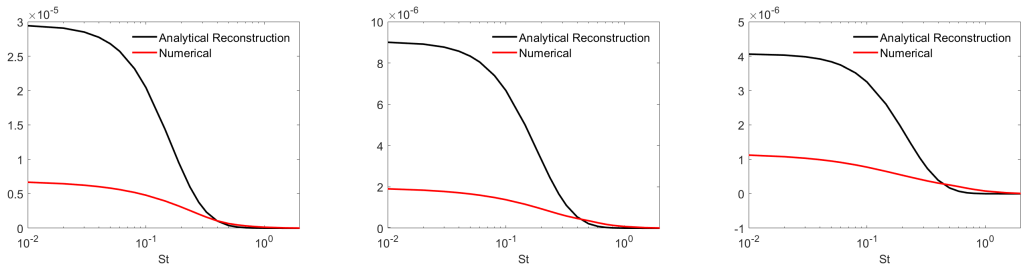

(a) (b) (c)

Figure 6.19: SP07: Comparison of the 3D $(\tilde{\eta}_1, \tilde{\eta}_T, \tilde{\tau})$ Fourier transform of the analytical reconstruction with the Numerical Fourier transform on the shear layer at the start of the potential core for (a) R_{1111} (b) R_{1212} (c) R_{2222}

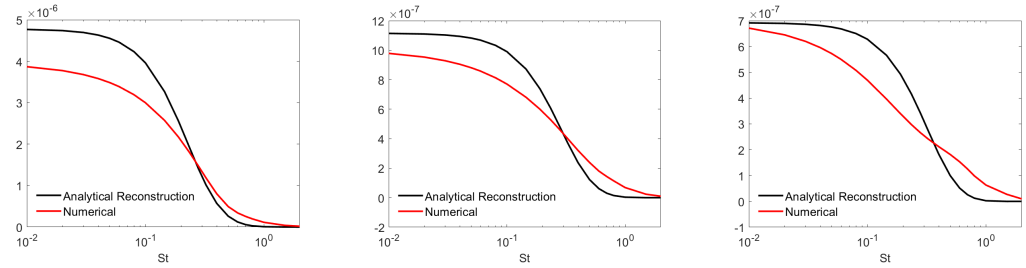

(a) (b) (c)

Figure 6.20: SP07: Comparison of the 3D $(\tilde{\eta}_1, \tilde{\eta}_2, \tilde{\tau})$ Fourier transform of the analytical reconstruction with the Numerical Fourier transform on the shear layer at the start of the potential core for (a) R_{1111} (b) R_{1212} (c) R_{2222} while setting $R_{ijkl}(\eta_2 > 0.3) = 0$

6.4 Summary

In this chapter we have analysed the spectral tensor, the effect of spatially dependent length scales and the effect of several approximations for the analytical calculation. At present, it is difficult to fully understand what impact these differences will have in the acoustic spectrum, since we still have to multiply

by the propagator and integrate over space. This will be analysed in the next chapter.

Figure 6.21 summarises the process so far and shows that we now have everything required to calculate the acoustic spectrum.

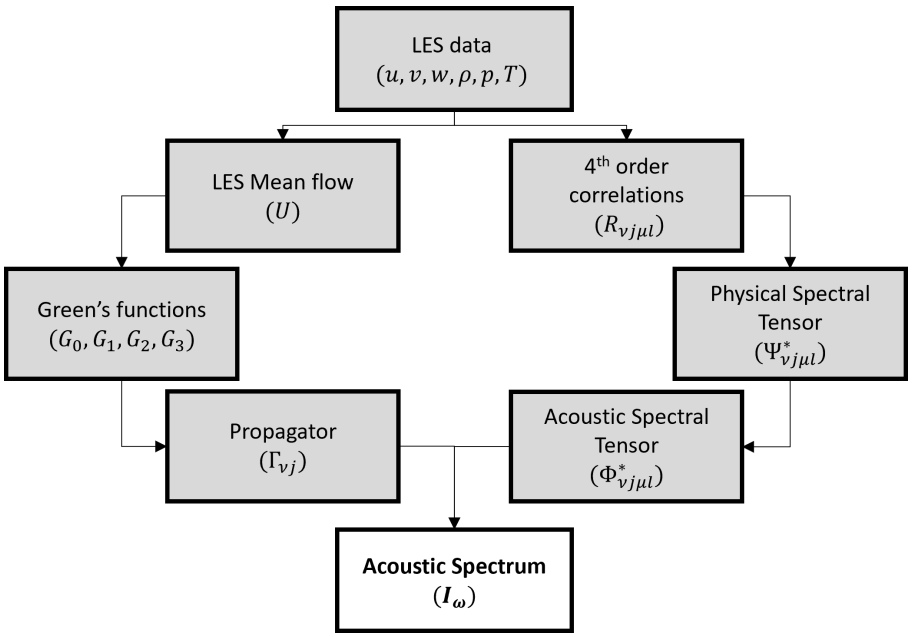

Figure 6.21: Chapter 6: Summary of process so far

Chapter 7

Jet Noise: Acoustic Predictions

In the previous chapters we have obtained the propagator components and the analytical reconstruction of the spectral tensor using an analytical function informed by the LES data. This chapter calculates the acoustic predictions for each jet and analyses the effect of certain correlation functions, and the amplification of terms in the acoustic predictions. We will also assess the performance of universal lengthscales across Mach number and temperature ratio. To my knowledge, this the the first time this type of analysis has been done.

Recall that in Chapter 4 we showed that the acoustic spectrum $I(\boldsymbol{x};\omega)$ could be written as the integral over space of the summation of the momentum-flux, enthalpy-flux and coupling terms:

$$I(\boldsymbol{x};\omega) = (2\pi)^2 \int_{V_\infty} \Big[I^{[1]}(\boldsymbol{x},\boldsymbol{y};\omega) + I^{[2]}(\boldsymbol{x},\boldsymbol{y};\omega) + I^{[3]}(\boldsymbol{x},\boldsymbol{y};\omega) \Big] d\boldsymbol{y} \qquad (7.0.1)$$

In cylindrical coordinates for an axisymmetric jet, this becomes

$$I(\boldsymbol{x};\omega) = (2\pi)^3 \int_{y_1} \int_r \Big[I^{[1]}(\boldsymbol{x},\boldsymbol{y};\omega) + I^{[2]}(\boldsymbol{x},\boldsymbol{y};\omega) + I^{[3]}(\boldsymbol{x},\boldsymbol{y};\omega) \Big] r dr dy_1 \quad (7.0.2)$$

7.1 Comparison against Ffowcs Williams-Hawking (FFWH) Calculation

FFWH predictions were carried out for the $Ma = 0.9$ jets and are compared with experimental data and our acoustic predictions using the acoustic analogy formulations in Figures 7.1, 7.2.

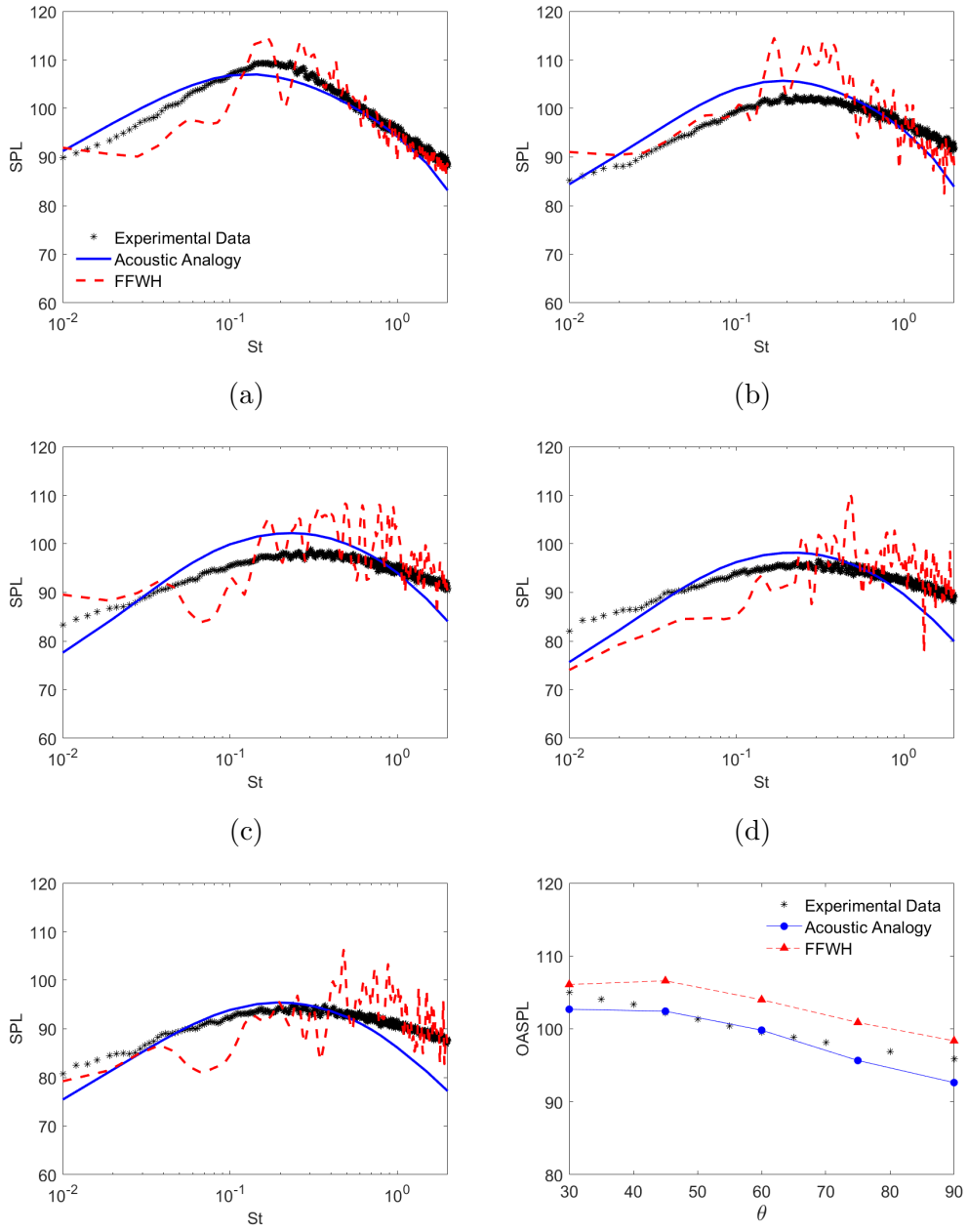

Figure 7.1: SP07: Compare SPL acoustic predictions using FFWH against the acoustic analogy for (a) $\theta = 30$ (b) $\theta = 45$ (c) $\theta = 60$ (d) $\theta = 75$ (e) $\theta = 90$ and then (f) OASPL

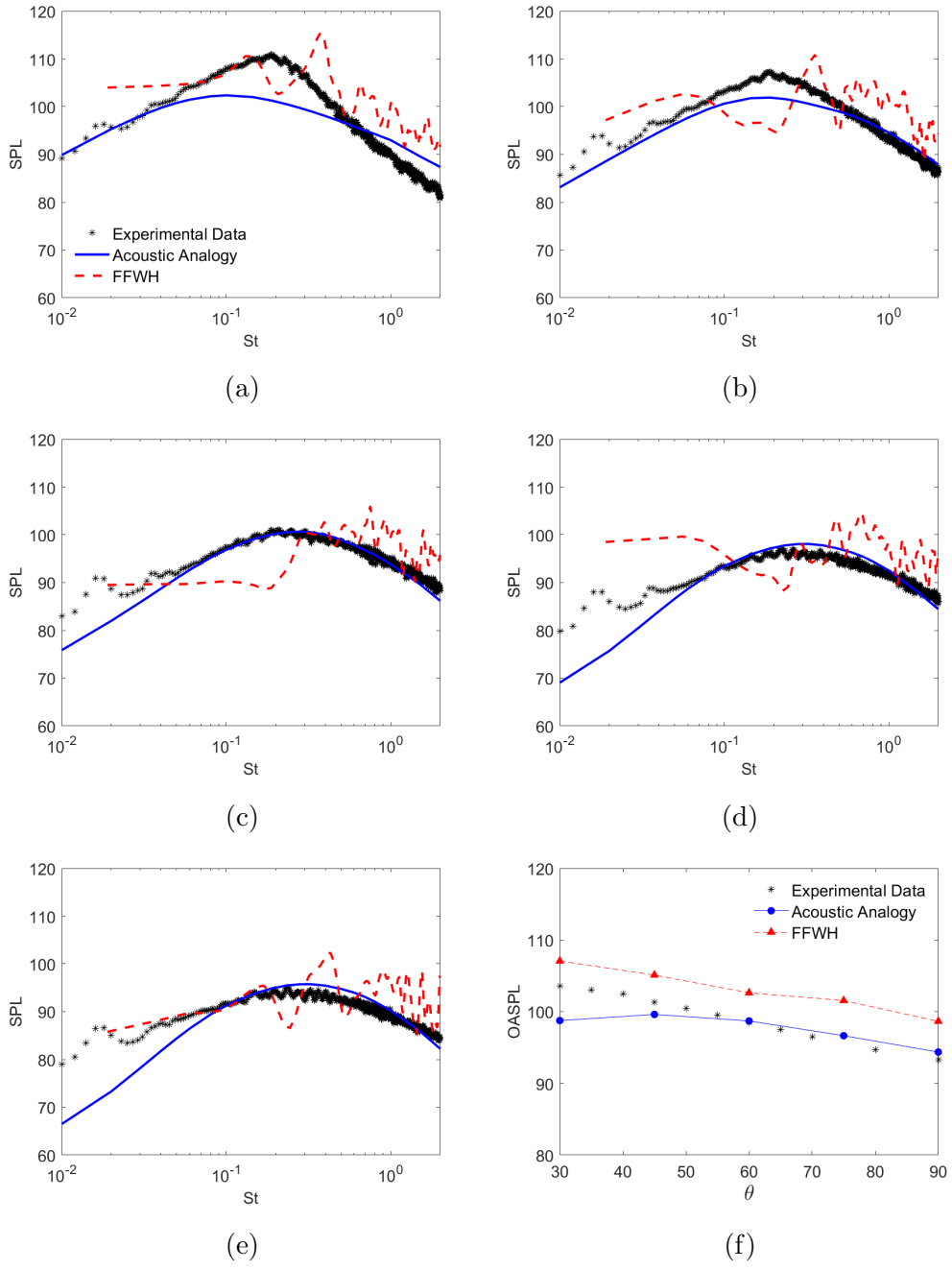

Figure 7.2: SP46: Compare SPL acoustic predictions using FFWH against the acoustic analogy for (a) $\theta = 30$ (b) $\theta = 45$ (c) $\theta = 60$ (d) $\theta = 75$ (e) $\theta = 90$ and then (f) OASPL

From these figures we see that the FFWH calculations are quite oscillatory in comparison to other FFWH results in the literature [13], especially in the high frequencies. The FFWH calculation is sensitive to the length of time it is run for, this might explain the oscillations which are present. To combat this we also calculate the OASPL which integrates over frequency and we find for both jets that the OASPL is over-predicted using this method. The acoustic analogy overall gives better predictions however do tend to under-predict the spectrum at high frequencies for the cold jet, and under-predict the low frequencies for the heated jet. The peak frequency is captured well for both jets (note that the under-prediction in $\theta = 30$ for SP46 is expected due to parallel flow assumptions), and the OASPL is also predicted well.

7.2 Effect of Approximations

7.2.1 Approximating the Acoustic Spectral Tensor

Recall that the acoustic spectral tensor Φ^*_{ijkl} was calculated from a linear combination of the physical spectral tensor Ψ^*_{ijkl}, which was shown in section 6.1.2. Therefore, one simplification of the spectral tensor would be to neglect the invariant terms Ψ^*_{mmnn}. Another simplification would be to assume $\Psi^*_{1122} = \Psi^*_{2211}$ since it would reduce the number of correlations required.

Figures 7.3-7.6 compare these approximations for SP07, SP03, SP46, and SP42 respectively. They show that the approximation of $\Psi^*_{1122} = \Psi^*_{2211}$ makes no noticeable change in the acoustic predictions for all jets. Additionally, neglecting the invariant also does not have a great impact for most jets, only affecting the low frequencies very slightly. For SP03 however, neglecting the invariant leads to large differences in the low frequencies for large far field angles and actually brings the predictions closer to experimental data.

The acoustic predictions shown in these figures clearly give better results for the $Ma = 0.9$ jets, where the experimental data is matched quite well for both the heated and unheated jets. The $Ma = 0.5$ jets are not predicted as well, for SP03 the high frequencies are especially under-predicted, and the low frequencies are over-predicted particularly for large far field angles. Whereas the heated jet SP42, is under-predicted for all frequencies. This could be due to two reasons: either there are frequency dependent length scales which we have neglected or

the difference could be due to the spatial distribution of length scales which came from $L_T = k^{3/2}/\epsilon$ which was calculated from the LES data. Since the mesh resolution decreases outside of the shear layer and downstream, L_T may not be captured accurately everywhere.

7.2.2 Effect of the Heated Spectral Tensor Components

It is also interesting to check the effect of the heated components of the acoustic spectrum. Recall that the formulation we use for the acoustic analogy reduces to a summation of three main components: momentum-flux, coupling and enthalpy-flux terms. Figures 7.7, 7.8 compare the SPL and OASPL when removing the coupling and enthalpy terms for SP46 and SP42 respectively. These figures show that the coupling terms have a very small impact at small far field angles (1dB), and are negligible at the large angles. Since they have very low impact on the acoustic spectrum results they can be neglected. Interestingly, the enthalpy-flux terms, on the other hand, have a larger impact on the large far field angles (7dB at peak St), particularly for the M=0.9 jet, where the impact on small angles is fairly small (3dB at peak St). The enthalpy terms also have a larger impact at high frequencies.

7.2.3 Approximating the Physical Spectral Tensor

When we were calculating the physical spectral tensor in the previous chapter we looked at several approximations, and found that we could take $\tilde{k}_T = 0$. We also assumed from that chapter that the approximation $\overline{H}'(\chi) = 0$ also gave a relatively good approximation at the end of the potential core. However, not all correlations were as well represented using this approximation and it was difficult to assess the performance at all spatial locations. Figures 7.9-7.12 will assess the impact of these approximations on the acoustic spectrum for SP07, SP03, SP46, and SP42 respectively.

Interestingly, from these figures it is clear that only the $\tilde{k}_T = 0$ approximation can be taken for all jets. Neglecting a_1, and using the approximation $\overline{H}'(\chi) = 0$ result in over-prediction of the acoustic predictions for both cold jets. Notably, however, for the heated jets these approximations have a negligible effect on the acoustic spectrum.

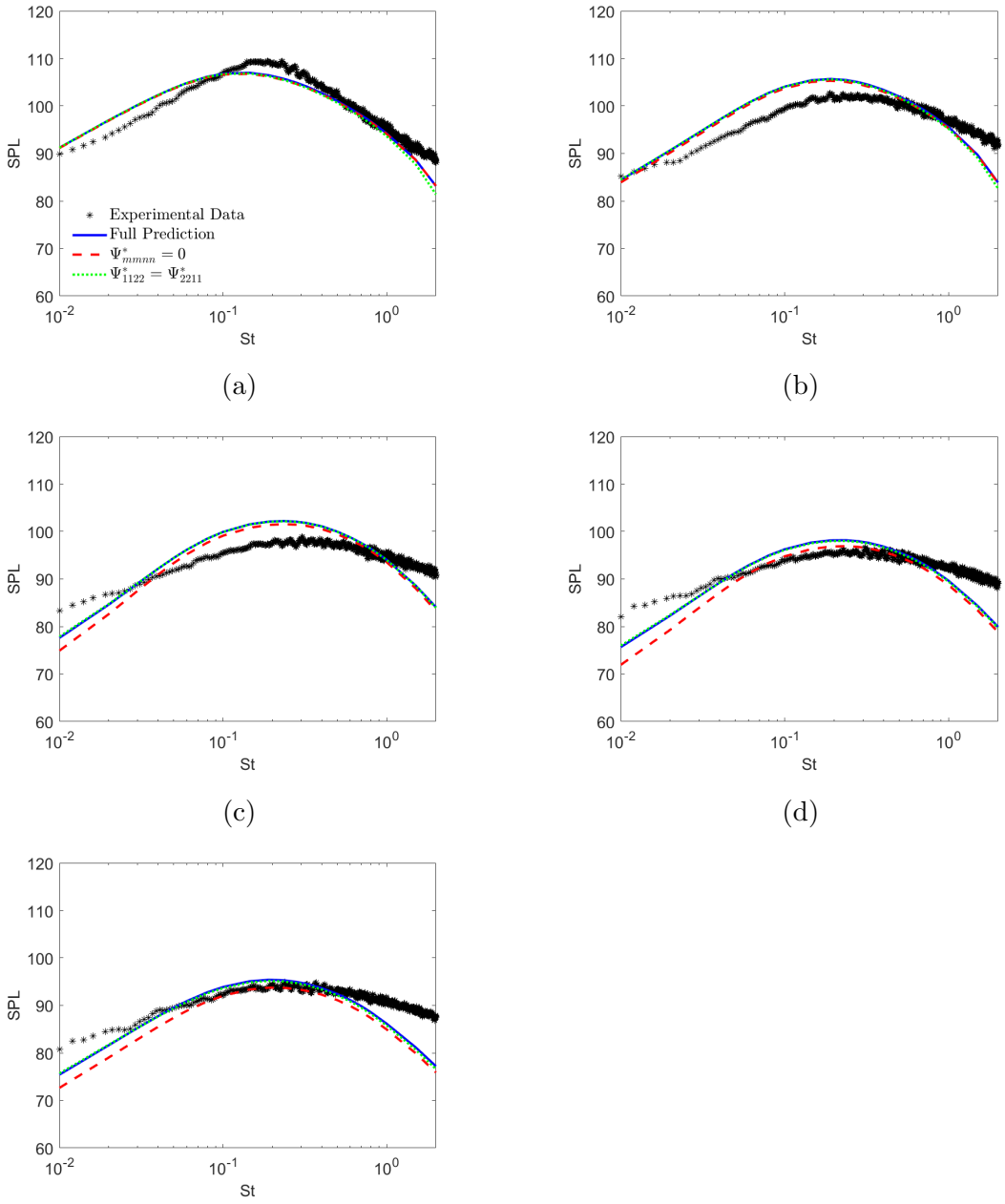

Figure 7.3: SP07: SPL acoustic predictions checking the effect of neglecting the invariant terms in the acoustic spectral tensor and assuming $\Psi^*_{1122} = \Psi^*_{2211}$ for (a) $\theta = 30$ (b) $\theta = 45$ (c) $\theta = 60$ (d) $\theta = 75$ (e) $\theta = 90$

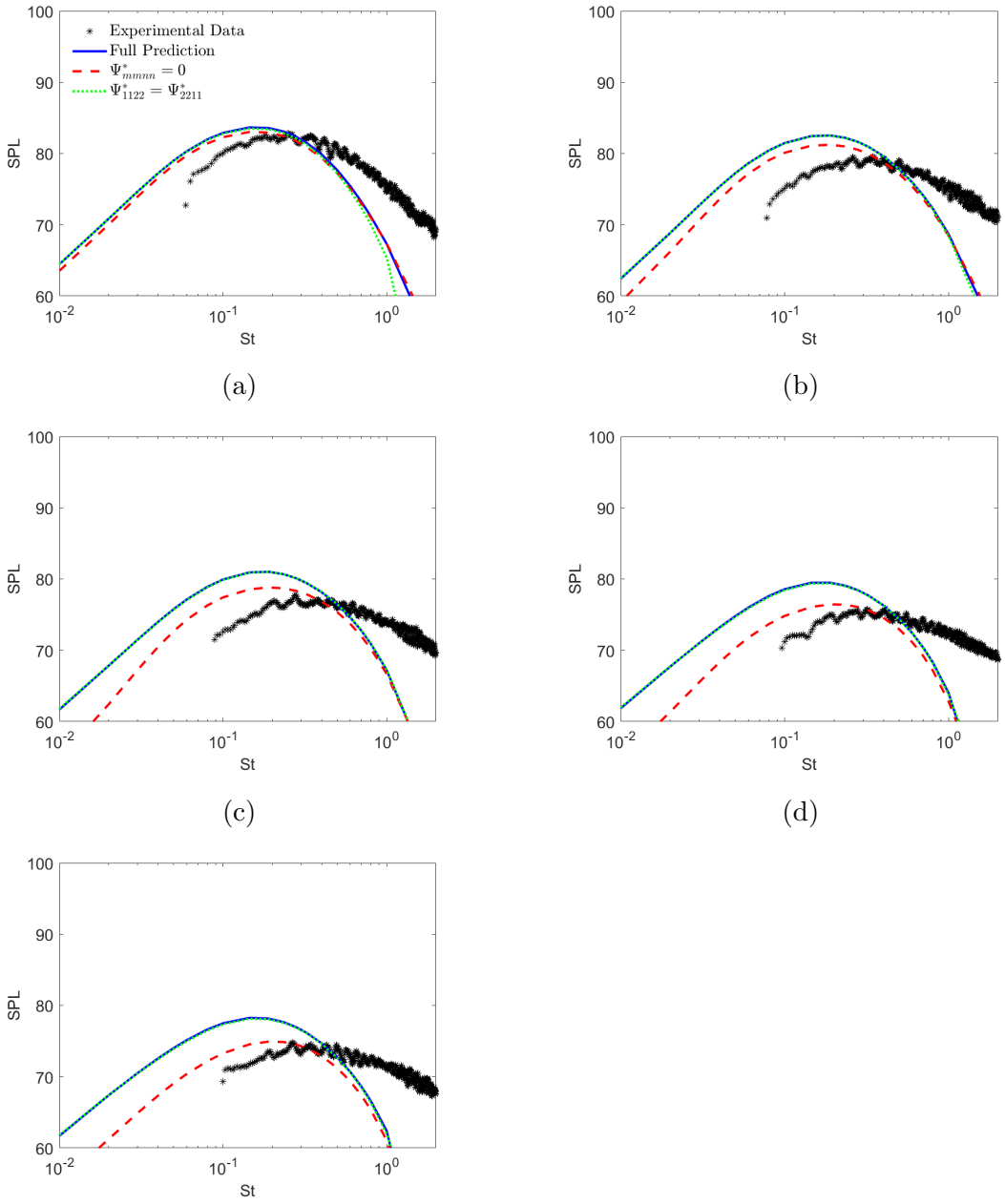

Figure 7.4: SP03: SPL acoustic predictions checking the effect of neglecting the invariant terms in the acoustic spectral tensor and assuming $\Psi^*_{1122} = \Psi^*_{2211}$ for (a) $\theta = 30$ (b) $\theta = 45$ (c) $\theta = 60$ (d) $\theta = 75$ (e) $\theta = 90$

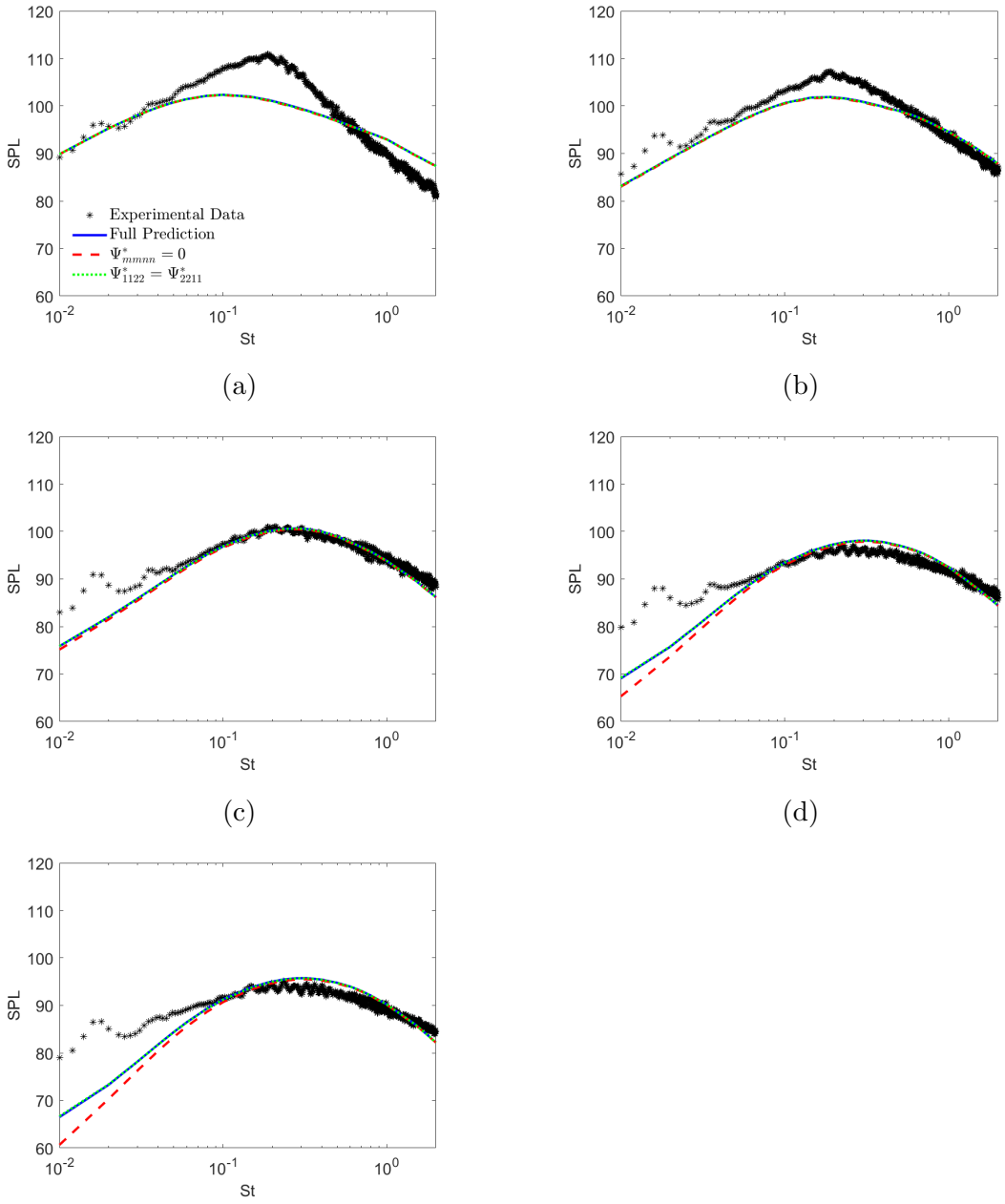

Figure 7.5: SP46: SPL acoustic predictions checking the effect of neglecting the invariant terms in the acoustic spectral tensor and assuming $\Psi^*_{1122} = \Psi^*_{2211}$ for (a) $\theta = 30$ (b) $\theta = 45$ (c) $\theta = 60$ (d) $\theta = 75$ (e) $\theta = 90$

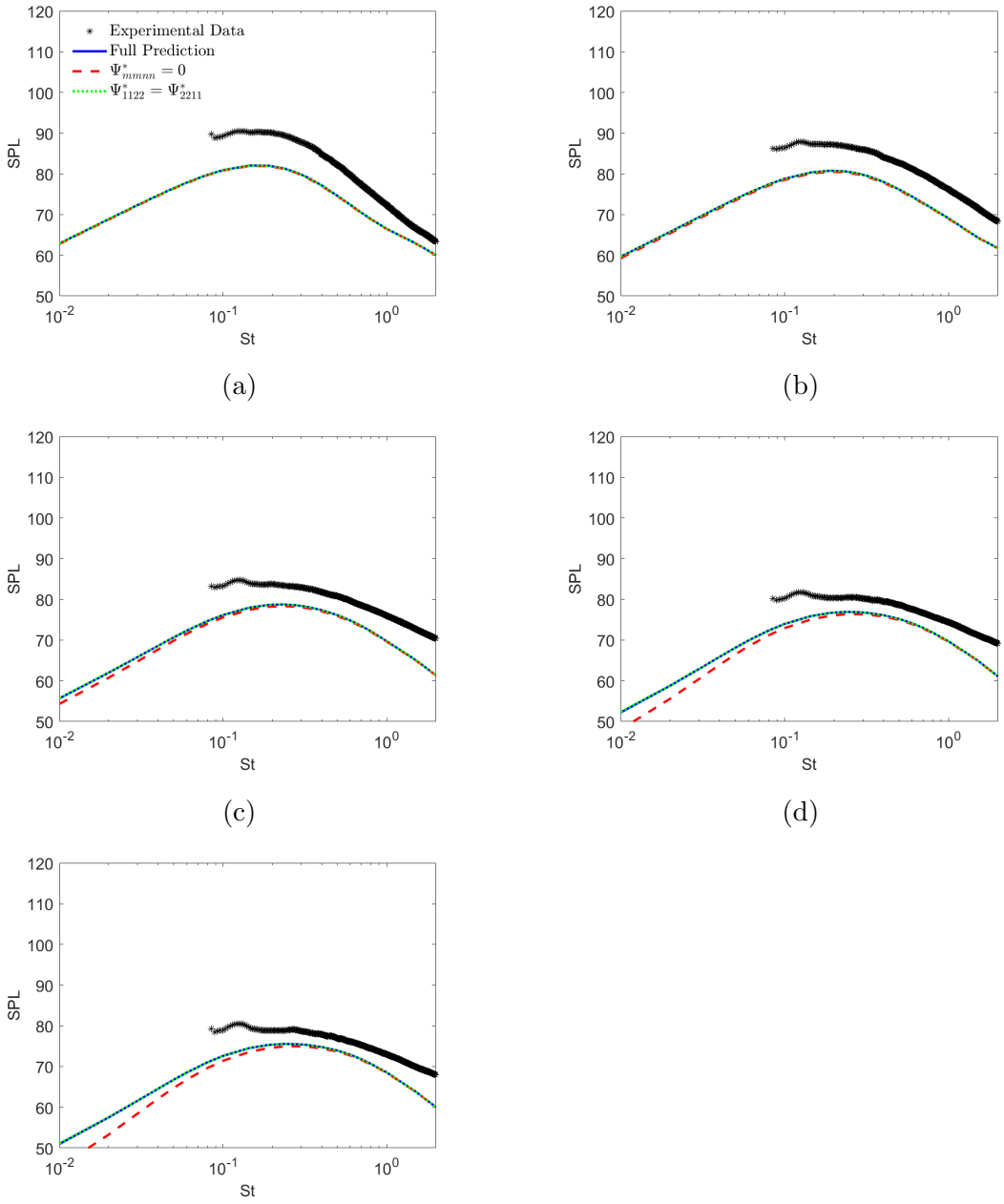

Figure 7.6: SP42: SPL acoustic predictions checking the effect of neglecting the invariant terms in the acoustic spectral tensor and assuming $\Psi^*_{1122} = \Psi^*_{2211}$ for (a) $\theta = 30$ (b) $\theta = 45$ (c) $\theta = 60$ (d) $\theta = 75$ (e) $\theta = 90$

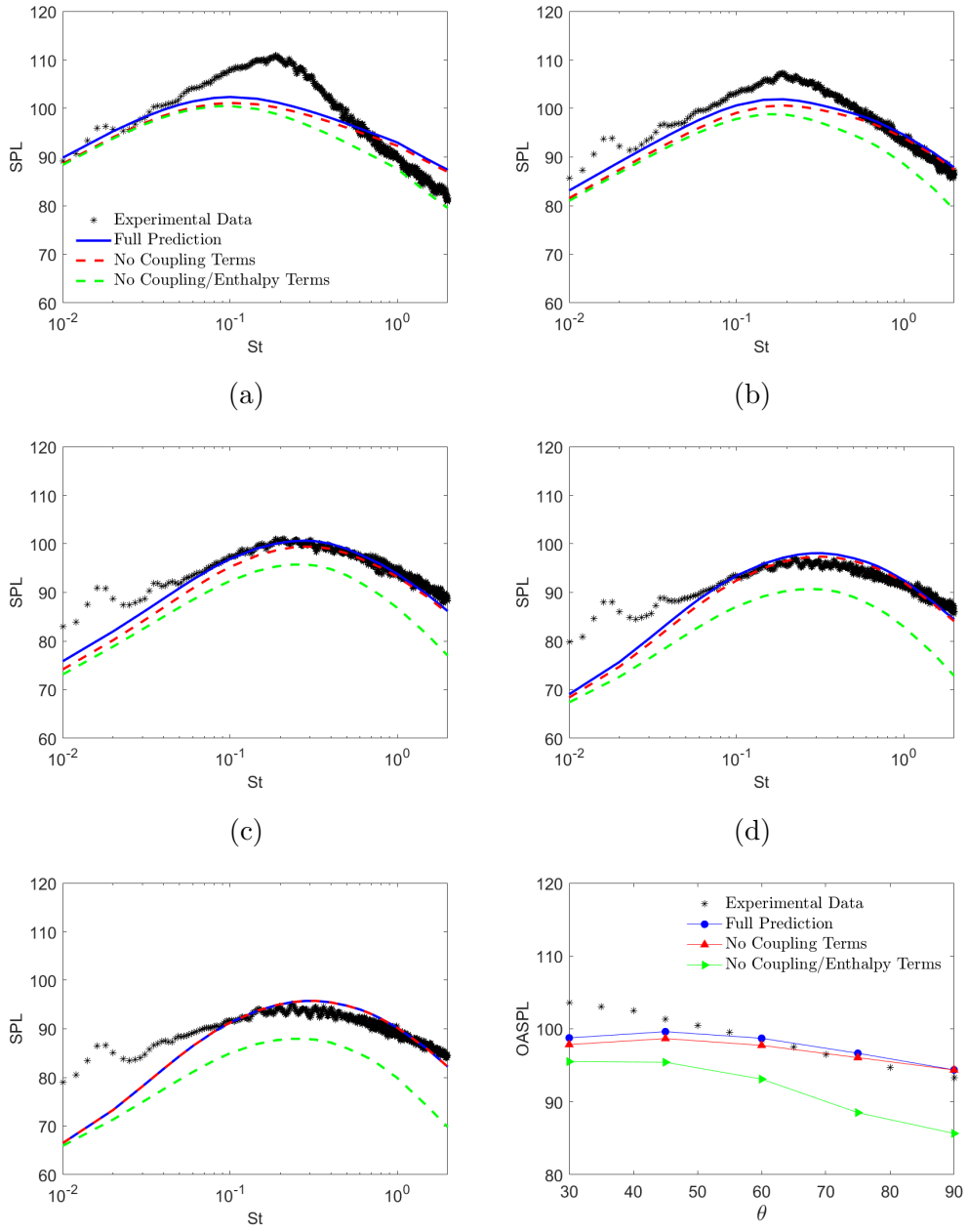

Figure 7.7: SP46: SPL acoustic predictions checking the effect of neglecting the coupling/enthalpy-flux terms in the acoustic spectrum for (a) $\theta = 30$ (b) $\theta = 45$ (c) $\theta = 60$ (d) $\theta = 75$ (e) $\theta = 90$ and (f) OASPL

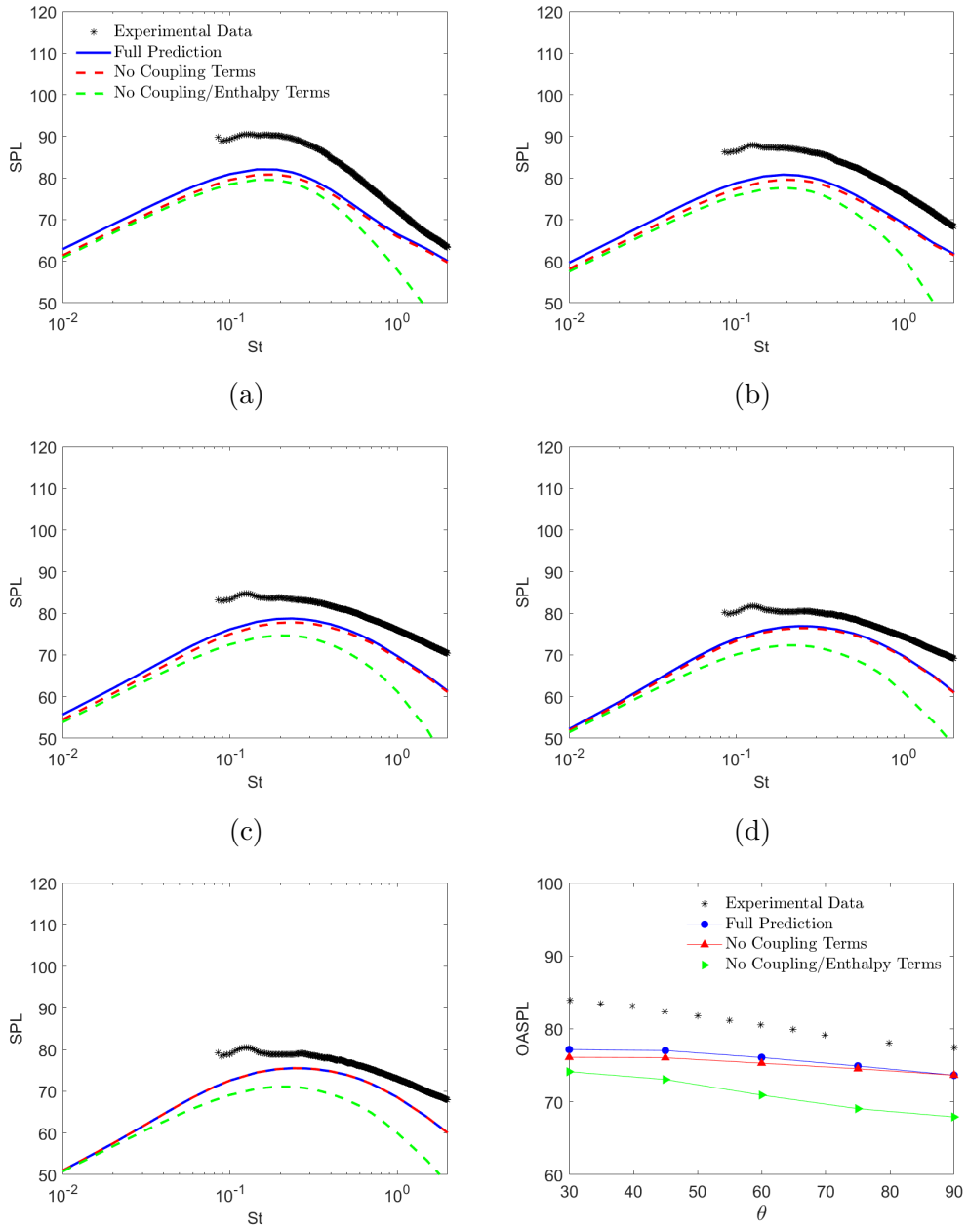

Figure 7.8: SP42: SPL acoustic predictions checking the effect of neglecting the coupling/enthalpy-flux terms in the acoustic spectrum for (a) $\theta = 30$ (b) $\theta = 45$ (c) $\theta = 60$ (d) $\theta = 75$ (e) $\theta = 90$ and (f) OASPL

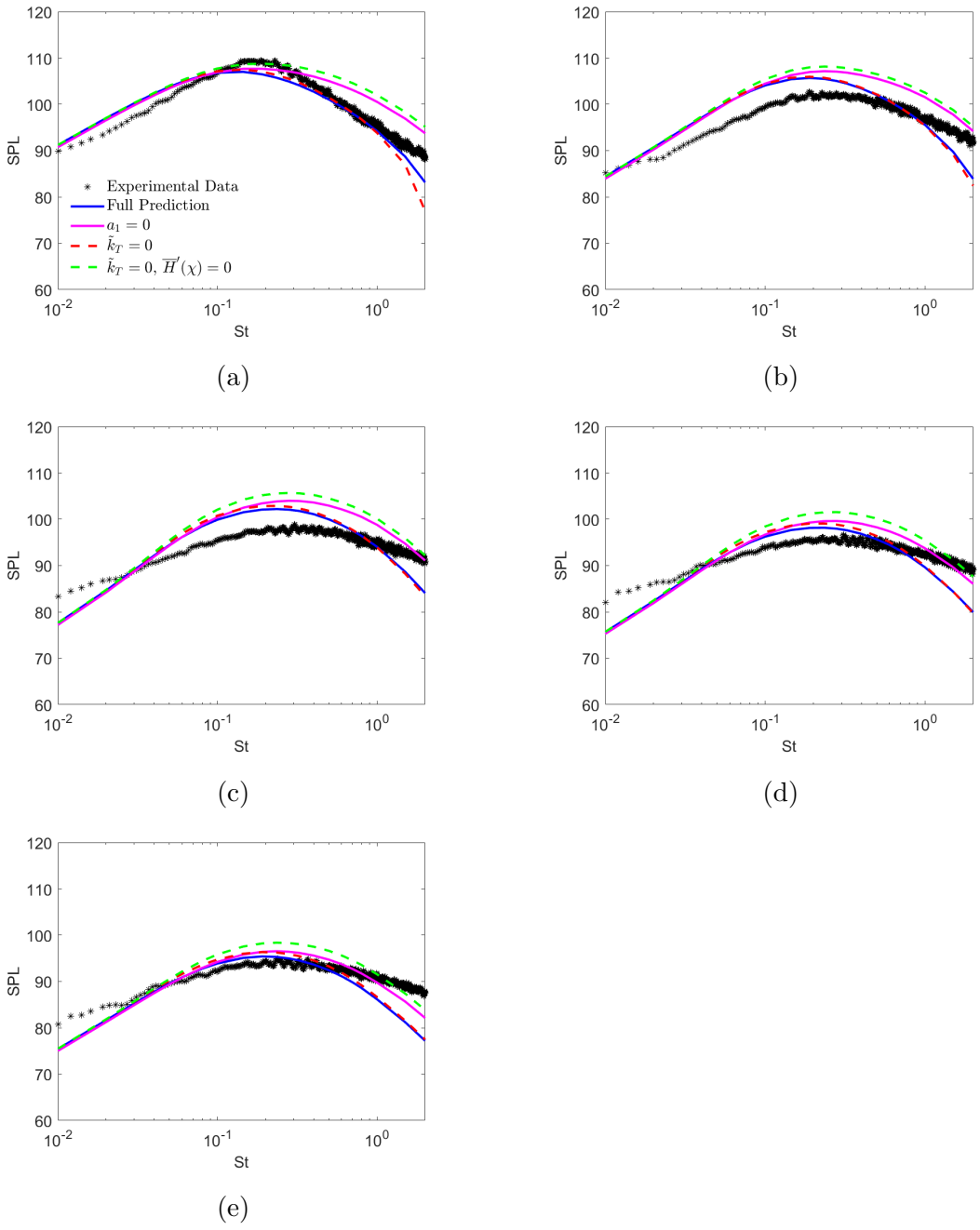

Figure 7.9: SP07: SPL acoustic predictions checking the effect of the spectral tensor approximations for (a) $\theta = 30$ (b) $\theta = 45$ (c) $\theta = 60$ (d) $\theta = 75$ (e) $\theta = 90$

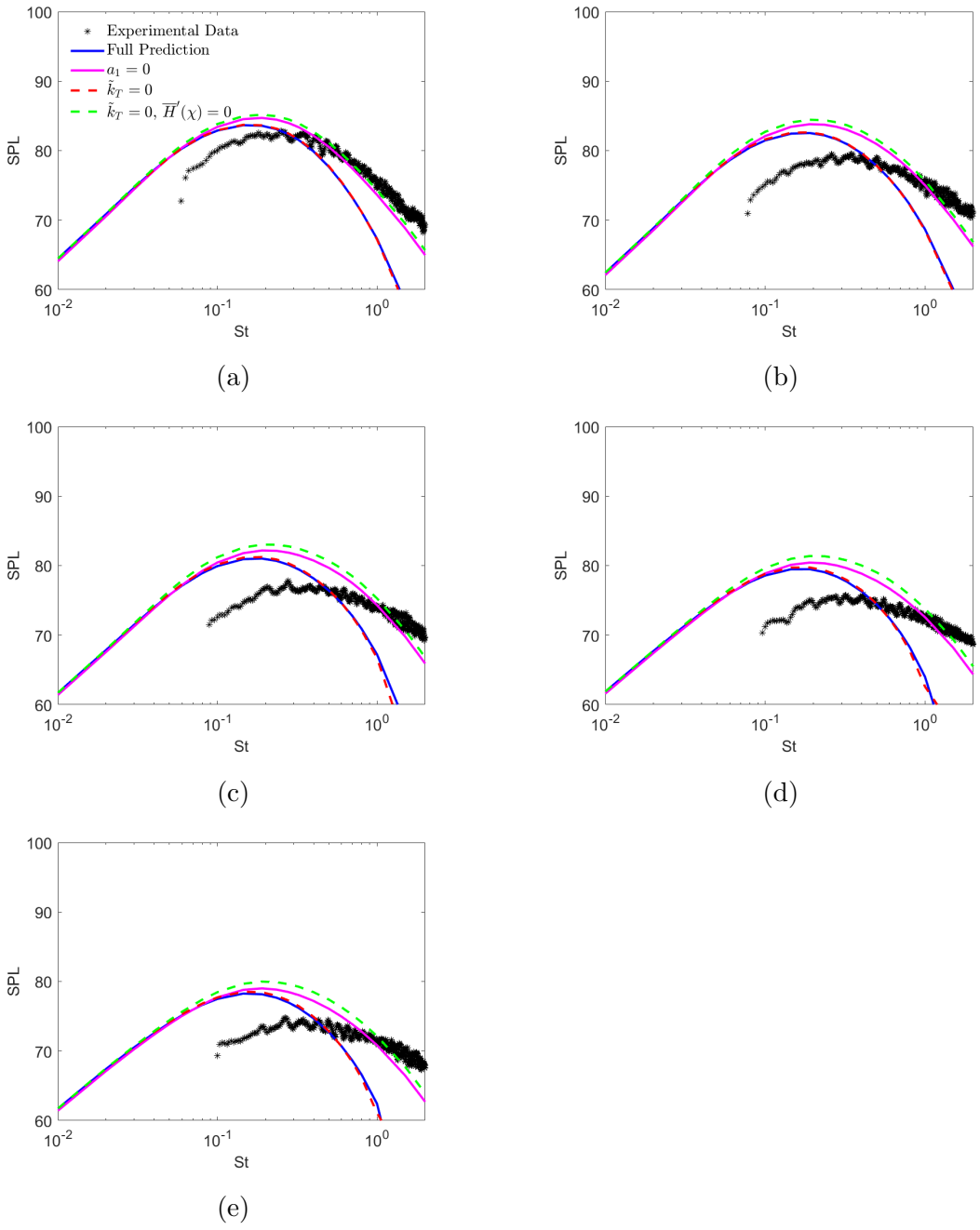

Figure 7.10: SP03: SPL acoustic predictions checking the effect of the spectral tensor approximations for (a) $\theta = 30$ (b) $\theta = 45$ (c) $\theta = 60$ (d) $\theta = 75$ (e) $\theta = 90$

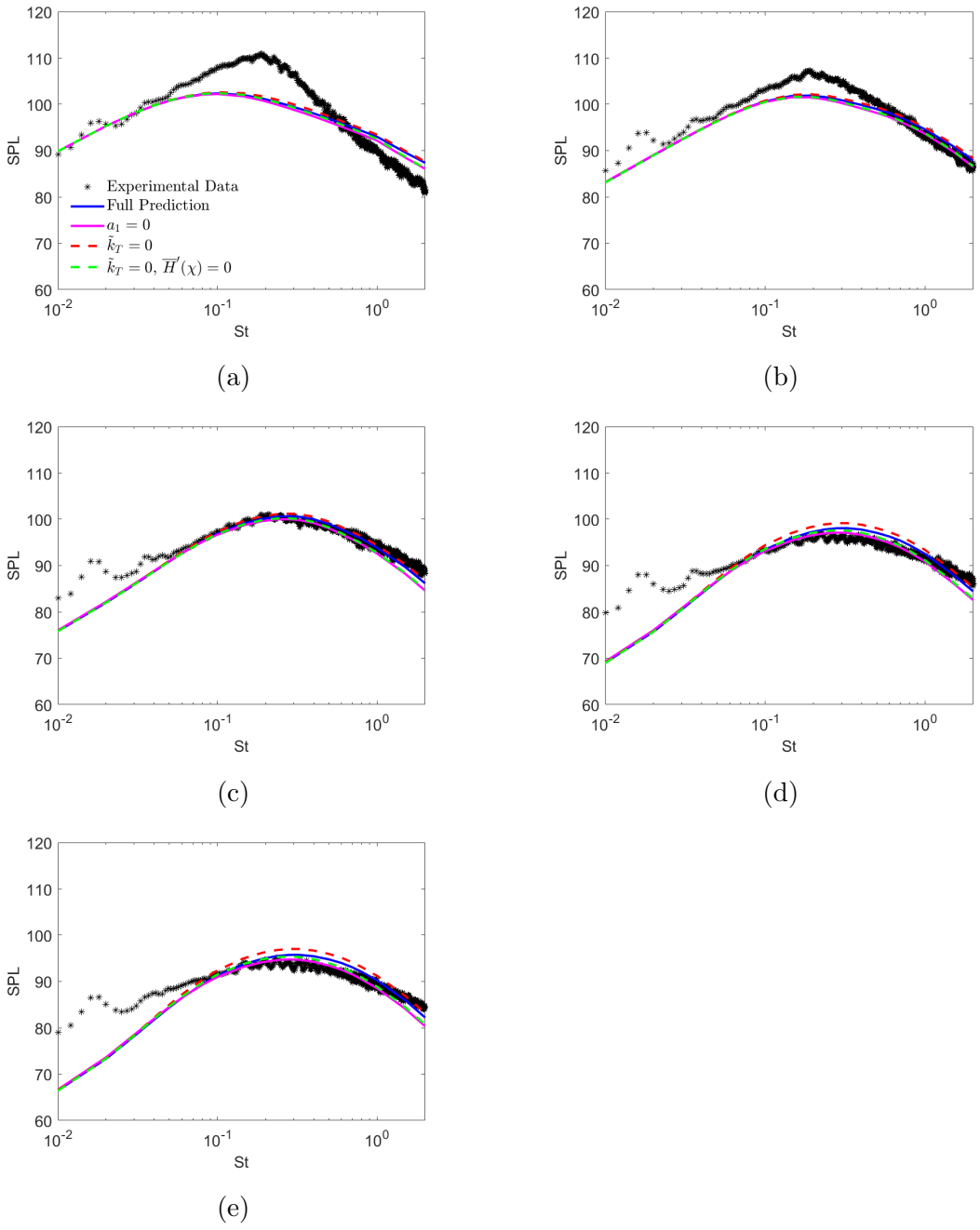

Figure 7.11: SP46: SPL acoustic predictions checking the effect of the spectral tensor approximations for (a) $\theta = 30$ (b) $\theta = 45$ (c) $\theta = 60$ (d) $\theta = 75$ (e) $\theta = 90$

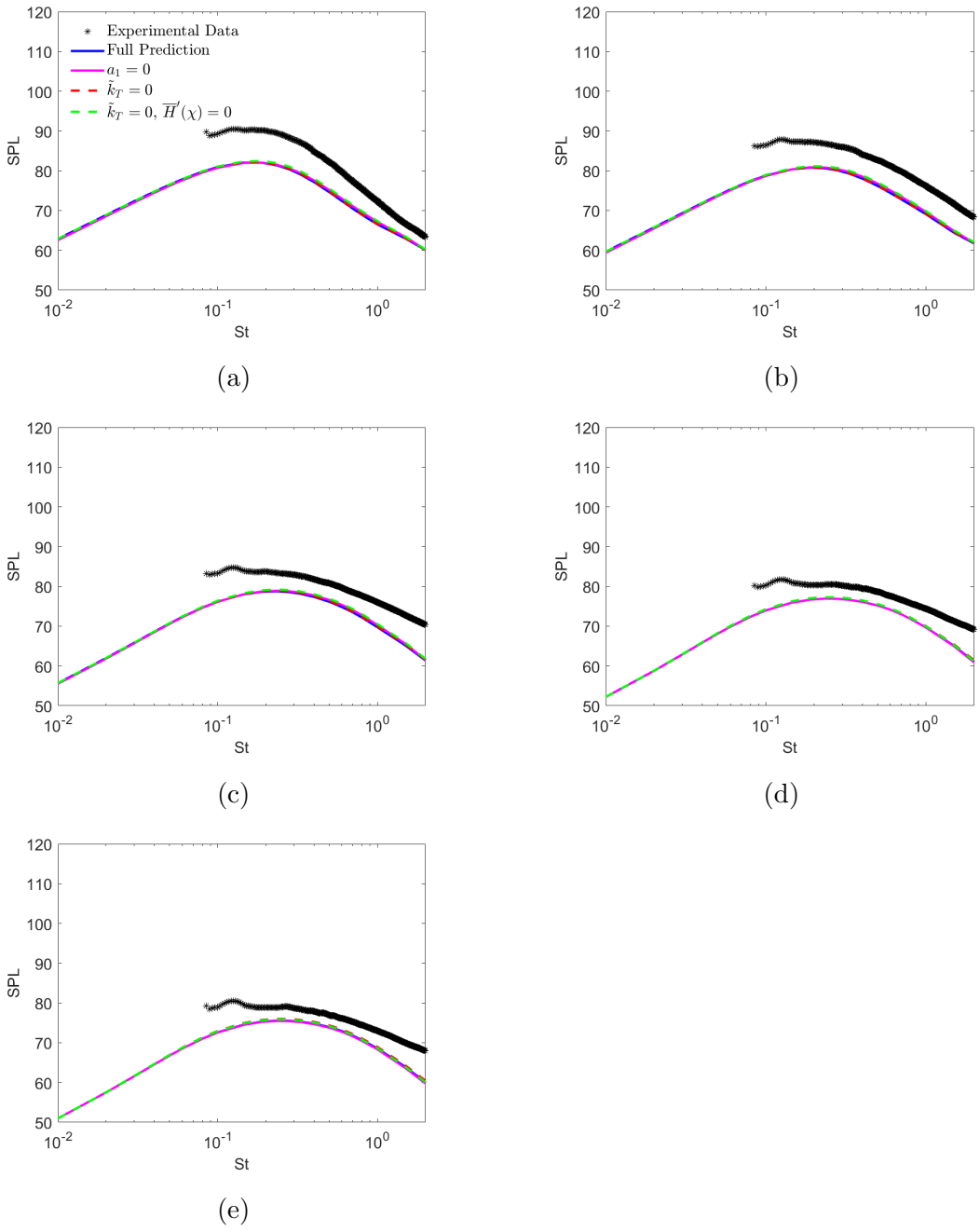

Figure 7.12: SP42: SPL acoustic predictions checking the effect of the spectral tensor approximations for (a) $\theta = 30$ (b) $\theta = 45$ (c) $\theta = 60$ (d) $\theta = 75$ (e) $\theta = 90$

7.3 Jet Comparison

Figures 7.13 and 7.14 show the effect of increasing the Mach number at fixed jet temperature ratio and the effect of increasing the temperature at fixed acoustic Mach number respectively. The first figure shows that increasing the Mach number at fixed temperature ratio increases the acoustic spectrum across all frequencies and far field angle, by around $20dB$.

The second figure shows that for both Mach numbers heating the jet appears to reduce the noise across low/peak frequency and across most far field angles, this effect is greater for $Ma = 0.9$ which experiences a 4dB reduction at $\theta = 30$, compared to the $2dB$ reduction for $Ma = 0.5$. Note that experiment shows that for low Mach numbers heating the jet should increase the jet noise, since our heated jet SP42 was under-predicted at all frequencies and our cold jet SP03 was over-predicted at high frequencies we do not obtain these results.

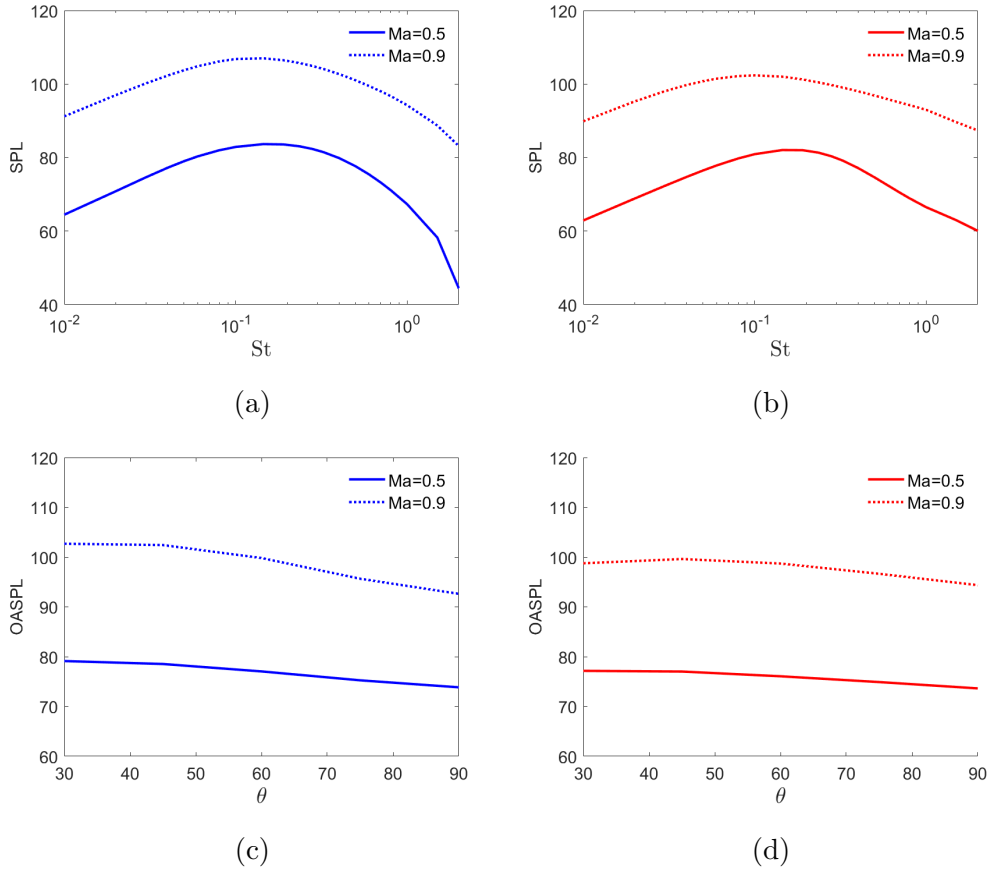

Figure 7.13: Effect of Ma on SPL predictions at $\theta = 30$ for (a) cold jets (b) hot jets, and effect on OASPL predictions for (c) cold jets (d) hot jets

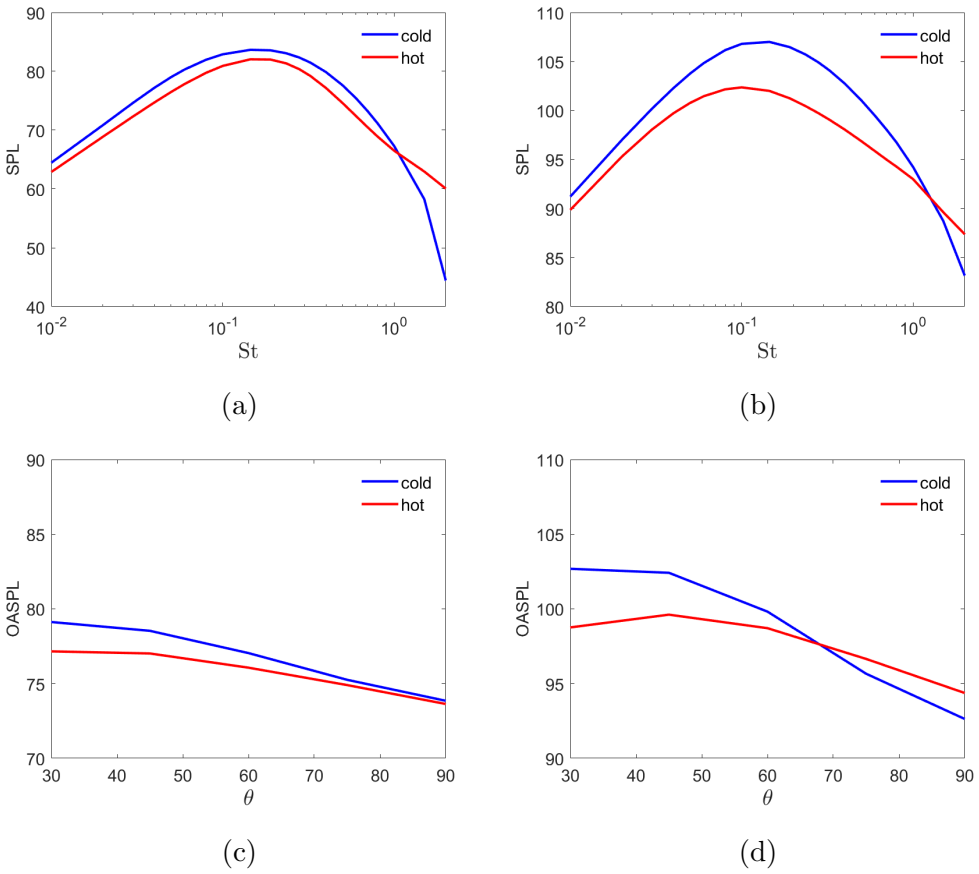

Figure 7.14: Effect of TR on SPL predictions at $\theta = 30$ for (a) $Ma = 0.5$ (b) $Ma = 0.9$, and effect on OASPL predictions for (c) $Ma = 0.5$ (d) $Ma = 0.9$

7.4 Universality

In the previous chapter universality of length scales across Mach number and jet temperature ratio was discussed. Figures 7.15-7.18 check the acoustic predictions using the universal length scales shown in Tables 5.6-5.8 for SP07, SP03, SP46, SP42 respectively. Note that this assumes universal length scales $l0, l1, l2$ on the shear layer at the start of the potential core. $L_T = k^{3/2}/\epsilon$ was assumed universal across Mach number which is shown in Appendix C.1 to be a reasonable assumption. Therefore $l0, l1, l2$ will still vary across temperature for all universality checks.

From these figures we can conclude that we can use universal lengthscales across Mach number since each jet shows close agreement with the original

predictions. However, universal lengthscales across Mach number and temperature ratio are shown to increase the noise predictions at high frequency for the cold jets, particularly at large far field angles. It should be noted however, that for the peak jet noise (i.e. at $\theta = 30, St = 0.2$) total universality gives similar predictions to the individual predictions. This means that using the length scales in Table 5.8 for any subsonic jet along with $L_T = k^{3/2}/\epsilon$, the meanflow of the jet and the amplitude of the correlations it is possible to calculate the peak jet noise.

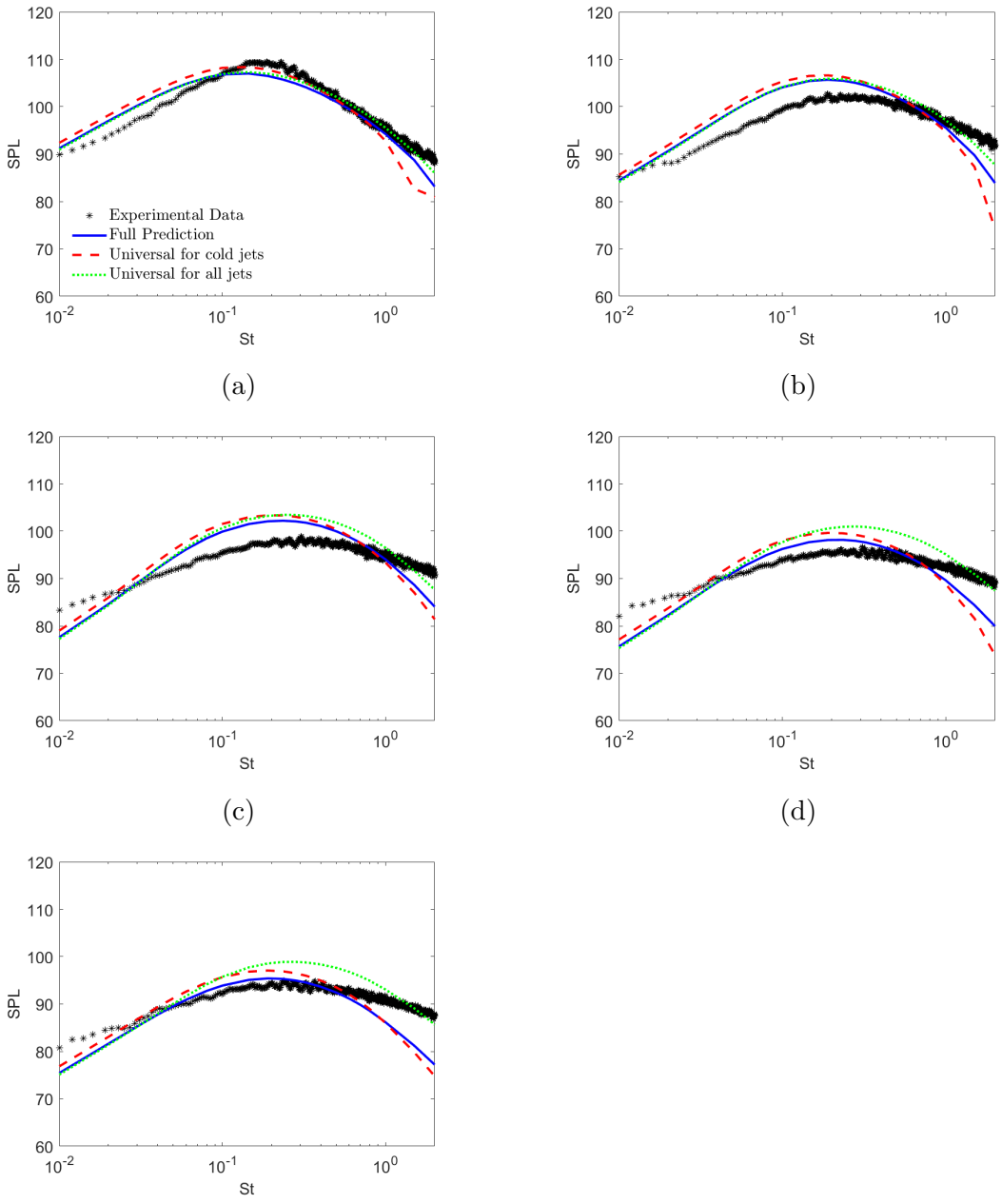

Figure 7.15: SP07: SPL acoustic predictions check effect of universal length scales for (a) $\theta = 30$ (b) $\theta = 45$ (c) $\theta = 60$ (d) $\theta = 75$ (e) $\theta = 90$

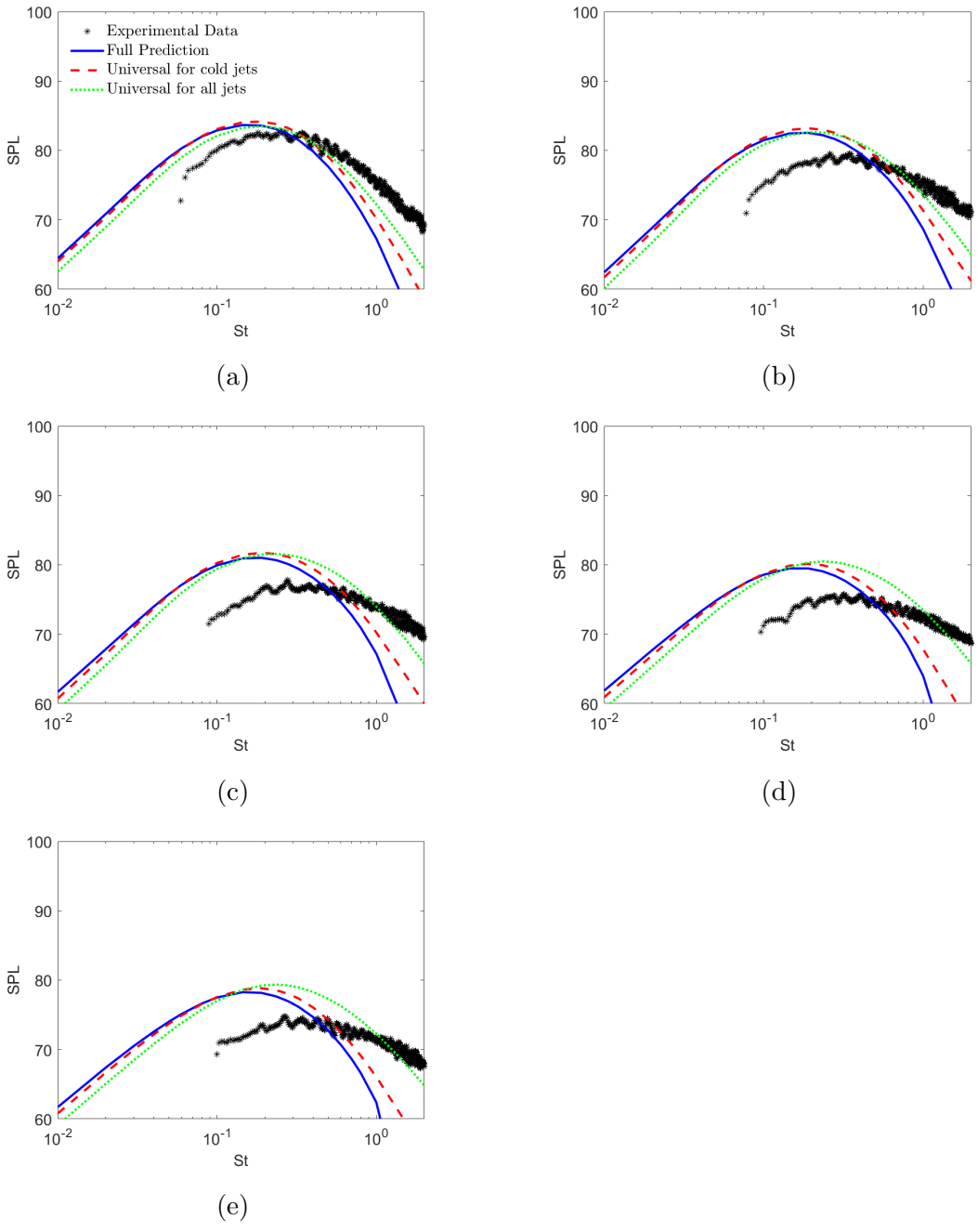

Figure 7.16: SP03: SPL acoustic predictions check effect of universal length scales for (a) $\theta = 30$ (b) $\theta = 45$ (c) $\theta = 60$ (d) $\theta = 75$ (e) $\theta = 90$

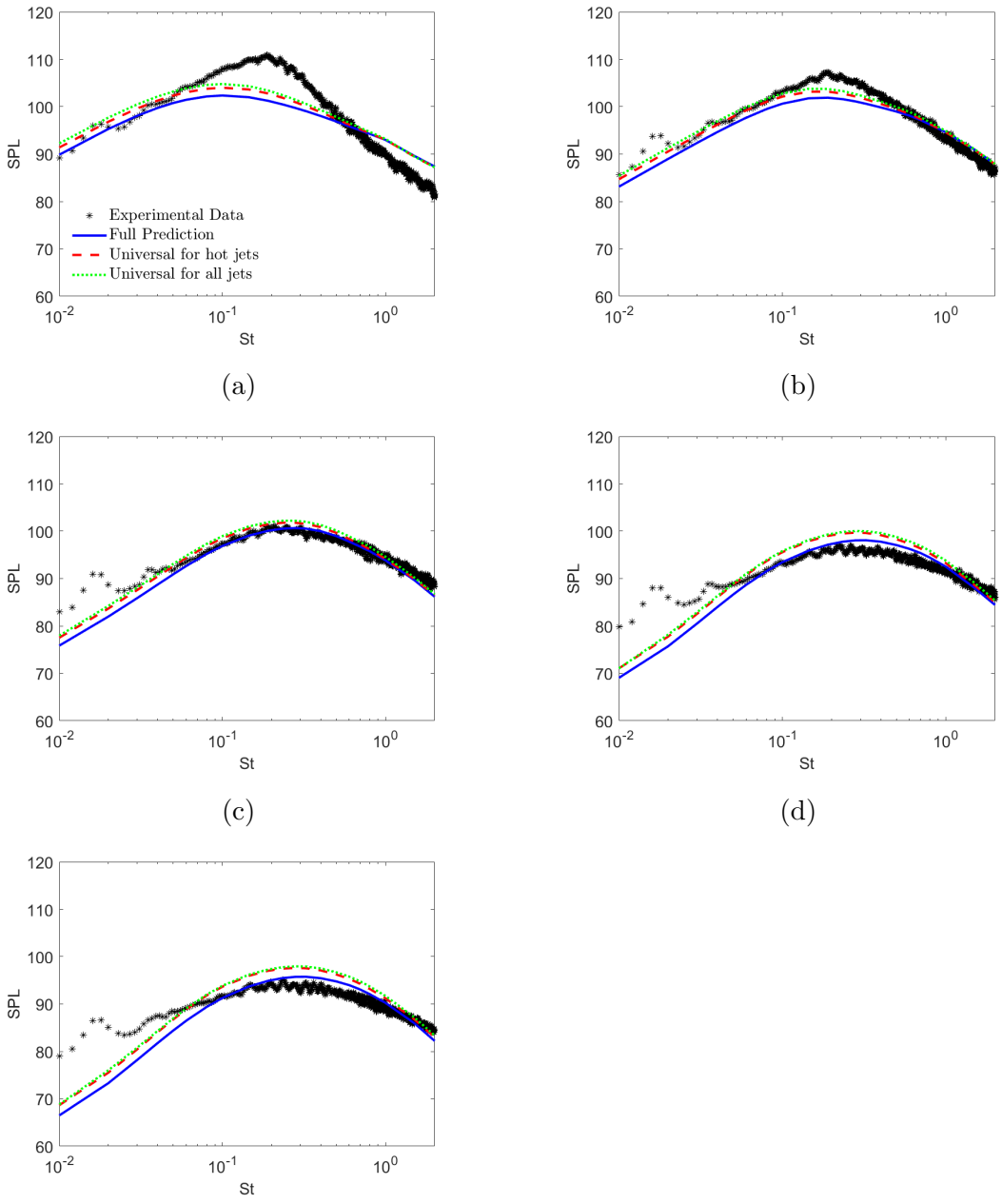

Figure 7.17: SP46: SPL acoustic predictions check effect of universal length scales for (a) $\theta = 30$ (b) $\theta = 45$ (c) $\theta = 60$ (d) $\theta = 75$ (e) $\theta = 90$

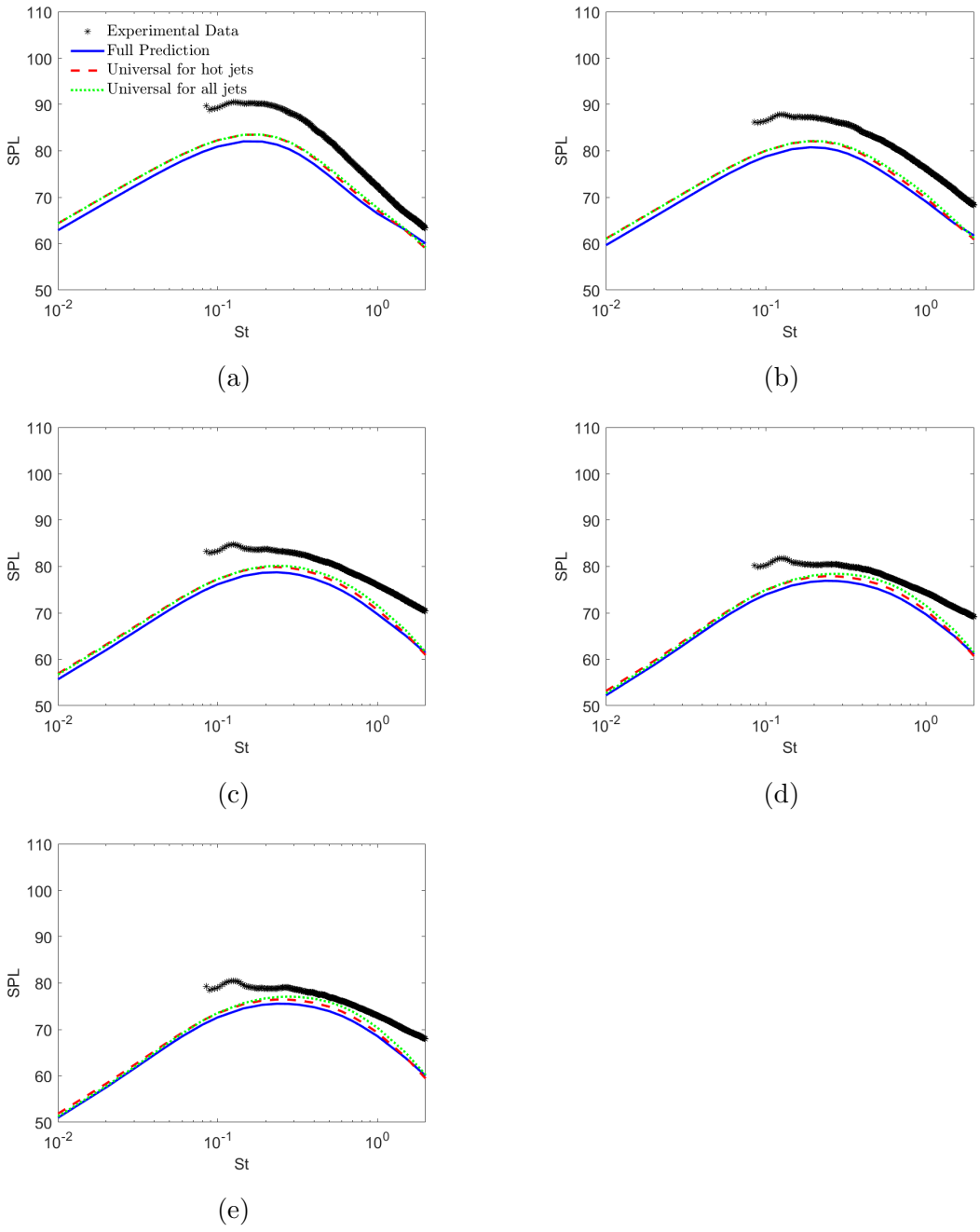

Figure 7.18: SP42: SPL acoustic predictions check effect of universal length scales for (a) $\theta = 30$ (b) $\theta = 45$ (c) $\theta = 60$ (d) $\theta = 75$ (e) $\theta = 90$

7.5 Summary

In this chapter we have calculated the acoustic predictions for all four jets using the propagator and analytical spectral tensor which were found in the previous chapters. We obtained good predictions against experimental data for the $M = 0.9$ jets, where the $M = 0.5$ jets were over/under predicted for some angles. However, the predictions allowed us to check the importance of certain components of the acoustic spectral tensor where we discovered that the invariant can be neglected as it has little impact on the predictions. We also found that we can replace R_{1122} with R_{2211} since it had negligible impact on the acoustic spectrum and will reduce the number of calculations required.

Then we checked the effect of various approximations of the physical spectral tensor, where we concluded that only the approximation of $\tilde{k}_T = 0$ is valid for all jets. Interestingly, neglecting the a_1 scale or setting $\overline{H}' = 0$ both result in over-prediction of the high frequencies in unheated jets, while having no impact on heated jets.

For heated jets we investigated the effect of the coupling and the enthalpy-flux terms. In both jets we found that coupling terms have a very small impact on the acoustic spectrum at small far field angles, and can be neglected. Whereas the enthalpy-flux terms have a much larger impact, particularly at large far field angles.

In general we found that by increasing the acoustic Mach number in both cold and heated cases this increased the peak jet noise by around $20dB$. We also found that heating the jets at fixed Mach number reduced the sound produced at most frequencies. From the literature it is expected that the slow $Ma = 0.5$ jet would in fact increase in sound when heated, and it is possible that we do not obtain these results since the SP42 jet was shown to under-predict the noise, and the SP03 jet was shown to over-predict the noise. The $Ma = 0.9$ results agree with the literature that a high subsonic jet would decrease in sound when heated.

Arguably the most important finding from this research is the fact that universal length scales can be used to obtain noise predictions for all jets. This could be used to obtain faster predictions using meanflow data from RANS rather than LES, which reduces the complexity of the predictions.

Now we have obtained jet noise predictions for four jets at several far field angles, this concludes the jet noise portion of this thesis. In the next chapter

we will move on to discuss the edge noise problem and obtain predictions for edge noise. Finally, in Chapter 9, we will be able to combine the predictions for jet noise and edge noise in a hybrid model to obtain predictions for installation noise.

Chapter 8

Edge Noise Modelling

This chapter of the thesis details work done on the edge noise problem. Sections 8.2 and 8.3 covers research which was presented at AIAA conference [98] and is in preparation for an archived journal publication. Section 8.4 was published as a journal article in 2021 [99], and section 8.5 is in preparation for journal publication.

8.1 Rapid Distortion Theory (RDT)

As discussed in the literature review, rapid distortion theory can be used when the interaction takes place over small length/timescales in comparison to the characteristic scales over which the turbulent eddies evolve. This means that the flow can be considered inviscid and is governed by the linearised Euler equations:

$$\frac{Dv_i}{D\tau} + \delta_{i1} v_j \frac{\partial U}{\partial y_j} + \frac{\partial p}{\partial y_i} = 0, \qquad i = 1, 2, 3 \tag{8.1.1}$$

$$\frac{Dp}{D\tau} + \frac{\partial}{\partial y_j} c^2 v_j = 0 \tag{8.1.2}$$

where $D/D\tau = \partial/\partial\tau + U\partial/\partial y_1$ is the convective derivative and $\boldsymbol{y} = (y_1, y_2, y_3) = (y_1, \boldsymbol{y}_T)$.

The physics of the problem (i.e. the viscosity which must be present due to the plate) enters through the Kutta condition on the vortex sheet which is produced downstream of the plate. A visualisation of the problem is shown in Figure 8.1

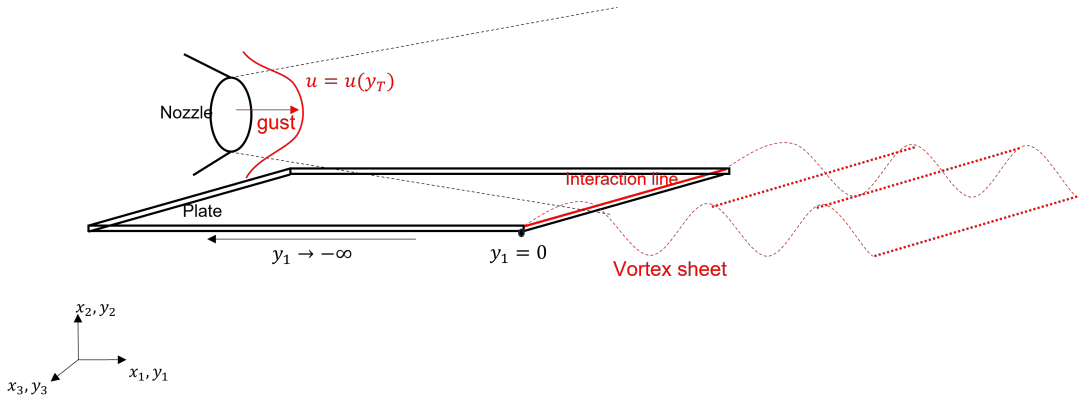

Figure 8.1: Visualisation of the edge noise problem

8.1.1 Solution Structure to (8.1.1) and (8.1.2)

Goldstein [59] showed that the velocity could be written in terms of a pseudo induced velocity: $v_i = \tilde{v}_i + \tilde{F}_i$, where $\boldsymbol{F} = 0$ when the level curves of the meanflow and solid surface align which we assume to be the case. Therefore, the velocity is defined simply by the psuedo induced velocity, given by:

$$v_i = \tilde{v}_i = \left(\frac{D\lambda_i}{D\tau} - \delta_{i1}\frac{\partial U}{\partial y_j}\lambda_j\right) \tag{8.1.3}$$

similarly, the pressure fluctuation was shown to be expressed in terms of a function $\phi(\boldsymbol{y}, \tau)$:

$$p = -\frac{D^3\phi}{D\tau^3} \tag{8.1.4}$$

Substituting these equations for velocity and pressure into the momentum equation, shows that:

$$\lambda_i = \Delta_i \phi \tag{8.1.5}$$

where we define

$$\Delta_i = \left(\frac{\partial}{\partial y_i}\frac{D}{D\tau} + 2\frac{\partial U}{\partial y_i}\frac{\partial}{\partial y_1}\right) \tag{8.1.6}$$

Therefore v_i can be written as:

$$v_i = \left(\delta_{ij}\frac{D}{D\tau} - \delta_{i1}\frac{\partial U}{\partial y_j}\right)\Delta_j\phi \tag{8.1.7}$$

To find ϕ we substitute v_i and p' into the energy equation (8.1.2) (details are in Appendix D.1) which results in:

$$L_a\phi = -\tilde{\omega}_c(\tau - y_1/U, \boldsymbol{y}_T) \tag{8.1.8}$$

where $\tilde{\omega}_c$ is an arbitrary convected quantity, and L_a is the operator defined as:

$$L_a = \frac{D^3}{D\tau^3} - \frac{\partial}{\partial y_i}\Big(c^2\Delta_i\Big) \tag{8.1.9}$$

Appendix D.2 shows that the momentum and continuity equations can also be written as

$$Lp = 0 \tag{8.1.10}$$

where

$$L = -\frac{D^3}{D\tau^3} - 2c^2\frac{\partial U}{\partial y_i}\frac{\partial^2}{\partial y_1 \partial y_i} + \frac{D}{D\tau}\frac{\partial}{\partial y_i}\Big(c^2\frac{\partial}{\partial y_i}\Big) \tag{8.1.11}$$

is the well known Rayleigh operator and of which, L_a is its adjoint.

We introduce the direct Green's function:

$$Lg(\boldsymbol{y},\tau|\boldsymbol{x},t) = \delta(\boldsymbol{x}-\boldsymbol{y})\delta(t-\tau) \tag{8.1.12}$$

Since L_a is the adjoint Rayleigh operator, $\phi Lg = gL_a\phi$, which means

$$\phi(\boldsymbol{y},\tau)\delta(\boldsymbol{x}-\boldsymbol{y})\delta(t-\tau) = -g(\boldsymbol{y},\tau|\boldsymbol{x},t)\tilde{\omega}_c(\tau - y_1/U, \boldsymbol{y}_T) \tag{8.1.13}$$

By definition of the delta function, integrating over all $(\boldsymbol{y},\tau)$ gives

$$\boxed{\phi(\boldsymbol{x},t) = -\int_{-\infty}^{\infty}\int_{V(\boldsymbol{y})} g(\boldsymbol{y},\tau|\boldsymbol{x},t)\tilde{\omega}_c(\tau - y_1/U, \boldsymbol{y}_T)d\boldsymbol{y}d\tau} \tag{8.1.14}$$

Since pressure and velocity were defined in terms of ϕ, this means they can also be written as Green's function integrals:

$$p(\boldsymbol{x},t) = \int_{-\infty}^{\infty}\int_{V(\boldsymbol{y})} G(\boldsymbol{y},\tau|\boldsymbol{x},t)\tilde{\omega}_c(\tau - y_1/U, \boldsymbol{y}_T)d\boldsymbol{y}d\tau \tag{8.1.15}$$

$$u_i(\boldsymbol{x},t) = -\int_{-\infty}^{\infty}\int_{V(\boldsymbol{y})} \tilde{G}_i(\boldsymbol{y},\tau|\boldsymbol{x},t)\tilde{\omega}_c(\tau - y_1/U, \boldsymbol{y}_T)d\boldsymbol{y}d\tau \tag{8.1.16}$$

where

$$G(\boldsymbol{y},\tau|\boldsymbol{x},t) = \frac{D^3}{Dt^3}g(\boldsymbol{y},\tau|\boldsymbol{x},t) \tag{8.1.17}$$

and

$$\tilde{G}_i(\boldsymbol{y},\tau|\boldsymbol{x},t) = \Big(\frac{D}{Dt}\delta_{ij} - \delta_{i1}\frac{\partial U}{\partial x_j}\Big)\Big(\frac{\partial}{\partial x_i}\frac{D}{D\tau} + 2\frac{\partial U}{\partial x_i}\frac{\partial}{\partial x_1}\Big)g(\boldsymbol{y},\tau|\boldsymbol{x},t) \tag{8.1.18}$$

However, the boundary conditions for the Green's function require the normal velocity perturbation , which is defined as:

$$|\nabla U|v_\perp(\boldsymbol{x},t) = v_i(\boldsymbol{x},t)\frac{\partial U}{\partial x_i} \tag{8.1.19}$$

and after substituting in the velocity, contracting indices and using $\partial U/\partial x_1 = 0$ can be written as

$$|\nabla U| v_\perp(\boldsymbol{x}, t) = \frac{\partial U}{\partial x_i} \int_{-\infty}^{\infty} \int_{V(\boldsymbol{y})} g_i(\boldsymbol{y}, \tau | \boldsymbol{x}, t) \tilde{\omega}_c(\tau - y_1/U, \boldsymbol{y}_T) d\boldsymbol{y} d\tau \tag{8.1.20}$$

where we define

$$g_i(\boldsymbol{y}, \tau | \boldsymbol{x}, t) = \frac{D}{D\tau}\Big(\frac{\partial}{\partial x_i}\frac{D}{D\tau} + 2\frac{\partial U}{\partial x_i}\frac{\partial}{\partial x_1}\Big) g(\boldsymbol{y}, \tau | \boldsymbol{x}, t) \tag{8.1.21}$$

where the pressure Green's function $G(\boldsymbol{y}, \tau | \boldsymbol{x}, t)$ is related to the normal velocity Green's function $g_i(\boldsymbol{y}, \tau | \boldsymbol{x}, t)$ by the relation (details in Appendix D.3):

$$\frac{\partial}{\partial x_i} G(\boldsymbol{y}, \tau | \boldsymbol{x}, t) = \frac{D^2}{Dt^2} g_i(\boldsymbol{y}, \tau | \boldsymbol{x}, t) \tag{8.1.22}$$

8.1.2 Frequency Domain

Since the acoustic spectrum is the Fourier transform of the mean squared pressure, we calculate the Fourier transform of (8.1.15) first:

$$\tilde{p}(\boldsymbol{x}, \omega) = \frac{1}{2\pi} \int_{-\infty}^{\infty} e^{i\omega t} \int_{-\infty}^{\infty} \int_{V} G(\boldsymbol{y}, \tau | \boldsymbol{x}, t) \tilde{\omega}_c(\tau - y_1/U(\boldsymbol{y}_T), \boldsymbol{y}_T) d\boldsymbol{y} d\tau dt \tag{8.1.23}$$

since $G(\boldsymbol{y}, \tau | \boldsymbol{x}, t)$ only depends on (t, τ) through their difference $(t - \tau)$, and we can switch the order of integration, this can be rewritten as:

$$\tilde{p}(\boldsymbol{x}, \omega) = \frac{1}{2\pi} \int_{V} \int_{-\infty}^{\infty} dt e^{i\omega t} \int_{-\infty}^{\infty} G(\boldsymbol{y} | \boldsymbol{x}, t - \tau) \tilde{\omega}_c(\tau - y_1/U(\boldsymbol{y}_T), \boldsymbol{y}_T) d\tau d\boldsymbol{y} \tag{8.1.24}$$

Therefore the integral over τ is a convolution and by definition the Fourier transform of a convolution is equal to the product of Fourier transforms, hence (8.1.24) becomes:

$$\tilde{p}(\boldsymbol{x}, \omega) = \int_{V} 2\pi \tilde{G}(\boldsymbol{y} | \boldsymbol{x}; \omega) \tilde{\Omega}(\boldsymbol{y}_T; \omega) d\boldsymbol{y} \tag{8.1.25}$$

where we define

$$\tilde{G}(\boldsymbol{y} | \boldsymbol{x}; \omega) = \frac{1}{2\pi} \int_{-\infty}^{\infty} G(\boldsymbol{y} | \boldsymbol{x}, t - \tau) e^{i\omega(t-\tau)} d(t - \tau) \tag{8.1.26}$$

and

$$\tilde{\Omega}(\boldsymbol{y}_T; \omega) = \frac{1}{2\pi} \int_{-\infty}^{\infty} \tilde{\omega}_c(\tau - y_1/U(\boldsymbol{y}_T), \boldsymbol{y}_T) e^{i\omega\tau} d\tau \tag{8.1.27}$$

we can use the substitution $z = \tau - y_1/U(\boldsymbol{y}_T)$ to rewrite $\tilde{\Omega}$:

$$\begin{aligned}\tilde{\Omega}(\boldsymbol{y}_T;\omega) &= \frac{1}{2\pi}e^{i\omega y_1/\boldsymbol{U(y_T)}}\int_{-\infty}^{\infty}\tilde{\omega}_c(z,\boldsymbol{y}_T)e^{i\omega z}dz \\ \tilde{\Omega}(\boldsymbol{y}_T;\omega) &= \frac{1}{2\pi}e^{i\omega y_1/\boldsymbol{U(y_T)}}\hat{\omega}_c(\boldsymbol{y}_T;\omega)\end{aligned} \tag{8.1.28}$$

So (8.1.25) becomes:

$$\tilde{p}(\boldsymbol{x},\omega) = 2\pi\int_V \tilde{G}(\boldsymbol{y}|\boldsymbol{x};\omega)\tilde{\Omega}(\boldsymbol{y}_T;\omega)e^{i\omega y_1/\boldsymbol{U(y_T)}}d\boldsymbol{y} \tag{8.1.29}$$

We can then split the volume integral into y_1, and A_T (the area of the transverse coordinates):

$$\tilde{p}(\boldsymbol{x},\omega) = 2\pi\int_{A_T}\tilde{\Omega}(\boldsymbol{y}_T;\omega)\int_{y_1}\tilde{G}(x_1-y_1,\boldsymbol{y}_T|\boldsymbol{x}_T;\omega)e^{i\omega y_1/\boldsymbol{U(y_T)}}dy_1 d\boldsymbol{y}_T \tag{8.1.30}$$

Again, the y_1 integral is a convolution, however, since we are not taking its Fourier transform this time, we use the convolution theorem to write it in terms of the inverse Fourier transform of the Fourier transformed variables:

$$\tilde{p}(\boldsymbol{x},\omega) = 2\pi\int_{A_T}\tilde{\Omega}(\boldsymbol{y}_T;\omega)2\pi\int_{k_1}\bar{G}(\boldsymbol{y}_T|\boldsymbol{x}_T;k_1,\omega)\bar{H}(k_1)e^{ik_1x_1}dk_1 \tag{8.1.31}$$

where we define

$$\bar{G}(\boldsymbol{y}_T|\boldsymbol{x}_T;k_1,\omega) = \frac{1}{2\pi}\int_{-\infty}^{\infty}\tilde{G}(x_1-y_1,\boldsymbol{y}_T|\boldsymbol{x}_T;\omega)e^{-ik_1(x_1-y_1)}d(x_1-y_1) \tag{8.1.32}$$

and

$$\begin{aligned}\bar{H}(k_1) &= \frac{1}{2\pi}\int_{y_1}e^{i\omega y_1/U(\boldsymbol{y}_T)}e^{-ik_1y_1}dy_1 \\ &= \frac{1}{2\pi}\int_{-\infty}^{\infty}e^{-iy_1(k_1-\omega/U(\boldsymbol{y}_T))}dy_1 \\ &= \delta(k_1-\omega/U(\boldsymbol{y}_T))\end{aligned} \tag{8.1.33}$$

Therefore, (8.1.30) becomes:

$$\tilde{p}(\boldsymbol{x},\omega) = (2\pi)^2e^{ik_1x_1}\int_{A_T}\bar{G}(\boldsymbol{y}_T|\boldsymbol{x}_T;k_1,\omega)\tilde{\Omega}(\boldsymbol{y}_T;\omega)d\boldsymbol{y}_T \tag{8.1.34}$$

where $k_1 = \omega/U(\boldsymbol{y}_T)$. Similarly, we can take Fourier transforms in the spanwise direction, which using the convolution theorem gives:

$$\hat{p}(x_1,x_2;k_1,k_3,\omega) = (2\pi)^3e^{ik_1x_1}\int_{y_2}\hat{\Omega}(y_2;k_3,\omega)\hat{G}(y_2|x_2;k_1,k_3,\omega)dy_2 \tag{8.1.35}$$

where we define:

$$\hat{\Omega}(y_2; k_3, \omega) = \frac{1}{2\pi} \int_{-\infty}^{\infty} \tilde{\Omega}(\boldsymbol{y}_T; \omega) e^{-ik_3 y_3} dy_3 \tag{8.1.36}$$

and

$$\hat{G}(y_2|x_2; k_1, k_3, \omega) = \frac{1}{(2\pi)} \int_{-\infty}^{\infty} \bar{G}(\boldsymbol{y}_T|\boldsymbol{x}_T; k_1, \omega) e^{-ik_3(x_3 - y_3)} d(x_3 - y_3) \tag{8.1.37}$$

which is the solution to the reduced Rayleigh equation (derived in Appendix D.5)

$$L_R \hat{G}(y_2|x_2; k_1, k_3, \omega) = \frac{\delta(y_2 - x_2)}{(2\pi)^3} \tag{8.1.38}$$

where

$$L_R(y_2; k_1, k_3, \omega) = \frac{d}{dy_2}\Big[\frac{c^2}{(\omega - U(y_2)k_1)^2}\frac{d}{dy_2}\Big] + \Big[1 - \frac{(k_1^2 + k_3^2)c^2}{(\omega - U(y_2)k_1)^2}\Big] \tag{8.1.39}$$

8.1.3 Physical Boundary Conditions

Since we are dealing with linear acoustics, the pressure fluctuation can be split into two: a 'gust' ($p^{(0)}$) and a 'scattered' ($p^{(s)}$) component:

$$p(\boldsymbol{x}, t) = p^{(0)}(\boldsymbol{x}, t) + p^{(s)}(\boldsymbol{x}, t) \tag{8.1.40}$$

Likewise, the normal velocity can also be split:

$$v_\perp(\boldsymbol{x}, t) = v_\perp^{(0)}(\boldsymbol{x}, t) + v_\perp^{(s)}(\boldsymbol{x}, t) \tag{8.1.41}$$

Goldstein et al [60] showed that only the scattered component generates sound. Since $\tilde{\omega}_c = \tilde{\omega}_c(\tau - y_1/U, \boldsymbol{y}_T)$ depends on (y_1, τ) via convected time, $(\tau - y_1/U)$, the autocovariance of $\tilde{\omega_c}$ is independent of y_1. Therefore, if $p^{(\sigma)}(\boldsymbol{x}, t)$ (where $\sigma = 0, s$) satisfy different boundary conditions in x_1 then $G(\boldsymbol{y}, \tau|\boldsymbol{x}, t)$ also satisfy discontinuous boundary conditions in the streamwise direction, as does its 3D Fourier transform:

$$\hat{G}(y_2|x_2; k_1, k_3, \omega) = \hat{G}^{(0)}(y_2|x_2; k_1, k_3, \omega) + \hat{G}^{(s)}(y_2|x_2; k_1, k_3, \omega) \tag{8.1.42}$$

and using (8.1.38) we can say

$$L_R \hat{G}^{(0)}(y_2|x_2; k_1, k_3, \omega) = \frac{\delta(y_2 - x_2)}{(2\pi)^3} \tag{8.1.43}$$

$$L_R \hat{G}^{(s)}(y_2|x_2; k_1, k_3, \omega) = 0 \tag{8.1.44}$$

where the homogeneous boundary condition for the gust Green's functions is:

$$n_j \frac{\partial \hat{G}^{(0)}}{\partial x_j}\Big|_{y_2=0} = 0 \qquad -\infty < y_1 < \infty \tag{8.1.45}$$

which is valid on surfaces parallel to $U(\boldsymbol{y}_T) = constant$. The scattered Green's function satisfies discontinuous boundary conditions (given in [60]) which are linked to the physical boundary conditions:

1. Continuity of normal velocity through plate
2. Continuity of normal velocity through plate/downstream of plate
3. Change in pressure through $x_2 = 0$ downstream of the trailing edge is zero

The coordinates of the problem are shown in Figure 8.2. Mathematically, these boundary conditions are defined below.

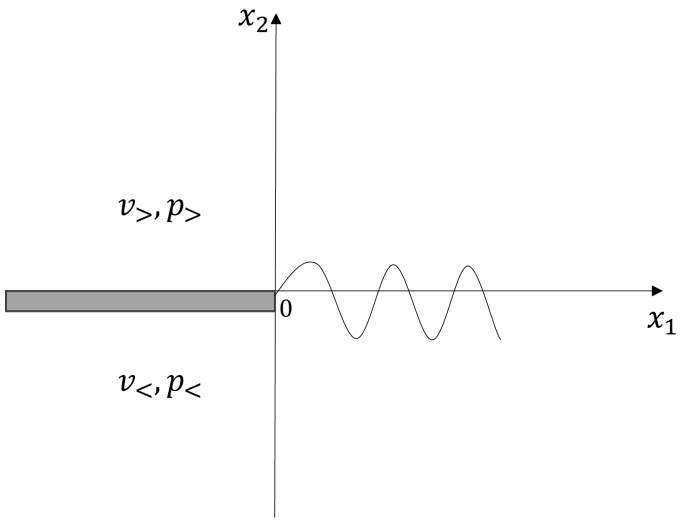

Figure 8.2: Plate boundary conditions

Condition 1

$$\int_{-\infty}^{\infty} e^{ik_1 x_1} v_>(0; k_1, k_3, \omega) dk_1 = 0 \qquad -\infty < x_1 < 0 \tag{8.1.46}$$

since

$$v_\perp(x_2; k_1, k_3, \omega) = \frac{-i}{(\omega - Uk_1)} \frac{1}{|\nabla U|} \frac{\partial U}{\partial x_2} \frac{d\hat{p}(x_2; k_1, k_3, \omega)}{dx_2} \tag{8.1.47}$$

and $\partial U/\partial x_2 = |\nabla U| sgn(dU/dx_2)$, and we have a monotonically increasing velocity (i.e. $sgn(dU/dx_2) = 1$), this reduces to

$$v_\perp(x_2; k_1, k_3, \omega) = \frac{-i}{(\omega - Uk_1)} \frac{d\hat{p}(x_2; k_1, k_3, \omega)}{dx_2} \tag{8.1.48}$$

now, we define $U(x_2 = 0) = U_>$ as the plate velocity, Goldstein et al (2013)[60] showed that the acoustic spectrum is independent of $U_>$, so we set it to zero, which results in:

$$v_\perp(x_2; k_1, k_3, \omega) = \frac{-i}{\omega} \frac{d\hat{p}(x_2; k_1, k_3, \omega)}{dx_2} \tag{8.1.49}$$

which gives us a condition for the pressure derivative on the plate:

$$\boxed{\int_{-\infty}^{\infty} e^{ik_1 x_1} \hat{p}'_>(0; k_1, k_3, \omega) dk_1 = 0 \qquad -\infty < x_1 < 0} \tag{8.1.50}$$

Condition 2

$$\int_{-\infty}^{\infty} e^{ik_1 x_1} \hat{p}'_>(0; k_1, k_3, \omega) dk_1 = \int_{-\infty}^{\infty} e^{ik_1 x_1} \hat{p}'_<(0; k_1, k_3, \omega) dk_1 \qquad -\infty < x_1 < \infty \tag{8.1.51}$$

Tells us

$$\int_{-\infty}^{\infty} e^{ik_1 x_1} \Big[\hat{p}'_>(0; k_1, k_3, \omega) dk_1 - \hat{p}'_<(0; k_1, k_3, \omega)\Big] dk_1 = 0 \qquad -\infty < x_1 < \infty \tag{8.1.52}$$

Therefore:

$$\boxed{\hat{p}'_>(0; k_1, k_3, \omega) = \hat{p}'_<(0; k_1, k_3, \omega) \qquad \forall x_1} \tag{8.1.53}$$

Condition 3

$$\underbrace{\bar{p}^0(x_1, 0; k_3, \omega) + \int_{-\infty}^{\infty} e^{ik_1 x_1} \hat{p}_>(0; k_1, k_3, \omega) dk_1}_{\text{pressure above plate}} = \underbrace{\int_{-\infty}^{\infty} e^{ik_1 x_1} \hat{p}_<(0; k_1, k_3, \omega) dk_1}_{\text{pressure below plate}} \tag{8.1.54}$$

for $0 < x_1 < \infty$. This can be rewritten as:

$$\boxed{\bar{p}^0(x_1, 0; k_3, \omega) + \int_{-\infty}^{\infty} e^{ik_1 x_1} \hat{p}'_>(0; k_1, k_3, \omega) \hat{p}_0(k_1, k_3, \omega) dk_1 = 0 \qquad 0 < x_1 < \infty} \tag{8.1.55}$$

where we define

$$\hat{p}_0(k_1, k_3, \omega) = \frac{\hat{p}_>(0; k_1, k_3, \omega)}{\hat{p}'_<(0; k_1, k_3, \omega)} - \frac{\hat{p}_<(0; k_1, k_3, \omega)}{\hat{p}'_<(0; k_1, k_3, \omega)} \tag{8.1.56}$$

These physical boundary conditions define a Wiener-Hopf problem, which Goldstein et al (2013)[60] showed could also be written with the Green's function being the dependent variable rather than pressure, and solved to give the acoustic spectrum. In 2019 [62] this formula was extended to curvilinear coordinates, which is what we need for the round jets considered in this thesis. The solution process is summarised in Figure 8.3.

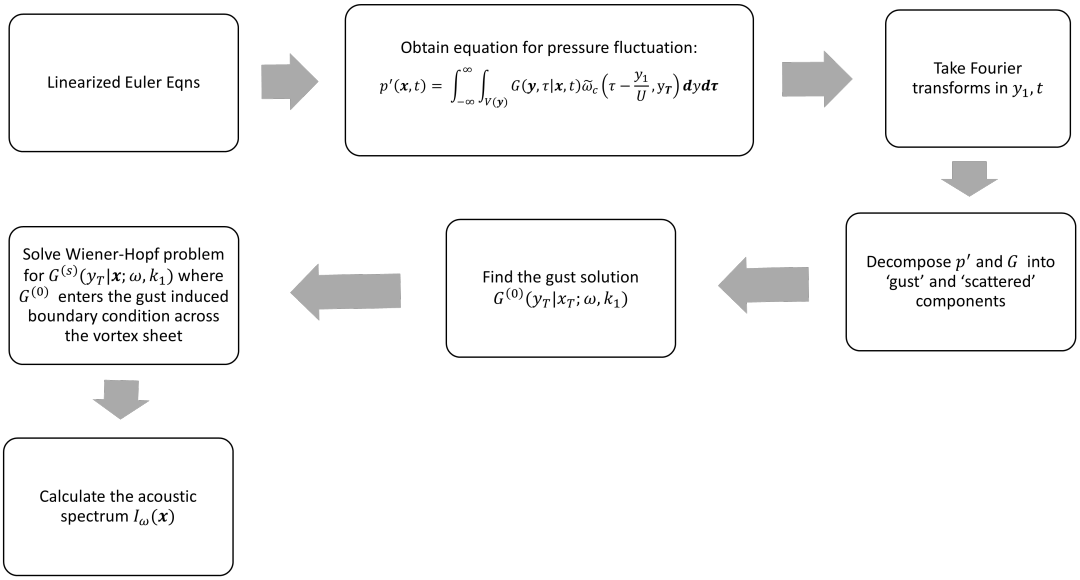

Figure 8.3: Flowchart summarising the RDT solution procedure

8.1.4 Acoustic Spectrum for Curvilinear Coordinates

Using asymptotic analysis to determine both $G^{(0)}(\boldsymbol{y},\tau|\boldsymbol{x},t)$ and $G^{(s)}(\boldsymbol{y},\tau|\boldsymbol{x},t)$ Goldstein et al (2019)[62] obtained the following formula for the acoustic spectrum valid at low frequencies:

$$I(\boldsymbol{x};\omega) = \left(\frac{k_\infty}{4\pi|\bar{\boldsymbol{x}}|}\right)^2 \int_{-\infty}^{0}\int_{-\infty}^{0} D(u,\tilde{u};\theta)\bar{S}(u,\tilde{u};k_3^*,\omega)\,du\,d\tilde{u}, \tag{8.1.57}$$

for an arbitrary mean flow which has level curves that are relatively concentric inasmuch as $U(y_2,y_3) = U(u(y_2,y_3))$ where u is the real part of the conformal mapping given by (Eq. 5.1) in Goldstein et al[62]. $D(u,\tilde{u};\theta)$ is the round jet directivity factor determined by application of the Wiener-Hopf technique (i.e.

Eq. 13 in Afsar *et al* (2017)[100] written in $(u, \tilde{u})$ co-ordinates where $\tilde{u}$ is another location along the level curve $u = const$):

$$D(u,\tilde{u};\theta) = \frac{(\beta - \cos\theta)[M(u)M(\tilde{u})]^{3/2}}{\sqrt{[1-\beta M(\tilde{u})][1-\beta M(u)][1-M(\tilde{u})\cos\theta][1-M(u)\cos\theta]}} \tag{8.1.58}$$

$$\bar{S}(u,\tilde{u};k_3^*,\omega) = \int_{-\infty}^{0}\int_{-\infty}^{0} S(u,\tilde{u}|v,\tilde{v};k_3^*,\omega)\left|\frac{dz}{dW}\right|^2\left|\frac{d\tilde{z}}{d\tilde{W}}\right|^2 dv\, d\tilde{v}, \tag{8.1.59}$$

where $v(y_2, y_3) = const.$ are the orthogonal curves to $u(y_2, y_3) = const.$ defined by the Cauchy-Riemann equations and $d\tilde{z}/d\tilde{W}$ is the appropriate inverse Jacobian function between the mapping $z(y_2, y_3) \to W(u, v))$ (details in App. A of [62]), which gives

$$\left|\frac{dz}{dW}\right|^2 = \frac{4}{(e^{-u} - 2\cos v + e^{u})^2} \tag{8.1.60}$$

By considering the upstream asymptote of the Fourier transform of the evolution equation for the convected quantity, $\tilde{\omega}_c$, Goldstein et al [62] also showed that the function $S(u, \tilde{u}|v, \tilde{v}; k_3^*, \omega)$ is defined by

$$\begin{aligned} S(u,\tilde{u};v,\tilde{v}) =& l_2^4 A(u,\tilde{u})(\rho_\infty c_\infty^2)^2\left[\frac{dU/du}{U^2(u)}\frac{dU/d\tilde{u}}{U^2(\tilde{u})}|\nabla u|\left|\tilde{\nabla}\tilde{u}\right|\omega^2\right] \\ &\times \frac{\tau_0 f}{\pi\sqrt{1+\tilde{\omega}^2}}K_1(f\sqrt{1+\tilde{\omega}^2}). \end{aligned} \tag{8.1.61}$$

Where the amplitude function $A(u, \tilde{u})$ was taken as

$$A(u,\tilde{u}) = A_0\sqrt{(u\tilde{u})^{\mu}(dU/du)(dU/d\tilde{u})\left|dW/dz\right|_{v=0}\left|d\tilde{W}/d\tilde{z}\right|_{\tilde{v}=0}} \tag{8.1.62}$$

and the jet mean flow near the plate by the function: $U(u) = U_d(1 - e^{-\kappa u^2 - \kappa_1 u^4})$.

This shows, among other things, that $S(u, \tilde{u}|v, \tilde{v}; k_3^*, \omega)$ is directly proportional to the Fourier transform of the streamwise-independent transverse velocity correlation function, R_{22}, for which considerable turbulence data exists (see Afsar *et al.* 2017)[100]. However, their turbulence model for R_{22} neglected to include a parameter which allows for negative correlation, which does occur within the experimental data. Our work therefore involves *more faithful modelling of* R_{22}.

Note that $\tilde{\omega}$ is the $O(1)$ scaled frequency, defined by $\tilde{\omega} = \omega\tau_0 = O(1)$ and the length scales (l_2, l_3) enter the transverse spectral decay function, $f = |\eta_2/l_2 + \eta_3/l_3|$.

There are also several parameters within this model (A_0, κ, κ_1) in the meanflow/ amplitude models and (l_2, l_3, τ_0) which are related to the turbulence structure of R_{22}. Ideally these parameters are found by comparison to experimental data as was done in the rectangular jet problem by Goldstein *et al.* (GLA17, p.499)[61]. However, in the literature these parameters were mostly chosen through hand-tuning which means it is likely that the optimum results were not found.

Additionally, since the numerical computation of (8.1.57) requires calculation of (8.1.59) at each point in the $(u, \tilde{u})$-domain and requires a call to a Bessel function library to evaluate $K_1(...)$, the acoustic spectrum calculation is potentially computationally expensive.

Therefore, the remainder of this chapter will discuss several extensions of this work:

1. Extension of the R_{22} model to have a more faithful representation of the turbulence;
2. Introduction of GPU parallelisation for the acoustic model to speed up the calculations;
3. Introduction of numerical optimisation to select model parameters based on comparison with experiment without the need of hand-tuning; and
4. Analysis of optimised parameters at off-design conditions.

8.2 Extension of the R_{22} Model

To better capture the anti-(negative) correlation in the structure of R_{22} we investigate adding additional terms to the model. R_{22} enters the source term (8.1.61) via its Fourier transform (Eq. 4.22 in [62]):

$$\frac{1}{2\pi}\int_{-\infty}^{\infty} e^{i\omega\hat{\tau}} R_{22}(\hat{\tau}, \hat{\eta}_2, \hat{\eta}_3) d\hat{\tau} \tag{8.2.1}$$

where $\hat{\tau} = \tilde{\tau} - [\tilde{y}_1/U(\tilde{u}) - y_1/U(u)]$, $\hat{\eta}_2 = \eta_2/l_2$, $\hat{\eta}_3 = \eta_3/l_3$ and

$$R_{22}(\hat{\tau}, \hat{\eta}_2, \hat{\eta}_3) = e^{-X(\hat{\tau}, \hat{\eta}_2, \hat{\eta}_3)} \tag{8.2.2}$$

and $X(\hat{\tau}, \hat{\eta}_2, \hat{\eta}_3) = \sqrt{[f(\hat{\eta}_2, \hat{\eta}_3)]^2 + \hat{\tau}^2/\tau_0^2}$. We extend this (amplitude normalised) function for R_{22} as a power series to include more terms:

$$R_{22}(\hat{\tau},\hat{\eta}_2,\hat{\eta}_3)=\Big[1+a_1\hat{\tau}\frac{\partial}{\partial\hat{\tau}}+a_2\hat{\tau}^2\frac{\partial^2}{\partial\hat{\tau}^2}+a_3\hat{\tau}^3\frac{\partial^3}{\partial\hat{\tau}^3}+...\Big]e^{-X(\hat{\tau},\hat{\eta}_2,\hat{\eta}_3)} \tag{8.2.3}$$

which gives the Fourier transform

$$\frac{1}{2\pi}\int_{-\infty}^{\infty}e^{i\omega\hat{\tau}}\Big[1+a_1\hat{\tau}\frac{\partial}{\partial\hat{\tau}}+a_2\hat{\tau}^2\frac{\partial^2}{\partial\hat{\tau}^2}+a_3\hat{\tau}^3\frac{\partial^3}{\partial\hat{\tau}^3}+...\Big]e^{-X(\hat{\tau},\hat{\eta}_2,\hat{\eta}_3)}d\hat{\tau} \tag{8.2.4}$$

The first additional (a_1) term enables the anti-correlation, so if we only consider the first two terms of the power series we can show that the term $\tau_0 f K_1(f\sqrt{1+\tilde{\omega}^2})/(\pi\sqrt{1+\tilde{\omega}^2})$ in (8.1.61) is replaced with:

$$\begin{aligned}&(1-a_1)\frac{\tau_0 f}{\pi\sqrt{1+\tilde{\omega}^2}}K_1(f\sqrt{1+\tilde{\omega}^2})+\\&\frac{a_1\tau_0 f^2\tilde{\omega}^2}{\pi(1+\tilde{\omega}^2)}\Big[\frac{1}{2}(K_0(f\sqrt{1+\tilde{\omega}^2})+K_2(f\sqrt{1+\tilde{\omega}^2}))+\frac{K_1(f\sqrt{1+\tilde{\omega}^2})}{f\sqrt{1+\tilde{\omega}^2}}\Big]\end{aligned} \tag{8.2.5}$$

(see Appendix D.6 for details.)

This simple extension of the old model for R_{22} is compared with experimental data in Figure 8.4(a) where we can see it has an anti-correlation region. However, Bridges' measurements show that the auto-correlation of R_{22} will possess finite amplitude algebraic oscillations–that is, they appear not to be a small perturbation of the main exponential decay, however, it is unclear as to whether these oscillations are related to physics. Therefore, we attempted to capture this feature of the turbulence structure by developing a set of models of increasing algebraic complexity in terms of the combination of suitably weighted trigonometric/transcendental functions multiplied by an appropriate exponentially decaying function of time delay. We look at three models (A, B, C) which were found using a linear regression code, these models do not have an analytical Fourier transform so the Fourier transforms must be calculated numerically. This increases the complexity of the acoustic model and also increases the computational time, which is summarised in Table. 8.1. To reduce the time required, we investigated parallel computing using a GPU. The models for R_{22} are:

Model A

$$R_{22}=(1-a_1+a_2\hat{\tau}^2-a_3\sin(b\hat{\tau}))e^{-\frac{\hat{\tau}^2}{c}} \tag{8.2.6}$$

Model B

$$R_{22} = (1 - a_1 + a_2\hat{\tau}^2 - a_3 \sin(b\hat{\tau}))e^{-\frac{\hat{\tau}^2}{c}} + (a_4 \cos(b_2\hat{\tau}))e^{-\frac{\hat{\tau}^2}{c_2}} \tag{8.2.7}$$

Model C

$$R_{22} = (1 - a_1 + a_2\hat{\tau}^2 - a_3 \sin(b\hat{\tau}))e^{-\frac{\hat{\tau}^2}{c}} + (a_4 \cos(b_2\hat{\tau}))e^{-\frac{\hat{\tau}^2}{c_2}} + (a_5 \cos(b_3\hat{\tau}))e^{-\frac{\hat{\tau}^2}{c_3}} \tag{8.2.8}$$

The model coefficients in (8.2.6–8.2.8) were found using the optimisation routine reported in Afsar *et al.* (2019)[101] and are:

Model A : $a_1 = 12.6340, a_2 = 6.2913, a_3 = 5.2367, b = -1.5782, c = 2.0305$

Model B : $a_1 = 12.5603, a_2 = 6.2155, a_3 = 5.2429, a_4 = 0.0355, b = -1.5679,$
$b_2 = -10.4573, c = 2.0530, c_2 = 50.0$

Model C : $a_1 = 1.7854, a_2 = 0.8735, a_3 = -0.1984, a_4 = -0.2196, a_5 = 0.2030,$
$b = -8.5513, b_2 = -0.4033, b_3 = 6.7250, c = 3.1649, c_2 = 18.2664,$
$c_3 = 1.4039$

Time (30 St)	Model 1	Model A	Model B	Model C
Each Case	10 mins	35 mins	3.2 hours	4.2 hours
9 Cases	1.5 hours	5.25 hours	28.8 hours	38.8 hours

Table 8.1: Compare acoustic model computational time using different R_{22} models growing in complexity for 1 case and 9 cases (3 Mach numbers & 3 polar angles)

Figure 8.5 compares the acoustic predictions using model 1 with the predictions from Goldstein et al [62]. We can see that the low frequencies are better predicted for $Ma = 0.9$, and the high frequencies are better predicted at $Ma = 0.5$ using this extended model.

8.2.1 Comparison with our LES

Figure 8.6 compares the experimental R_{22} with the R_{22} calculated from our LES results for the four jets analysed in the previous chapters. We see that the

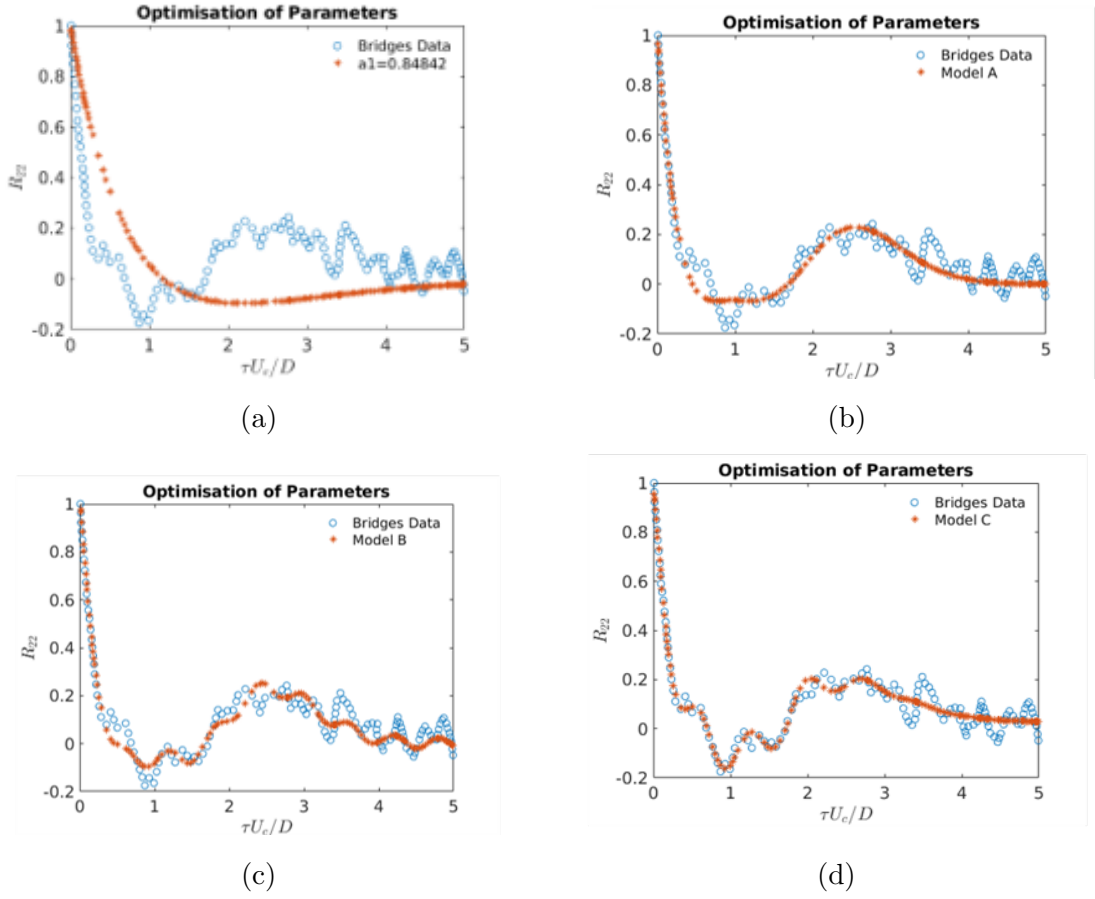

(a) (b)

(c) (d)

Figure 8.4: Models for R_{22} (a) Model 1 (b) Model A (c) Model B (d) Model C

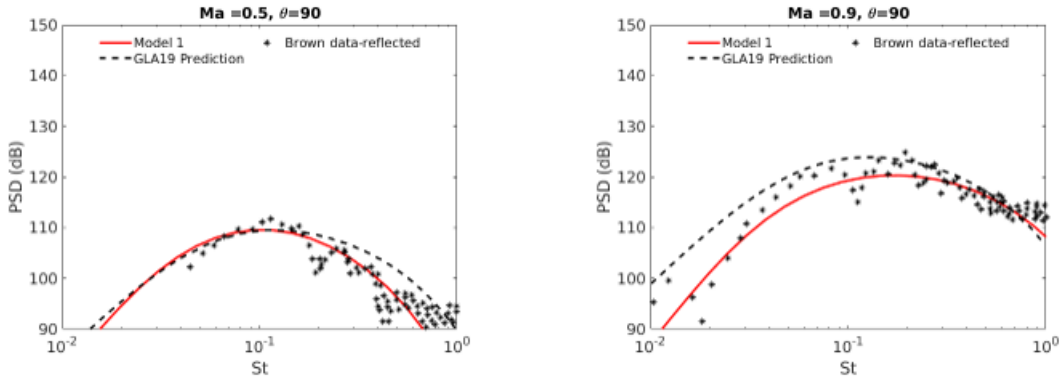

(a) (b)

Figure 8.5: Acoustic predictions using model 1 R_{22} compared with Goldstein et al [62] for (a) $Ma = 0.5$ (b) $Ma = 0.9$

initial decorrelation is captured with the LES for all four jets, but they also do not capture the oscillations, this implies that the oscillations are not related to physics. Therefore model 1 will also give a good representation of the turbulence from the LES.

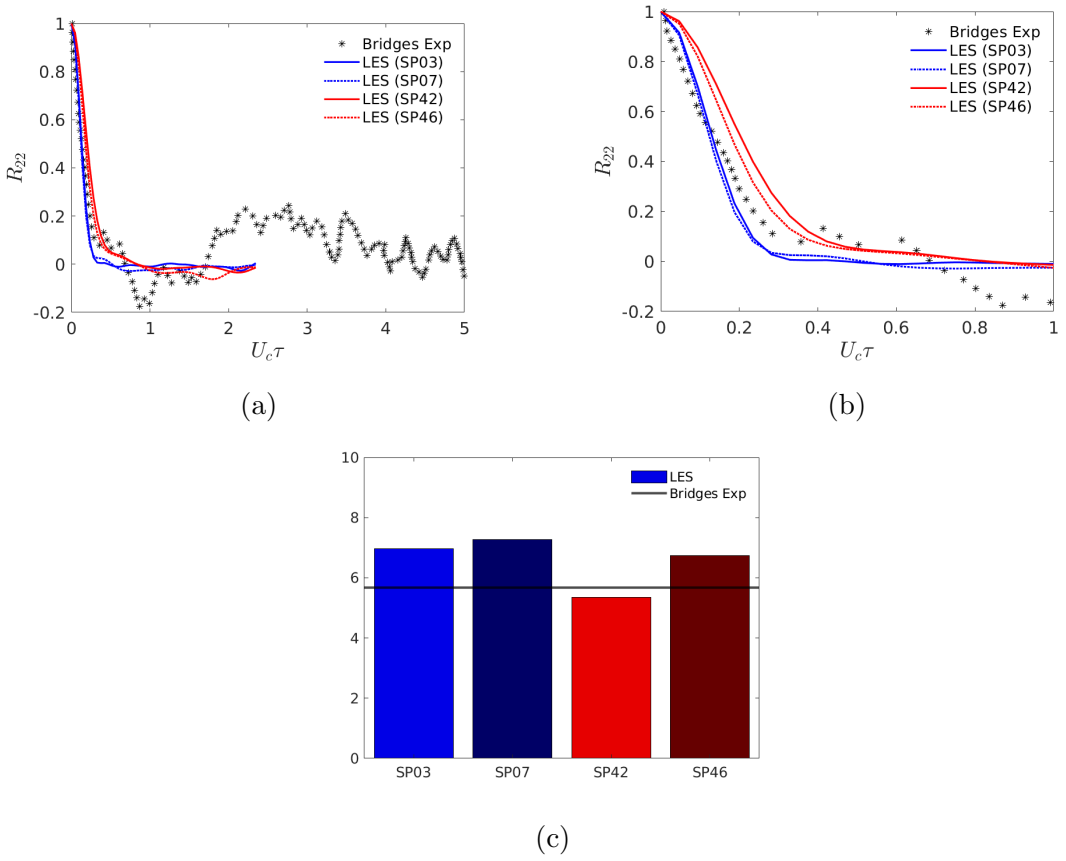

Figure 8.6: Comparison of Bridges R_{22} with our LES cases (at $r = 0.5, y_1$ =start of potential core) for (a) all data (b) initial decorrelation region, and (c) comparison of the decorrelation time constant for all cases

8.3 Parallel Computing

As mentioned above, the acoustic problem reduces to a four-dimensional integral with an integrand that (for model 1) includes several Bessel functions. To evaluate these Bessel functions the AMOS library is used, however, this library is outdated, written in Fortran 77 and takes a long time to run. Profiling led to the discovery that roughly 97% of computation time was spent within the AMOS library.

Therefore we looked to parallelise the code. This was done by using OpenACC directives to enable compilation for either a multi-core CPU or offload to a GPU.

8.3.1 Theory

Central Processing Unit: CPU

Figure 8.7 shows a basic description of the CPU. The orange squares represent Arithmetic Logic Units (ALUs) which carry out the arithmetic and logic operations, of which there are normally 4 in each core. The green square represents the control unit, of which there is one per core. The control unit sends instructions to the ALU as well as moving data from registers to ALU's and caches/main memory. Registers contain very small amounts of data that are to be operated on (input register) or are an output of an operation (output register). The number and size of caches depends on the individual CPU. However, most CPU's today have at least 2 levels of cache and most have 3 (some processors may even have 4 levels). Here, cache levels 1,2 and 3 are shown. The size of cache increases in each level, and only L1 (and normally L2) are contained on the physical core. The threads will look for data first in L1, then L2, then L3 and finally the system memory if the data is still not found. The amount of time the thread spends searching for data/instruction increases as the level of cache increases, since they become larger. Typically there is one thread per core, unless the processor uses hyper-threading (a technique in which a single core uses logic to act like two cores) in which case there can be two threads per core. Cores within a CPU share the system memory (DRAM), which means that it is important to define certain variables as private otherwise multiple threads can be trying to access and change the same variable, which will give wrong results.

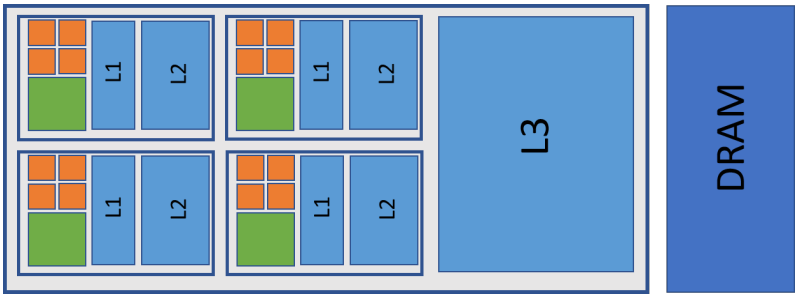

Figure 8.7: Basic Architecture of a 4 core CPU

Graphical Processing Unit: GPU

The GPU market is dominated by NVIDIA and AMD, however, since we only use NVIDIA the descriptions that follow refer to NVIDIA components (they may be named differently for AMD). In this work we use the Tesla K40c. A GPU has two main components: streaming multi-processors (SM's), which are like the cores of a CPU; there can be more than one, and the device memory (like RAM for the CPU). Figure 8.8 shows the basic architecture of a GPU, it should be noted that this shows Kepler architecture (which is used on the Tesla K40c) with 192 CUDA cores in each streaming multi-processor that can run single precision operations, and 64 cores that can run double precision operations. Since the Tesla K40c has 15 SM's it has 960 double precision cores.

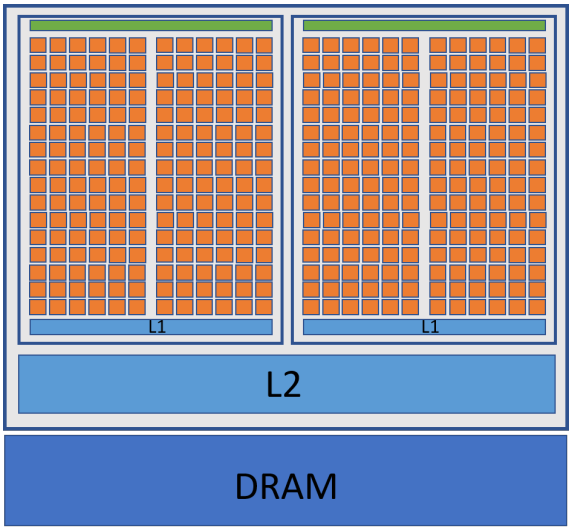

Figure 8.8: Basic Architecture of a GPU with 2 streaming multi-processors

Since GPU's have hundreds of cores, their potential speed up is much greater than that of a CPU. However, they typically have much smaller memory which is not always ideal. Additionally, a program cannot be run on a GPU alone and since CPU and GPU normally have their own independent memory, it is necessary to transfer data to and from the GPU. This limits speed up and needs to be minimised to achieve maximum results. It may be faster to run a program on the CPU over multiple cores than transferring a lot of data to and from the GPU.

A CPU aims to minimise latency while accessing its memory which is accomplished through the use of several data caches to be able to find the most

used data quickly. On the other hand, a GPU aims to hide latency through the use of many threads. This is illustrated in Figure 8.9, which is adapted from [102].

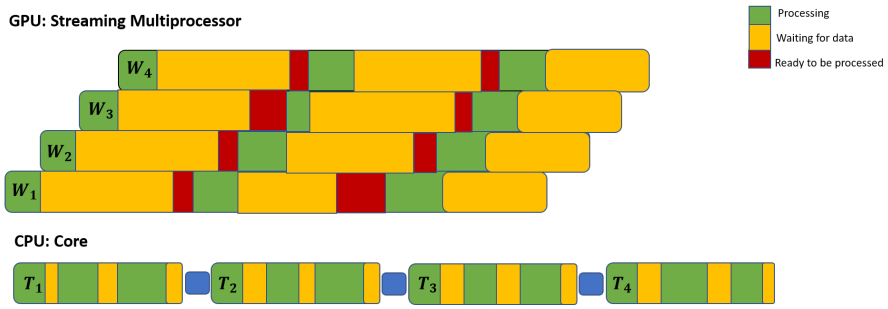

Figure 8.9: CPU: Low Latency, GPU: High Throughput

Increasing the number of threads in a CPU improves performance until it reaches a point where threads cannot access the caches concurrently. At this point, latency increases as threads need to wait until they can get access to data. On the other hand, when the number of threads in a process is very large the program uses thread level parallelism which hides this latency by running other threads while some are waiting to access memory. Figure 8.10 shows how the number of threads affects performance, and highlights the multi-core region (that used by multi-core CPU) and the multi-thread region (that used by GPU) [103].

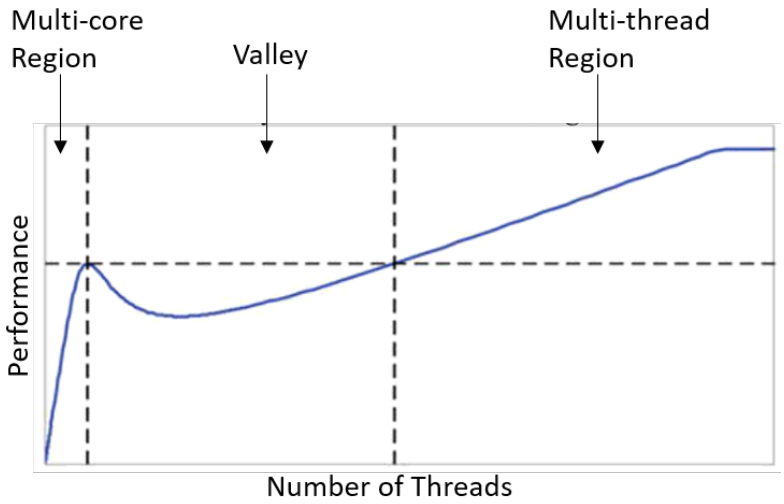

Figure 8.10: Performance vs. number of threads

OpenMP

OpenMP enables parallelisation of code via multiple cores of a CPU, it has recently added the capability of offloading to the GPU, however we use OpenACC for this since it was designed for that specific purpose and has been around longer.

OpenMP involves the addition of directives within the code to create parallel regions, this means that the entire program need not be parallelised, we can focus on the areas which slow down the code and would benefit most. Therefore, we create a parallel region on the outer loop which has the maximum number of iterations. So the nested integrals will be calculated as indicated in Figure 8.11. We use a 4-core machine which, theoretically, should result in a speed up of four.

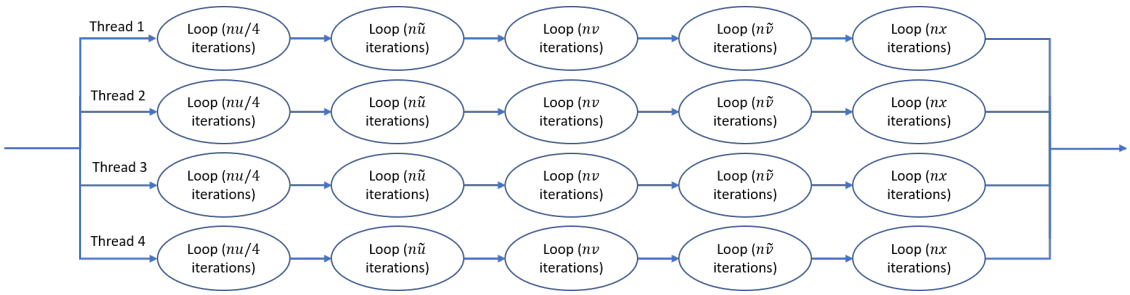

Figure 8.11: Using OpenMP to parallelise outer integral over 4 cores

OpenACC

OpenACC also enables parallelism through the use of directives. and can use kernels or parallel regions. Using a kernel means that the compiler will decide which loops can be parallelised or not, whereas using a parallel region means that it will be parallelised and it is up to the programmer to ensure that there is no data dependencies which could result in wrong results. Our program is too complicated to use kernels, therefore we use a parallel region.

The GPU and CPU do not have shared memory, this means that data must be explicitly copied between them. The amount of data to be copied should ideally be reduced to save time. This is done by first ensuring that data which is not loop dependent is copied to the device prior to entering the parallel region. Memory space can also be created on the device for variables which are not yet defined, and updated on each iteration. Figure 8.12 shows the basic program architecture where we parallelise on the outer loop.

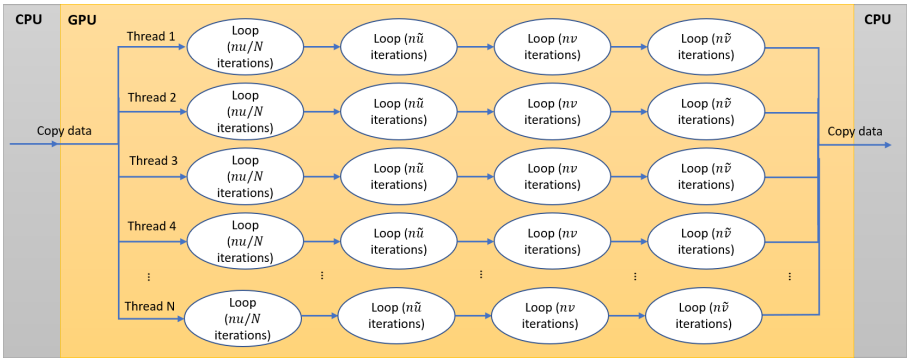

Figure 8.12: Basic program architecture parallelising the outer loop on the GPU

8.3.2 Speed up

We discovered that using model 1 for R_{22} did not require many iterations to achieve convergence in the integrals, therefore, the GPU was not fully utilised. Figure 8.13 shows that so few iterations were needed for convergence to 0dp that offloading to the GPU actually slows down the code since the initialisation of the GPU takes longer than the code takes to run. It also shows that even for 2dp convergence, speed up is low due to number of iterations not fully utilising the GPU and the complexity of the code meaning each iteration does not take long to compute.

Model		Spatial Convergence					Time (s)			Speed Up
							Serial		GPU	
		nu	$n\tilde{u}$	nv	$n\tilde{v}$	TOTAL	1 St	30 St	30 St	30 St
Model 1 (a1)	0dp	50	10	10	10	50,000	0.156	4.481	14.342	0.3
	1dp	1000	20	20	10	4,000,000	10.474	313.11	37.808	8.3
	2dp	1000	20	20	20	8,000,000	19.690	593.93	71.971	8.3

Figure 8.13: Model 1: speed up for different levels of convergence. $(nu, n\tilde{u}, nv, n\tilde{v})$ are the number of iterations in loops $(u, \tilde{u}, v, \tilde{v})$. Total refers to the total number of iterations across all loops.

However, since Models A-C require an additional loop through the numerical Fourier transform, this obviously increases the total number of iterations required in the model. Therefore, these models will benefit more from using GPU parallelisation, and indeed it is shown in Figure 8.14 that the using the

GPU achieves a speed up of 30 times.

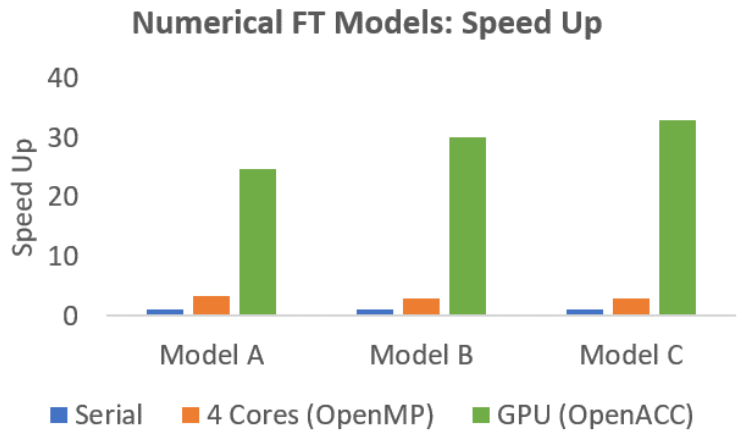

Figure 8.14: Speed Up for models including a numerical Fourier transform

However, this is still quite low since the GPU is not fully utilised. If we increase the number of outer iterations we can get a better speed up, as indicated in Figure 8.15. Speed up doubles until it reaches 4000 iterations at which point the GPU is saturated. Beyond this, speed up still increases but at a slower rate until it reaches the maximum (for the Tesla K40c) of 130.

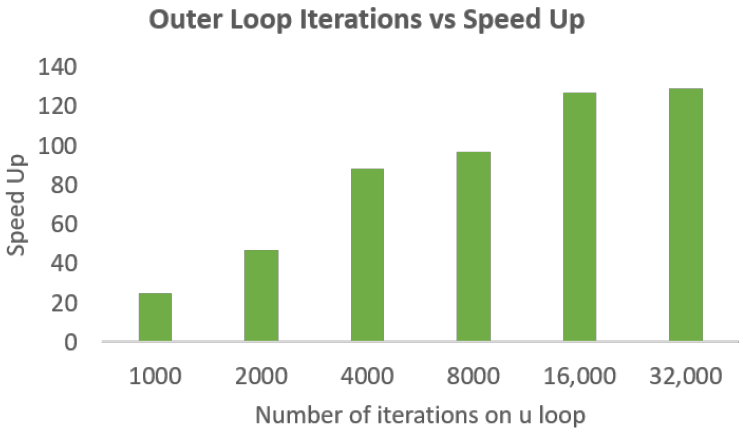

Figure 8.15: Model A: Increasing the number of iterations in the outer loop

The acoustic predictions using model 1 for R_{22} were good, and since we assume that the oscillations present in Bridges experimental data for R_{22} are not physical, model 1 is also a good representation of the turbulence. Therefore,

since convergence to 0dp is fine for the acoustic spectrum, we do not use the GPU for the remaining calculations in this section.

8.4 Optimisation of Parameters for a Fixed Plate Location

All acoustic models are formulated with arbitrary 'tuning' parameters to quantify the degree of spatial and temporal decorrelation of the turbulence, as well as the permanence of a finite anti-correlation region in spatial and temporal separation [98]. Previous modelling approaches, however, tuned these scales by hand to obtain good agreement with the acoustic data.

In this section we show that this form of empiricism can be avoided entirely by using an appropriate numerical optimisation routine to determine the parameters for an objective function that seeks to minimise the difference between the functional form of the turbulence model and turbulence data as well as minimising the difference between acoustic predictions and acoustic data.

A (single-objective) optimisation problem can be described in terms of minimising the objective function $J(\boldsymbol{x}, \boldsymbol{\psi})$, where $x_i (i = 1, n)$ are the n design variables which are modified to find the optimum, and $\boldsymbol{\psi}$ are the state parameters which describe the system [104]. The objective function may also be subject to (in general) a total (m, p) of (inequality/equality) constraints that take the form:

$$\begin{aligned} g_j(\boldsymbol{x}) &\leq 0 \qquad j = 1, m \\ h_k(\boldsymbol{x}) &= 0 \qquad k = 1, p, \end{aligned} \tag{8.4.1}$$

Additionally, the design variables may be bounded (known as side constraints):

$$x_{i,\mathrm{LOWER}} \leq x_i \leq x_{i,\mathrm{UPPER}} \qquad i = 1, n \tag{8.4.2}$$

(An optimisation problem is considered unconstrained if the only constraints are the design variable bounds.) Optimisation algorithms can find multiple solutions to this problem which are known as local optimums. Therefore, optimisation algorithms can be split into two categories: local optimisation methods (which find the local minimum for the starting conditions) and global optimisation methods (which aim to find the global minimum of the search space). Figure 8.16 shows the family of optimisation techniques.

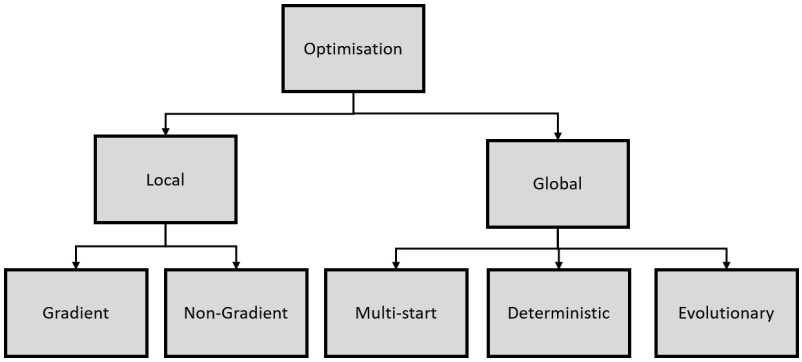

Figure 8.16: Family of optimisation techniques

The majority of local methods use gradient information to find the optimum. They do this through a 2 step process, mainly finding the search direction through the gradient information and finding the optimum step size through a one-dimensional search. There are several methods to do this [105, 106, 107, 108]. A valid search direction is one which improves the objective function and does not violate constraints. Different local methods use different algorithms to find the search direction and step size .

Figure 8.17 demonstrates an example of a gradient method, the algorithm will first find a search direction which improves the value of the objective function and then calculates the optimum step size. On each iteration of the optimiser the solution moves closer to the local optimum.

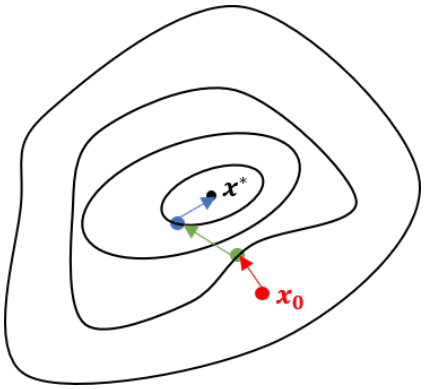

Figure 8.17: Example of a gradient method in two dimensions. Step 1: Find search direction which improves objective function. Step 2: Find optimum step size

The Karush-Kuhn-Tucker (KKT) conditions are used to determine whether a local optimum has been found [109]. These are:

- The optimum design point $\boldsymbol{x}^*$ must lie within the bounds and not violate conditions.

- The gradient of the Lagrangian must vanish at the design point i.e.

$$\nabla f(\boldsymbol{x}^*) + \sum_{j=1}^{m} \lambda_j \nabla g_j(\boldsymbol{x}^*) + \sum_{k=1}^{p} \mu_k \nabla h_k(\boldsymbol{x}^*) = \mathbf{0}$$

  where $\lambda_j \geq 0$ and μ_k are unrestricted in sign.

- Each inequality constraint has $\lambda_j g_j(\boldsymbol{x}) = 0 \quad j = 1, m$

If the problem has multiple local minima, the gradient methods described above will converge to the closest minimum which will not necessarily be the global. Each minimum has a basin of attraction, where a design point initialised within the basin converges to that local minimum. Hence, local optimisation strongly depends on the location of the initial design point. Global optimisation methods aim to find the global optimum, however, it should be noted that it cannot be guaranteed that the global optimum will be found, only that it would be if the algorithm could run indefinitely. Global optimisation can be split into three types of algorithm: multi-start algorithms, evolutionary algorithms and deterministic algorithms. Multi-start algorithms perform local optimisations at different starting locations, and choose the best local optimum to be the global optimum. Evolutionary algorithms are stochastic and heuristic, they advance a population of design parameters through the search space to find the global optimum. Deterministic algorithms typically require manipulation of the objective function and are designed to solve specific classes of problem[109], an overview of these is described in [110], and will not be further discussed here.

Optimisation methods have been used for this kind of problem in aeroacoustics before, for example the Multipoint Approximation Method (MAM) [111, 112, 113]. This method was designed for computationally expensive and noisy objective functions, so it uses trust regions and a series of approximations to the objective function. It is similar to the Multi-start algorithm in that it uses multiple starting locations, however it differs by approximating the objective function. In our work, the objective function is not computationally expensive, therefore we investigate the Multi-start method instead.

This section reviews the various types of optimisation that can be used for problems of this type paying particular attention to evolutionary algorithms.

Popular evolutionary algorithms include the Genetic Algorithm (GA) [114] which was inspired by Darwin's principle of survival of the fittest, particle swarm optimisation (PSO) [115] which is based on a social model and differential evolution (DE) [116].

Specifically, we discuss the advantages and disadvantages of three methods (the non-evolutionary Multi-start [117, 118, 119] , and the evolutionary algorithms: particle swarm optimisation (PSO) [115] and multi-population adaptive inflationary differential evolution algorithm (MP-AIDEA)[96] which is an extension to the original differential evolution algorithm) for a problem of this type and the results that are obtained for the parameters under different objective functions for the turbulence and/or final acoustic predictions (i.e. when comparison is made to turbulence and/or acoustic data).

8.4.1 Defining the Objective Function

We use model 1 for R_{22} which was summarised in previous sections and when the auto-correlation ($\boldsymbol{\eta} = 0$) is:

$$R_{22}(\tau) \sim (1 - a_1\tau)e^{-\tau}, \tag{8.4.3}$$

where τ is the time-delay between the two space-time points being correlated.

The objective functions are then defined as the mean squared error between the acoustic/turbulence models (8.1.57 & 8.4.3) and the relevant experimental data[57][74], as described in (8.4.4).

$$\begin{aligned} J_A(\boldsymbol{x}, \boldsymbol{\psi}) &= \frac{1}{N_A} \sum_{i=1}^{N_A} (I(\boldsymbol{x}, \omega_i, \boldsymbol{\psi}) - E_A(\boldsymbol{x}, \omega_i, \boldsymbol{\psi}))^2 \\ J_R(\boldsymbol{x}, \boldsymbol{\psi}) &= \frac{1}{N_R} \sum_{i=1}^{N_R} (R_{22}(\boldsymbol{x}, \tau_i, \boldsymbol{\psi}) - E_R(\boldsymbol{x}, \tau_i, \boldsymbol{\psi}))^2, \end{aligned} \tag{8.4.4}$$

where: N_A, N_R is the number of experimental data points we are optimising against for acoustics and R_{22} respectively, $I(\boldsymbol{x}, \omega_i, \boldsymbol{\psi})$ is the acoustic spectrum result using the model for frequency ω_i, and $E_A(\boldsymbol{x}, \omega_i, \boldsymbol{\psi})$ is the experimental data for frequency ω_i. Likewise $R_{22}(\boldsymbol{x}, \tau_i, \boldsymbol{\psi})$ is the result using our turbulence model at time τ_i, and E_R is the corresponding experimental data.

The state parameters ($\boldsymbol{\psi}$) are the minimum set of parameters which describe the system and how it responds to input [104]. Our problem can be thought of

as an 'input/output system' where an input turbulence spectrum interacts with the streamwise discontinuity at the trailing-edge and produces noise. The sound radiation will depend on the acoustic Mach number of the jet (Ma), the location where the noise measurements take place (far field angle, θ, measured with respect to the jet axis and azimuthal angle, ϕ). On the other hand the turbulence correlation function, R_{22}, is independent of these parameters, and instead depends on the location where the turbulence is measured $(y/D, r/D)$. Where we define y/D to be the streamwise location from the nozzle exit normalised by the nozzle diameter and r/D to be the radial location from the jet centerline also normalised by the nozzle diameter. The experimental set-up can be found in several papers [57, 61, 62].

The $O(1)$ parameters (a_1, l_2, l_3, τ_0) in the model are selected in order to find the optimum acoustic spectrum predictions across acoustic Mach number (Ma) and far-field angle θ, whilst maintaining a physically admissible turbulence structure. In the following sections we discuss the different optimisation methods that can be used to achieve this.

8.4.2 Evolutionary versus Non-evolutionary Optimisation Algorithms

The non-evolutionary Multi-start method is the most straightforward global optimisation routine. It follows on from local optimisation in that it simply performs a local optimisation algorithm at several different starting points within the design space[117, 118, 119]. The local optima can then be compared to find the global optimum. As the number of starting points increase, the probability of finding the global optimum also increase. Often, a Design of Experiments (DOE) is performed prior to multi-start to initialise design points within known basins.

Evolutionary algorithms are specifically designed to work on black box problems, i.e. they do not need direct access to the inner workings of the objective function nor do they need gradient information. Consequently, they can be used for non-smooth functions and it is not required that the programmer knows anything about the structure of the objective function. Evolutionary algorithms are known to be robust and have a good chance of finding the global optimum since they advance a fixed population of design variables through the

search space. However, they are computationally expensive and require the tuning of parameters to solve each problem[109]. There are several types of evolutionary algorithm, three of the most popular are the Genetic Algorithm (GA), Particle Swarm optimisation (PSO) and Differential Evolution (DE).

Particle Swarm optimisation (PSO)[115] was developed from a social model. Each particle utilises not only its own past experience to find an optimum but also that of the group at large. It involves initialising the population and a velocity vector for each particle. The velocity vector is then updated by including information from the particles past and from the group. A basic description of this method is shown in Figure 8.18.

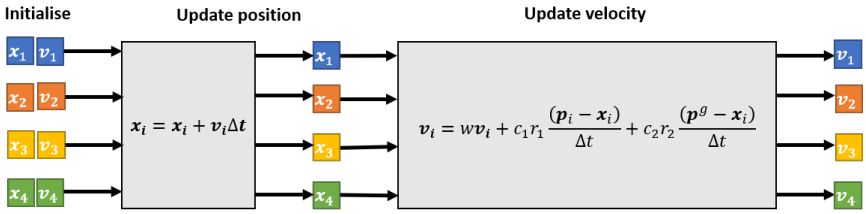

Figure 8.18: Example of particle swarm optimisation for a population of 4 vectors

The time step, $\Delta t = 1$ is typically used [109]. $\boldsymbol{p}_i$ is the best location found so far by particle i and $\boldsymbol{p}^g$ is the best location found so far by the group.There are three parameters which need to be tuned for the specific optimisation problem. These are, the inertia parameter w, and the trust parameters (c_1, c_2). If the inertia parameter was set to be small (around 0-0.5) the algorithm would perform poorly, likely converging to a local optimum, increasing this value (to around 1.4) typically results in global optimisation since it allows a larger design space to be searched [109]. The trust parameter c_1 represents how much the particle trusts itself, and c_2 represents how much it trusts the group. If $c_1 > c_2$ it is likely that the particles will simply move around the design space independently whereas if $c_2 > c_1$ it is more likely that the particles will converge prematurely to a local optimum [115]. The choices of parameters are very important and some recommendations are given in [120]. There have also been modifications to PSO to better handle optimisation problems with constraints [121].

Differential Evolution (DE)[116] also initialises a population of design points and then utilises information from these points to mutate and find the next generation of design points. Differential evolution has three components:

mutation, crossover and selection. There are several different methods of differential evolution but the 'classic' method is named DE/rand/1/bin, this implies that random vectors are chosen to calculate the difference vectors in the mutation equation, only one difference vector is calculated, and binary crossover is used. For this method, the mutation equation is:

$$x_i'^{g+1} = x_{r_1}^g + F(x_{r_2}^g - x_{r_3}^g) \tag{8.4.5}$$

where g is the generation, i is the individual in the population, and $(r_1, r_2, r_3 \neq i)$ are random parents in the population. The parameter F is the differential weight and controls the amplification of the differential, it typically lies within the interval 0.4-1 [122]. The mutation is demonstrated in Figure 8.19 for two dimensions. Another common version of mutation is DE/target-to-best/1/bin, which includes the difference of the current point and the best point so far:

$$x_i'^{g+1} = x_i^g + F(x_{best}^g - x_i^g) + F(x_{r_1}^g - x_{r_2}^g) \tag{8.4.6}$$

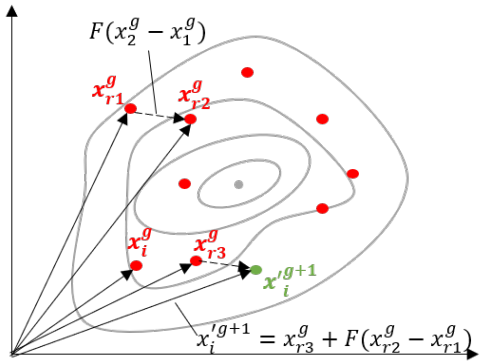

Figure 8.19: Example of Differential Evolution mutation in 2D (DE/rand/1/bin) (adapted from [116])

Following mutation the algorithm utilises crossover. The second parameter of differential evolution which needs to be tuned by the programmer is the crossover ratio: $0 < CR < 1$. There are different methods of crossover but the most common is binary. For each individual in the population and for each dimension a random number $r(0, 1)$ is generated, if $r < CR$ the mutated design is used for that dimension and if $r > CR$ the parent design is used for that dimension. Crossover is designed to increase the diversity of the population.

Lastly, selection compares the objective function using the parent vector to the objective function using the new vector. The best is chosen to be the design

point for the next generation for that individual. The process for differential evolution is demonstrated in Figure 8.20.

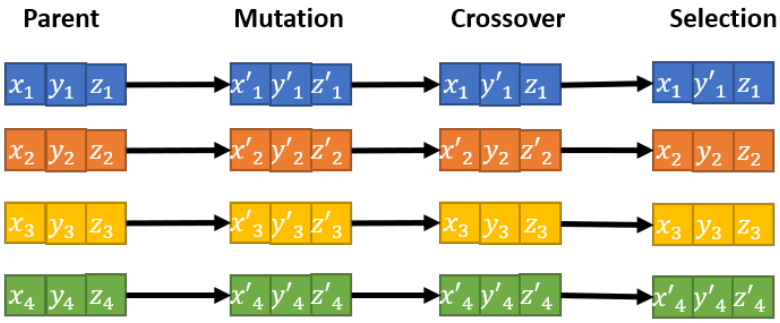

Figure 8.20: Example of the Differential Evolution algorithm

There are several variations of the evolutionary algorithms which make them more complex and robust. An extension of the differential evolution algorithm, which we use in this paper, is the multi-population adaptive inflationary differential evolution algorithm (MP-AIDEA)[96]. This uses multiple populations and combines basic differential evolution with monotonic basin hopping (MBH) to reduce the risk of converging to a minimum which is not global, it also adapts the optimisation parameters autonomously. It is a further advancement on the inflationary differential evolution algorithm (IDEA) which only uses a single population and requires the parameters to be chosen by the programmer [123].

When a minimum has been found the monotonic basin hopping (MBH) [124] method generates a new point within the neighbourhood of this minimum (where the neighbourhood is defined as 2Δ). A local search is performed from this point and if the minimum found is better than the previous one it is chosen and a new point generated in its neighbourhood, and so on. If no better points are found for $n_{samples}$ then a restart can be performed. The parameter Δ needs to be chosen carefully, if too small the local search will be unable to escape the current basin, and if too large it would become a random search.

IDEA uses MBH when the population contracts within a radius defined as the contraction limit (a parameter to be defined), when the population reaches this limit it is unlikely to be able to escape and search elsewhere in the design space, hence the need for a restart. Instead of using a local search within MBH it uses differential evolution. Additionally, to improve convergence it runs a local

optimisation routine at the converged point to ensure it is truly a local minimum, before using MBH to basin hop. Figure 8.21 demonstrates this.

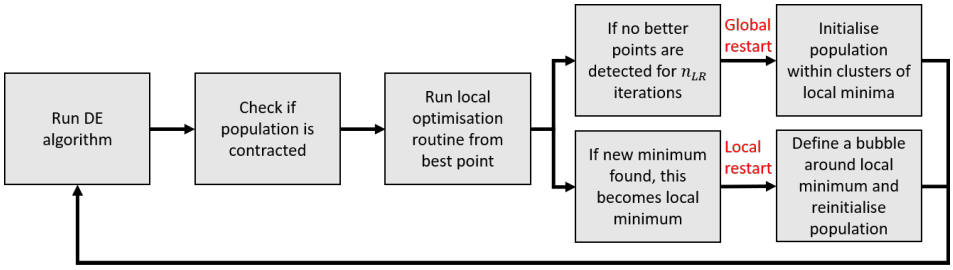

Figure 8.21: Description of the Inflationary Differential Evolution algorithm (IDEA)

MP-AIDEA adapted IDEA to adjust the main parameters (crossover probability CR, differential weight F, local restart bubble δ_{local}, and the number of local restarts n_{LR}) autonomously. This makes the algorithm easier to apply to different problems. For full details of the algorithm refer to [96]. To adapt the values of δ_{local} and n_{LR} the restart of the population needs to be evaluated, therefore, multiple populations are used and evolved in parallel. The parameter n_{LR} is removed in this algorithm and a procedure to decide whether a local or global restart should be run is implemented instead. Figure 8.22 demonstrates the algorithm.

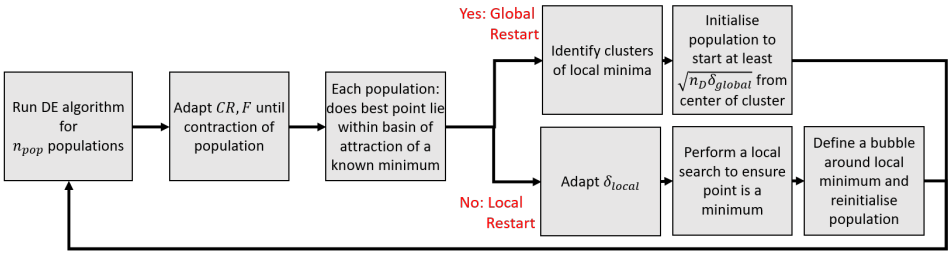

Figure 8.22: Description of the Multi-Population Adaptive Inflationary Differential Evolution algorithm (MP-AIDEA)

8.4.3 Possible Routes to Minimising the Objective Function

There are various approaches to determine the parameters in the model. One way is by hand as in Goldstein et al[62], but here we use the following methods:

Method 1: optimise the acoustic model to find the 4 parameters.

Method 2: optimise the R_{22} model to find a_1 and hand-tune the other 3 parameters for acoustic predictions.

Method 3: optimise the R_{22} model to find a_1, and optimise the acoustic model to find the other 3 parameters.

Table 8.2 sets out the optimisation problem which is to be solved for each method, where the objective functions J_A, J_R were defined in (8.4.4).

Table 8.2: Optimisation problem statement for each method.

	Method 1		Method 2		Method 3	
	Acoustics	R_{22}	Acoustics	R_{22}	Acoustics	R_{22}
Objective function	$J_A(\boldsymbol{x}, \boldsymbol{\psi}) = 0$	-	-	$J_R(\boldsymbol{x}, \boldsymbol{\psi}) = 0$	$J_A(\boldsymbol{x}, \boldsymbol{\psi}) = 0$	$J_R(\boldsymbol{x}, \boldsymbol{\psi}) = 0$
State parameters ($\boldsymbol{\psi}$)	Ma, θ, ϕ	-	-	$x/D, y/D$	Ma, θ, ϕ	$x/D, y/D$
Design parameters ($\boldsymbol{x}$)	a_1, l_2, l_3, τ_0	-	-	a_1	l_2, l_3, τ_0	a_1
Constraints	g_1	-	-	g_2	g_3	g_2

There are no equality or inequality constraints for this problem, only side constraints which were chosen to be:

$$\begin{aligned} g_1 &: 0 < a_1 < 1, 0 < l_2 < 5, 1 < l_3 < 10, 1 < \tau_0 < 10 \\ g_2 &: 0 < a_1 < 1 \\ g_3 &: 0 < l_2 < 5, 1 < l_3 < 10, 1 < \tau_0 < 10 \end{aligned} \tag{8.4.7}$$

The acoustic spectrum results using these methods will be compared to experimental results from [57] for three acoustic Mach numbers $Ma = 0.5, 0.7, 0.9$ above the plate where $\phi = 90$, and at the far field angle $\theta = 90$ where jet surface interaction is greatest.

We also compare the R_{22} model using the values found for a_1 against experimental data from Bridges [74] at $y/D = 6, r/D = 0.5$, i.e. at the end of the potential core on the shear layer.

To reduce the time taken in optimisation, for each acoustic Mach number 30 points were chosen from the experimental acoustic data. The acoustic model was then run for each of these points to calculate the objective function. The points chosen from the experimental data can be seen in Figure 8.23.

We compare the results from three optimisation routines: the multi-population adaptive inflationary differential evolution algorithm (*MP-AIDEA*), particle swarm optimisation (*PSO*), and multi-start. The multi-start and particle swarm optimisation optimisations were done using the in-built *Matlab* routines. Multi-start was carried out using 500 starting points.

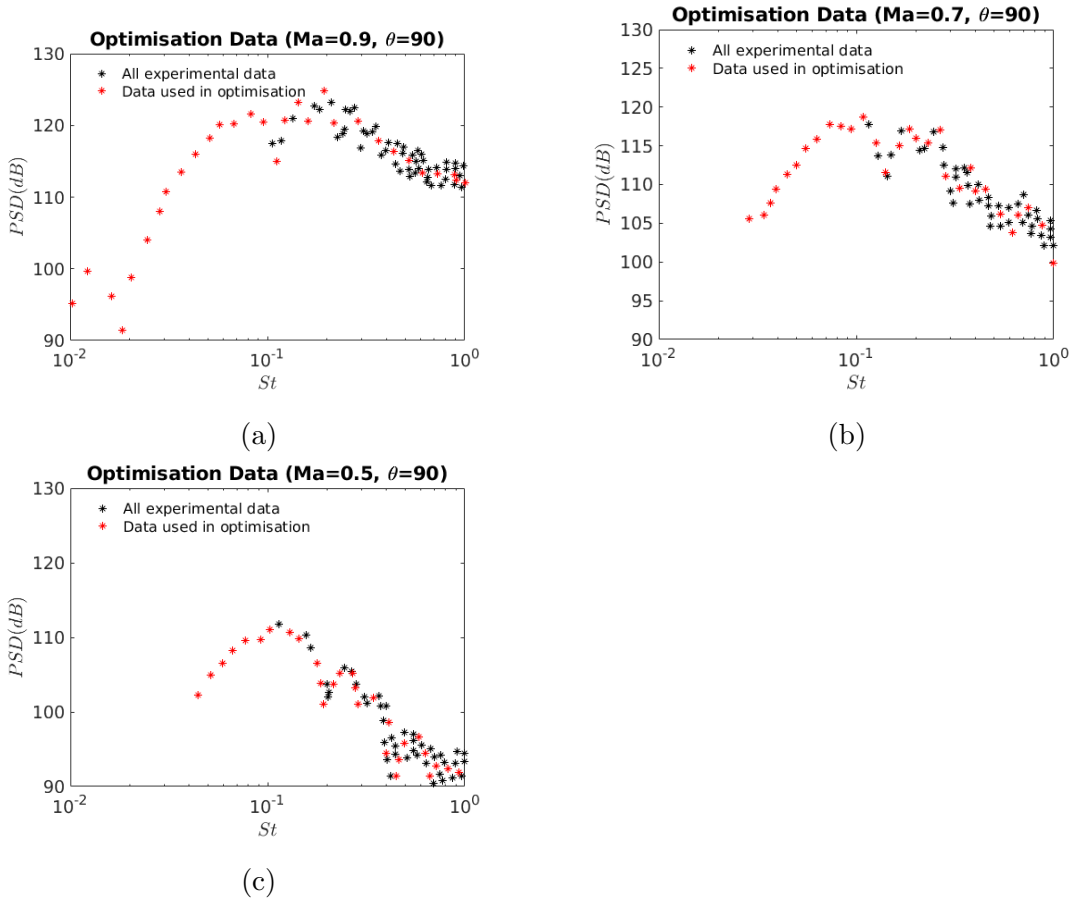

Figure 8.23: Chosen points from experimental data to calculate the objective function (a) $Ma = 0.9$ (b) $Ma = 0.7$ (c) $Ma = 0.5$

8.4.4 Results and Discussion

Since the optimisation routines are stochastic, we ran them several times for $Ma = 0.9, \theta = 90$ to see if they consistently converged. Figure 8.24 shows the variance of parameters found using particle swarm optimisation. Likewise, Figures 8.25 and 8.26 show the variance of parameters for MP-AIDEA and Multi-Start respectively. The range of objective function values corresponding

to these parameters obtained from each routine are then shown in Figure 8.27.

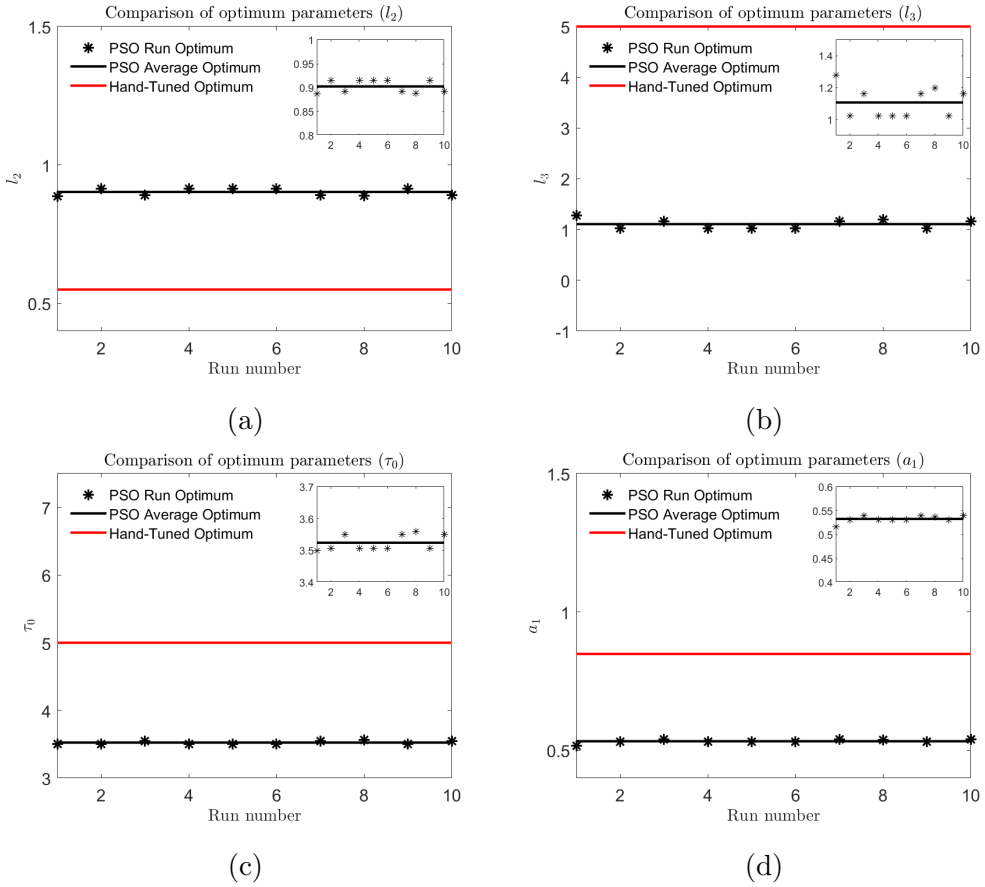

Figure 8.24: Parameter variance across 10 runs of PSO (a) l_2 (b) l_3 (c) τ_0 (d) a_1

Tables 8.3,8.4, and 8.5 compare the parameters found through each method and optimisation routine, the resulting objective function value ($fval$) and the time taken for the optimisation routine to run.

Figure 8.28 compares the acoustic spectrum for methods 1 and 3 using each optimisation routine. Then in Figures 8.29 and 8.30 we compare the acoustic spectrum for methods 1, 2, and 3 using the evolutionary algorithms and Multi-start respectively.

Method 1 was used to find the four parameters through optimisation of our acoustic model against the experimental data in Goldstein et al[62]. Figure 8.28 shows that the predictions are particularly good for $Ma = 0.7$, and $Ma = 0.9$ for all optimisation routines. For Ma=0.5 multi-start gives a poorer prediction due to the change in l_3 which affects low frequency roll-off. From this figure, it is shown that MP-AIDEA and PSO give more or less the same acoustic predictions

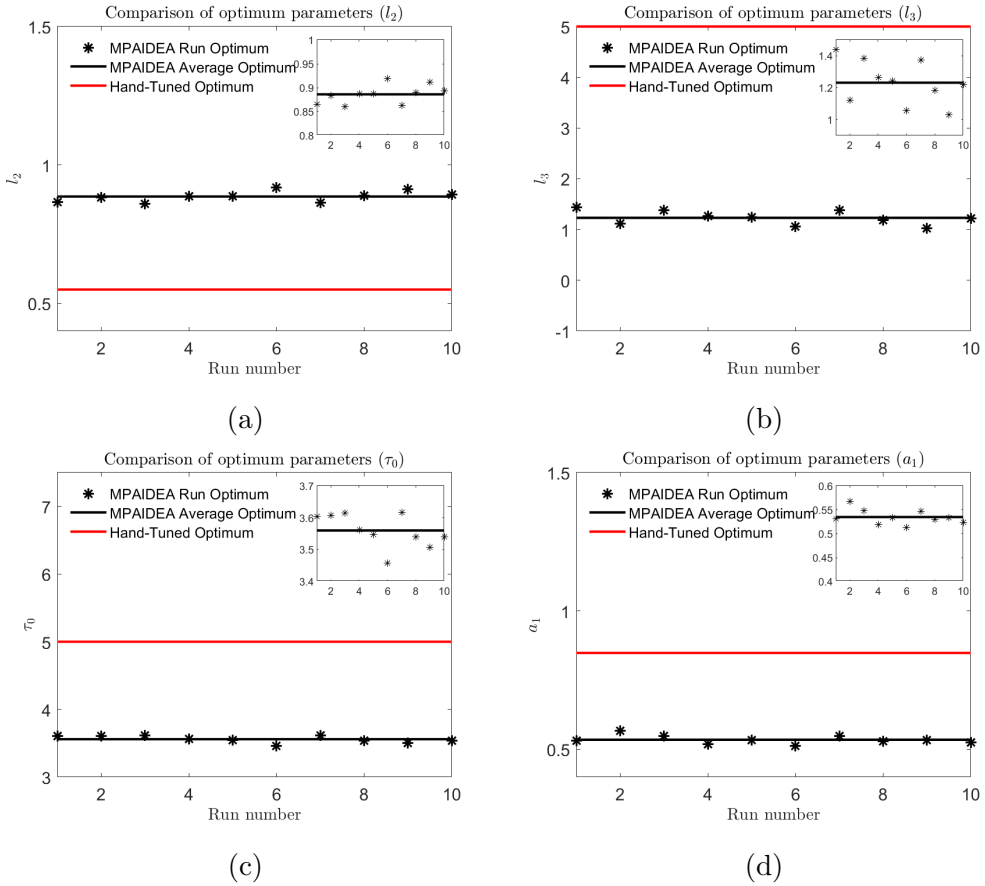

Figure 8.25: Parameter variance across 10 runs of MP-AIDEA (a) l_2 (b) l_3 (c) τ_0 (d) a_1

Table 8.3: $Ma = 0.9$, $\theta = 90$: Comparison of parameters found from the optimisation methods.

Ma = 0.9, $\theta = 90$							
	Method 1			Method 2	Method 3		
	MP-AIDEA	Multi-Start	PSO	Hand-Tuned	MP-AIDEA	Multi-Start	PSO
a_1	0.52	0.56	0.54	0.85	0.85	0.85	0.85
l_2	0.89	0.82	0.89	0.55	0.68	0.57	0.69
l_3	1.22	2.37	1.16	5.00	1.12	9.19	1.07
τ_0	3.54	4.35	3.55	5.00	4.08	5.48	4.08
fval	**9.21**	**9.73**	**9.20**	**11.36**	**9.97**	**10.48**	**9.96**
Time (s)	**9,501**	**5,684**	**14,921**	**-**	**7,075**	**4,450**	**7,393**

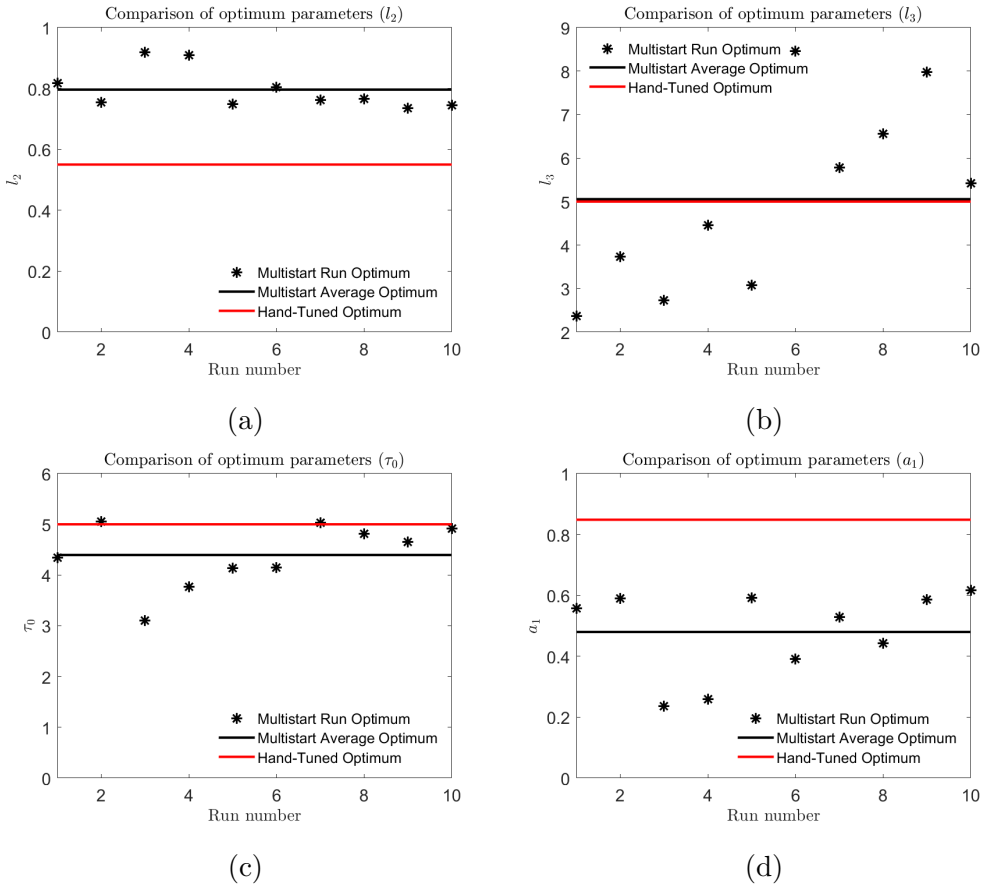

Figure 8.26: Parameter variance across 10 runs of Multi-Start (a) l_2 (b) l_3 (c) τ_0 (d) a_1

Table 8.4: $Ma = 0.7$, $\theta = 90$: Comparison of parameters found from the optimisation methods.

Ma = 0.7, $\theta = 90$							
	Method 1			Method 2	Method 3		
	MP-AIDEA	Multi-Start	PSO	Hand-Tuned	MP-AIDEA	Multi-Start	PSO
a_1	0.59	0.56	0.60	0.85	0.85	0.85	0.85
l_2	1.39	1.14	1.37	0.90	1.05	0.89	1.06
l_3	1.02	3.22	1.00	5.00	1.00	2.80	1.00
τ_0	3.71	3.73	3.64	5.00	3.75	4.28	3.75
fval	**4.91**	**5.15**	**4.18**	**5.70**	**4.27**	**5.12**	**4.26**
Time (s)	**9,596**	**5,841**	**8,944**	**-**	**7,183**	**4,610**	**7,264**

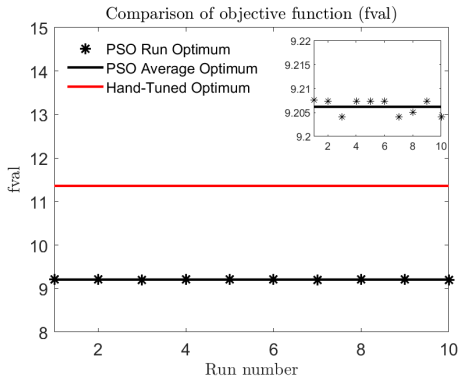

(a)

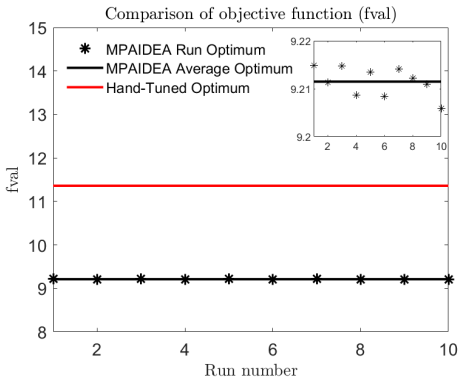

(b)

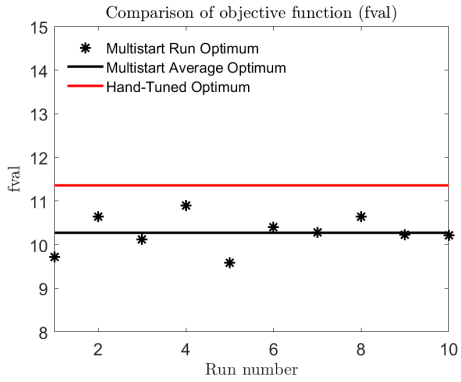

(c)

Figure 8.27: Objective function value range across 10 runs (a) PSO (b) MP-AIDEA (c) Multi-Start

Table 8.5: $Ma = 0.5$, $\theta = 90$: Comparison of parameters found from the optimisation methods.

Ma = 0.5, $\theta = 90$							
	Method 1			Method 2	Method 3		
	MP-AIDEA	Multi-Start	PSO	Hand-Tuned	MP-AIDEA	Multi-Start	PSO
a_1	0.01	0.10	0.00	0.85	0.85	0.85	0.85
l_2	2.52	2.18	2.57	1.30	1.51	1.30	1.49
l_3	1.01	1.01	1.00	5.00	1.00	2.50	1.00
τ_0	2.61	2.04	2.69	5.00	3.68	3.52	3.54
fval	**14.29**	**15.47**	**14.24**	**20.75**	**15.68**	**17.90**	**15.66**
Time (s)	**9,538**	**6,044**	**7,766**	**-**	**7,098**	**4,700**	**7,507**

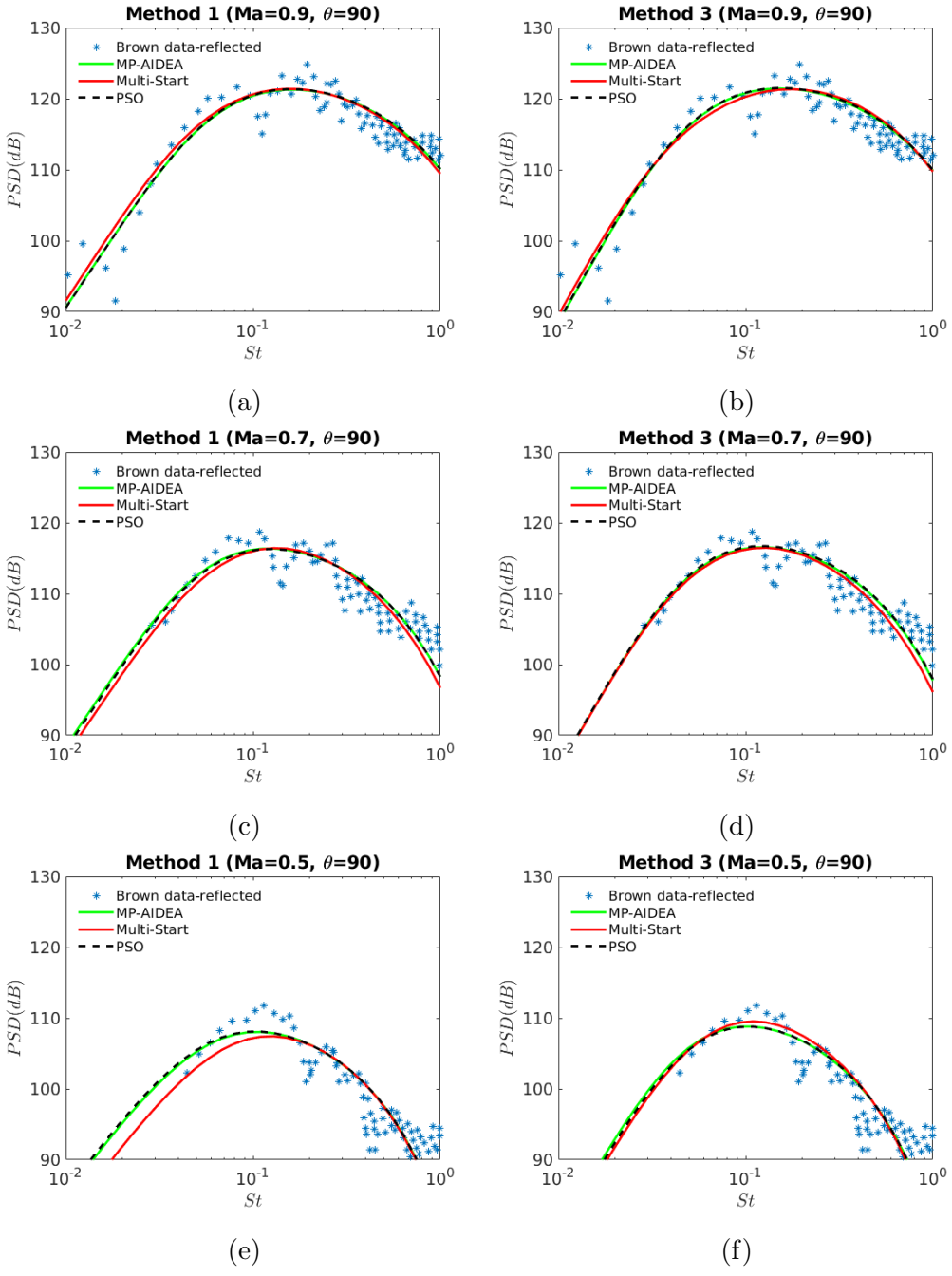

Figure 8.28: Comparison of acoustic predictions using different optimisation routines for method 1 and 3 at $\theta = 90$

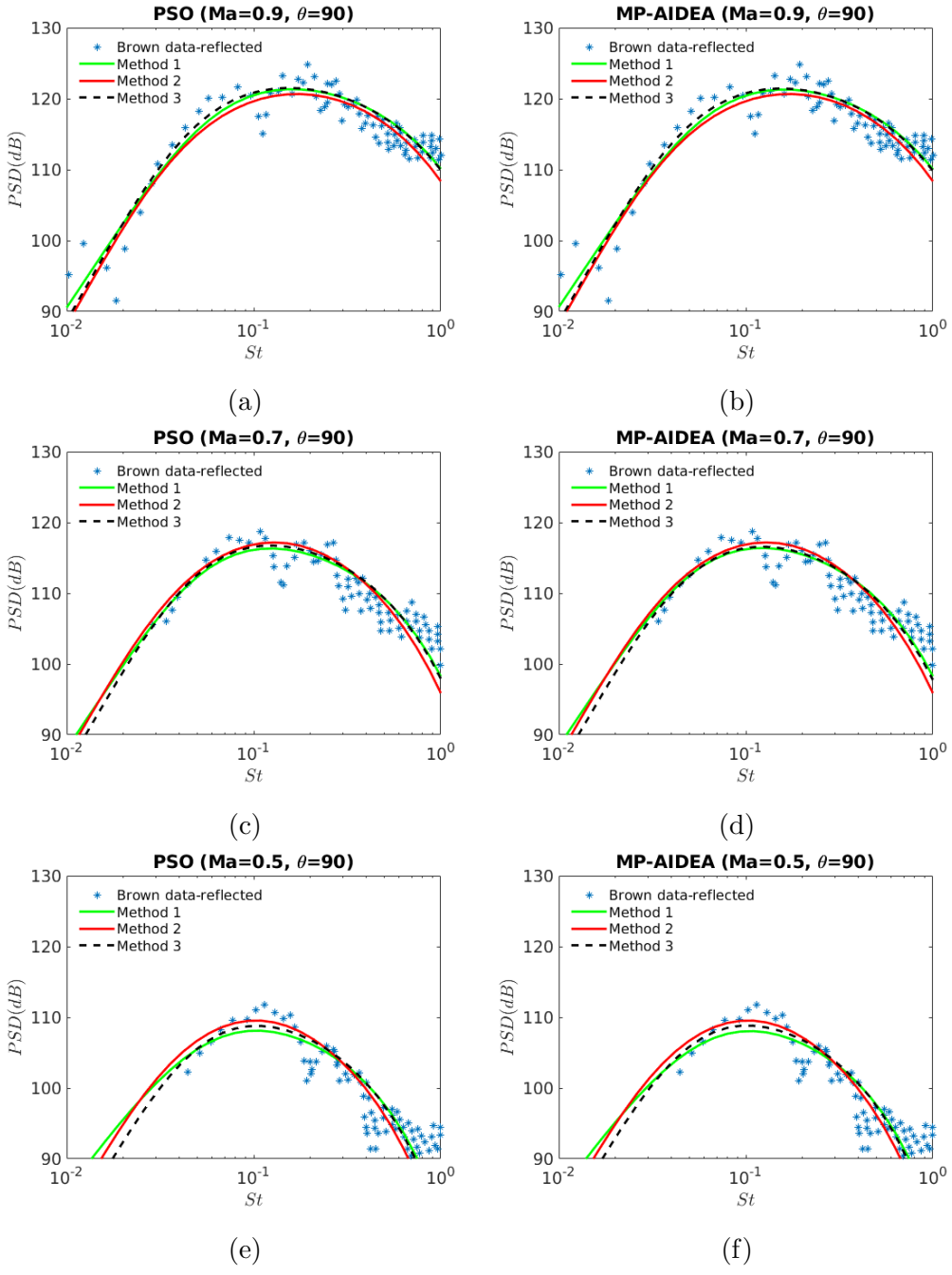

Figure 8.29: Comparison of the acoustic predictions for methods 1, 2 and 3 using particle swarm optimisation (PSO) and MP-AIDEA

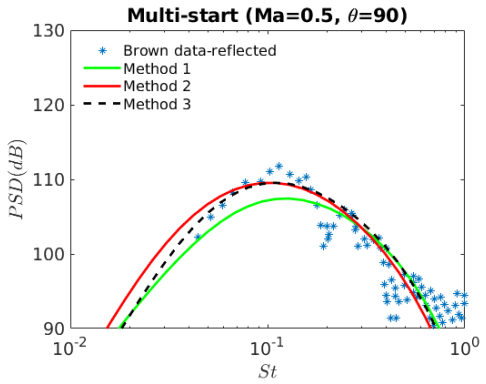

(a)

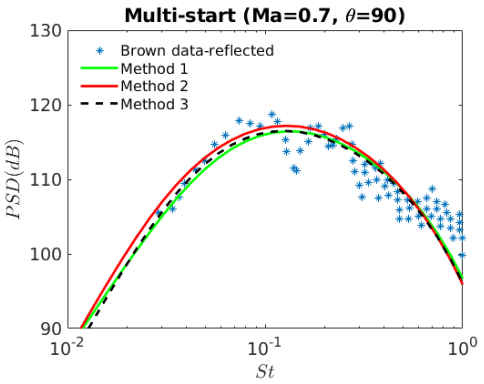

(b)

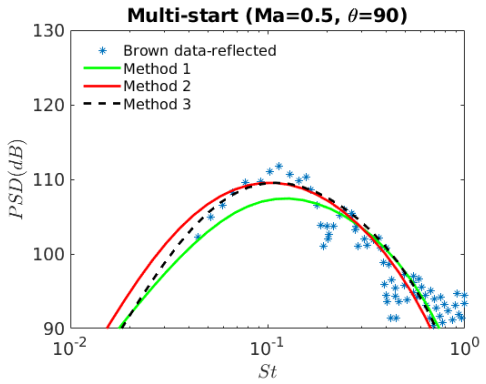

(c)

Figure 8.30: Comparison of the acoustic predictions for methods 1, 2 and 3 using multi-start (a) $Ma = 0.9$ (b) $Ma = 0.7$ (c) $Ma = 0.5$

for all acoustic Mach numbers.

However, the turbulence correlation function R_{22} that we use is a function of a_1: $R_{22} \sim (1 - a_1\tau)e^{-\tau}$and the values for a_1 that were found from this method for each optimisation routine do not give a good representation of R_{22}, as shown in Figure 8.31. The initial decay is too slow and there is little to no anti-correlation region, this is particularly the case for $Ma = 0.5$. Note, that we have allowed $\tau U_c/D \to 10$ to show where the model goes to zero, there is no turbulence data at these locations most likely due to measurement difficulties.

In methods 2 and 3, we optimised the R_{22} model separately against experimental data from Bridges $(y/D = 6, r/D = 0.5)$[74]. This means that the anti-correlation region is represented and the initial decay is steeper, as shown in Figure 8.31 for methods 2 and 3. Only the initial de-correlation is of interest, therefore we have used a simple model for R_{22}. A different model could be used to capture the oscillations but this would make the acoustic model much more complicated (as shown in the previous section) and have no improvement on the acoustic spectrum predictions.

For method 3 we use the this R_{22} optimised value a_1 (0.85) in the acoustic model and then optimise the other parameters against the acoustic data to find the best prediction. This allows us to find the optimal predictions for the acoustic spectrum while also having a good representation of the turbulence structure. It results in slightly poorer acoustic predictions, with the exception of Multi-start for $Ma = 0.7$, as noted in Tables 8.3, 8.4, and 8.5. However, Figure 8.28 shows that they still give very good predictions for the level of accuracy that we require. Since this method also allows R_{22} to be better represented, overall it is deemed to be better than method 1.

In method 2, we also use this value ($a_1 = 0.85$) in the acoustic model and hand tune the other parameters to find the best prediction. We aimed to find one set of parameters for all acoustic Mach numbers. However, it was found that due to the level shift in the acoustic spectrum, one parameter (l_2) must change for each Mach number. As this method did not require different optimisation routines, the results are included in Figures 8.29, and 8.30 and are identical in each. We can see that the predictions are similar to methods 1 and 3. However, hand tuning these parameters is not ideal as it relies on human judgement as to what is a 'good' prediction.

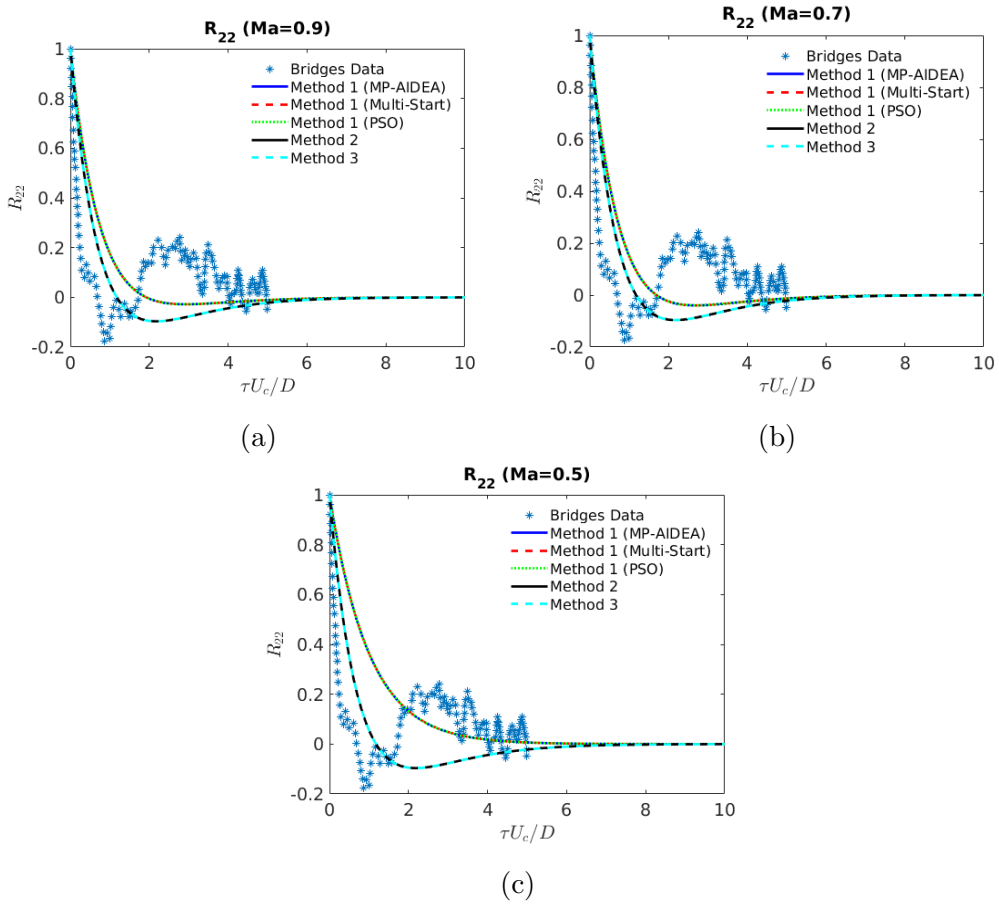

Figure 8.31: Comparison of R_{22} for different optimisation methods and routines (a) $Ma = 0.9$ (b) $Ma = 0.7$ (c) $Ma = 0.5$

It is easy to see in Figures 8.29 and 8.30 that the three methods of optimisation give similar acoustic predictions for all optimisation routines, with only Multi-start giving a noticeable change in prediction for $Ma = 0.5$. Note that from Figure 8.27 only PSO and MP-AIDEA consistently converged to a minimum objective function value ($fval = 9.2$), Multi-start displayed a more widely varying value, possibly due to the number of starting points chosen (500). Figure 8.26 shows that the parameters found for Multi-start also vary widely on each run of the routine, hence it is less likely that acoustic predictions found using multi-start are optimal. On the other hand, Figures 8.24 and 8.25 show that the parameters found by PSO and MP-AIDEA respectively, only vary slightly.

We can conclude that our acoustic spectrum model for the trailing-edge noise problem is 'parametrically flat', i.e. the objective function is not noticeably sensitive to the variation of parameters (l_2, l_3, a_1, τ_0) within their specified range. Both evolutionary optimisation routines that we have used in this paper have given good results and almost identical predictions. The time taken in optimising method 1 naturally took longer than method 3 since an extra parameter was being found. In general, it was found that method 1 was faster using particle swarm optimisation, however method 3 was faster using MP-AIDEA. However, for the number of starting points that was chosen, multi-start was fastest of all, and since the objective function value was still smaller than method 2, if there was a time constraint which restricted the use of evolutionary algorithms, it would be worthwhile to use Multi-start rather than hand-tuning the problem.

8.5 Robustness of Model at Off-design Conditions

The previous section discussed the optimisation of parameters for a fixed plate at the location which produces peak edge noise (on the shear layer at the end of the potential core). In this section we discuss the robustness of the model at off-design conditions (i.e. at different vertical plate locations h). Figure 8.32 shows the variation of experimental data depending on the plate location. It is clear that as the plate moves away from the jet axis the edge noise decreases until it reaches the point where jet noise dominates and it is negligible. Likewise as the plate edge moves closer to the nozzle edge noise also decreases until negligible.

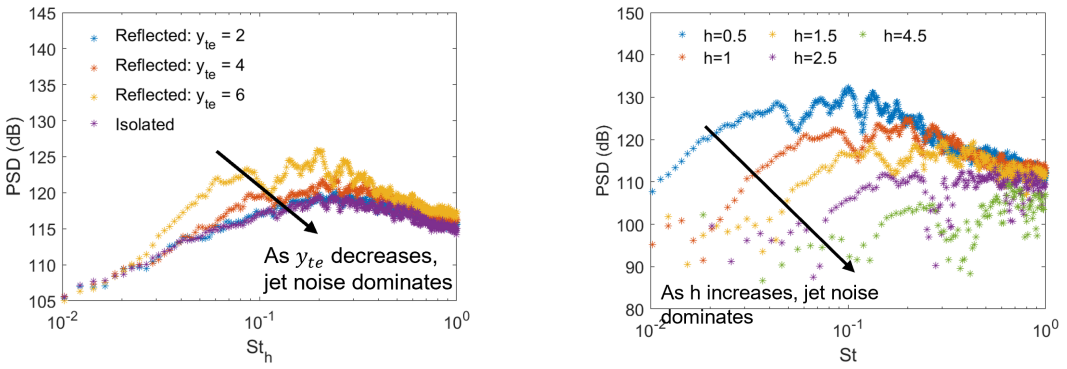

(a) (b)

Figure 8.32: $Ma = 0.9, \theta = 90$: Variation of experimental edge noise (a) with y_{te} (b) with h

Figure 8.33 uses the model parameters from the previous section (referred to as the 2021 Model) and compares the acoustic predictions with experiment varying h. Since the model parameters were optimised for $h = 1$ those predictions are good, however it is clear that the model under/over predicts the acoustic spectrum if the plate is located closer to/further from the jet centerline respectively. In this section we look at optimising extra parameters (κ, κ_1 from the meanflow, and μ from the amplitude function) to see if the model can work for other plate locations.

To understand the individual effects of parameters in the acoustic model, Figure 8.34 shows a design of experiments. We see the main effect of κ, κ_1 is to change the broadband amplitude of the acoustic predictions, μ also changes the amplitude but has a greater impact on the high frequencies, and τ_0 has an effect on amplitude but its most important feature is that it moves the peak noise to different frequencies. Based on experiments, we expect modifying κ, κ_1, τ_0 to have the largest impact to obtain more accurate predictions, since we need to move the peak frequency and adjust the amplitude for $h \neq 1$.

We also modified the meanflow profile by including an additional parameter h_0:

$$U(u) = \begin{cases} U_d(1 - e^{-\kappa(u-h_0)^2 - \kappa_1(u-h_0)^4}) & u < h_0 \\ 0 & u \geq h_0 \end{cases} \tag{8.5.1}$$

this allows the *core region* (i.e. where $U(u) = 0$) to increase as $|h_0|$ increases as shown in Figure 8.35. It should be noted that the meanflow profile in (8.5.1) is identical to that of the 2021 model if $h_0 = 0$.

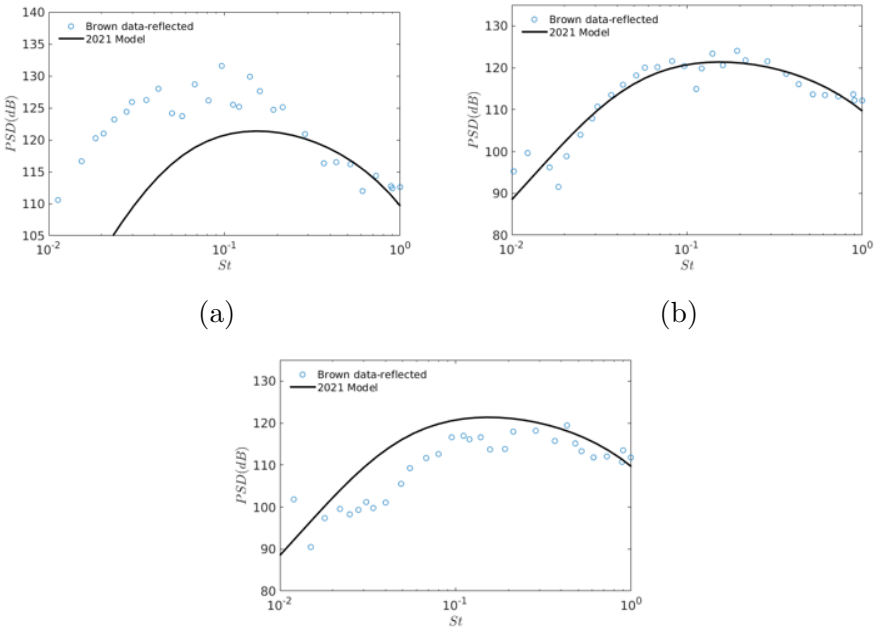

(a) (b)

(c)

Figure 8.33: $Ma = 0.9, \theta = 90$: Acoustic predictions using the 2021 Model for different h values (a) $h = 0.5$ (b) $h = 1$ (c) $h = 1.5$

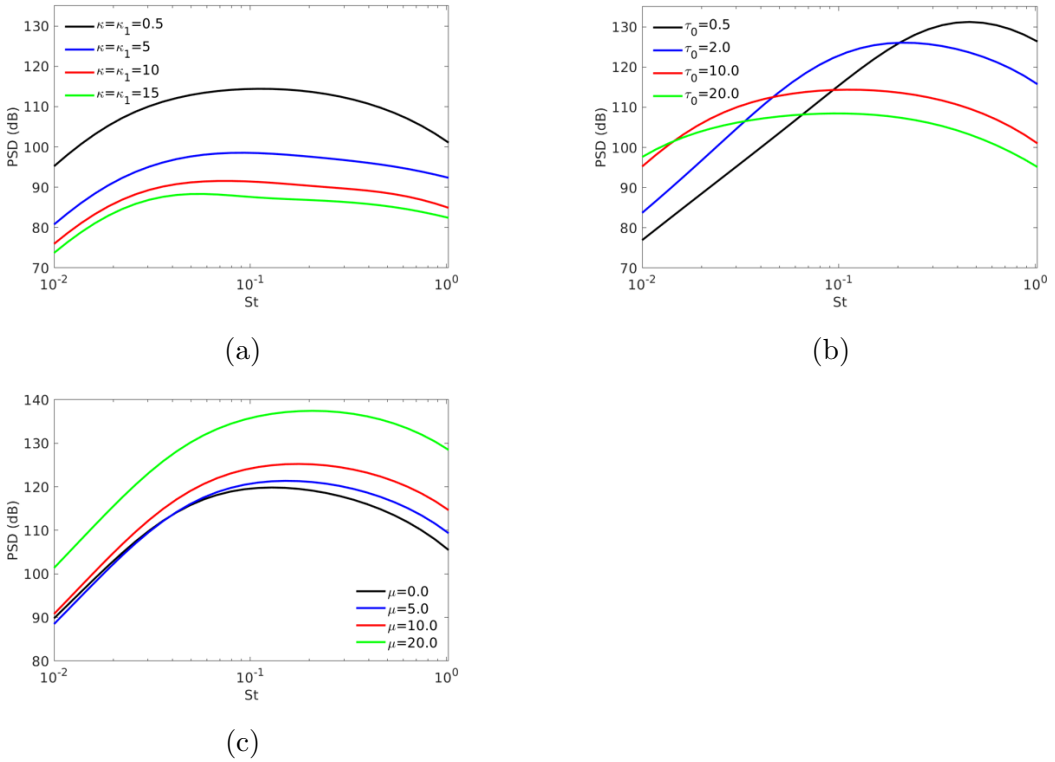

(a) (b)

(c)

Figure 8.34: Design of Experiments varying (a) κ, κ_1, (b) τ_0, (c) μ

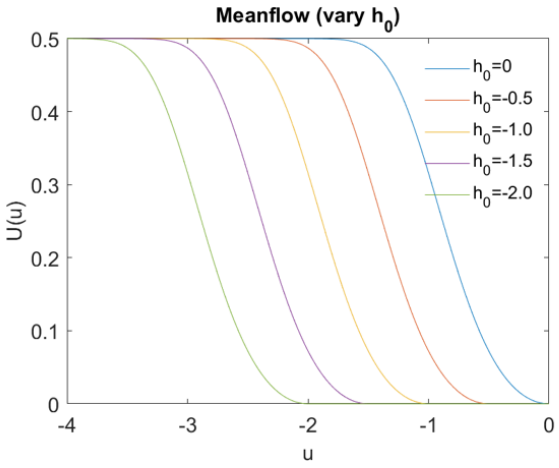

Figure 8.35: Meanflow profile modifying h_0 ($\kappa = \kappa_1 = 0.5$)

To investigate the universality of parameters across plate location we look at several different optimisation routes where we optimise certain parameters while keeping others fixed. These routes are summarised in Figure 8.36.

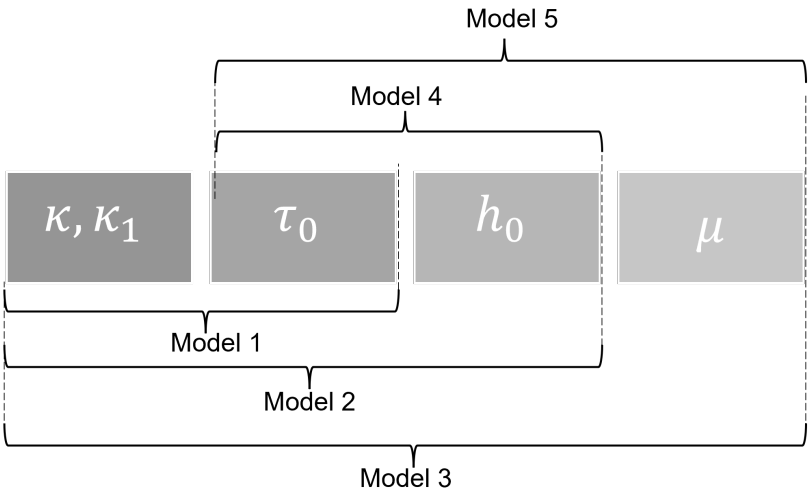

Figure 8.36: Different routes to optimisation of meanflow parameters, when parameters are not optimised they are kept at their 2021 values ($\kappa = \kappa_1 = 0.5, h_0 = 0, \mu = 5$)[99]

Figure 8.37 compares the acoustic spectrum obtained from each model for $Ma = 0.9, \theta = 90$ at different vertical plate locations h. It is easy to see that when the plate is close to the nozzle every model gives good acoustic predictions. It is only when the plate is further away that the different models give varying levels of accurate predictions. This is particularly the case for $Ma = 0.9$ at $h = 2.5$,

however it should also be noted that for this degree of vertical separation the edge noise is near negligible in comparison to jet noise. Therefore, based on these acoustic predictions, models 1-3 seem to give the best results across the range of plate locations, this indicates the importance of the κ, κ_1 meanflow parameters which were not optimised in the 2021 model [99]. The objective function error is compared for models 1-3 in Figure 8.38 and we see for small $h \leq 1.5$ (where edge noise is a significant portion of noise) the models perform similarly, with model 3 being slightly better, however at large h, model 3 is significantly better. Since, ideally it is preferred to have as few free parameters as possible, model 1 should be chosen as the best model.

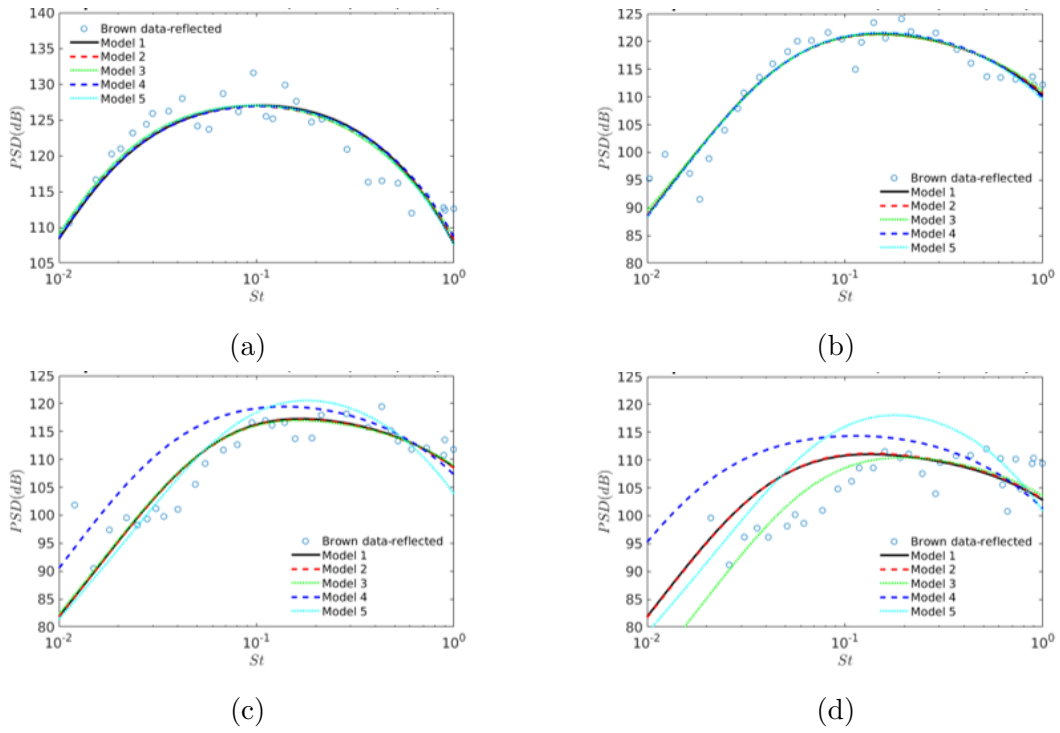

Figure 8.37: Compare models for an optimised acoustic spectrum for $Ma = 0.9, \theta = 90$ at (a) $h = 0.5$, (b) $h = 1$, (c) $h = 1.5$, (d) $h = 2.5$

Figure 8.39 compares the optimised parameters from models 1-5 and the 2021 model for different plate locations h at $Ma = 0.9$, $\theta = 90$. Note that for $h = 0.5, 1$ the optimised parameters vary across the models, but as we have already shown in Figure 8.37 the acoustic spectrum remains more-or-less constant across models for low h. This is further proof of a flat objective function; a large range of parameter values can result in good acoustic predictions.

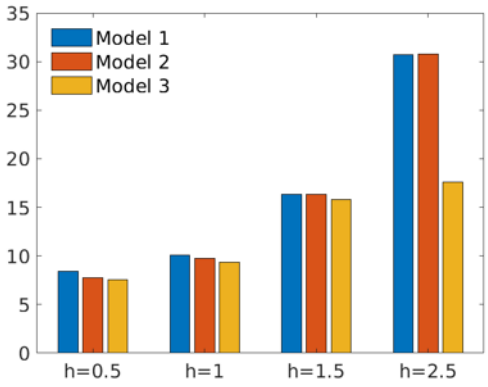

Figure 8.38: Comparison of objective function error from models 1-3 for $Ma = 0.9, \theta = 90$ (smaller error = better acoustic prediction)

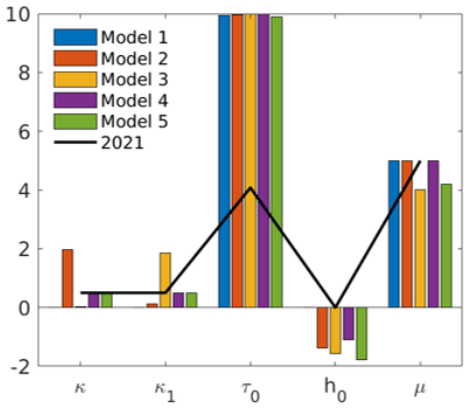

(a)

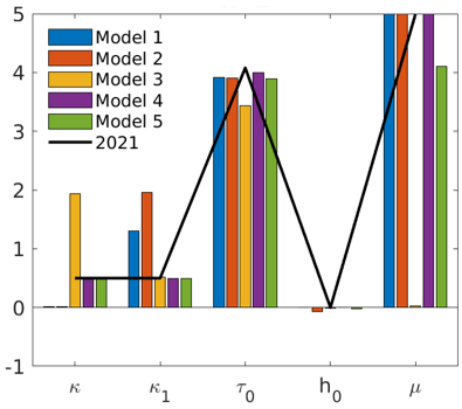

(b)

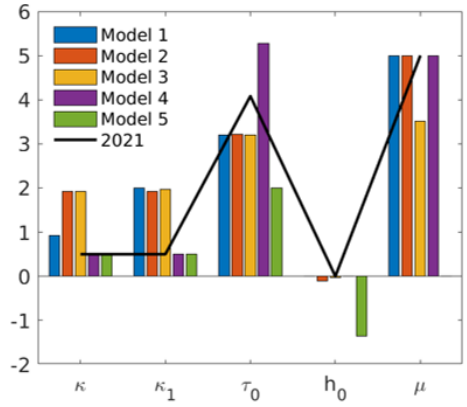

(c)

Figure 8.39: Compare optimised parameters from models 1-5 for $Ma = 0.9, \theta = 90$ at (a) $h = 0.5$, (b) $h = 1$, (c) $h = 1.5$

Figure 8.40 compare the optimised parameters at different plate locations for models 1-3 for $Ma = 0.9$. This shows that the optimisation varies different parameters to achieve the correct acoustic spectrum, there does not appear to be a consistent change of parameters as h increases. However, since the previous figures showed there were different parameter choices to obtain good predictions, it is likely that there is a balance of parameters.

It is important to note that the optimisation for all models in this section is to optimise meanflow parameters, this is required due to the lack of experimental/computational meanflow data at different vertical plate locations. Since we cannot use a physical meanflow profile we instead use optimisation to choose meanflow parameters that give correct acoustic predictions. Unfortunately, this means that although the acoustics are physical and react accordingly (smaller h gives larger sound), the meanflow may or may not be physical. If computational/experimental data for the meanflow is available in the future, it would allow a physical meanflow profile to be used in the model and remove the need for these optimised scales.

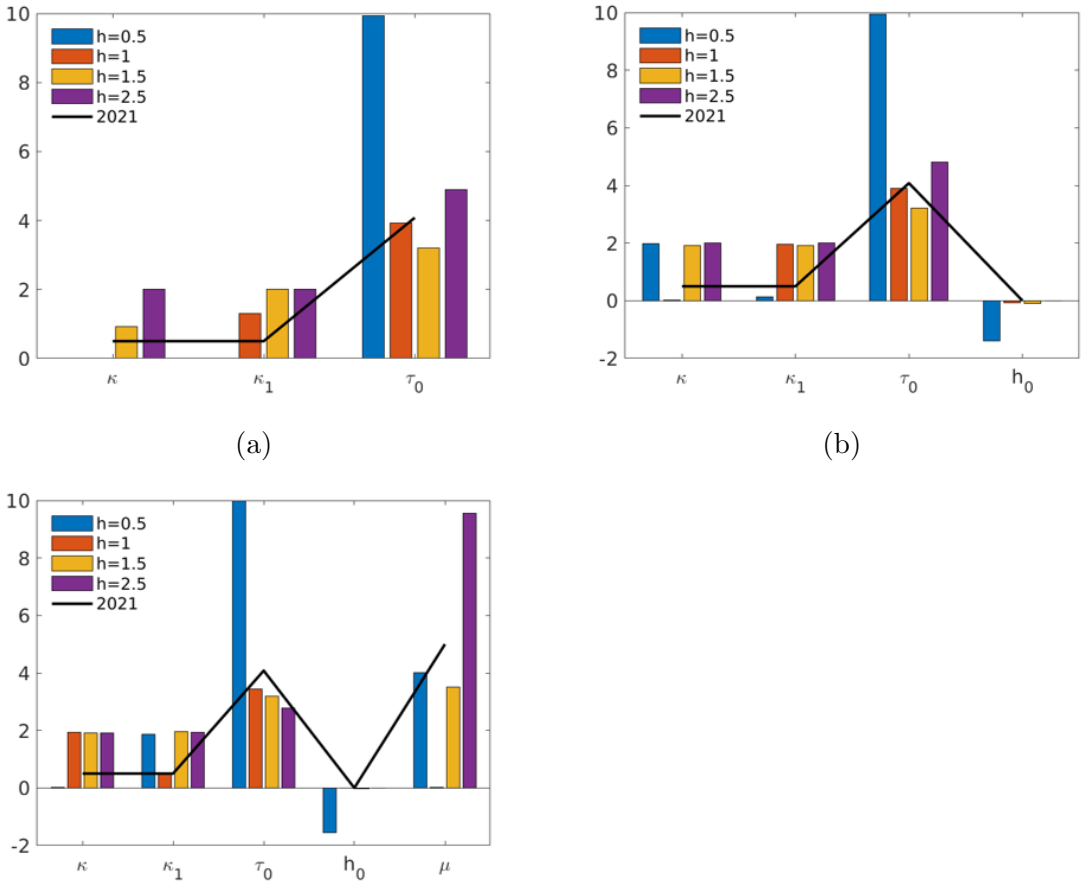

(a) (b)

(c)

Figure 8.40: Compare optimised parameters for varying h for $Ma = 0.9, \theta = 90$ using (a) Model 1, (b) Model 2, (c) Model 3

8.6 Summary

Aeroacoustic models for turbulence interaction problems will always require a set of parameters that define the rate of temporal and spatial decorrelation. For the trailing-edge noise problem the acoustic spectrum (8.1.57) is proportional to the Fourier transform of the streamwise-independent transverse velocity correlation function, $R_{22}(\tilde{v}-u,\tilde{v}-v;\omega)$. In this chapter we extended the model for R_{22} to include a term which enabled an anti-correlation region to be represented resulting in a more faithful representation of the turbulence structure than in Goldstein et al [62] which improved acoustic predictions.

The Fourier transform of R_{22} depends on $O(1)$ parameters (l_2, l_3, a_1, τ_0, κ, κ_1, μ, h_0). These parameters can be chosen by hand-tuning, however this will not result in a 'mathematically' optimal choice of parameters, and could result in under/over prediction of the acoustic spectrum. It also adds to the time taken in assessing its predictive capability.

In this chapter we also highlighted how optimisation routines, both evolutionary and non-evolutionary, can be used to determine what the optimal parameters are, resulting in slightly better acoustic predictions.

To find acoustic predictions across a range of Mach number at a fixed plate location we found only l_2 needed to change, and since this decreases linearly as the Mach number increases it can be found for any Mach number without the need for optimisation showing that the model is robust at a fixed plate location. However, we found that varying the vertical plate location does require an optimisation of meanflow scales due to a lack of experimental/computational meanflow data. For the model to be more predictive at arbitrary h, this data is required, and could be a subject for future research.

Now that we have investigated both jet noise and edge noise, in the next chapter we will combine them both and look at the installation effects.

Chapter 9

Installation Noise

So far in this thesis we have obtained acoustic predictions for both jet noise and edge noise for several jets. This chapter combines these predictions to obtain the installation noise. Figure 9.1 shows a pictorial representation of the different jet and edge noise sources.

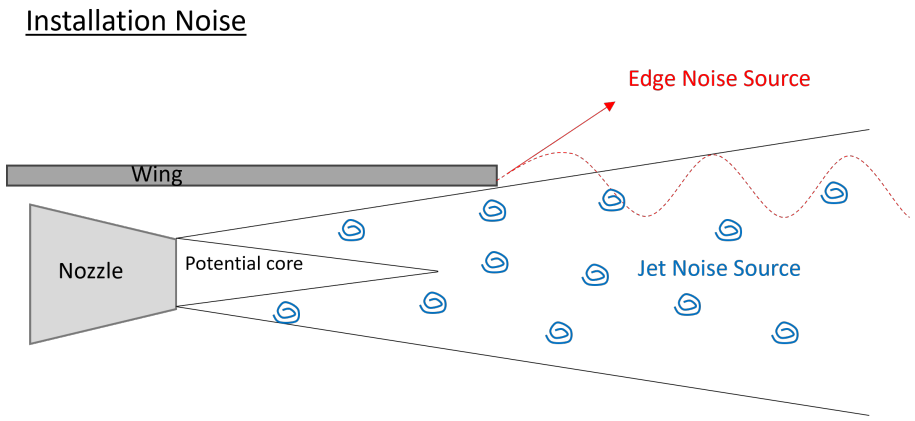

Figure 9.1: Pictorial representation of noise sources involved in the total installation noise

Installation noise is therefore a combination of three terms; in words this is:

$$\text{Installation Noise} = \text{Edge Noise} + \text{Jet Noise} + \text{Coupling} \tag{9.0.1}$$

where the coupling terms refer to the statistical interaction between the jet and edge noise components. The main assumption we make is that the coupling terms are negligible and we can simply say that the installation noise is formed from the addition of the jet and edge noise. Since we only considered cold jets for the

edge noise problem, here we only look at the installation noise for cold jets SP03 and SP07.

9.1 Predictions

Figure 9.2 shows the predicted installation noise for the isothermal jets at several far field angles. These angles were chosen since edge noise is largest at the sideline area. It is evident from comparison with Chapters 7 and 8 that these predictions are dominated by the edge noise and jet noise is negligible in comparison, which is to be expected at these angles.

The overall sound pressure level was calculated for edge noise, and then installation noise as shown in Figures 9.3 and 9.4 respectively. These figures also show that edge noise is the dominant noise source at these angles. We also see that the predictions using our hybrid model are within 2dB of the experimental data at the angles considered.

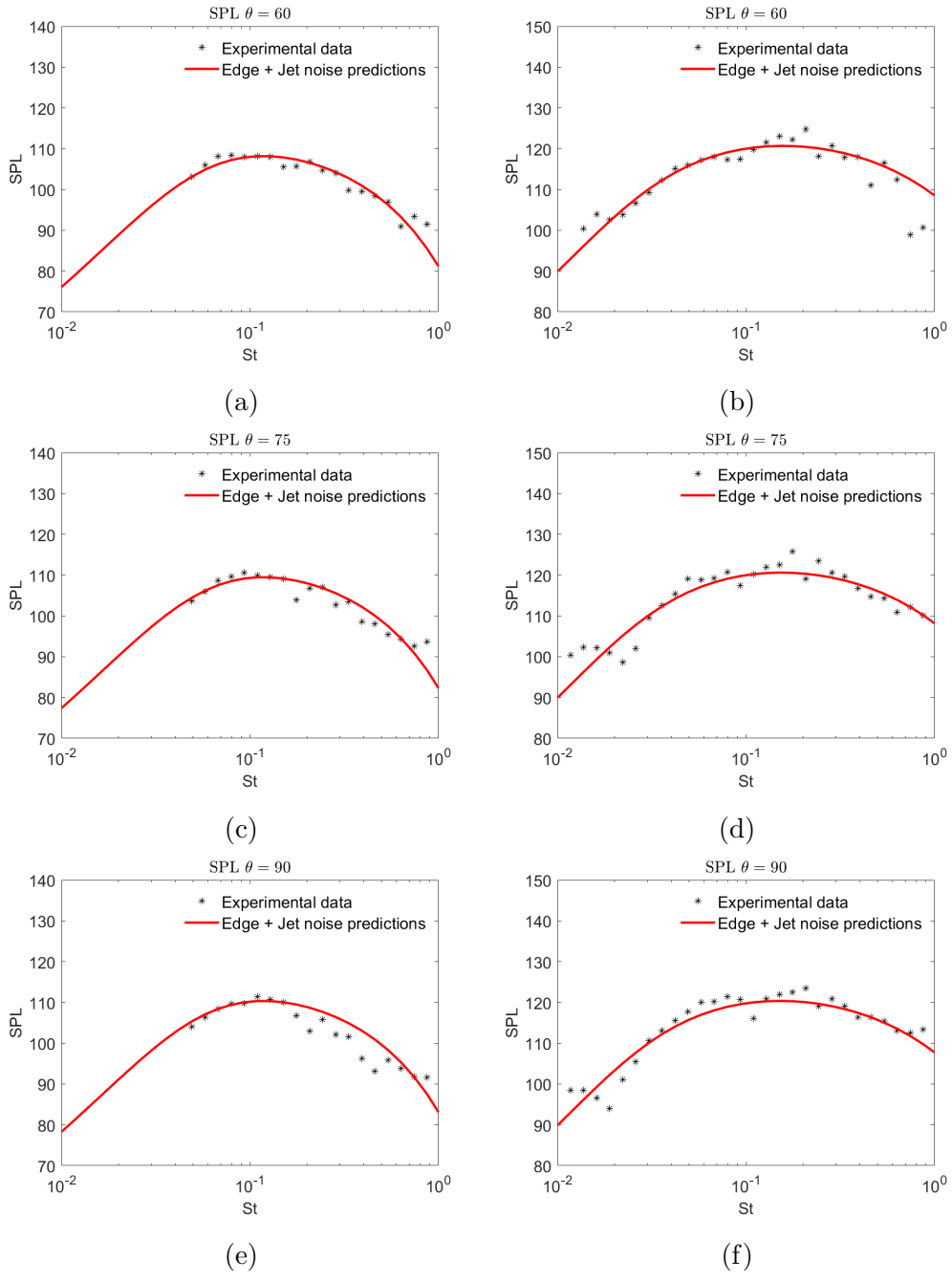

Figure 9.2: Installation noise predictions compared against experiment for (a,c,e) SP03 (b,d,f) SP07

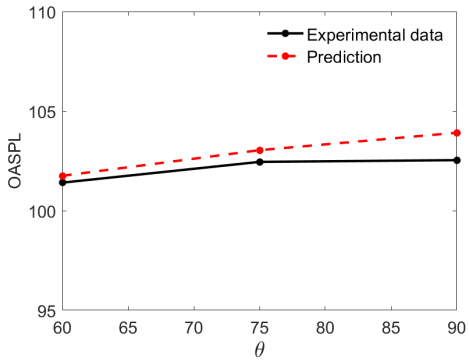

(a)

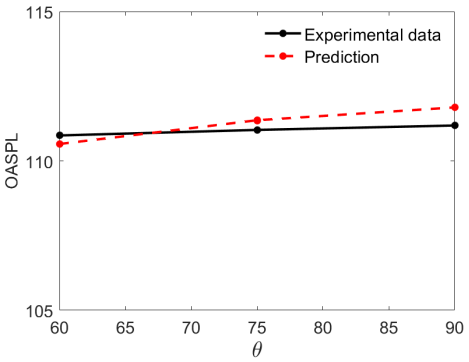

(b)

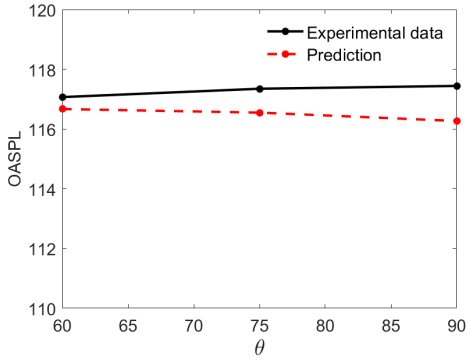

(c)

Figure 9.3: OASPL for edge noise for (a) $Ma = 0.5$ (b) $Ma = 0.7$ (c) $Ma = 0.9$

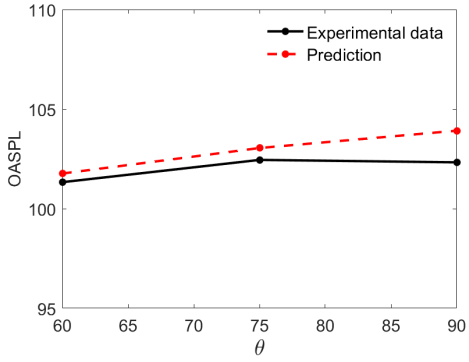

(a)

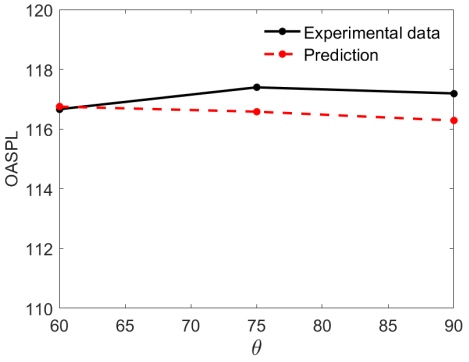

(b)

Figure 9.4: OASPL for installation noise for (a) SP03 (b) SP07

Chapter 10

Conclusions and Future Work

10.1 Conclusions

The main research aims of this PhD were to investigate the turbulence statistics for a range of subsonic jets considering the effect of acoustic Mach number and jet temperature ratio. We stated in Chapter 2 (p.17) that our work in this thesis seeks to reduce the uncertainty regarding the source term construction within the acoustic analogy approach. We conducted a formal assessment of the contribution of the individual correlation function terms in the source structure given by Afsar et al [27] repeated here in (4.3.29)-(4.3.31). This assessment was performed using a first of its kind spectral (i.e. space-time Fourier transforms) analysis using an LES database of 4 axisymmetric jets to quantify the amplitude and spectral decay rates of the correlation functions.

To simplify the formula we considered universality of length scales within the turbulence correlation functions (analytical formula (6.1.23)) asking whether these could be used to obtain a universal spectral tensor and universal acoustic predictions. Lastly, we investigated whether jet surface interaction noise could be better predicted using a more faithful representation of the turbulence. Here we will summarise some of our main results:

Effect of Mach number and jet temperature ratio

- Increasing the acoustic Mach number also increased the jet noise across all frequencies and far field angles (see Figures 7.13, 7.14);
- Heating the jet at a constant acoustic Mach number resulted in a reduction

of the jet noise for most far field angles and frequencies (maximum reduction of $2-4dB$ at $\theta = 30$ for $Ma = 0.5, 0.9$ respectively).

Our results for the SPL and OASPL of the low speed $Ma = 0.5$ do not agree with experimental results where it is expected that heating the jet will increase the jet noise. This is likely due to the acoustic predictions from the heated SP42 jet being under-predicted. Interestingly, for the $Ma = 0.9$ jets we found that heating the jet increases the noise slightly at the sideline positions ($\theta > 70^{\circ}$).

Approximations to the spectral tensor

- Axisymmetry approximations were found to be appropriate for our LES jets and therefore the representations of the starting equation (4.3.25) to the AGF [27] formula, repeated here at (4.3.29)-(4.3.31) could be used;
- The spectral tensor could be simplified by neglecting the invariant terms within the $\Phi^{*}_{\nu j \mu l}$ formulation, and approximating $R_{1122} = R_{2211}$, this is shown in Figures 7.3-7.6;
- Evolutionary optimisation could be used to find the optimum parameters that govern the spatial/temporal rate of decay of turbulence correlation functions.

We formulated the spectral tensor using an analytical model (6.1.19) informed by LES for the lengthscales and anti-correlation parameter a_1. This model has been used previously in [67] however the lengthscale parameters (c_0, c_1, c_2) were hand chosen in that paper to fit the acoustic predictions. In this thesis we optimise the lengthscales and a_1 against the now full turbulence data from the LES using an evolutionary algorithm described in Section 8.4.2 to obtain a more accurate model of the turbulence data for each correlation function and each jet as shown in Figures 5.10-5.13. This reduced the time taken for model determination since we do not rely on any hand-tuning. Using this model we also showed that we can take $\tilde{k}_T = 0$ in (6.1.19) since it has negligible impact on the spectral tensor and the acoustic predictions as shown in Figures 6.15, 6.16, 7.9-7.12. We also found from these figures that for both heated jets setting $a_1 = 0$ also had negligible impact on the spectral tensor and acoustic predictions, however this parameter remains important for isothermal jets as it affects the high frequency decay.

Universality

One of the main questions we posed in this thesis was whether there existed universality in the turbulence length scale parameters for jet noise prediction? We discovered:

- It is not possible to have a 'universal correlation function' because the spatial decay is dependant on correlation function, as shown in Figures 5.14-5.16;
- There is universality across acoustic Mach number for all correlation functions;
- There is not universality across jet temperature ratio for some correlation functions.

Although we found that universality did not exist across temperature ratio for some correlation functions, we did find that the peak noise ($\theta = 30^{\circ}, St = 0.2$) could in fact be captured by such universal length scales across temperature and Mach number as shown in Figures 7.15-7.18. So if only the peak noise is desired, the length scales in Table 5.8 could give a reasonable estimation for any subsonic jet (between $Ma = 0.5 - 0.9$) at any temperature ratio (between $TR = 1 - 2.7$).

Jet surface interaction

- By including the anti-correlation parameter (a_1) in the turbulence model for R_{22} (see (8.4.3)) it was possible to obtain both a better representation of the turbulence, and better acoustic predictions as shown in Figures 8.29 and 8.31;
- Evolutionary optimisation can be used to find the optimal turbulence and acoustic parameters for agreement with turbulence and acoustic data;
- The acoustic model can be used for different vertical plate locations when parameters governing the meanflow profile are optimised for acoustic predictions.

We also investigated various optimisation algorithms to find the optimal parameters and found MP-AIDEA gave the optimum results in the shortest

time. However, it was also noted that a non-evolutionary algorithm, multistart, could also be used if time was a limiting factor since it is roughly two times faster and still gives more optimal results compared to hand-tuning.

When using the acoustic model for different vertical plate locations it was necessary to modify the meanflow profile. In the absence of experimental/ computational meanflow data we instead allow the meanflow to change by including the meanflow parameters within the acoustic optimisation.

10.2 Future Work

Acoustic modelling will always require parameters which govern the rate of spatial/temporal decay and anti-correlation of the turbulence. In this thesis we have obtained these parameters through mathematical optimisation of an analytical turbulence model against the LES turbulence data. In doing so we have made several assumptions such as the functional form itself and that the lengthscales c_i and convective velocity U_c are constant, all of which could be checked in future work.

We also assumed that the meanflow is parallel which allowed us to simplify the Green's function solution. Future work therefore could consider a non-parallel flow which could result in better acoustic predictions at $\theta = 30^{\circ}$.

As noted in Chapter 7, our acoustic predictions tend to under-predict the high frequencies. This could be due to our assumption that the length scales do not depend on frequency. Therefore, another consideration for future work is to look at frequency dependent length scales and see if the acoustic spectrum is better captured at the high frequencies.

In Chapter 8, we noted that when using the acoustic model for various vertical plate locations it was necessary to optimise the meanflow parameters for each location. This was to enable a change in meanflow profile which will occur when the plate is moved, however due to the lack of experimental/computational meanflow data it is uncertain as to how it will change. Therefore, future work could involve obtaining this data and implementing it into the model to remove the need for this optimisation which will increase the generality of the model and improve the predictive capability.

In our unified model we have assumed that the coupling terms between jet

noise and edge noise can be neglected, so future work can further investigate the coupling terms. Additionally, we have only considered edge noise for cold jets, so it would be interesting to check if heating has an effect on edge noise.

Currently the workflow for calculating the jet noise predictions is complicated and somewhat disjointed with several codes to calculate correlations, spectral tensors and propagators separately, which are finally combined to calculate the acoustic predictions. To improve ease of use and potentially have industrial applications it would be useful to merge the codes and simplify the input parameters to reduce the skill required to operate it. Since we have found universality in the turbulence correlation scales, this could allow a simplified tool to be created.

The hope is that the work we have conducted in this thesis will lay the foundation for any such future study.

Appendix A

Goldstein's Acoustic Analogy 2002

A.1 Derivation

Goldstein split the fluid variables in (3.1.2)-(3.1.4) into a 'base' component and a fluctuating component, i.e. $p = \bar{p} + p'$, $\rho = \bar{\rho} + \rho'$, $h_0 = \tilde{h_0} + h_0'$, $v_i = \tilde{v}_i + v'$, where the overbar denotes time averaging, i.e.

$$\overline{p} = \frac{1}{2T} \lim_{T \to \infty} \int_{-T}^{T} p(\boldsymbol{y}, \tau) d\tau$$

and the tilde denotes Favre averaging, i.e. $\tilde{v}_i = \overline{\rho v_i}/\overline{\rho}$.

The time averaged Euler equations are derived in [85] and given by:

$$\frac{\partial}{\partial y_j}(\overline{\rho}\tilde{v}_j) = 0 \tag{A.1.1}$$

$$\frac{\partial}{\partial y_j}(\overline{\rho}\widetilde{v_j v_i}) + \frac{\partial \bar{p}}{\partial y_i} = \frac{\partial \tilde{T}_{ij}}{\partial y_j} \qquad i = 1, ..3 \tag{A.1.2}$$

$$\frac{\partial}{\partial y_j}(\overline{\rho}\tilde{v}_j\tilde{h}_0) = \frac{1}{2}\frac{\partial}{\partial y_j}(v_j\tilde{T}_{kk}) + \frac{\partial \tilde{H}_j}{\partial y_j} \tag{A.1.3}$$

where $\tilde{T}_{ij} = -\overline{\rho}\widetilde{(v_i' v_j')}$ and $\tilde{H}_j = \tilde{H}_j = \overline{\rho}\widetilde{(v_j' h_0')}$.

These time averaged equations can then be subtracted from the original Euler equations as was done by Goldstein (2002)[125].

A.1.1 Mass Equation

$$\frac{\partial}{\partial \tau}(\bar{\rho}+\rho') = \frac{\partial}{\partial y_j}(\bar{\rho}+\rho')(\tilde{v}_j + v_j') - \frac{\partial}{\partial y_j}(\overline{\rho}\tilde{v}_j) = 0 \tag{A.1.4}$$

Clearly $\partial\bar{\rho}/\partial\tau = 0$, hence this equation simplifies to:

$$\frac{\partial \rho'}{\partial \tau} + \frac{\partial}{\partial y_j}(\rho'\tilde{v}_j + \rho v_j') = 0 \tag{A.1.5}$$

Goldstein (2002) introduced a nonlinear variable u_j which represents the momentum fluctuation, i.e. $u_j = \rho v_j'$, this leads to the equation:

$$\boxed{\frac{\partial \rho'}{\partial \tau} + \frac{\partial}{\partial y_j}(\rho'\tilde{v}_j + u_j) = 0} \tag{A.1.6}$$

A.1.2 Momentum Equation

Likewise, subtracting the time averaged momentum equations from the full Euler equation gives:

$$\begin{aligned}&\frac{\partial}{\partial \tau}(\bar{\rho}+\rho')(\tilde{v}_i + v_i') + \frac{\partial}{\partial y_j}(\bar{\rho}+\rho')(\tilde{v}_i + v_i')(\tilde{v}_j + v_j') + \frac{\partial}{\partial y_j}(\bar{p}+p') \\ &- \frac{\partial}{\partial y_j}(\overline{\rho v_j v_i}) - \frac{\partial \bar{p}}{\partial y_j} = -\frac{\partial \tilde{T}_{ij}}{\partial y_j} \quad i = 1,..3\end{aligned} \tag{A.1.7}$$

which simplifies to

$$\frac{\partial}{\partial \tau}(u_i + \rho'\tilde{v}_i) + \frac{\partial}{\partial y_j}(u_i\tilde{v}_j + \rho'\widetilde{v_j v_i} + u_j\tilde{v}_i + \delta_{ij}p') = \frac{\partial T'_{ij}}{\partial y_j} \quad i = 1,..3 \tag{A.1.8}$$

where $T'_{ij} = -(\rho v_i' v_j' - \bar{\rho}\widetilde{v_i' v_j'})$

Goldstein (2002) then introduced a tensor $\tilde{\tau}_{ij} = \delta_{ij}\bar{p} + \bar{\rho}\widetilde{v_i' v_j'}$. Then using the time averaged momentum equation (A.1.2) the spatial derivative is:

$$\frac{\partial}{\partial y_j}\bar{\rho}\widetilde{v}_i\tilde{v}_j = -\frac{\partial}{\partial y_j}\tilde{\tau}_{ij} \tag{A.1.9}$$

Then using the time averaged continuity equation (A.1.1) this reduces to:

$$\tilde{v}_j\frac{\partial \tilde{v}_i}{\partial y_j} = -\frac{1}{\bar{\rho}}\frac{\partial \tilde{\tau}_{ij}}{\partial y_j} \tag{A.1.10}$$

The red terms in (A.1.8) can be rewritten as:

$$\tilde{v}_i\Big[\frac{\partial \rho'}{\partial \tau} + \frac{\partial u_j}{\partial y_j} + \frac{\partial}{\partial y_j}\rho'\tilde{v}_j\Big] + u_j\frac{\partial \tilde{v}_i}{\partial y_j} + \rho'\tilde{v}_j\frac{\partial \tilde{v}_i}{\partial y_j} \tag{A.1.11}$$

where the square brackets are equal to zero using (A.1.6), and the last term can be rewritten using (A.1.10) resulting in:

$$-\frac{\rho'}{\bar{\rho}}\frac{\partial\tilde{\tau}_{ij}}{\partial y_j}+u_j\frac{\partial\tilde{v}_i}{\partial y_j} \tag{A.1.12}$$

which gives the final result for the momentum equation:

$$\boxed{\frac{\partial u_i}{\partial\tau}+\frac{\partial}{\partial y_j}(u_i\tilde{v}_j)+\frac{\partial p'}{\partial y_i}+u_j\frac{\partial\tilde{v}_i}{\partial y_j}-\left(\frac{\rho'}{\bar{\rho}}\right)\frac{\partial\tilde{\tau}_{ij}}{\partial y_j}=\frac{\partial T'_{ij}}{\partial y_j}\qquad i=1,..3.} \tag{A.1.13}$$

A.1.3 Energy Equation

Similarly we subtract the time averaged energy equation from the full energy equation. The stagnation enthalpy is expanded as $h_0 = h + v^2/2$, which after splitting variables into their base flow + fluctuating components becomes $h_0 = \tilde{h} + h' + (\tilde{v}_i + v'_i)^2/2$. Therefore we can say $h_0 = \tilde{h}_0 + h'_0$, where $\tilde{h}_0 = \tilde{h} + \tilde{v}_i^2/2$ and $h'_0 = h' + \tilde{v}_i v'_i + v_i'^2/2$. So the energy equation is:

$$\begin{aligned}
&\frac{\partial}{\partial\tau}\left[(\bar{\rho}+\rho')(\tilde{h}+h')-(\bar{p}+p')\right]+\frac{1}{2}\frac{\partial}{\partial\tau}(\bar{\rho}+\rho')(\tilde{v}_j+v'_j)^2+\frac{\partial}{\partial y_j}(\bar{\rho}+\rho')(\tilde{v}_i+v'_i)(\tilde{h}+h')\\
&+\frac{1}{2}\frac{\partial}{\partial y_j}(\bar{\rho}+\rho')(\tilde{v}_j+v'_j)(\tilde{v}_i+v'_i)^2-\frac{\partial}{\partial y_j}(\bar{\rho}\tilde{v}_j\tilde{h}_0)\\
&=\frac{1}{2}\frac{\partial}{\partial y_j}(v_j\tilde{T}_{kk})-\frac{\partial\tilde{H}_j}{\partial y_j}
\end{aligned} \tag{A.1.14}$$

This equation is simplified to:

$$\begin{aligned}
&\frac{\partial}{\partial\tau}\left[\rho'\tilde{h}+\rho h'+\frac{1}{2}\rho'\tilde{v}^2+u_i\tilde{v}_i-p'\right]+\frac{\partial}{\partial y_j}\left[(\rho'\tilde{h}+\rho h')\tilde{v}_j+\frac{1}{2}\rho'\tilde{v}_j\tilde{v}^2+u_i\tilde{v}_i\tilde{v}_j+u_j\tilde{h}_0\right]\\
&=\frac{1}{2}\frac{\partial T'_{kk}}{\partial\tau}+\frac{1}{2}\frac{\partial}{\partial y_j}(v_j\tilde{T}_{kk})+\frac{\partial\tilde{H}_j}{\partial y_j}
\end{aligned} \tag{A.1.15}$$

where $\tilde{H}_j = -(\rho v'_j h'_0 - \bar{\rho}\widetilde{v'_j h'_0})$. The red term can be expanded:

$$\begin{aligned}
\rho'\tilde{h}+\rho h' &= \rho'\tilde{h}+(\bar{\rho}+\rho')(h-\tilde{h})\\
&= \rho h-\bar{\rho}\tilde{h}\\
&= \rho h-\overline{\rho h}
\end{aligned} \tag{A.1.16}$$

Then using the perfect gas assumption $p = \rho RT$, $h = c_P T$, $\rho h = \frac{\gamma}{\gamma-1}p$, therefore:

$$\rho'\tilde{h} + \rho h' = \frac{\gamma p}{\gamma - 1} - \overline{\frac{\gamma}{\gamma - 1}p} = \frac{\gamma}{\gamma - 1}p' \tag{A.1.17}$$

Therefore, (A.1.15) can be written as:

$$\begin{aligned}&\frac{\partial}{\partial\tau}\left[\frac{p'}{\gamma-1} + \frac{1}{2}\rho'\tilde{v}^2 + u_i\tilde{v}_i\right] + \frac{\partial}{\partial y_j}\left[\frac{\gamma}{\gamma-1}p'\tilde{v}_j + \frac{1}{2}\rho'\tilde{v}_j\tilde{v}^2 + u_i\tilde{v}_i\tilde{v}_j + u_j\tilde{h}_0\right] \\ &= \frac{1}{2}\frac{\partial T'_{kk}}{\partial\tau} + \frac{1}{2}\frac{\partial}{\partial y_j}(\tilde{v}_j T'_{kk}) + \frac{\partial H'_j}{\partial y_j}\end{aligned} \tag{A.1.18}$$

To simplify the equation further we replace $\tilde{h}_0$ by its definition and split $\gamma p'\tilde{v}_j/(\gamma-1) = p'\tilde{v}_j/(\gamma-1) + p'\tilde{v}_j$. This leads to the LHS of the equation becoming:

$$\begin{aligned}&\underbrace{\frac{1}{\gamma-1}\frac{\partial p'}{\partial\tau} + \frac{1}{\gamma-1}\frac{\partial}{\partial y_j}(p'\tilde{v}_j) + \frac{\partial}{\partial y_j}(u_j\tilde{h})}_{\text{term 1}} \\ &\underbrace{+\frac{\partial}{\partial\tau}\left[\frac{1}{2}\rho'\tilde{v}^2 + u_i\tilde{v}_i\right] + \frac{\partial}{\partial y_j}\left[p'\tilde{v}_j + \frac{1}{2}\rho'\tilde{v}_j\tilde{v}^2 + u_i\tilde{v}_i\tilde{v}_j + u_j\frac{1}{2}\tilde{v}^2\right]}_{\text{term 2}}\end{aligned} \tag{A.1.19}$$

Then term 2 can be further simplified by looking first at the red terms and using the definition of $\tilde{\tau}_{ij}$:

$$\begin{aligned}\frac{\partial}{\partial\tau}(u_i\tilde{v}_i) + \frac{\partial}{\partial y_j}(u_i\tilde{v}_i\tilde{v}_j) &= \tilde{v}_i\frac{\partial u_i}{\partial\tau} + \frac{\partial}{\partial y_j}(u_i\tilde{v}_i\tilde{v}_j) \\ &= \tilde{v}_i\frac{\partial u_i}{\partial\tau} + u_i\tilde{v}_j\frac{\partial\tilde{v}_i}{\partial y_j} + \tilde{v}_i\frac{\partial}{\partial y_j}(u_i\tilde{v}_j) \\ &= \tilde{v}_i\frac{\partial u_i}{\partial\tau} + \tilde{v}_i\frac{\partial}{\partial y_j}(u_i\tilde{v}_j) - \frac{u_i}{\bar{\rho}}\frac{\partial\tau'_{ij}}{\partial y_j}\end{aligned} \tag{A.1.20}$$

Therefore the second term becomes:

$$\begin{aligned}\text{term 2} = p'\frac{\partial\tilde{v}_j}{\partial y_j} - \frac{u_i}{\bar{\rho}}\frac{\partial\tau'_{ij}}{\partial y_j} + \\ + \left\{\frac{\partial}{\partial\tau}\left[\frac{1}{2}\rho'\tilde{v}^2\right] + \frac{\partial}{\partial y_j}\left[\frac{1}{2}\rho'\tilde{v}_j\tilde{v}^2 + u_j\frac{1}{2}\tilde{v}^2\right] + \tilde{v}_i\frac{\partial u_i}{\partial\tau} + \tilde{v}_i\frac{\partial}{\partial y_j}(u_i\tilde{v}_j) + \tilde{v}_j\frac{\partial p'}{\partial y_j}\right\}\end{aligned} \tag{A.1.21}$$

when we have also expanded the $\partial(p'\tilde{v}_j)/\partial y_j$ term. The red term can be written as:

$$\frac{1}{2}\frac{\partial}{\partial\tau}(\rho'\tilde{v}^2)+\frac{1}{2}\frac{\partial}{\partial y_j}(\rho'\tilde{v}_j\tilde{v}^2+u_j\tilde{v}^2)=\frac{1}{2}\tilde{v}^2\underbrace{\left[\frac{\partial\rho'}{\partial\tau}+\frac{\partial}{\partial y_j}(\rho'\tilde{v}_j)+\frac{\partial u_j}{\partial y_j}\right]}_{=0}+\rho'\tilde{v}_j\tilde{v}_i\frac{\partial\tilde{v}_i}{\partial y_j}+u_j\tilde{v}_i\frac{\partial\tilde{v}_i}{\partial y_j}$$

The term in square brackets is equal to zero from the continuity equation (A.1.6). Again, we use $\tilde{\tau}_{ij}$ to replace $\rho'\tilde{v}_j\tilde{v}_i\partial\tilde{v}_i/\partial y_j$. Inserting this back into the curly brackets gives:

$$\left\{\tilde{v}_i\frac{\partial u_i}{\partial\tau}+\tilde{v}_i\frac{\partial}{\partial y_j}(u_i\tilde{v}_j)+\tilde{v}_i\frac{\partial p'}{\partial y_i}-\tilde{v}_i(\frac{\rho'}{\bar{\rho}})\frac{\partial\tau'_{ij}}{\partial y_j}+u_j\tilde{v}_i\frac{\partial\tilde{v}_i}{\partial y_j}\right\} \tag{A.1.22}$$

Note that this is equivalent to $\tilde{v}_i\partial T'_{ij}/\partial_j$. Hence, term 2 reduces to:

$$\text{term 2}=p'\frac{\partial\tilde{v}_j}{\partial y_j}-\frac{u_i}{\bar{\rho}}\frac{\partial\tau'_{ij}}{\partial y_j}+\tilde{v}_i\frac{\partial T'_{ij}}{\partial y_j} \tag{A.1.23}$$

Inserting both term 1 and 2 back into the energy equation gives:

$$\boxed{\frac{1}{(\gamma-1)}\frac{\partial p'}{\partial\tau}+\frac{1}{(\gamma-1)}\frac{\partial}{\partial y_j}(p'\tilde{v}_j)+p'\frac{\partial\tilde{v}_j}{\partial y_j}+\frac{\partial}{\partial y_j}(u_j\tilde{h})-\frac{u_i}{\bar{\rho}}\frac{\partial\tau'_{ij}}{\partial y_j}=Q\prime} \tag{A.1.24}$$

where

$$Q'=-\tilde{v}_j\frac{\partial T'_{ij}}{\partial y_i}+\frac{1}{2}\delta_{ij}\frac{\partial T'_{ij}}{\partial\tau}+\frac{1}{2}\delta_{ij}\frac{\partial}{\partial y_k}(\tilde{v}_kT'_{ij})+\frac{\partial H'_j}{\partial y_j} \tag{A.1.25}$$

A.1.4 Summary

It is convenient to replace $\tilde{\tau}_{ij}$ with its definition which gives the final equations in Goldstein's acoustic analogy (2002):

$$\frac{\partial\rho'}{\partial\tau}+\frac{\partial}{\partial y_j}(\rho'\tilde{v}_j+u_j)=0 \tag{A.1.26}$$

$$\frac{\partial u_i}{\partial\tau}+\frac{\partial}{\partial y_j}(\tilde{v}_ju_j)+\frac{\partial p'}{\partial y_j}+\tilde{u}_j\frac{\partial\tilde{v}_i}{\partial y_j}+\rho'\tilde{v}_k\frac{\partial\tilde{v}_i}{\partial y_k}=\frac{\partial T'_{ij}}{\partial y_j}\qquad i=1,2,3. \tag{A.1.27}$$

$$\frac{1}{(\gamma-1)}\frac{\partial p'}{\partial\tau}+\frac{1}{(\gamma-1)}\frac{\partial}{\partial y_j}(p'\tilde{v}_j)+p'\frac{\partial\tilde{v}_j}{\partial y_j}+\frac{\partial}{\partial\ y_j}(u_j\tilde{h})+u_i\tilde{v}_k\frac{\partial\tilde{v}_i}{\partial y_k}=Q' \tag{A.1.28}$$

Now we have a set of differential equations which have a linear operator acting on the fluid variables, meaning that they can be solved using Green's theorem.

A.2 Standard Solution to a Sturm-Liouville Problem

A Sturm-Liouville problem is of the form:

$$\frac{d}{dr}\Big[P(r;k_1,\omega)r\frac{d}{dr}\Big]G_0^{(m)}(r|R;k_1,\omega)+rQ(r;k_1,\omega)G_0^{(m)}(r|R;k_1,\omega)=-\delta(R-r) \tag{A.2.1}$$

Now, by properties of the delta function the right hand side of this equation is zero when $r \neq R$, and can therefore be written as:

$$L_0^{(m)}\Big[G_0^{(m)}(r|R;\omega)\Big]=0 \tag{A.2.2}$$

There will be two independent solutions for this equation, which we can define as $v_1(r), v_2(r)$. Since these are linearly independent we can define two new variables (w_1, w_2) which are a combination of them, where w_1 satisfies the boundary conditions for $r < R$ and w_2 satisfies the boundary conditions for $r > R$.

$$\begin{aligned} w_1(r) &= C_1v_1(r)+C_2v_2(r) \\ w_2(r) &= C_3v_1(r)+C_4v_2(r) \end{aligned} \tag{A.2.3}$$

However, the Green's function must also be continuous across $r = R$, therefore it is defined as:

$$G_0^{(m)}(r|R)=\begin{cases} w_1(r)w_2(R) & r<R \\ w_2(r)w_1(R) & r>R \end{cases} \tag{A.2.4}$$

Now, look at the jump in the derivative of $G_0^{(m)}$:

$$\begin{aligned} \Delta G_{0,r}^{(m)}(r|R;k_1,\omega) &= \lim_{\epsilon\to 0}\Big[G_{0,r}^{(m)}(R+\epsilon|R;k_1,\omega)-G_{0,r}^{(m)}(R-\epsilon|R;k_1,\omega)\Big] \\ &= \lim_{\epsilon\to 0}\Big[w_1(R)w_{2,r}(R+\epsilon)-w_2(R)w_{1,r}(R-\epsilon)\Big] \\ &= w_1(R)w_{2,r}(R)-w_2(R)w_{1,r}(R) \\ &= W(w_1,w_2)|_R \end{aligned} \tag{A.2.5}$$

when the subscript r denotes a derivative with respect to r, and $W(w_1, w_2)$ is the Wronskian. Appendix A.2.2 shows that the jump must be $\Delta G_{0,r}^{(m)} = -1/(P(R)R)$. Therefore we define the invariant $J(w_1, w_2)$:

$$J(w_1,w_2)=-P(r;k_1,\omega)rW(w_1,w_2)|_r \tag{A.2.6}$$

Note, that by Abel's Theorem (shown in Appendix A.2.3), $J(w_1, w_2)$ is independent of r and can be evaluated anywhere along the radial axis, we evaluate at $r = R$ for convenience. Therefore, we can define the Green's function solutions to be:

$$G_0^{(m)}(r|R) = \begin{cases} \frac{w_1(r)w_2(R)}{J(w_1,w_2)} & r < R \\ \frac{w_2(r)w_1(R)}{J(w_1,w_2)} & r > R \end{cases} \tag{A.2.7}$$

which can be written as:

$$G_0^{(m)}(r|R) = \frac{w_1(r)w_2(R)H(R-r) + w_2(r)w_1(R)H(r-R)}{J(w_1, w_2)} \tag{A.2.8}$$

A.2.1 Verification of the Solution

This section inserts the solution for $G_0^{(m)}$ into the left hand side of (A.2.1) to verify that it does give the right hand side. First we need the first and second order derivatives for $G_0^{(m)}$:

$$\begin{aligned} G_{0,r}^{(m)}(r|R;k_1,\omega) = \frac{1}{J}\Big[& w_2(R)\Big(w_{1,r}(r)H(R-r) + w_1(r)H_r(R-r)\Big) \\ & + w_1(R)\Big(w_{2,r}(r)H(r-R) + w_2(r)H_r(r-R)\Big)\Big] \end{aligned} \tag{A.2.9}$$

Since the definition of $H_r(r) = \delta(r)$, this can be written as:

$$\begin{aligned} G_{0,r}^{(m)}(r|R;k_1,\omega) = \frac{1}{J}\Big[& w_2(R)\Big(w_{1,r}(r)H(R-r) - w_1(r)\delta(R-r)\Big) \\ & + w_1(R)\Big(w_{2,r}(r)H(r-R) + w_2(r)\delta(r-R)\Big)\Big] \end{aligned} \tag{A.2.10}$$

and since the Dirac-δ function is even those terms cancel leaving:

$$G_{0,r}^{(m)}(r|R;k_1,\omega) = \frac{1}{J}\Big[w_2(R)w_{1,r}(r)H(R-r) + w_1(R)w_{2,r}(r)H(r-R)\Big] \tag{A.2.11}$$

The differentiate again:

$$\begin{aligned} G_{0,rr}^{(m)}(r|R;k_1,\omega) = \frac{1}{J}\Big[& w_2(R)w_{1,rr}(r)H(R-r) - w_2(R)w_{1,r}\delta(R-r) \\ & + w_1(R)w_{2,rr}(r)H(r-R) + w_1(R)w_{2,r}(r)\delta(r-R)\Big] \end{aligned} \tag{A.2.12}$$

Again, using $\delta(r-R) = \delta(R-r)$ and the definition of the Wronskian gives:

$$\begin{aligned} G_{0,rr}^{(m)}(r|R;k_1,\omega) = \frac{1}{J}\Big[& w_2(R)w_{1,rr}(r)H(R-r) + w_1(R)w_{2,rr}(r)H(r-R) \\ & + \delta(R-r)W(w_1,w_2)_R\Big] \end{aligned} \tag{A.2.13}$$

Inserting these derivative into the LHS of (A.2.1), letting $\overline{P}(r) = rP(r)$ then gives:

$$\begin{aligned}
&\overline{P}_r(r)G^{(m)}_{0,r}(r|R) + \overline{P}(r)G^{(m)}_{0,rr}(r|R) + rQ(r)G^{(m)}_0(r|R) = \\
&= \frac{\overline{P}_r(r)}{J}\Big[w_2(R)w_{1,r}(r)H(R-r) + w_1(R)w_{2,r}(r)H(r-R)\Big] \\
&+ \frac{\overline{P}(r)}{J}\Big[w_2(R)w_{1,rr}(r)H(R-r) + w_1(R)w_{2,rr}(r)H(r-R) \\
&+ \delta(R-r)W(w_1,w_2)_R\Big] \\
&+ rQ(r)\Big[w_2(R)w_1(r)H(R-r) + w_2(r)w_1(R)H(r-R)\Big]
\end{aligned} \tag{A.2.14}$$

This can be rewritten as

$$\begin{aligned}
&\frac{H(R-r)}{J}w_2(R)\Big[\overline{P}_r(r)w_{1,r} + \overline{P}(r)w_{1,rr} + rQ(r)w_1\Big] \\
&+\frac{H(r-R)}{J}w_1(R)\Big[\overline{P}_r(r)w_{2,r} + \overline{P}(r)w_{2,rr} + rQ(r)w_2\Big] \\
&+ \frac{P(r)r}{J}W(w_1,w_2)\delta(R-r)
\end{aligned} \tag{A.2.15}$$

where the first two terms go to zero from the definition of w_1, w_2. Therefore inserting $J = -P(r)rW(w_1,w_2)$ the equation becomes:

$$\frac{P(r)r}{-P(r)rW(w_1,w_2)}W(w_1,w_2)\delta(R-r) = -\delta(R-r) \tag{A.2.16}$$

which is the right hand side of (A.2.1) and therefore confirms that w_1, w_2 are solutions to the problem.

A.2.2 Jump in the Green's Function

The jump in the Green's function can be derived through integrating the Sturm-Liouville problem from (A.2.1):

$$P(r;k_1,\omega)r\frac{d}{dr}G^{(m)}_0(r|R;k_1,\omega) + \underbrace{\int_0^r rQ(r;k_1,\omega)G^{(m)}_0(r|R;k_1,\omega)dr}_{f(r|R)} = -H(r-R)+\alpha(R) \tag{A.2.17}$$

which can be rearranged to

$$\frac{d}{dr}G^{(m)}_0(r|R;k_1,\omega) = -\frac{1}{P(r;k_1,\omega)r}\Big[H(r-R) + f(r|R) - \alpha(R)\Big] \tag{A.2.18}$$

Since there is a Heaviside function present it is obvious that there will be a jump in the derivative of G_0 at $r = R$. We define this jump as Δ and We look at a point slightly above (r^+) and below (r^-) $r = R$:

$$\begin{aligned}\Delta\frac{dG_0^{(m)}}{dr} = &-\frac{1}{P(r^+;k_1,\omega)r^+}\Big(H(r^+-R)+f(r^+|R)-\alpha(R)\Big)\\ &-\Big[-\frac{1}{P(r^-;k_1,\omega)r^-}\Big(H(r^--R)+f(r^-|R)-\alpha(R)\Big)\Big]\end{aligned} \tag{A.2.19}$$

By definition of the Heaviside function $H(r^+ - R) = 1$ and $H(r^- - R) = 0$. Therefore, when we take the limit $r^+ = r^- = R$ the jump is:

$$\Delta\frac{dG_0^{(m)}}{dr} = -2\frac{1}{P(R;k_1,\omega)R} \tag{A.2.20}$$

A.2.3 Abel's Theorem: $J(w_1, w_2)$ is a Constant in r

If the invariant is constant, then its derivative will be zero. This will be checked in this section.

We can write the derivative as:

$$J_r(w_1,w_2) = -\Big[\overline{P}_r(r)W(w_1,w_2)+\overline{P}W_r(w_1,w_2)\Big] \tag{A.2.21}$$

where the subscript denotes the derivative and $\overline{P}(r) = P(r)r$. The derivative of the Wronskian is given by:

$$\begin{aligned}W_r(w_1,w_2) &= w_{1,r}w_{2,r}+w_1w_{2,rr}-w_{2,3}w_{1,r}-w_2w_{1,rr}\\ &= w_1w_{2,rr}-w_2w_{1,rr}\end{aligned} \tag{A.2.22}$$

Therefore:

$$-J_r(w_1,w_2) = \overline{P}_r(w_1w_{2,r}-w_2w_{1,r})+\overline{P}(w_1w_{2,rr}-w_2w_{1,rr}) \tag{A.2.23}$$

Note that $\overline{P}_r w_{1,r} + \overline{P}w_{1,rr} + rQ(r)w_1 = 0$ from the definition of the problem, likewise for w_2. Therefore the derivative of J can be written as:

$$\begin{aligned}-J_r(w_1,w_2) &= w_1(\overline{P}_r w_{2,r}+\overline{P}w_{2,rr})-w_2(\overline{P}_r w_{1,r}+\overline{P}w_{1,rr})\\ &= w_1(-rQ(r)w_2)-w_2(-rQ(r)w_1)\\ &= 0\end{aligned} \tag{A.2.24}$$

Therefore, since the derivative w.r.t. r is zero, then $J(w_1, w_2)$ is constant and can be evaluated at any r.

Appendix B

Space-time LES: Additional Plots

B.1 Axisymmetric Turbulence

Figures B.1, B.2, and B.3 compare the axisymmetric and isotropic approximations [88] for both the diagonal and hermitian forms of the correlations for SP07, SP42, and SP46 respectively.

Figure B.4 then compares the approximations on the shear layer, confirming that the LES data is axisymmetric for all jets, and therefore the axisymmetric form of the acoustic spectrum can be used.

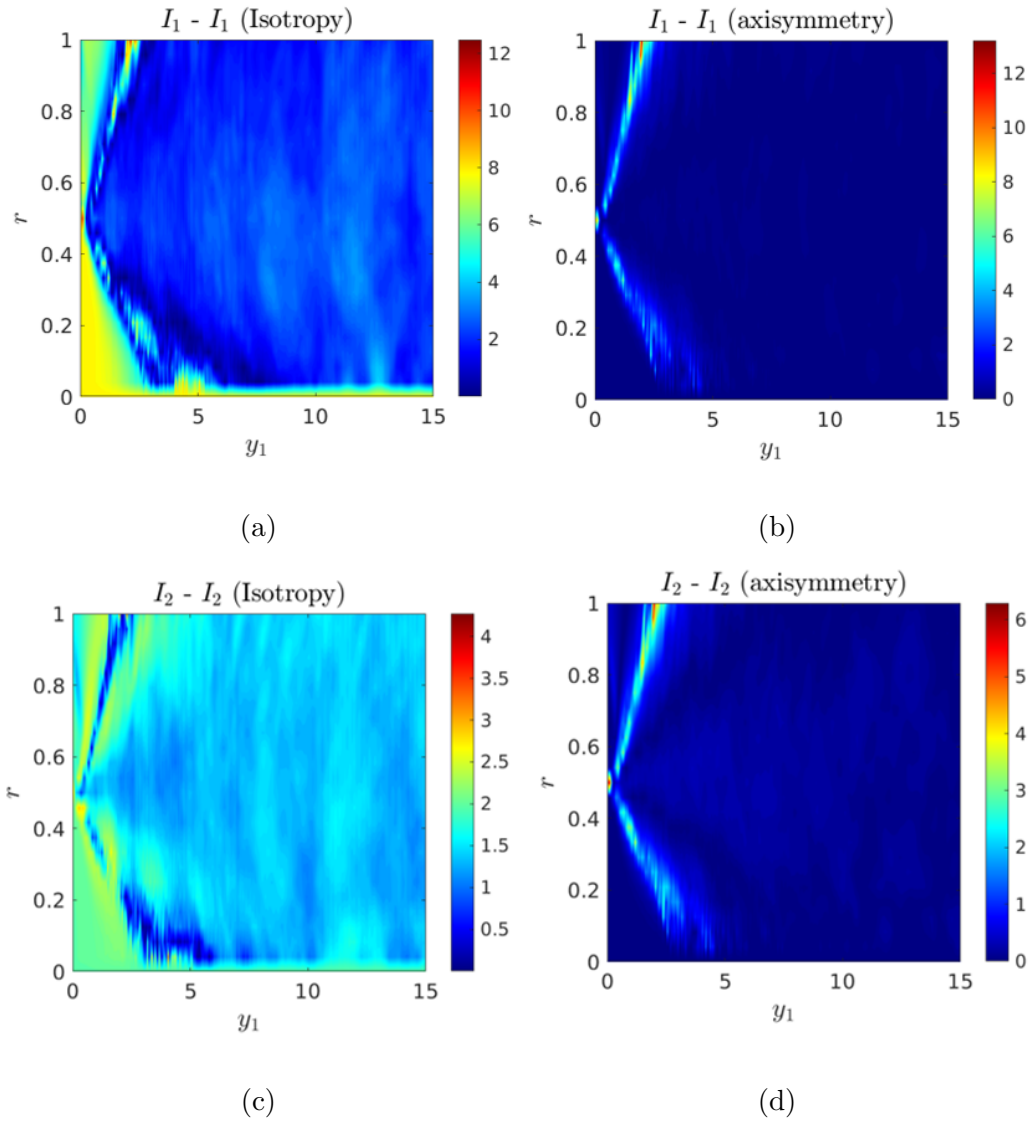

Figure B.1: SP07: Compare diagonal quadratic form using (a) isotropic and (b) axisymmetric approximations, and compare hermitian form using (c) isotropic and (d) axisymmetric approximations

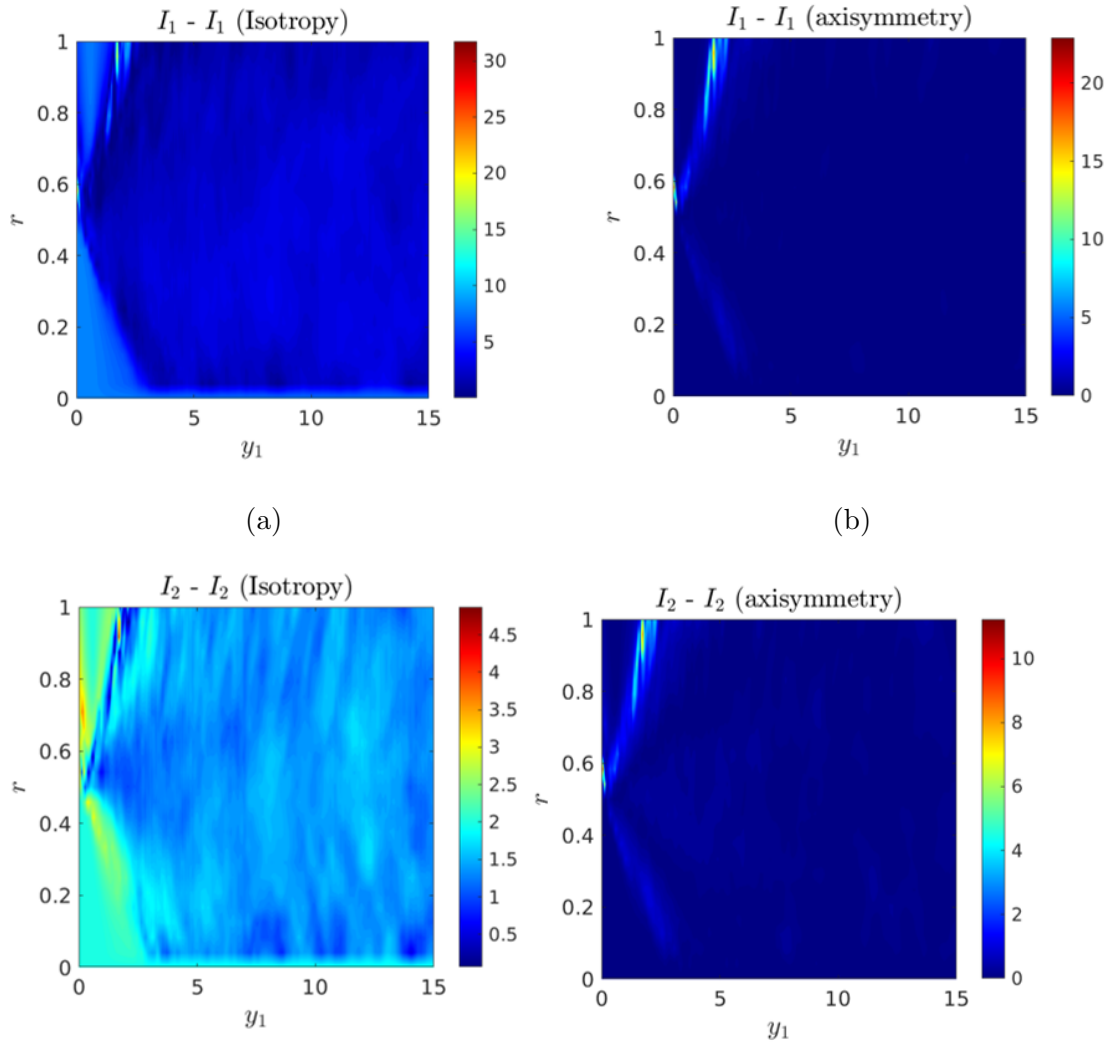

Figure B.2: SP42: Compare diagonal quadratic form using (a) isotropic and (b) axisymmetric approximations, and compare hermitian form using (c) isotropic and (d) axisymmetric approximations

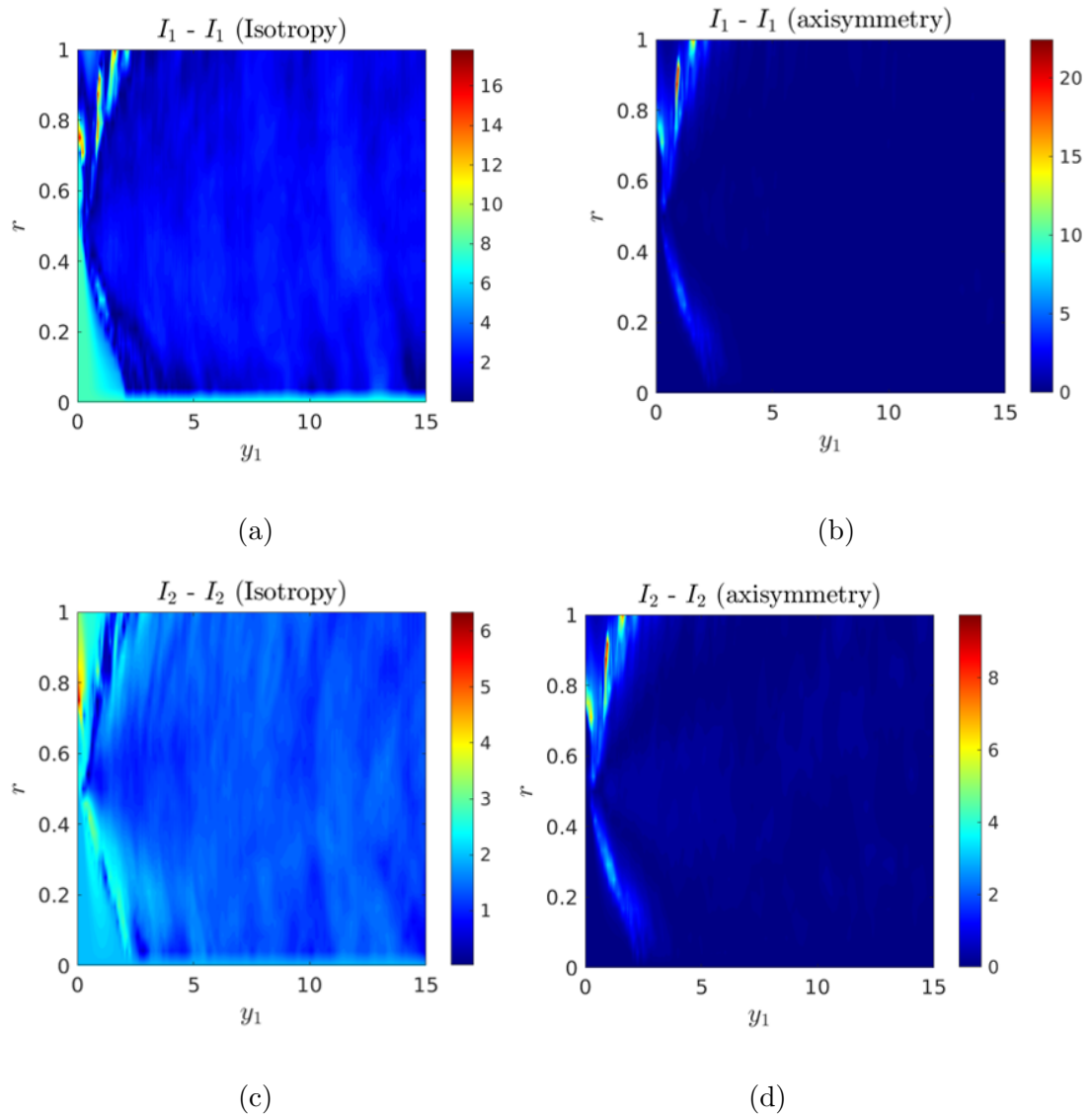

Figure B.3: SP46: Compare diagonal quadratic form using (a) isotropic and (b) axisymmetric approximations, and compare hermitian form using (c) isotropic and (d) axisymmetric approximations

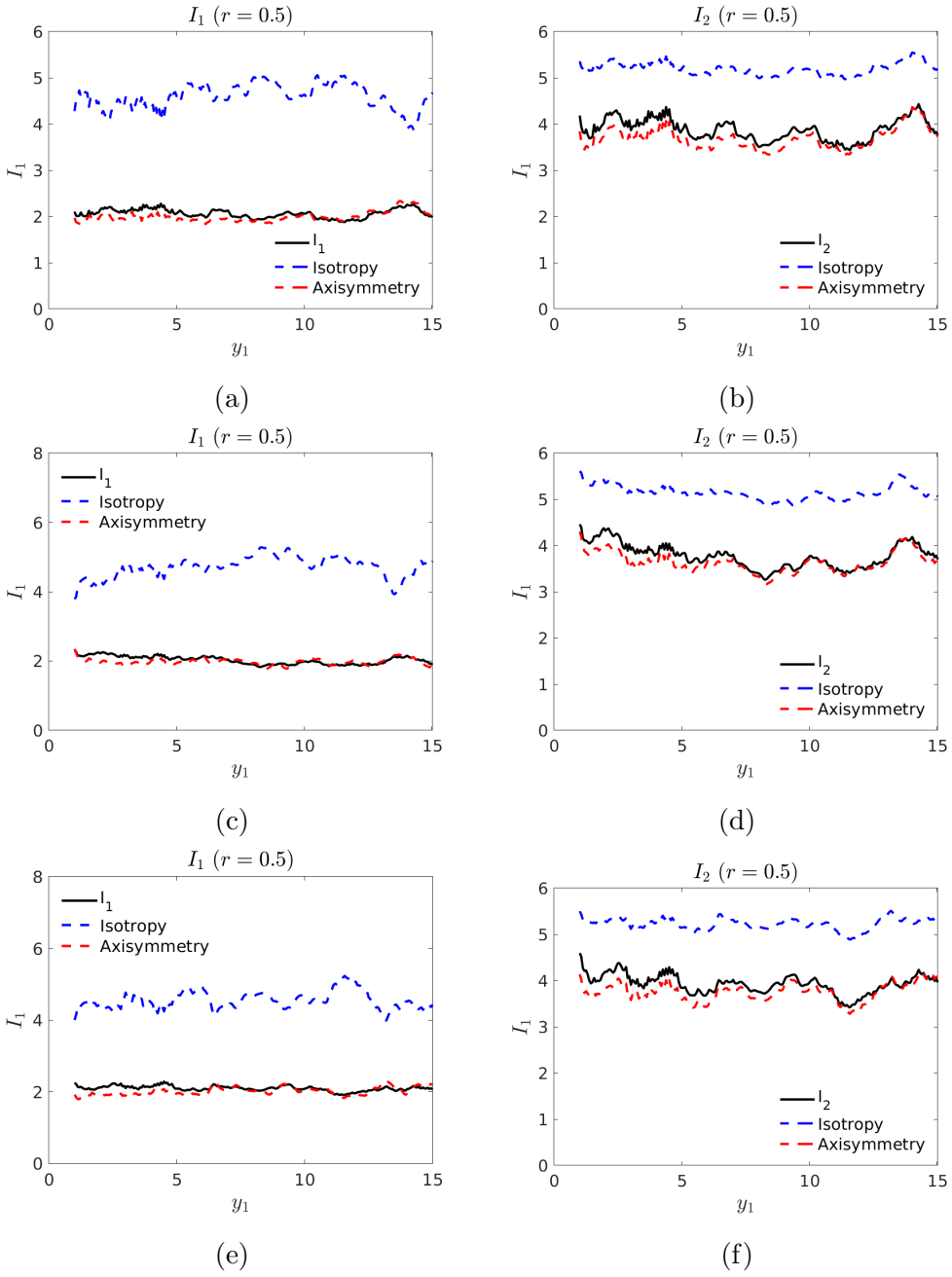

Figure B.4: Check the axisymmetry approximation on the shear layer using (a) SP07: diagonal form (b) SP07: hermitian form (c) SP42: diagonal form (d) SP42: hermitian form (e) SP46: diagonal form (f) SP46: hermitian form

B.2 Space-time Correlations

Figures B.5 and B.6 compare the optimised model with the numerical data for SP07 when $\eta_2 = 0$, and $\eta_1 = 0$ respectively. Similar to SP03, these show that in general the model fits the data well. Figures B.7 and B.8 compare the optimised model with the numerical data for SP42 for the momentum flux correlations when $\eta_2 = 0$, and $\eta_1 = 0$ respectively. Lastly, Figures B.9 and B.10 compare the optimised model with the numerical data for SP46 for the momentum flux correlations when $\eta_2 = 0$, and $\eta_1 = 0$ respectively, and Figures B.11 and B.12 compare the model for the coupling/enthalpy flux correlations.

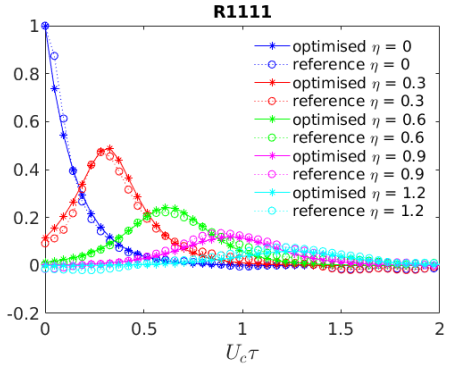

(a)

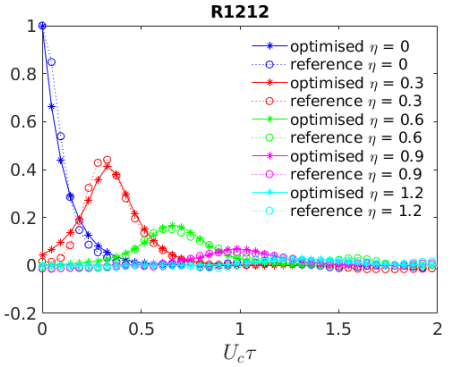

(b)

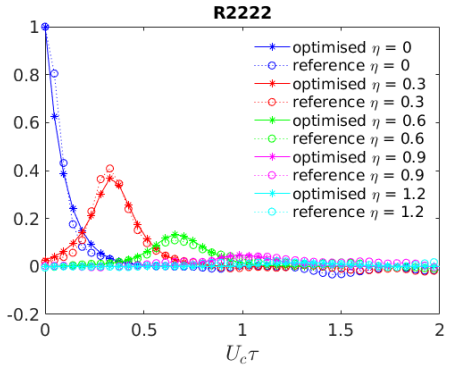

(c)

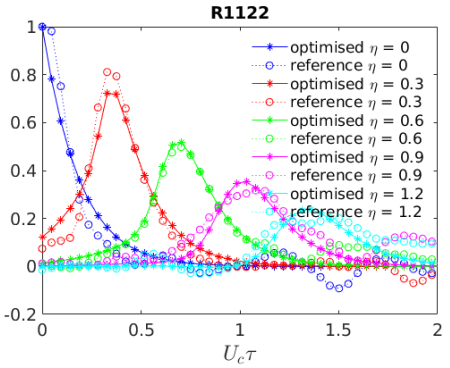

(d)

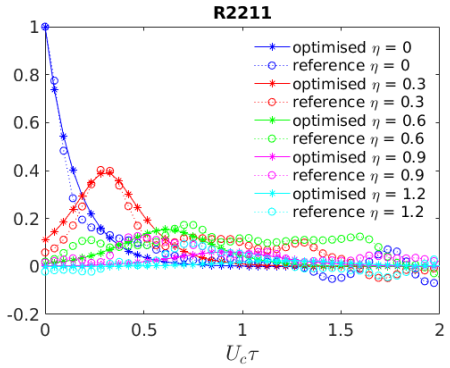

(e)

Figure B.5: SP07: comparison of the optimised model with the numerical data (when $\eta_2 = 0$) for (a) R_{1111} (b) R_{1212} (c) R_{2222} (d) R_{1122} (e) R_{2211}

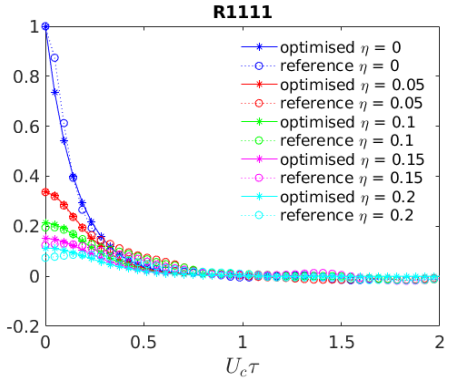

(a)

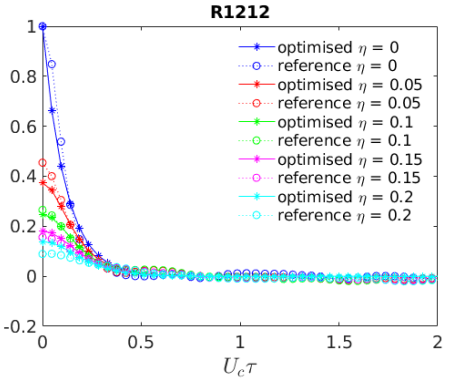

(b)

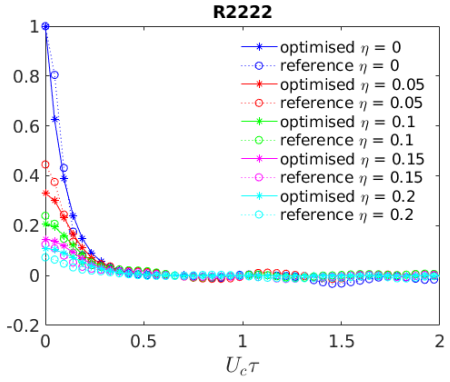

(c)

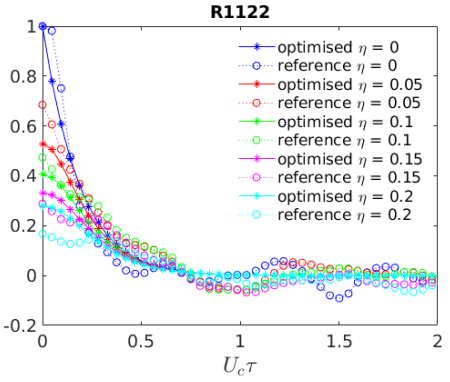

(d)

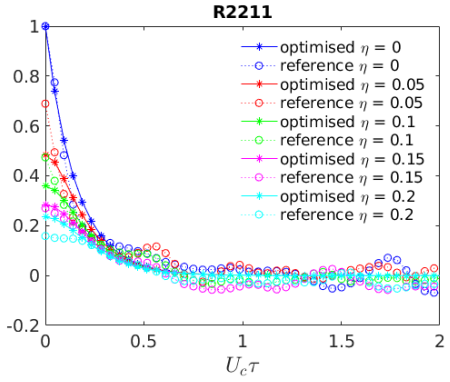

(e)

Figure B.6: SP07: comparison of the optimised model with the numerical data (when $\eta_1 = 0$) for (a) R_{1111} (b) R_{1212} (c) R_{2222} (d) R_{1122} (e) R_{2211}

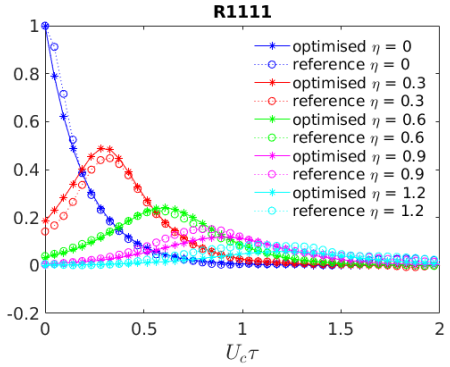

(a)

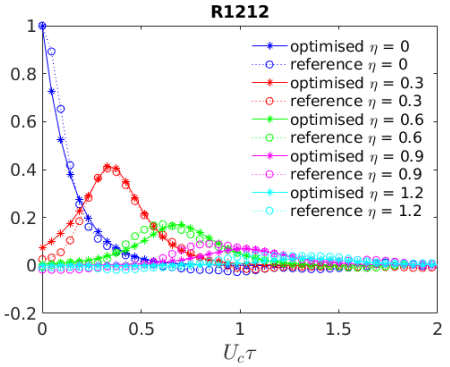

(b)

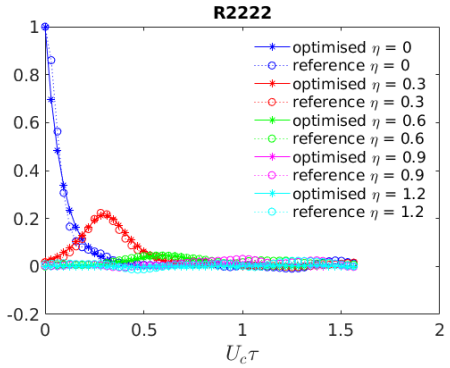

(c)

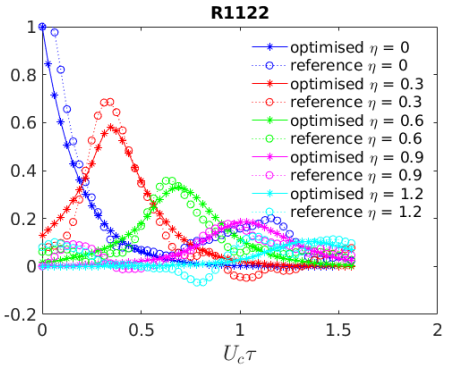

(d)

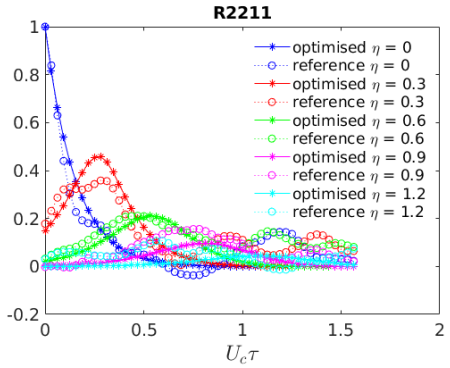

(e)

Figure B.7: SP42: comparison of the optimised model with the numerical data (when $\eta_2 = 0$) for (a) R_{1111} (b) R_{1212} (c) R_{2222} (d) R_{1122} (e) R_{2211}

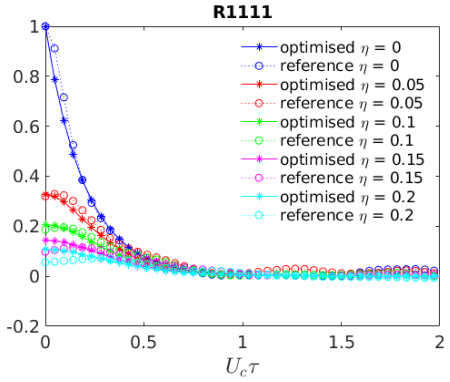

(a)

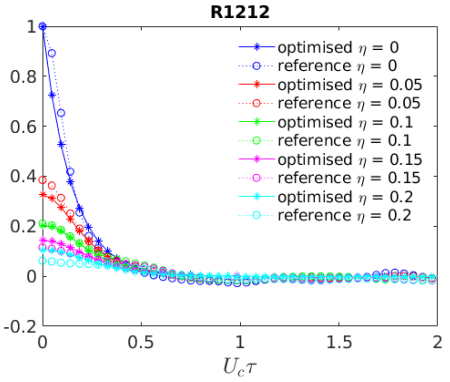

(b)

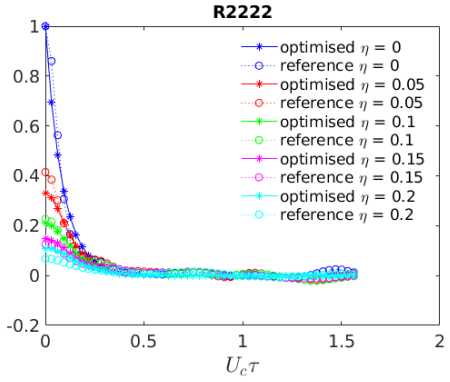

(c)

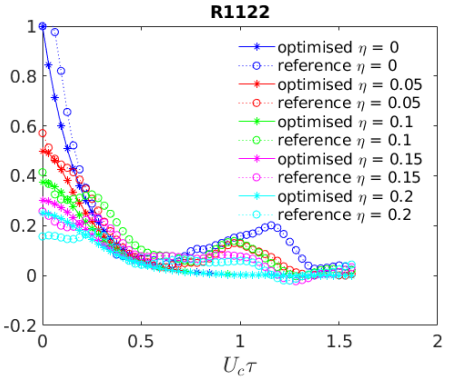

(d)

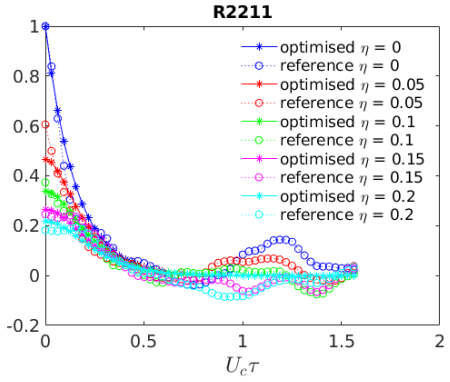

(e)

Figure B.8: SP42: comparison of the optimised model with the numerical data (when $\eta_1 = 0$) for (a) R_{1111} (b) R_{1212} (c) R_{2222} (d) R_{1122} (e) R_{2211}

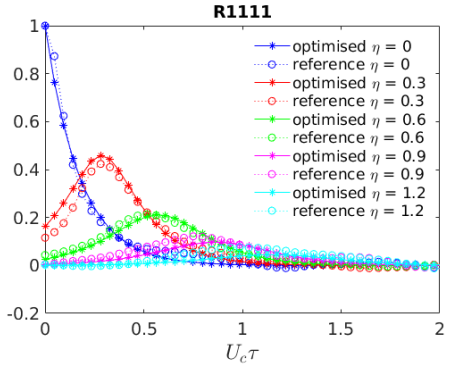

(a)

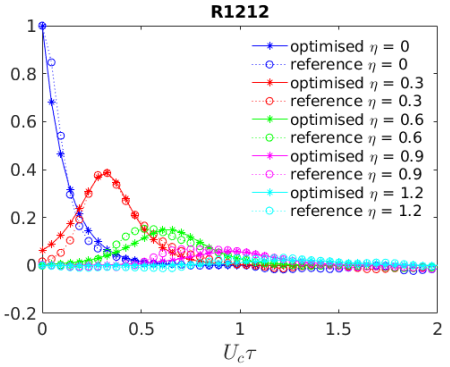

(b)

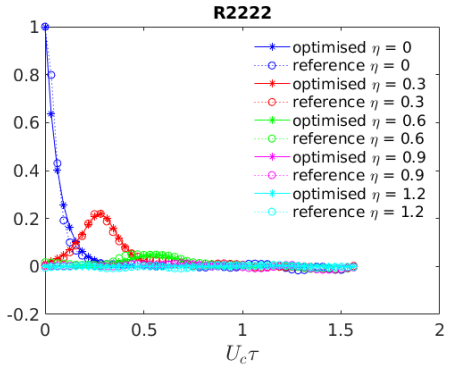

(c)

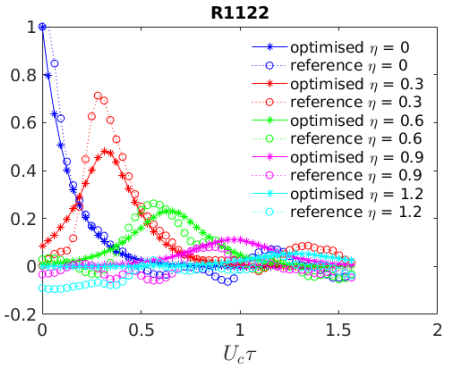

(d)

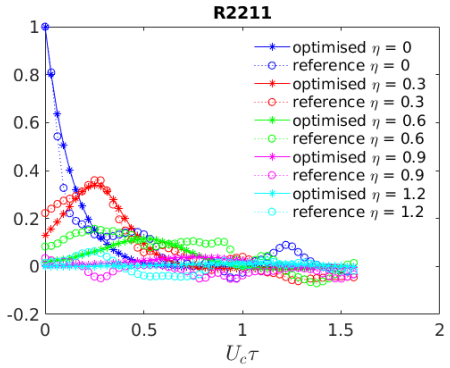

(e)

Figure B.9: SP46: comparison of the optimised model with the numerical data (when $\eta_2 = 0$) for (a) R_{1111} (b) R_{1212} (c) R_{2222} (d) R_{1122} (e) R_{2211}

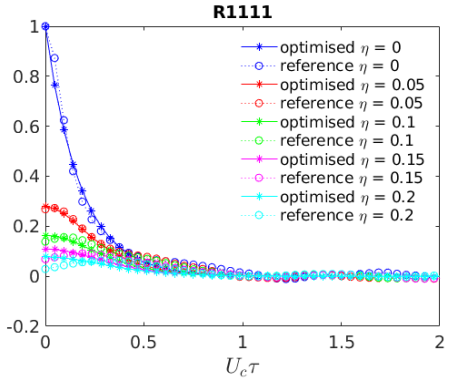

(a)

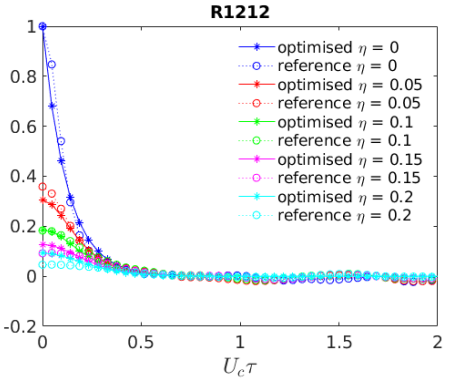

(b)

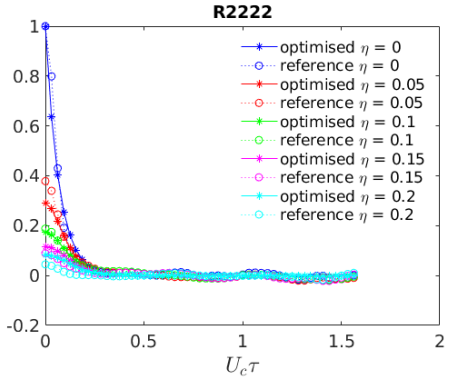

(c)

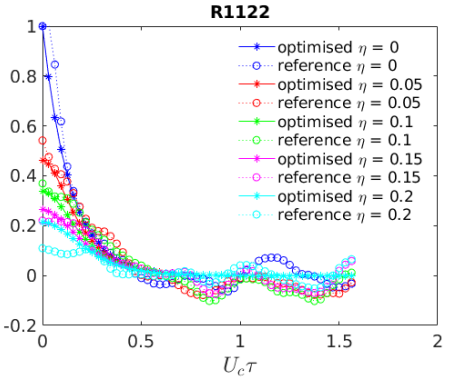

(d)

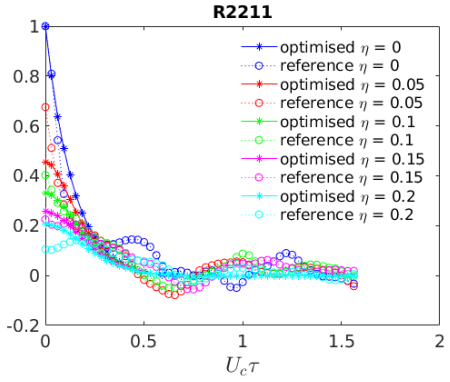

(e)

Figure B.10: SP46: comparison of the optimised model with the numerical data (when $\eta_1 = 0$) for (a) R_{1111} (b) R_{1212} (c) R_{2222} (d) R_{1122} (e) R_{2211}

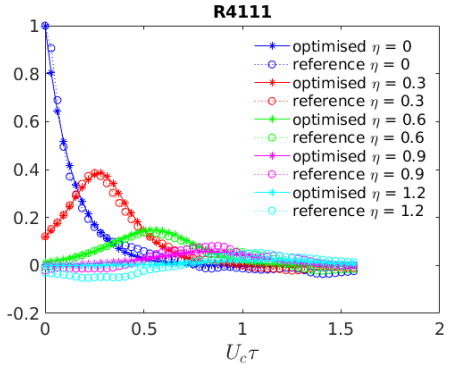

(a)

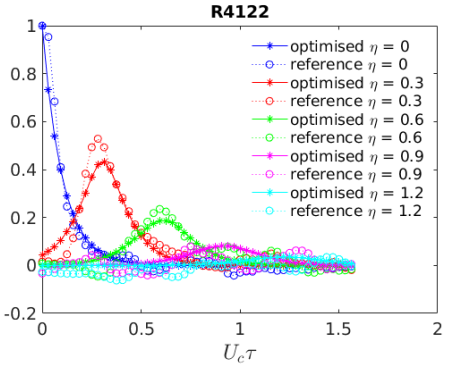

(b)

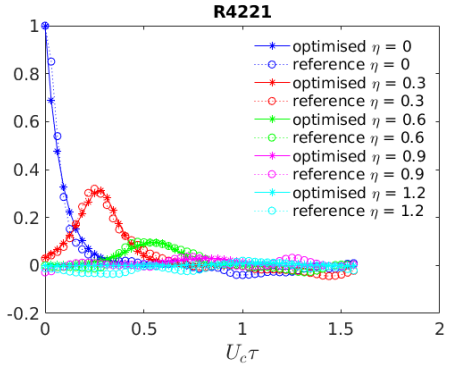

(c)

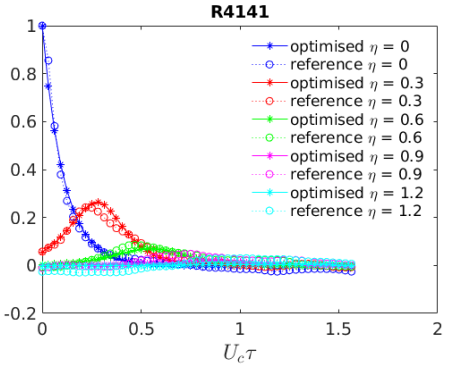

(d)

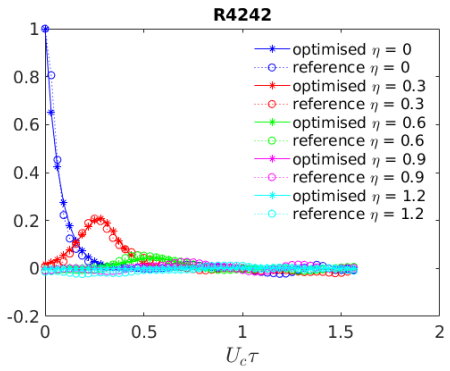

(e)

Figure B.11: SP46: comparison of the optimised model with the numerical data (when $\eta_2 = 0$) for coupling and enthalpy flux correlations (a) R_{4111} (b) R_{4122} (c) R_{4221} (d) R_{4141} (e) R_{4242}

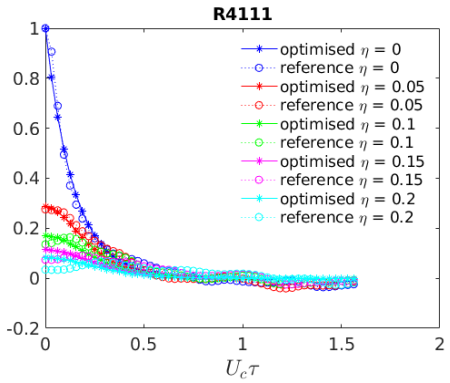

(a)

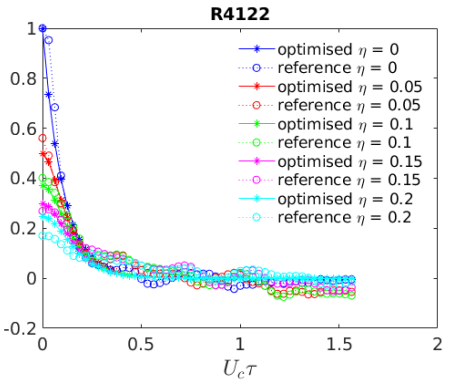

(b)

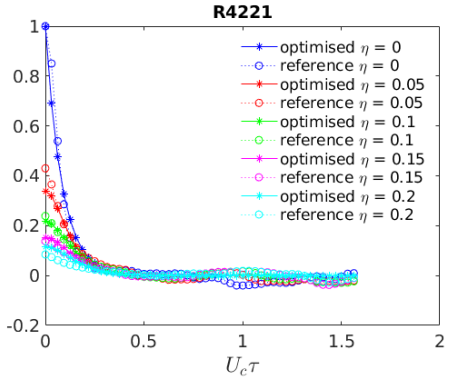

(c)

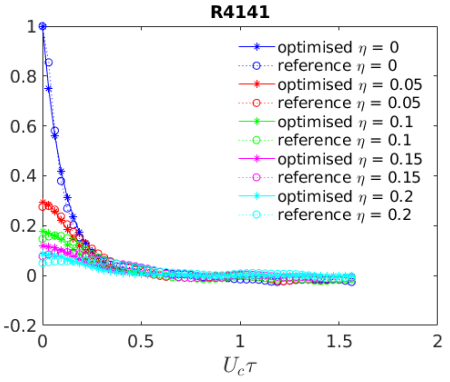

(d)

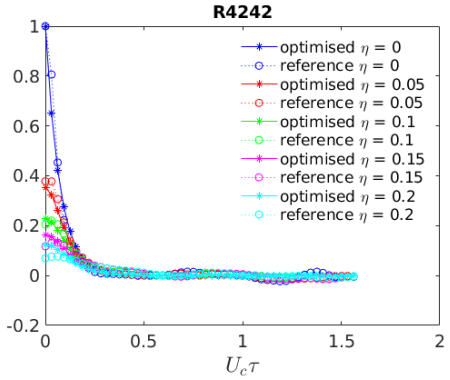

(e)

Figure B.12: SP46: comparison of the optimised model with the numerical data (when $\eta_1 = 0$) for coupling and enthalpy flux correlations (a) R_{4111} (b) R_{4122} (c) R_{4221} (d) R_{4141} (e) R_{4242}

B.3 Quasi-normality Approximation

Figures B.13, B.14, and B.15 compare the fourth order correlations calculated directly from the LES data with the quasi-normality approximations on the shear layer at the start of the potential core.

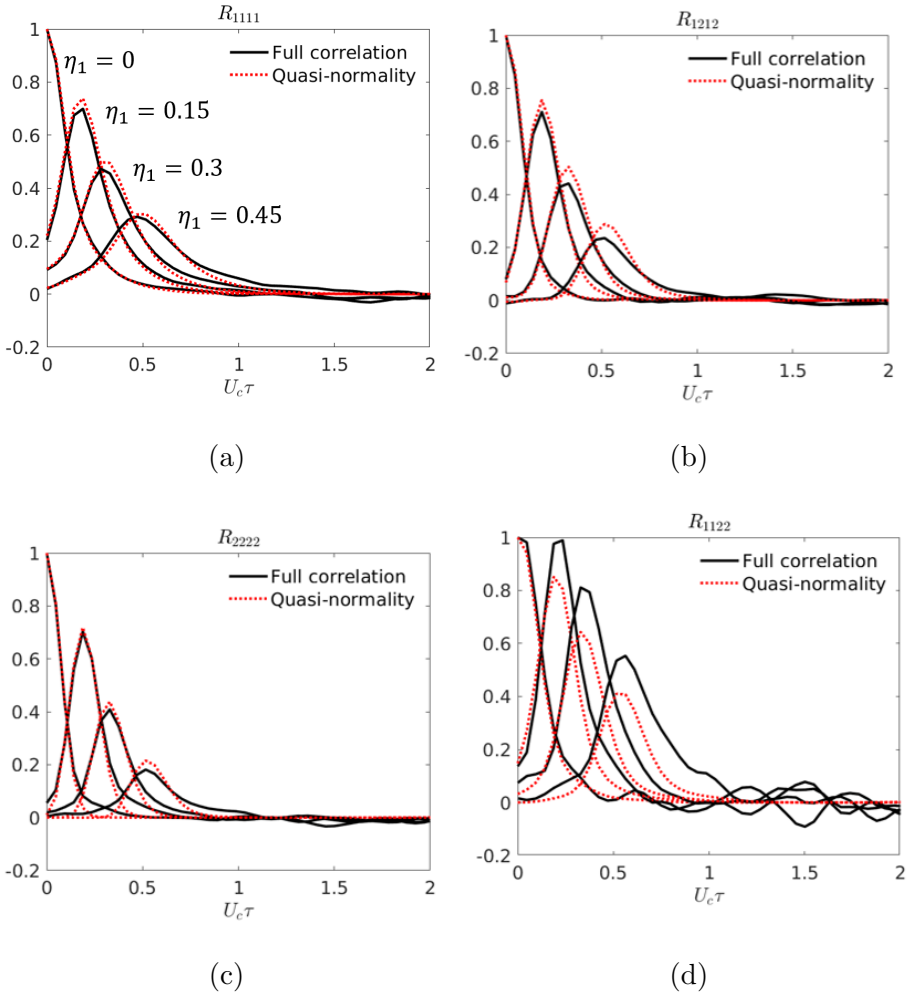

Figure B.13: SP07: comparison of the quasi-normality approximation at $(y_1, r) = (y_1^{start}, 0.5)$ for (a) R_{1111} (b) R_{1212} (c) R_{2222} (d) R_{1122}

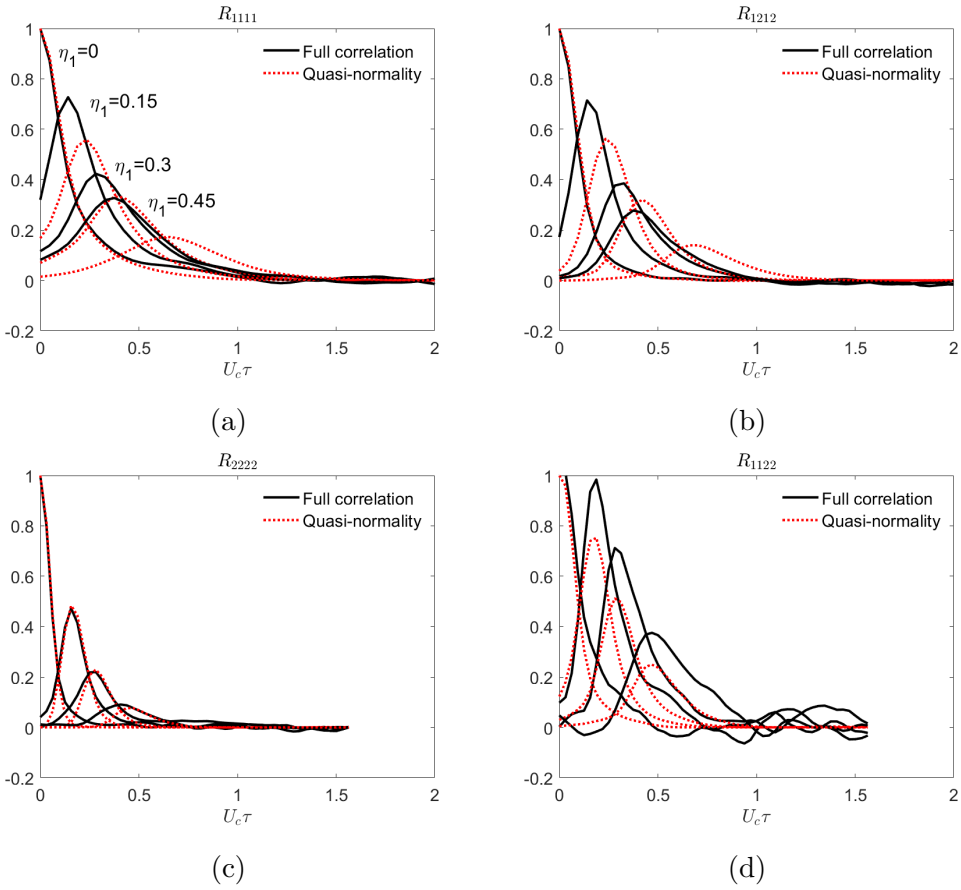

Figure B.14: SP46: comparison of the quasi-normality approximation at $(y_1, r) = (y_1^{start}, 0.5)$ for (a) R_{1111} (b) R_{1212} (c) R_{2222} (d) R_{1122}

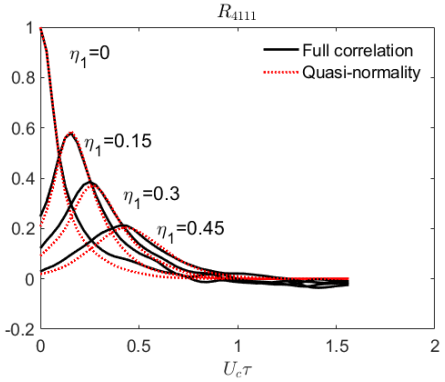

(a)

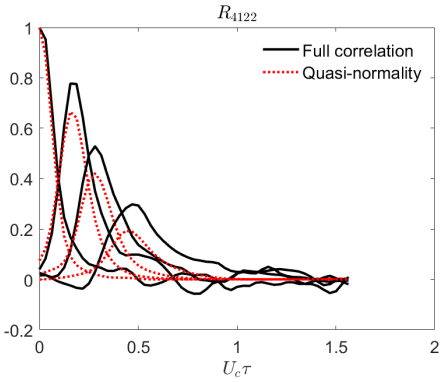

(b)

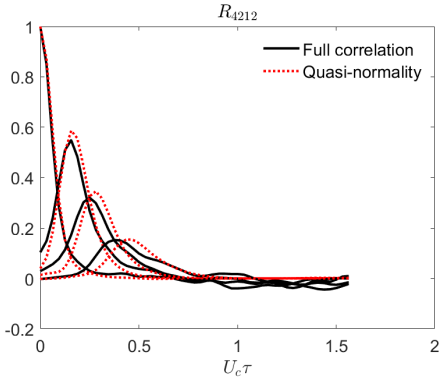

(c)

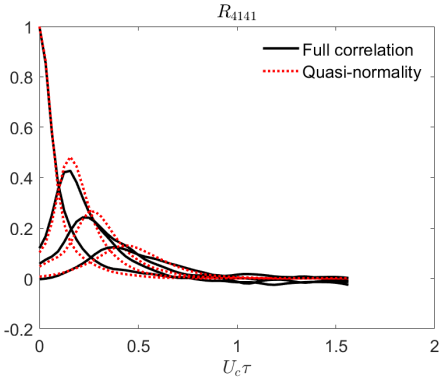

(d)

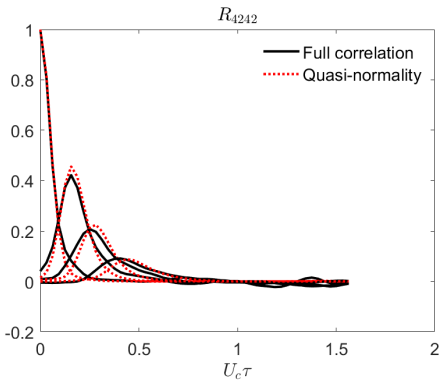

(e)

Figure B.15: SP46: comparison of the quasi-normality approximation at $(y_1, r) = (y_1^{start}, 0.5)$ for (a) R_{4111} (b) R_{4122} (c) R_{4221} (d) R_{4141} (e) R_{4242}

Appendix C

Further Parametric Studies on the Spectral Tensor

C.1 Analytical Spectral Tensor: Full Equation

Note that for all figures in this section, the assumption $l_2 = 0.04$ is used for R_{1122}, R_{2211} and R_{4122}. Figure C.1 compares L_T for each of the four jets, and shows that there are some issues with L_T for SP03. Therefore, since this figure also shows that for heated jets L_T is roughly universal across Mach number, we assume that L_T from SP07 will be a good representation for SP03.

Figure C.2 shows the momentum-flux physical spectral tensors Ψ^*_{ijkl} for SP03 at $St = 0.1, \theta = 30$. Compared to SP07 we see that the turbulence is less spread out and more focused close to the shear layer at the end of potential core.

Figures C.3 and C.4 show the momentum-flux, and coupling/enthalpy-flux spectral tensors respectively for SP42 at $St = 0.1, \theta = 30$. Similar to SP46, these figures show that the enthalpy flux terms are the strongest in magnitude, which agrees with the initial assessment of the amplitudes of the correlations in Chapter 5.

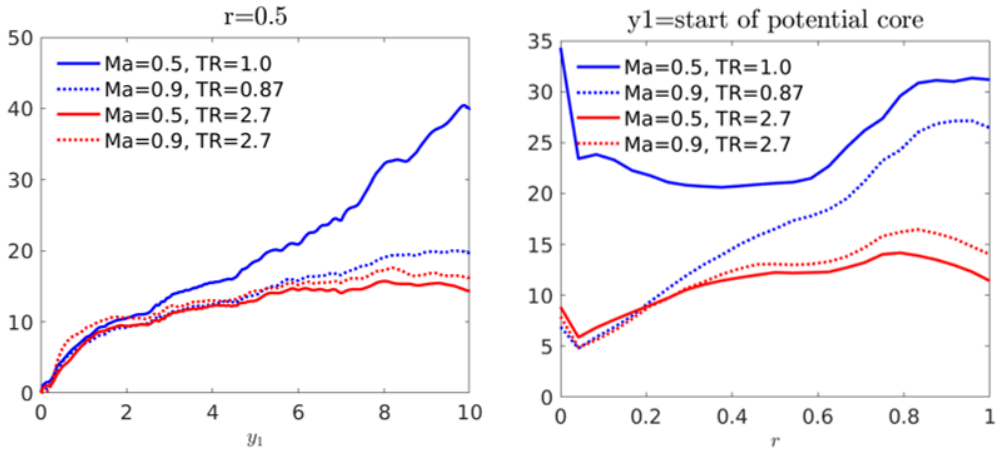

(a) (b)

Figure C.1: Universality of $L_T = k^{3/2}/\epsilon$ at (a) $r = 0.5$ (b) y_1 =start of potential core

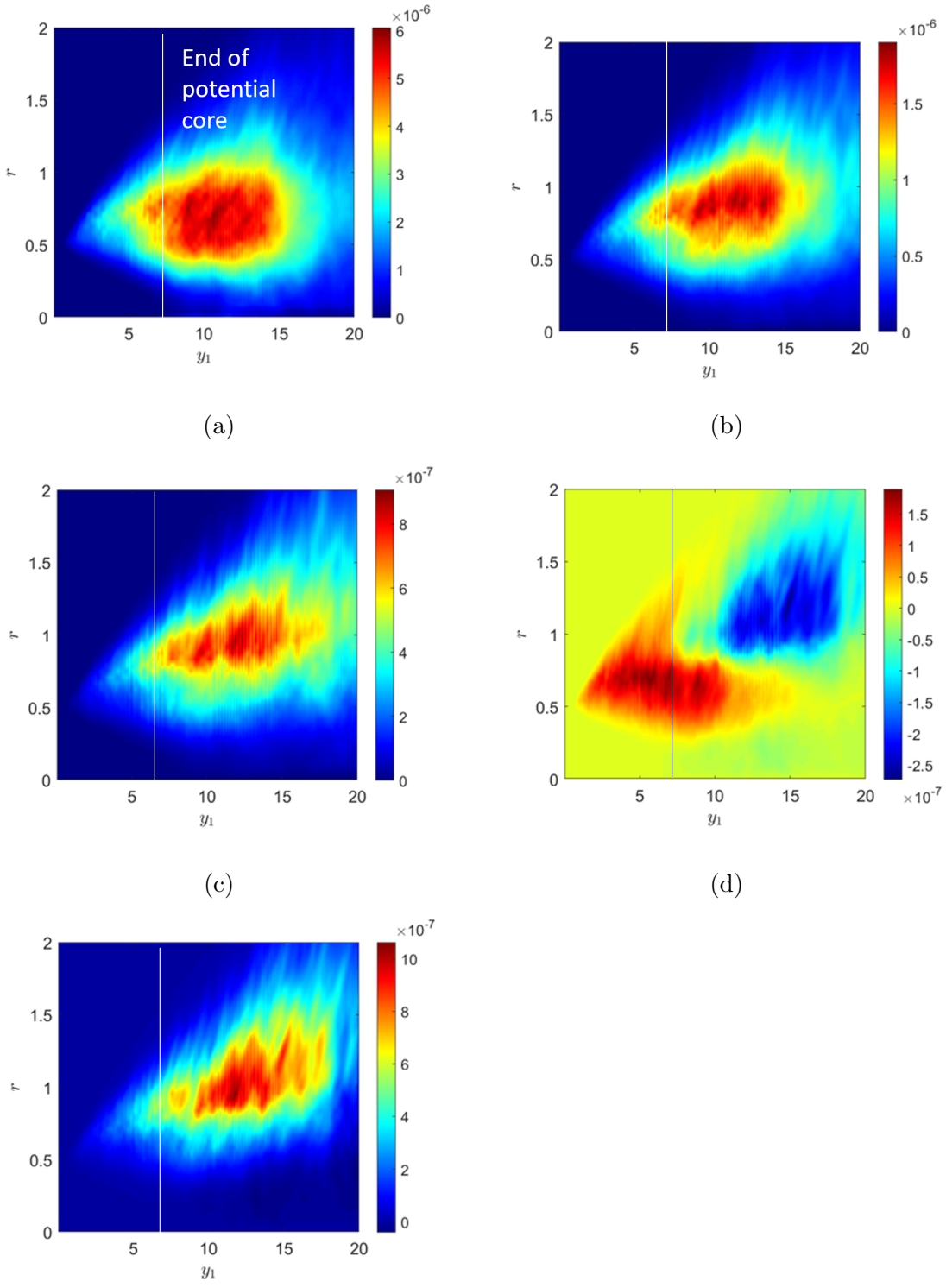

(a) (b) (c) (d) (e)

Figure C.2: SP03: contour plots at $St = 0.1, \theta = 30$ for (a) Ψ^*_{1111} (b) Ψ^*_{1212} (c) Ψ^*_{2222} (d) Ψ^*_{1122} (e) Ψ^*_{2211}

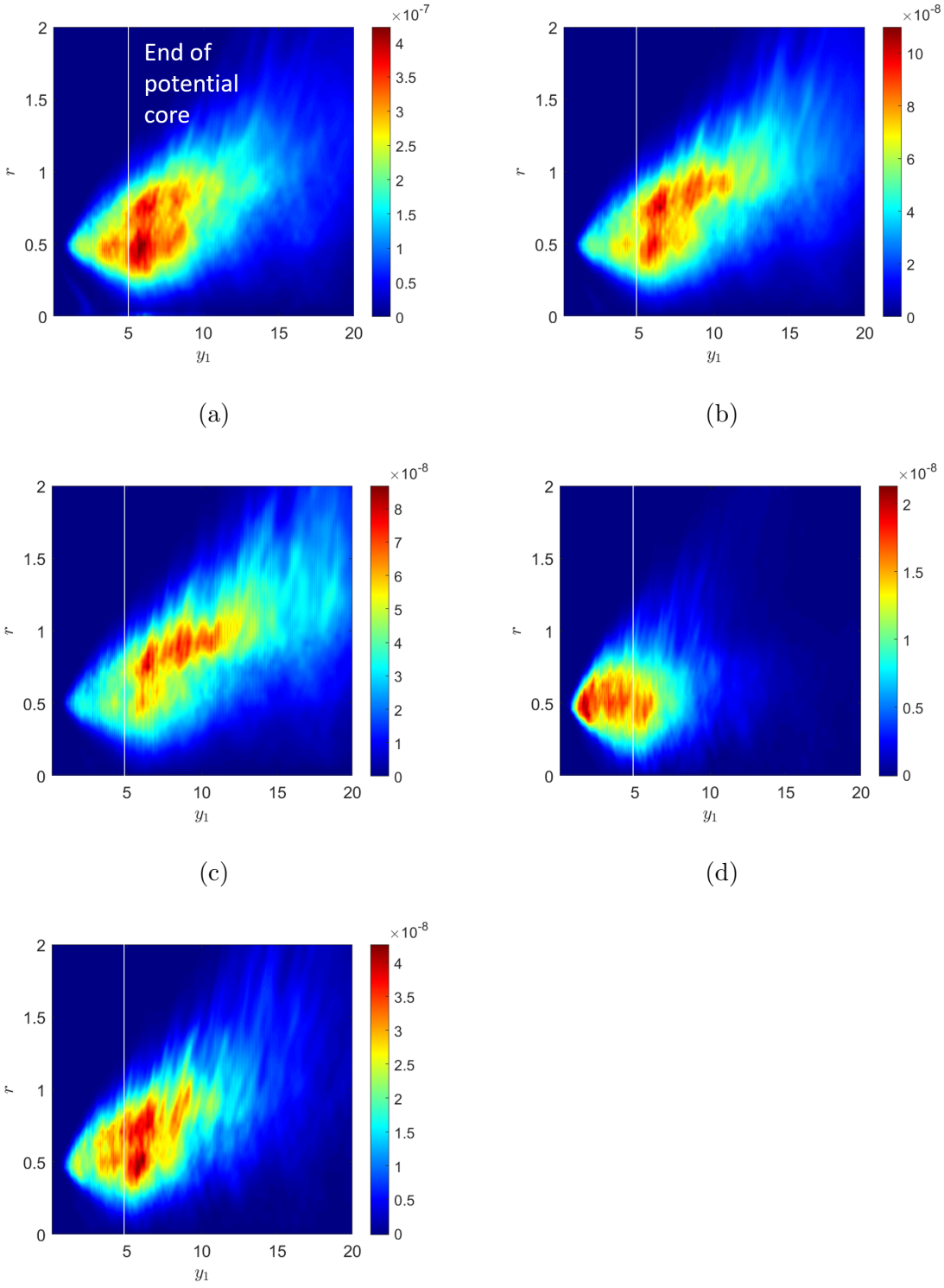

(a) (b) (c) (d) (e)

Figure C.3: SP42: contour plots at $St = 0.1, \theta = 30$ for (a) Ψ^*_{1111} (b) Ψ^*_{1212} (c) Ψ^*_{2222} (d) Ψ^*_{1122} (e) Ψ^*_{2211}

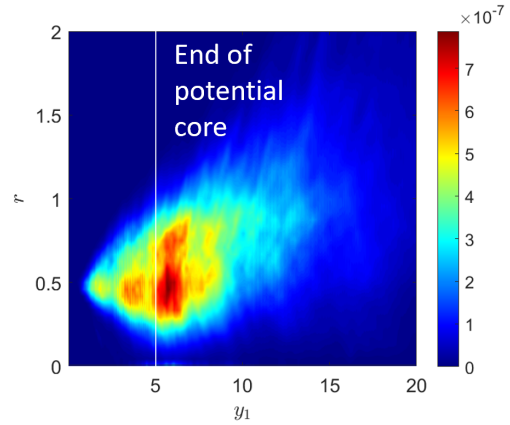

(a)

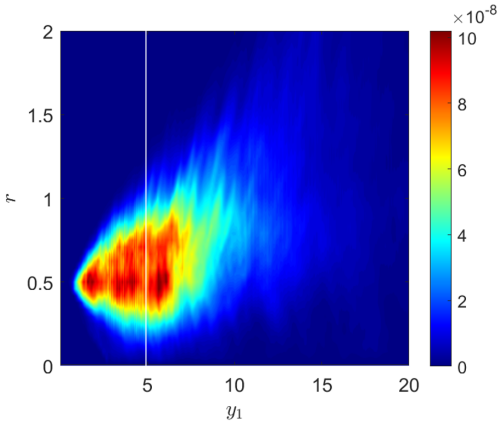

(b)

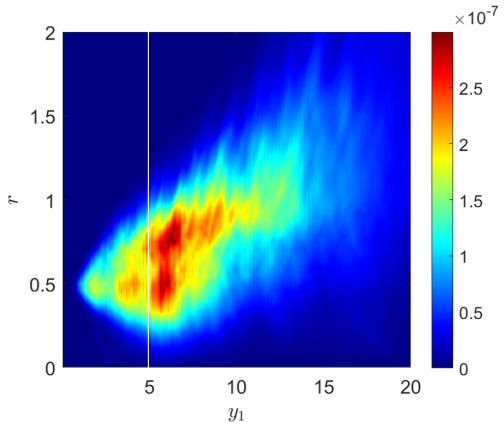

(c)

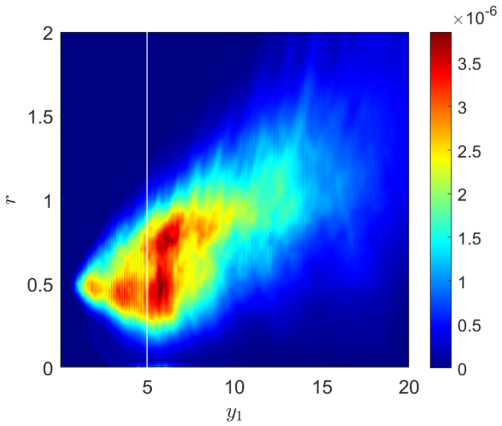

(d)

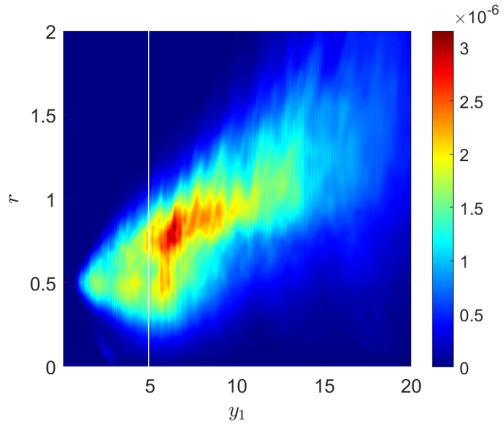

(e)

Figure C.4: SP42: contour plots at $St = 0.1, \theta = 30$ for (a) Ψ^*_{4111} (b) Ψ^*_{4122} (c) Ψ^*_{4221} (d) Ψ^*_{4141} (e) Ψ^*_{4242}

Appendix D

Mathematical Formulations for RDT

D.1 Equation for ϕ

To find ϕ we substitute (8.1.4),(8.1.7) into the energy equation (8.1.2) which results in:

$$-\frac{D}{D\tau}\Big(\frac{D^3\phi}{D\tau^3}\Big)+\underbrace{\frac{\partial}{\partial y_i}\left[c^2\Big(\delta_{ij}\frac{D}{D\tau}-\delta_{i1}\frac{\partial U}{\partial y_j}\Big)\Delta_j\phi\right]}_{\text{2nd term}}=0 \tag{D.1.1}$$

Following contraction of indices, the second term becomes:

$$\frac{\partial}{\partial y_i}\Big(c^2\frac{D}{D\tau}\Delta_i\phi\Big)-c^2\frac{\partial U}{\partial y_j}\frac{\partial}{\partial y_1}\Delta_j\phi \tag{D.1.2}$$

replacing $\Delta_i\phi$:

$$\frac{\partial}{\partial y_i}\left[c^2\frac{D}{D\tau}\Big(\frac{\partial}{\partial y_i}\frac{D}{D\tau}+2\frac{\partial U}{\partial y_i}\frac{\partial}{\partial y_1}\Big)\phi\right]-c^2\frac{\partial U}{\partial y_j}\frac{\partial}{\partial y_1}\Big(\frac{\partial}{\partial y_j}\frac{D}{D\tau}+2\frac{\partial U}{\partial y_j}\frac{\partial}{\partial y_1}\Big)\phi \tag{D.1.3}$$

$$\underbrace{\frac{\partial}{\partial y_i}\Big(c^2\frac{D}{D\tau}\frac{\partial}{\partial y_i}\frac{D\phi}{D\tau}\Big)}_{\text{1st term}}+2\frac{\partial}{\partial y_i}c^2\frac{\partial U}{\partial y_i}\frac{D}{D\tau}\frac{\partial\phi}{\partial y_1}-c^2\frac{\partial U}{\partial y_j}\frac{\partial}{\partial y_1}\frac{\partial}{\partial y_j}\frac{D\phi}{D\tau}-2c^2\frac{\partial U}{\partial y_j}\frac{\partial U}{\partial y_j}\frac{\partial^2\phi}{\partial y_1^2} \tag{D.1.4}$$

Using the identity:

$$\frac{D}{D\tau}\frac{\partial}{\partial y_i}=\frac{\partial}{\partial y_i}\frac{D}{D\tau}-\frac{\partial U}{\partial y_i}\frac{\partial}{\partial y_1} \tag{D.1.5}$$

the first term becomes:

$$\frac{\partial}{\partial y_i}\left[c^2\frac{D}{D\tau}\Big(\frac{D}{D\tau}\frac{\partial\phi}{\partial y_i}+\frac{\partial U}{\partial y_i}\frac{\partial\phi}{\partial y_1}\Big)\right]$$

$$\frac{\partial}{\partial y_i}\Big(\frac{D^2}{D\tau^2}c^2\frac{\partial\phi}{\partial y_i}\Big)+\frac{\partial}{\partial y_i}\Big(c^2\frac{\partial U}{\partial y_i}\frac{D}{D\tau}\frac{\partial\phi}{\partial y_1}\Big) \tag{D.1.6}$$

Using the identity

$$\frac{D^2}{D\tau^2}\frac{\partial}{\partial y_i}=\frac{\partial}{\partial y_i}\frac{D^2}{D\tau^2}-2\frac{\partial U}{\partial y_i}\frac{\partial}{\partial y_1}\frac{D}{D\tau} \tag{D.1.7}$$

this becomes:

$$\frac{D^2}{D\tau^2}\frac{\partial}{\partial y_i}\Big(c^2\frac{\partial\phi}{\partial y_i}\Big)+2\frac{\partial U}{\partial y_i}\frac{\partial}{\partial y_1}\frac{D}{D\tau}\Big(c^2\frac{\partial\phi}{\partial y_i}\Big)+\frac{\partial}{\partial y_i}\Big(c^2\frac{\partial U}{\partial y_i}\frac{D}{D\tau}\frac{\partial\phi}{\partial y_1}\Big) \tag{D.1.8}$$

substituting this back into (D.1.4) gives

$$\frac{D^2}{D\tau^2}\frac{\partial}{\partial y_i}\Big(c^2\frac{\partial\phi}{\partial y_i}\Big)+\underbrace{3\frac{\partial}{\partial y_i}c^2\frac{\partial U}{\partial y_i}\frac{D}{D\tau}\frac{\partial\phi}{\partial y_1}}_{\text{2nd term}}+2\frac{\partial U}{\partial y_i}\frac{\partial}{\partial y_1}c^2\frac{D}{D\tau}\Big(\frac{\partial\phi}{\partial y_i}\Big)$$

$$-\underbrace{c^2\frac{\partial U}{\partial y_j}\frac{\partial}{\partial y_1}\frac{\partial}{\partial y_j}\frac{D\phi}{D\tau}}_{\text{4th term}}-2c^2\frac{\partial U}{\partial y_j}\frac{\partial U}{\partial y_j}\frac{\partial^2\phi}{\partial y_1^2} \tag{D.1.9}$$

The second and fourth terms can be rewritten as

$$3\Big(\frac{D}{D\tau}\frac{\partial}{\partial y_i}+\frac{\partial U}{\partial y_i}\frac{\partial}{\partial y_1}\Big)c^2\frac{\partial U}{\partial y_i}\frac{\partial\phi}{\partial y_1}-c^2\frac{\partial U}{\partial y_j}\frac{\partial}{\partial y_1}\Big(\frac{D}{D\tau}\frac{\partial\phi}{\partial y_j}+\frac{\partial U}{\partial y_j}\frac{\partial\phi}{\partial y_1}\Big) \tag{D.1.10}$$

which after cancellation of terms brings (D.1.9) to

$$\frac{D^2}{D\tau^2}\frac{\partial}{\partial y_i}\Big(c^2\frac{\partial}{\partial y_i}\phi\Big)+\frac{\partial U}{\partial y_i}c^2\frac{\partial}{\partial y_1}\frac{D}{D\tau}\frac{\partial}{\partial y_i}\phi+3\frac{D}{D\tau}\frac{\partial}{\partial y_i}c^2\frac{\partial U}{\partial y_i}\frac{\partial}{\partial y_1}\phi \tag{D.1.11}$$

Substituting this back into the energy equation (D.1.1):

$$\frac{D}{D\tau}\left[-\frac{D^3\phi}{D\tau^3}+\underbrace{\frac{D}{D\tau}\frac{\partial}{\partial y_i}\Big(c^2\frac{\partial\phi}{\partial y_i}\Big)}_{\text{2nd term}}+\frac{\partial U}{\partial y_i}c^2\frac{\partial^2\phi}{\partial y_1\partial y_i}+3\frac{\partial}{\partial y_i}c^2\frac{\partial U}{\partial y_i}\frac{\partial\phi}{\partial y_1}\right]=0 \tag{D.1.12}$$

rearrange the second term:

$$\Big(\frac{\partial}{\partial y_i}\frac{D}{D\tau}-\frac{\partial U}{\partial y_i}\frac{\partial}{\partial y_1}\Big)c^2\frac{\partial\phi}{\partial y_i}$$

$$\frac{\partial}{\partial y_i}\frac{D}{D\tau}c^2\frac{\partial\phi}{\partial y_i}-\frac{\partial U}{\partial y_i}\frac{\partial}{\partial y_1}c^2\frac{\partial\phi}{\partial y_i}$$

$$\frac{\partial}{\partial y_i}\Big(c^2\frac{D}{D\tau}\frac{\partial\phi}{\partial y_i}\Big) - \frac{\partial U}{\partial y_i}c^2\frac{\partial^2\phi}{\partial y_1 y_i}$$

$$\frac{\partial}{\partial y_i}\left[c^2\Big(\frac{\partial}{\partial y_i}\frac{D\phi}{D\tau} - \frac{\partial U}{\partial y_i}\frac{\partial\phi}{\partial y_1}\Big)\right] - \frac{\partial U}{\partial y_i}c^2\frac{\partial^2\phi}{\partial y_1 y_i}$$

using

$$c^2\Delta_i = c^2\frac{\partial}{\partial y_i}\frac{D}{D\tau} + 2c^2\frac{\partial U}{\partial y_i}\frac{\partial}{\partial y_1} \tag{D.1.13}$$

this becomes

$$\frac{\partial}{\partial y_i}\Big(c^2\Delta_i\phi\Big) - 3\frac{\partial}{\partial y_i}\Big(c^2\frac{\partial U}{\partial y_i}\frac{\partial\phi}{\partial y_1}\Big) - \frac{\partial U}{\partial y_i}c^2\frac{\partial^2\phi}{\partial y_1\partial y_i} \tag{D.1.14}$$

Substituting this back into the energy equation and cancelling terms leaves:

$$-\frac{D}{D\tau}\left[\frac{D^3\phi}{D\tau^3} - \frac{\partial}{\partial y_i}\Big(c^2\Delta_i\phi\Big)\right] = 0 \tag{D.1.15}$$

which can be written in terms of an operator L_a:

$$-\frac{D}{D\tau}\Big(L_a\phi\Big) = 0 \tag{D.1.16}$$

Integrating gives:

$$L_a\phi = -\tilde{\omega}_c(\tau - y_1/U, y_T) \tag{D.1.17}$$

where $\tilde{\omega}_c$ is an arbitrary convected quantity.

D.2 Introducing the Adjoint Operator, L_a

Taking the gradient of the momentum equation (8.1.1) and multiplying by c^2 allows a single equation for p' to be found when also taking the convective derivative of the continuity equation (8.1.2). The momentum equation becomes

$$\frac{\partial}{\partial y_i}\frac{Dc^2u_i}{D\tau} + \frac{\partial}{\partial y_j}\Big(\delta_{1j}c^2\frac{\partial U}{\partial y_i}u_i\Big) + \frac{\partial}{\partial y_i}\Big(c^2\frac{\partial p'}{\partial y_i}\Big) = 0$$

$$\Big(\frac{D}{D\tau}\frac{\partial}{\partial y_i} + \frac{\partial U}{\partial y_i}\frac{\partial}{\partial y_1}\Big)c^2u_i + c^2\frac{\partial U}{\partial y_i}\frac{\partial u_i}{\partial y_1} + \frac{\partial}{\partial y_i}\Big(c^2\frac{\partial p'}{\partial y_i}\Big) = 0 \tag{D.2.1}$$

Taking the convective derivative of the continuity equation:

$$\frac{D^2p'}{D\tau^2} + \frac{D}{D\tau}\frac{\partial}{\partial y_i}\Big(c^2u_i\Big) = 0$$

so

$$\frac{D}{D\tau}\frac{\partial}{\partial y_i}\Big(c^2 u_i\Big) = -\frac{D^2 p'}{D\tau^2} \tag{D.2.2}$$

Using this equation in (D.2.1) gives:

$$-\frac{D^2 p'}{D\tau^2} + 2c^2\frac{\partial U}{\partial y_i}\frac{\partial u_i}{\partial y_1} + \frac{\partial}{\partial y_i}\Big(c^2\frac{\partial p'}{\partial y_i}\Big) = 0 \tag{D.2.3}$$

Taking the convective derivative again:

$$-\frac{D^3 p'}{D\tau^3} + 2c^2\frac{\partial U}{\partial y_i}\frac{\partial}{\partial y_1}\frac{Du_i}{D\tau} + \frac{D}{D\tau}\frac{\partial}{\partial y_i}\Big(c^2\frac{\partial p'}{\partial y_i}\Big) = 0 \tag{D.2.4}$$

using the momentum equation to replace $Du_i/D\tau$ in the second term and taking $\partial U/\partial y_1 = 0$ since we are dealing with a parallel flow results in:

$$-\frac{D^3 p'}{D\tau^3} - 2c^2\frac{\partial U}{\partial y_i}\frac{\partial^2 p'}{\partial y_1 \partial y_i} + \frac{D}{D\tau}\frac{\partial}{\partial y_i}\Big(c^2\frac{\partial p'}{\partial y_i}\Big) = 0 \tag{D.2.5}$$

which can be written as

$$Lp' = 0 \tag{D.2.6}$$

where

$$L = -\frac{D^3}{D\tau^3} - 2c^2\frac{\partial U}{\partial y_i}\frac{\partial^2}{\partial y_1 \partial y_i} + \frac{D}{D\tau}\frac{\partial}{\partial y_i}\Big(c^2\frac{\partial}{\partial y_i}\Big) \tag{D.2.7}$$

To find the adjoint operator, L_a, we use the definition: $uLv = vL_a u$ plus conservation terms. Following integration by parts, this results in the adjoint operator:

$$L_a = \frac{D^3}{D\tau^3} - \frac{\partial}{\partial y_j}\Big(2c^2\frac{\partial U}{\partial y_j}\frac{\partial}{\partial y_1}\Big) - \frac{\partial}{\partial y_j}c^2\frac{\partial}{\partial y_i}\frac{D}{D\tau} \tag{D.2.8}$$

using (8.1.6) this becomes

$$L_a = \frac{D^3}{D\tau^3} - \frac{\partial}{\partial y_j}c^2\Delta_j \tag{D.2.9}$$

D.3 Green's Function Relations

We can find a relation between the pressure Green's function G and the normal velocity Green's function g_i by looking at the gradient of G:

$$\frac{\partial}{\partial x_i}G(\boldsymbol{y},\tau|\boldsymbol{x},t) = \frac{\partial}{\partial x_i}\frac{D^3}{Dt^3}g(\boldsymbol{y},\tau|\boldsymbol{x},t) \tag{D.3.1}$$

which is

$$\frac{\partial}{\partial x_i}G(\boldsymbol{y},\tau|\boldsymbol{x},t) = \frac{D^2}{Dt^2}\Big(\frac{D}{Dt}\frac{\partial}{\partial x_i} + 3\frac{\partial U}{\partial x_i}\frac{\partial}{\partial x_1}\Big)g(\boldsymbol{y},\tau|\boldsymbol{x},t) \tag{D.3.2}$$

$$\frac{\partial}{\partial x_i}G(\boldsymbol{y},\tau|\boldsymbol{x},t) = \frac{D^2}{Dt^2}\Big(\frac{\partial}{\partial x_i}\frac{D}{Dt} + 2\frac{\partial U}{\partial x_i}\frac{\partial}{\partial x_1}\Big)g(\boldsymbol{y},\tau|\boldsymbol{x},t) \tag{D.3.3}$$

Therefore,

$$\frac{\partial}{\partial x_i}G(\boldsymbol{y},\tau|\boldsymbol{x},t) = \frac{D^2}{Dt^2}g_i(\boldsymbol{y},\tau|\boldsymbol{x},t) \tag{D.3.4}$$

D.4 Fourier Transforms

D.4.1 Time

Look at a Fourier transform of the form:

$$I(\boldsymbol{y},\boldsymbol{x};\omega) = \frac{1}{2\pi}\int_{-\infty}^{\infty} e^{i\omega(t-\tau)}\frac{\partial f(\boldsymbol{y}|\boldsymbol{x},t-\tau)}{\partial t}d(t-\tau) \tag{D.4.1}$$

if we let $\bar{t} = t - \tau$ where $t > \tau$, then $\partial/\partial t = \partial/\partial\bar{t}|_\tau$ and $\partial/\partial\tau = -\partial/\partial\bar{t}|_t$

Integrating by parts gives:

$$I(\boldsymbol{y},\boldsymbol{x};\omega) = \frac{1}{2\pi}\int_{-\infty}^{\infty}\frac{\partial}{\partial\bar{t}}e^{i\omega\bar{t}}f(\boldsymbol{y}|\boldsymbol{x},\bar{t})d\bar{t} - \frac{i\omega}{2\pi}\int_{-\infty}^{\infty}e^{i\omega\bar{t}}f(\boldsymbol{y}|\boldsymbol{x},\bar{t})d\bar{t} \tag{D.4.2}$$

Assuming f is a 'good' function (i.e. is bounded at $\pm\infty$) the first term can be neglected and we are left with:

$$I(\boldsymbol{y},\boldsymbol{x};\omega) = \frac{1}{2\pi}\int_{-\infty}^{\infty}e^{i\omega\bar{t}}(-i\omega)f(\boldsymbol{y}|\boldsymbol{x},\bar{t})d\bar{t} \tag{D.4.3}$$

which, using $\partial/\partial t = \partial/\partial\bar{t}|_\tau$ and relating (D.4.3) with (D.4.1) gives the result:

$$\frac{\partial}{\partial t} = -i\omega \tag{D.4.4}$$

Similarly,

$$\frac{\partial}{\partial\tau} = i\omega \tag{D.4.5}$$

D.4.2 Space

Similarly, look at a Fourier transform of the form:

$$I(\boldsymbol{y}_T, \boldsymbol{x}_T; k_1) = \frac{1}{2\pi}\int_{-\infty}^{\infty} e^{-ik_1(x_1-y_1)}\frac{\partial f(\boldsymbol{y}_T|\boldsymbol{x}_T, x_1-y_1)}{\partial x_1}d(x_1-y_1) \tag{D.4.6}$$

if we let $z = x_1 - y_1$ where $x_1 > y_1$, then $\partial/\partial x_1 = \partial/\partial z|_{y_1}$ and $\partial/\partial y_1 = -\partial/\partial z|_{x_1}$ Integrating by parts gives:

$$I(\boldsymbol{y}_T, \boldsymbol{x}_T; k_1) = \frac{1}{2\pi}\int_{-\infty}^{\infty}\frac{\partial}{\partial z}e^{-ik_1 z}f(\boldsymbol{y}_T|\boldsymbol{x}_T, z)dz + \frac{ik_1}{2\pi}\int_{-\infty}^{\infty}e^{-ik_1 z}f(\boldsymbol{y}_T|\boldsymbol{x}_T, z)dz \tag{D.4.7}$$

Assuming f is a 'good' function (i.e. is bounded at $\pm\infty$) the first term can be neglected and we are left with:

$$I(\boldsymbol{y}_T, \boldsymbol{x}_T|k_1) = \frac{1}{2\pi}\int_{-\infty}^{\infty}e^{-ik_1 z}(ik_1)f(\boldsymbol{y}_T|\boldsymbol{x}_T, z)dz \tag{D.4.8}$$

which, using $\partial/\partial x_1 = \partial/\partial z|_{y_1}$ and relating (D.4.8) with (D.4.6) gives the result:

$$\frac{\partial}{\partial x_1} = ik_1 \tag{D.4.9}$$

Similarly,

$$\frac{\partial}{\partial y_1} = -ik_1 \tag{D.4.10}$$

D.5 Reduced Rayleigh Equation

Taking the third order convective derivative (in x, t coordinates) of the direct Green's function equation gives:

$$L(\boldsymbol{y}, \tau)\frac{D^3}{Dt^3}g(\boldsymbol{y}, \tau|\boldsymbol{x}, t) = \frac{D^3}{Dt^3}\delta(\boldsymbol{y}-\boldsymbol{x})\delta(\tau - t) \tag{D.5.1}$$

which, using (8.1.17) gives

$$L(\boldsymbol{y}, \tau)G(\boldsymbol{y}, \tau|\boldsymbol{x}, t) = \frac{D^3}{Dt^3}\delta(\boldsymbol{y}-\boldsymbol{x})\delta(\tau - t) \tag{D.5.2}$$

Taking Fourier transforms in time and the streamwise direction using results from Appendix D.4, which show $D/Dt = (ik_1U(\boldsymbol{x}_T) - i\omega)$ gives the right hand side:

$$\begin{aligned}\frac{1}{(2\pi)^2}\int_{-\infty}^{\infty}\int_{-\infty}^{\infty}e^{i[\omega(t-\tau)-k_1(x_1-y_1)]}\frac{D^3}{Dt^3}\delta(\boldsymbol{y}-\boldsymbol{x})\delta(\tau-t)d(x_1-y_1)d(t-\tau)& \\ = \frac{-i(k_1U(\boldsymbol{x}_T)-\omega)^3}{(2\pi)^2}\delta(\boldsymbol{x}_T-\boldsymbol{y}_T)&\end{aligned} \tag{D.5.3}$$

and the left hand side:

$$\frac{1}{(2\pi)^2}\int_{-\infty}^{\infty}\int_{-\infty}^{\infty} e^{i[\omega(t-\tau)-k_1(x_1-y_1)]}L(\boldsymbol{y},\tau)G(\boldsymbol{y}_T|\boldsymbol{x}_T,x_1-y_1,t-\tau)d(x_1-y_1)d(t-\tau)$$
$$= \bar{L}(\boldsymbol{y}_T;k_1,\omega)\bar{G}(\boldsymbol{y}_T|\boldsymbol{x}_T;k_1,\omega) \tag{D.5.4}$$

via the convolution theorem. Where we define,

$$\bar{L}(\boldsymbol{y}_T;k_1,\omega) = (i\omega - U(\boldsymbol{y}_T)ik_1)\Big[(ik_1)^2c^2 + \frac{\partial}{\partial y_T}c^2\frac{\partial}{\partial y_T} - (i\omega - U(\boldsymbol{y}_T)ik_1)^2\Big] + 2\frac{\partial U}{\partial y_T}c^2(ik_1)\frac{\partial}{\partial y_T} \tag{D.5.5}$$

and

$$\bar{G}(\boldsymbol{y}_T|\boldsymbol{x}_T;k_1,\omega) = \frac{1}{(2\pi)^2}\int_{-\infty}^{\infty}\int_{-\infty}^{\infty} e^{i[\omega(t-\tau)-k_1(x_1-y_1)]}G(\boldsymbol{y},\tau|\boldsymbol{x},t)d(x_1-y_1)d(t-\tau) \tag{D.5.6}$$

The operator $\bar{L}$ can be rewritten as:

$$\bar{L} = i(\omega - U(\boldsymbol{y}_T)k_1)^3\bar{L_0} \tag{D.5.7}$$

where we define:

$$\bar{L}_0 = 1 - \frac{k_1^2c^2}{(\omega - U(\boldsymbol{y}_T)k_1)^2} + \frac{\partial}{\partial y_T}\Big(\frac{c^2}{(\omega - U(\boldsymbol{y}_T)k_1)^2}\frac{\partial}{\partial y_T}\Big) \tag{D.5.8}$$

Therefore, combining left and right hand side gives:

$$\bar{L}_0(\boldsymbol{y}_T;k_1,\omega)\bar{G}(\boldsymbol{y}_T|\boldsymbol{x}_T;k_1,\omega) = \frac{(\omega - U(\boldsymbol{x}_T)k_1))^3}{(\omega - U(\boldsymbol{y}_T)k_1)^3}\frac{\delta(\boldsymbol{y}_T-\boldsymbol{x}_T)}{(2\pi)^2} \tag{D.5.9}$$

which can be rewritten as:

$$\bar{L}_0(\boldsymbol{y}_T;k_1,\omega)\bar{G}(\boldsymbol{y}_T|\boldsymbol{x}_T;k_1,\omega) = \frac{f(U(\boldsymbol{x}_T);k_1,\omega)}{f(U(\boldsymbol{y}_T);k_1,\omega)}\frac{\delta(\boldsymbol{y}_T-\boldsymbol{x}_T)}{(2\pi)^2} \tag{D.5.10}$$

where $f(U(z);k_1,\omega) = \Big(\omega - U(z)k_1\Big)$. Integrating both sides across an infinite transverse area A_T reduces the right hand side to $1/(2\pi)^2$ which can then be taken to the left hand side by multiplying by a delta function:

$$\int_{A_T}\bar{L}_0(\boldsymbol{y}_T;k_1,\omega)\bar{G}(\boldsymbol{y}_T|\boldsymbol{x}_T;k_1,\omega) - \frac{1}{(2\pi)^2}\delta(\boldsymbol{y}_T-\boldsymbol{x}_T)dy_T = 0 \tag{D.5.11}$$

It then follows that

$$\bar{L}_0(\boldsymbol{y}_T; k_1, \omega)\bar{G}(\boldsymbol{y}_T|\boldsymbol{x}_T; k_1, \omega) = \frac{1}{(2\pi)^2}\delta(\boldsymbol{y}_T - \boldsymbol{x}_T) \tag{D.5.12}$$

Similarly, the spanwise Fourier transform can also be taken, which when we assume $U(\boldsymbol{y}_T) = U(y_2)$ gives:

$$L_R(y_2; k_1, k_3, \omega)\hat{G}(y_2|x_2; k_1, k_3, \omega) = \frac{\delta(y_2 - x_2)}{(2\pi)^3} \tag{D.5.13}$$

where L_R is in the form of a Sturm-Liouville operator:

$$L_R(y_2; k_1, k_3, \omega) = \frac{d}{dy_2}\Big[\frac{c^2}{(\omega - U(y_2)k_1)^2}\frac{d}{dy_2}\Big] + \Big[1 - \frac{(k_1^2 + k_3^2)c^2}{(\omega - U(y_2)k_1)^2}\Big] \tag{D.5.14}$$

and $\hat{G}$ is the 3D Fourier transform of G:

$$\hat{G}(y_2|x_2; k_1, k_3, \omega) = \frac{1}{(2\pi)}\int_{-\infty}^{\infty} e^{-ik_3(x_3 - y_3)}\bar{G}(\boldsymbol{y}_T|\boldsymbol{x}_T; k_1, \omega)d(x_3 - y_3) \tag{D.5.15}$$

D.6 Extend model for R_{22}

We have a Fourier transform of a power series representation of R_{22}, considering only two terms of this series gives:

$$\frac{1}{2\pi}\int_{-\infty}^{\infty} e^{i\omega\hat{\tau}}\Big[1 + a_1\hat{\tau}\frac{\partial}{\partial\hat{\tau}}\Big]e^{-X}d\hat{\tau} \tag{D.6.1}$$

Calculating the derivative,

$$\frac{\partial}{\partial\hat{\tau}}e^{-X} = -e^{-\sqrt{f^2 + \frac{\hat{\tau}^2}{\tau_0^2}}}\Big[\frac{1}{2}\Big(f^2 + \frac{\hat{\tau}^2}{\tau_0^2}\Big)^{-1/2}\Big]\frac{2\hat{\tau}}{\tau_0^2} = -\frac{\hat{\tau}}{X\tau_0^2}e^{-X} \tag{D.6.2}$$

For a spatial separation of $\boldsymbol{\eta} = 0$, $f = 0, X = \frac{\hat{\tau}}{\tau_0}$ and R_{22} becomes:

$$R_{22} = \Big(1 - a_1\frac{\hat{\tau}}{\tau_0}\Big)e^{-\frac{\hat{\tau}}{\tau_0}} \tag{D.6.3}$$

To calculate the Fourier transform (D.6.1) we look at the individual terms. The first term simply becomes:

$$\frac{1}{2\pi}\int_{-\infty}^{\infty} e^{-X}e^{i\omega\hat{\tau}}d\hat{\tau} \tag{D.6.4}$$

Using the fact that $\hat{\tau}e^{i\omega\hat{\tau}} = \frac{1}{i}\frac{\partial}{\partial\omega}e^{i\omega\hat{\tau}}$, the second term can be rewritten as:

$$\frac{a_1}{2\pi i}\frac{\partial}{\partial\omega}\int_{-\infty}^{\infty} e^{i\omega\hat{\tau}}\frac{\partial}{\partial\hat{\tau}}e^{-X}d\hat{\tau} \tag{D.6.5}$$

Which, integrating by parts gives;

$$\frac{a_1}{2\pi i}\frac{\partial}{\partial\omega}\left[\left[e^{i\omega\hat{\tau}}e^{-X}\right]_{-\infty}^{\infty} - \int_{-\infty}^{\infty} i\omega e^{i\omega\hat{\tau}}e^{-X}d\hat{\tau}\right] \tag{D.6.6}$$

The first term is bounded in the limits and therefore eliminated. Hence, the a_1 term can be written as:

$$-\frac{a_1}{2\pi}\frac{\partial}{\partial\omega}\omega\int_{-\infty}^{\infty} e^{i\omega\hat{\tau}}e^{-X}d\hat{\tau} \tag{D.6.7}$$

Therefore, the Fourier transform of R_{22} is:

$$\left[1 - a_1\frac{\partial}{\partial\omega}\omega\right]\frac{1}{2\pi}\int_{-\infty}^{\infty} e^{i\omega\hat{\tau}}e^{-X}d\hat{\tau} \tag{D.6.8}$$

and since,

$$\frac{1}{2\pi}\int_{-\infty}^{\infty} e^{i\omega\hat{\tau}}e^{-X}d\hat{\tau} = \frac{\tau_0 f}{\pi\sqrt{1+\tilde{\omega}^2}}K_1(f\sqrt{1+\tilde{\omega}^2}) \tag{D.6.9}$$

this becomes,

$$\left[1 - a_1\frac{\partial}{\partial\omega}\omega\right]\frac{\tau_0 f}{\pi\sqrt{1+\tilde{\omega}^2}}K_1(f\sqrt{1+\tilde{\omega}^2}) \tag{D.6.10}$$

using the chain rule this is:

$$\left(1 - a_1 - \omega a_1\frac{\partial}{\partial\omega} + ...\right)\frac{\tau_0 f}{\pi\sqrt{1+\tilde{\omega}^2}}K_1(f\sqrt{1+\tilde{\omega}^2}) \tag{D.6.11}$$

The derivative with respect to omega is calculated using the substitution $u = f\sqrt{1+\tilde{\omega}^2}$ and the chain rule:

$$\frac{\partial}{\partial\omega} = \frac{\partial}{\partial u}\frac{\partial u}{\partial\tilde{\omega}}\frac{\partial\tilde{\omega}}{\partial\omega} \tag{D.6.12}$$

Simply,

$$\frac{\partial u}{\partial\tilde{\omega}} = \frac{f\tilde{\omega}}{\sqrt{1+\tilde{\omega}^2}}, \qquad \text{and} \qquad \frac{\partial\tilde{\omega}}{\partial\omega} = \tau_0 \tag{D.6.13}$$

And, using the product rule,

$$\frac{\partial}{\partial u}\left[\frac{\tau_0 f^2}{\pi u}K_1(u)\right] = \frac{\tau_0 f^2}{\pi u}\frac{\partial}{\partial u}K_1(u) - \frac{\tau_0 f^2}{\pi u^2}K_1(u) \tag{D.6.14}$$

and the identity $\partial K_1(u)/\partial u = -(K_0(u) + K_2(u))/2$ gives,

$$\frac{\partial}{\partial u}\Big[\frac{\tau_0 f^2}{\pi u}K_1(u)\Big] = \frac{\tau_0 f^2}{\pi u}\Big[-\frac{1}{2}(K_0(u)+K_2(u)) - \frac{K_1(u)}{u}\Big] \tag{D.6.15}$$

Therefore, the derivative with respect to omega is:

$$\frac{\tau_0 f^2}{\pi u}\Big[-\frac{1}{2}(K_0(u)+K_2(u)) - \frac{K_1(u)}{u}\Big]\frac{f\tilde{\omega}}{\sqrt{1+\tilde{\omega}^2}}\tau_0 \tag{D.6.16}$$

Which simplifies to;

$$\frac{\tau_0^2 f^3 \tilde{\omega}}{\pi u\sqrt{1+\tilde{\omega}^2}}\Big[-\frac{1}{2}(K_0(u)+K_2(u)) - \frac{K_1(u)}{u}\Big] \tag{D.6.17}$$

Returning to original variables we get;

$$\frac{\tau_0^2 f^2 \tilde{\omega}}{\pi(1+\tilde{\omega}^2)}\Big[-\frac{1}{2}(K_0(f\sqrt{1+\tilde{\omega}^2})+K_2(f\sqrt{1+\tilde{\omega}^2})) - \frac{K_1(f\sqrt{1+\tilde{\omega}^2})}{f\sqrt{1+\tilde{\omega}^2}}\Big] \tag{D.6.18}$$

Inserting this into (D.6.11) gives,

$$\begin{aligned}&(1-a_1)\frac{\tau_0 f}{\pi\sqrt{1+\tilde{\omega}^2}}K_1(f\sqrt{1+\tilde{\omega}^2}) - \omega a_1 \\ &\text{x}\frac{\tau_0^2 f^2 \tilde{\omega}}{\pi(1+\tilde{\omega}^2)}\Big[-\frac{1}{2}(K_0(f\sqrt{1+\tilde{\omega}^2})+K_2(f\sqrt{1+\tilde{\omega}^2})) - \frac{K_1(f\sqrt{1+\tilde{\omega}^2})}{f\sqrt{1+\tilde{\omega}^2}}\Big]\end{aligned} \tag{D.6.19}$$

Substituting $\omega = \tilde{\omega}/\tau_0$ gives,

$$\begin{aligned}&(1-a_1)\frac{\tau_0 f}{\pi\sqrt{1+\tilde{\omega}^2}}K_1(f\sqrt{1+\tilde{\omega}^2}) + \\ &\quad\frac{a_1\tau_0 f^2\tilde{\omega}^2}{\pi(1+\tilde{\omega}^2)}\Big[\frac{1}{2}(K_0(f\sqrt{1+\tilde{\omega}^2})+K_2(f\sqrt{1+\tilde{\omega}^2})) + \frac{K_1(f\sqrt{1+\tilde{\omega}^2})}{f\sqrt{1+\tilde{\omega}^2}}\Big]\end{aligned} \tag{D.6.20}$$

Bibliography

[1] M. Basner et al. “Auditory and non-auditory effects of noise on health”. In: *The Lancet* 383 (9925) (2014), pp. 1325–1332.

[2] J. Lees. *Aircraft Noise and Public Health: The Evidence is Loud and Clear*. (Online, accessed: 15.09.2020). 2016. URL: https://www.aef.org.uk/uploads/Aircraft-Noise-and-Public-Health-the-evidence-is-loud-and-clear-final-reportONLINE.pdf.

[3] WHO. *Burden of disease from environmental noise Quantification of healthy life years lost in Europe*. 2011. URL: https://www.who.int/quantifying_ehimpacts/publications/e94888.pdf. (accessed: 15.09.2020).

[4] S. Calder. *An overview of aviation noise*. 2023. URL: https://www.caa.co.uk/Consumers/Environment/Noise/Noise/. (accessed: 01.03.2023).

[5] R. Tossani. *The Long Read: Collision Course*. 2022. URL: https://www.rethinktokyo.com/news/2022/04/27/long-read-collision-course/1651065992. (accessed: 02.03.2023).

[6] S. Calder. *Heathrow third runway will be built, insists airport boss as he heads for departures*. 2023. URL: https://www.independent.co.uk/travel/news-and-advice/heathrow-third-runway-john-holland-kaye-b2274409.html. (accessed: 01.03.2023).

[7] G. Topham. *Heathrow third runway noise would affect 2.2m people, analysis finds*. 2018. URL: https://www.theguardian.com/environment/2018/apr/09/heathrow-third-runway-noise-affect-people-government-documents. (accessed: 15.09.2020).

[8] Eurocontrol. *Aviation Outlook 2050*. 2022. URL: https://www.eurocontrol.int/sites/default/files/2022-04/eurocontrol-aviation-outlook-2050-report.pdf. (accessed: 23.03.2023).

[9] N. Cumpsty and A. Heyes. *Jet Propulsion*. 3rd ed.. Cambridge University Press, 2015, pp. 335–342.

[10] ICAO. *Reduction of noise at source*. URL: https://www.icao.int/environmental-protection/Pages/Reduction-of-Noise-at-Source.aspx. (accessed: 04.04.2023).

[11] R. J. Astley et al. "Predicting and reducing aircraft noise". In: 14th International Congress on Sound and Vibration, 2007.

[12] M.J. Lighthill. "On sound generated aerodynamically: I. General Theory". In: *Proc. R.Soc. Lond. A* 221 (1952), pp. 564–587.

[13] G.A. Brès and S.K. Lele. "Modelling of jet noise: a perspective from large-eddy simulations". In: *Proc. R.Soc. Lond. A* 377:20190081 (2019).

[14] L. Rego et al. "Noise amplification effects due to jet-srface interaction". In: vol. AIAA 2019-0001. AIAA Scitech 2019 Forum, 2019.

[15] O.M. Philips. "On the generation of sound by supersonic turbulent shear layers". In: *J. Fluid Mech.* 9 (1960), pp. 1–28.

[16] J.E. Ffowcs Williams. "Some thoughts on the effect of aircraft motion and eddy convection on the noise from air jets". In: *Univ. Southampton Aero. Astr. Rep.* 155 (1960).

[17] J.E. FFowcs Williams. "The noise from turbulence convected at high speed". In: *Proc. R.Soc. Lond. A* 255 (1963), pp. 469–503.

[18] M.E. Goldstein and S.J. Leib. "The aeroacoustics of slowly diverging supersonic jets". In: *J. Fluid Mech.* 600 (2008), pp. 291–337.

[19] C.K.W Tam, M. Golebiowski, and J.M. Seiner. "Two components of turbulent mixing noise from supersonic jets". In: *AIAA Conference 96-1716* (1996).

[20] G.M. Lilley. "On the noise from jets". In: *AGARD, CP-131, 13.1-13.12* (1974).

[21] A. Khavaran and J. Bridges. "Modeling of turbulence generated noise in jets". In: *AIAA Paper 2004-2983* (2004).

[22] M.E. Goldstein. “A generalized acoustic analogy”. In: *J. Fluid Mech.* 488 (2003), pp. 315–333.

[23] M.E. Goldstein and S.J. Leib. “The role of instability waves in predicting jet noise”. In: *J. Fluid Mech.* 525 (2005), pp. 37–72.

[24] A. Samanta et al. “Robustness of acoustic analogies for predicting mixing-layer noise”. In: *AIAA J.* 44 (2006), pp. 2780–2786.

[25] P.J Morris and K.B.M.Q Zaman. “Velocity measurements in jets with application to noise source modeling”. In: vol. AIAA-2009-17. 47th AIAA Aerospace Sciences Meeting, 2009.

[26] S.A Karabasov et al. “Jet Noise: Acoustic Analogy informed by Large Eddy Simulation.” In: *AIAA Journal* 48(7) (2010), pp. 1312–1325.

[27] M.Z. Afsar, M.E. Goldstein, and A.Fagan. “Enthalpy-Flux/Momentum-Flux Coupling in the Acoustic Spectrum of Heated Jets.” In: *AIAA Journal* 49(11) (2011), pp. 2522–2532.

[28] C.C. Kiris et al. “The LAVA computational fluid dynamics solver”. In: vol. AIAA 2014-0070. AIAA Scitech 2014 Forum, 2014.

[29] P. Lew et al. “An extended lattice Boltzmann methodology for high subsonic jet noise prediction”. In: vol. AIAA 2014-2755. 20th AIAA/CEAS Aeroacoustics Conference, 2014.

[30] W.C. Van der Velden et al. “Jet noise prediction: validation and physical insight”. In: vol. AIAA 2018-3617. AIAA Aviation Forum 2018, 2018.

[31] K.Kailasnath et al. “Efficient supersonic jet noise simulations using JENRE”. In: vol. AIAA 2014-3740. AIAA Propulsion and Energy, 2014.

[32] G.A. Brès et al. “Large eddy simulations of co-annular turbulent jet using a Voroni-based mesh generation framework.” In: vol. AIAA 2018-3320. AIAA Aviation Forum 2018, 2018.

[33] S.C. Crow and F.H. Champagne. “Orderly structure in jet turbulence”. In: *J.Fluid Mech.* 48(3) (1971), pp. 547–591.

[34] G.L. Brown and A. Roshko. “On density effects and large structures in turbulent mixing layers”. In: *J. Fluid Mech.* 64 (1974), pp. 775–816.

[35] J. Laufer, R.H. Schlinker, and R.E. Kaplan. “Experiments on supersonic jet noise”. In: *AIAA J.* 14 (1976), pp. 489–497.

[36] C.K. Tam and K.C. Chen. “Turbulent Mixing Noise from Supersonic Jets”. In: *AIAA J.* 32 (1994), pp. 1774–1780.

[37] C.K.W. Tam, M. Golebiowski, and J.M. Seiner. “On the two components of turbulent mixing noise from supersonic jets”. In: vol. AIAA-1996-1716. 2nd AIAA/CEAS Aeroacoustics Conference, 1996.

[38] K. Viswanathan. “Analysis of the two similarity components of jet noise”. In: *AIAA J.* 40(9) (2002), pp. 1735–1744.

[39] K. Viswanathan. “Aeroacoustics of hot jets”. In: *J. Fluid Mech.* 516 (2004), pp. 39–82.

[40] M.D. Dahl and D. Papamoschou. “Analytical predictions and measurements of the noise radiated from supersonic coaxial jets”. In: *AIAA J.* 38 (2000), pp. 584–591.

[41] C.K.W. Tam. “Influence of nozzle geometry on the noise of high speed jets”. In: *AIAA J.* 36 (1998), pp. 1396–1400.

[42] C.K.W Tam. “A phenomenological approach to jet noise: the two-source model”. In: *Proc. R.Soc. Lond. A* 377: 20190078 (2019).

[43] C.K.W Tam and L. Aurialt. “Jet mixing noise from fine-scale turbulence”. In: *AIAA J* 37 (1999), pp. 145–153.

[44] X. Xu and X. Li. “Anisotropic source modelling for turbulent jet noise prediction”. In: *Proc. R.Soc. Lond. A* 377: 20190078 (2019).

[45] E. Mollo-Christensen. “Measurements of near field pressure of subsonic jets”. In: Advis. Group Aeronaut. Res. Dev, Paris, 1963.

[46] J. Lau, M.Fisher, and H.Fuchs. “The intrinsic structure of turbulent jets”. In: *J. Sound and Vib.* 22 (1972), pp. 379–384.

[47] D.G.Crighton and P.Huerre. “Shear-layer pressure fluctuations and superdirective acoustic sources”. In: *J. Fluid Mech.* 220 (1990), pp. 355–368.

[48] P. Jordan and T. Colonius. “Wave packets and turbulent jet noise”. In: *Annu. Rev. Fluid Mech.* 45 (2013), pp. 173–195.

[49] D.G. Crighton and M. Gaster. “Stability of slowly diverging jet flow”. In: *J. Fluid Mech.* 77 (1976), pp. 397–413.

[50] A. Michalke. "Survey on jet instability theory". In: *Prog. Aerosp. Sci.* 21 (1984), pp. 159–199.

[51] C.K.W. Tam and P.J. Morris. "The radiation of sound by the instability waves of a compressible plane turbulent shear layer". In: *J. Fluid Mech.* 98 (1980), pp. 349–381.

[52] C. Chang et al. "Linear and nonlinear PSE for compressible boundary layers". In: vol. Tech. Rep. 93-70. Inst. Comput. Appl. Sci. Eng., 1993.

[53] W. Olsen and D. Boldman. "Trailing edge noise data with comparison to theory." In: vol. AIAA-1979-1524. 12th Fluid and Plasma Dynamics Conference, 1979.

[54] M.E. Wang. "Wing effect on jet-noise propagation." In: *Journal of Aircraft* 18.4 (1981), pp. 295–302.

[55] R.W. Head and M.J Fisher. "Jet/surface interaction noise: Analysis of farfield low frequency augmentation of jet noise due to the presence of a solid shield." In: 3rd AIAA Aeroacoustics Conference, 1976.

[56] I.S. Southern. "Exhaust noise in flight: The role of acoustic installation effects." In: 6th AIAA Aeroacoustics Conference, 1980.

[57] C. A. Brown. "Jet-surface interaction test: far-field noise results." In: *Trans ASME J. Engng Gas Turbines Power* 135 (2013).

[58] J.E. Ffowcs and L.H. Hall. "Aerodynamic sound generation by turbulent flow in the vicinity of a scattering half plane". In: *J. Fluid Mech.* 40(4) (1970), pp. 657–670.

[59] M.E. Goldstein. "Scattering and distortion of the unsteady motion on transversely sheared mean flows." In: *J. Fluid Mech.* 91(4) (1979), pp. 601–632.

[60] M.E Goldstein, M.Z Afsar, and S.J. Leib. "Non-homogeneous rapid distortion theory on transversely sheared mean flows". In: *J. Fluid Mech.* 736 (2013), pp. 532–569.

[61] M. E. Goldstein, S. J. Leib, and M. Z. Afsar. "Generalized rapid distortion theory on transversely sheared mean flows with physically realizable upstream boundary conditions: application to the trailing edge problem". In: *J. Fluid Mech.* 824 (2017), pp. 477–512.

[62] M. E. Goldstein, S. J. Leib, and M. Z. Afsar. “Rapid distortion theory on transversely sheared mean flows of arbitrary cross-section”. In: *J. Fluid Mech.* 881 (2019), pp. 551–584.

[63] M. Bondarenko, Z. Hu, and X. Zhang. “Large-eddy simulation of the interaction of a jet with a wing”. In: vol. AIAA 2012-2254. 18th AIAA/CEAS Aeroacoustics Conference, 2012.

[64] V. Semiletov et al. “Jet and jet-wing noise modelling based on the caberet miles flow solver and the ffowcs williams-hawkings method”. In: *International Journal of Aeroacoustics* 15(6-7) (2016), pp. 631–645.

[65] L. Rego et al. “Jet-installation noise and near-field characteristics of jet–surface interaction.” In: *JFM* 895 (2020), A2.

[66] C. Brown et al. “A machine learning approach to jet-surface interaction noise modeling”. In: vol. AIAA 2020-1728. AIAA Scitech 2020 Forum, 2020.

[67] M.Z. Afsar, A.Sescu, and V.Sassanis. “Effect of non-parallel mean flow on the acoustic spectrum of heated supersonic jets: Explanation of ’jet quietening’”. In: *Phys. Fluids* 31 (2019), p. 205107.

[68] H.K. Tanna. “An experimental study of jet noise, part 1: turbulent mixing noise”. In: *Journal of Sound and Vibration* 50(3) (1977), pp. 405–428.

[69] O. Es-Sahli et al. “Investigation of wakes generated by fractal plates in the compressible regime using large-eddy simulations”. In: *Physics of Fluids* 32 (2020), p. 105106.

[70] H. Colby et al. “Numerical Investigation of a Rectangular Jet Exhausting Over a Flat Plate with Periodic Surface Deformations at the Trailing Edge”. In: *Aerospace Journal* 8 (2021), p. 314.

[71] J.S. Haywood et al. “Triple Hill’s Vortex Synthetic Eddy Method”. In: *Flow, Turbulence and Combustion* 108 (2021), pp. 627–659.

[72] C.K.W. Tam and J.C. Webb. “Dispersion-relation-preserving finite difference schemes for Computational Aeroacoustics”. In: *Journal of Computational Physics* 107 (1993), pp. 262–281.

[73] C. Bogey and C. Bailly. “A family of low dispersive and low dissipative explicit schemes for flow and noise computation”. In: *Journal of Computational Physics* 194 (2004), pp. 194–214.

[74] J. E. Bridges. “Effect of Heat on Space-Time Correlations in Jets”. In: vol. AIAA-2006-2534. 12th AIAA/CEAS Aeroacoustics Conference, 2006.

[75] J.C. Lau, P.J. Morris, and M. Fisher. “Measurements in subsonic and supersonic free jets using a laser velocimeter”. In: *J. Fluid Mech* 93 (1979), pp. 1–27.

[76] V.H. Arakeri et al. “On the use of microjets to suppress turbulence in a Mach 0.9 axisymmetric jet”. In: *J. Fluid Mech* 490 (2003), pp. 75–98.

[77] C.J. Moore. “The role of shear-layer instability waves in jet exhaust noise”. In: *J. Fluid Mech* 80 (1977), pp. 321–367.

[78] A.P. Markesteijn and S. Karabasov. “CABARET solutions on graphics processing units for NASA jets: Grid sensitivity and unsteady inflow condition effect”. In: *C.R. Mecanique* 346 (2018), pp. 948–963.

[79] H. Xia. “Turbulent jet characteristics for axisymmetric and serrated nozzles”. In: *Computers & Fluids* 110 (2015), pp. 189–197.

[80] A.F. Mielke and K.A. Elam. “Dynamic measurement of temperature, velocity, and density in hot jets using Rayleigh scattering”. In: *Exp Fluids* 47 (2009), pp. 673–688.

[81] A.F. Mielke, K.A. Elam, and C.J Sung. “Multi-Property Measurements at High Sampling Rates Using Rayleigh Scattering”. In: *AIAA Journal* 47:4 (2009), pp. 850–862.

[82] J.E Bridges and M.P. Wernet. “The NASA Subsonc Jet Particle Image Velocimetry (PIV) Dataset”. In: vol. NASA/TM-2011-216807. NASA, 2011.

[83] N.R. Panchapakesan and J.L Lumley. “Turbulence measurements in axisymmetric jets of air and helium. Part 1. Air jet.” In: *J. Fluid Mech.* 246 (1993), pp. 197–223.

[84] H.J. Hussein, S.P. Capp, and W.K. George. “Velocity measurements in a hig-Reynolds-number, momentum-conserving, axisymmetric, turbulent jet”. In: *J. Fluid Mech.* 258 (1994), pp. 31–75.

[85] M. Afsar. *Theory and modelling of jet noise. part ii: Jet noise theory.* Cambridge University, 2009.

[86] M.Z. Afsar et al. "Towards the prediction of supersonic jet noise using a unified asymptotic approximation for the adjoint vector Green's function". In: vol. AIAA 2017-3030. 23rd AIAA/CEAS Aeroacoustics Conference, 2017.

[87] C.K.W. Tam and D.E. Burton. "Sound generated by instability waves of supersonic flows. Part 2. Axisymmetric jets". In: *J.Fluid Mech.* 138 (1984), pp. 273–295.

[88] M.Z.A. Koshuriyan et al. "On the axisymmetric turbulence approximation for even-order correlation functions in complex dual-stream jets". In: *Phys. Fluids (in prep)* (2024).

[89] Q. Liu and H.Lai. "Flow developing properties of a compressible parallel jet". In: *AIP Advances* 11(2) (2021), p. 025214.

[90] V. Semiletov and S.Karabasov. "On the properties of fluctuating turbulent stress sources for high-speed jet noise". In: vol. AIAA 2016-2867. 22nd AIAA/CEAS Aeroacoustics Conference, 2016.

[91] A.S. Monin and A.M. Yaglom. *Statistical fluid mechanics, volume II: mechanics of turbulence.* Dover Publications, 2013, p. 11.

[92] G.K. Batchelor. *The theory of homogeneous turbulence.* Cambridge University Press, 1953.

[93] P. Moin. "Revisiting Taylor's hypothesis". In: *J.Fluid Mech.* 640 (2009), pp. 1–4.

[94] J.A.B. Wills. "On convection velocities in turbulent shear flows". In: *J.Fluid Mech.* 20(3) (1964), pp. 417–432.

[95] M.Z.A. Koshuriyan, S. Stirrat, and A. Sescu. "Taylor's hypothesis in high-order turbulence correlations". In: 20th International Conference on Flow Dynamics, 2023.

[96] M. Di Carlo, M.Vasile, and E.Minisci. "Adaptive multi-population inflationary differential evolution." In: *Soft Computing* 24 (2020), pp. 3861–3891.

[97] G. A Campbell and R. M Foster. "Fourier integrals for practical applications". In: Van nostrand, 1954, p. 122.

[98] M.Z Afsar, S.A Stirrat, and I.W Kokkinakis. "Investigation of fast GPU-based algorithms for jet-surface interaction noise calculations". In: vol. AIAA-2020-2564. 2020 AIAA Aviation, Aeronautics Forum, and Exposition, 2020.

[99] S. Stirrat, M. Z. Afsar, and E. Minisci. "Assessment of optimization methods for aero-acoustic prediction of trailing-edge interaction noise in axisymmetric jets". In: *MDPI Mathematics* 9(9) (2021), p. 998.

[100] M. Z. Afsar, S. J. Leib, and R. E. Bozak. "Effect of de-correlating turbulence on the low frequency decay of jet-surface interaction noise in sub-sonic unheated air jets using a CFD-based approach". In: *J. Sound and Vib.* 386 (2017), pp. 177–207.

[101] M. Z. Afsar, A. Sescu, and E. Minisci. "Modeling supersonic heated jet noise at fixed jet Mach number using an asymptotic approach for the acoustic analogy Green's function and an optimized turbulence model". In: vol. AIAA-2019-2731. 25th AIAA/CEAS Aeroacoustics Conference, 2019.

[102] C Woolley. "Profiling and Tuning OpenACC Code". In: GPU Technology Conference (GTC) 2012, 2012.

[103] Z. Guz et al. "Many-Core vs. Many-Thread Machines: Stay Away From the Valley". In: *IEEE Computer Architecture Letters* 8.1 (2009), pp. 25–28.

[104] M. Gunzburger. "Adjoint equation-based methods for control problems in incompressible, viscous flows". In: *Flow, Turbulence and Combustion* 65 (2000), pp. 249–272.

[105] G.N. Vanderplaats. *Multidiscipline Design Optimization.* Vanderplaats Research and Development, Inc., Colorado Springs, 2007.

[106] R.T. Haftka and Z. Gürdal. *Elements of Structural Optimization.* 3rd ed.. Kluwer Academic Publishers, 1993.

[107] J.S. Arora. *Introduction to Optimum Design.* 2nd ed.. Elsevier Academic Press, 2004.

[108] J.A. Snyman. *Practical Mathematical Optimization.* Springer, 2005.

[109] G. Venter. "Review of Optimization Techniques." In: *In: Encyclopedia of aerospace engineering, Wiley & Sons* (2010).

[110] A. Neumaier. "Complete search in continuous global optimization and constraint satisfaction." In: *ACTA NUMERICA* 13 (2004), pp. 271–370.

[111] V.V Toropov. "Simulation approach to structural optimization." In: *Structural Optimization* 1 (1989), pp. 37–46.

[112] V.V Toropov, A.A Filatov, and A.A Polynkin. "Multiparameter structural optimization using FEM and multipoint explicit approximations." In: *Structural Optimization* 6 (1993), pp. 7–14.

[113] Y.M. Korolev, S.A Karabasov, and V.V. Toropov. "Automatic Optimizer vs Human Optimizer for Low-Order Jet Noise Modeling". In: vol. AIAA-2015-2215. 21st AIAA/CEAS Aeroacoustics Conference, 2015.

[114] J.H Holland. *Adaption in Natural and Artificial Systems.* University of Michigan Press, 1975.

[115] J. Kennedy and R.C Eberhart. "Particle swarm optimization". In: Proceedings of the 1995 IEEE International Conference on Neural Networks, 1995, pp. 1942–1948.

[116] R. Storn and K. Price. "Differential evolution - A simple and efficient heuristic for global optimization over continuous spaces." In: *Journal of Global Optimization* 11(4) (1997), pp. 341–359.

[117] R. Martí. *Multi-Start Methods.* Handbook of Metaheuristics. International Series in Operations Research & Management Science Vol. 57. Springer, 2003.

[118] S.E Cox et al. "A comparison of global optimization methods for the design of a high-speed civil transport ." In: *Journal of Gobal Optimization* 21(4) (2001), pp. 415–432.

[119] D. Haim et al. "Comparison of optimization software packages for an aircraft multidisciplinary design optimization problem." In: *Design Optimization* 1 (1999), pp. 9–23.

[120] M.E. Pedersen. *Good parameters for particle swarm optimization.* Luxembourg: Hvass Laboratories, 2010.

[121] E. Mezura-Montes and C.A Coello Coello. “Constraint-handling in nature-inspired numerical optimization: Past, present and future.” In: *Swarm and Evolutionary Computation* (2011), pp. 173–194.

[122] S. Das and P.N Suganthan. “Differential Evolution: A Survey of the State-of-the-Art.” In: *IEEE Transactions on Evolutionary Computation* 15(1) (2011), pp. 4–31.

[123] M. Vasile, E. Minisci, and M. Locatelli. “An Inflationary Differential Evolution Algorithm for Space Trajectory Optimization”. In: *IEEE Transactions on Evolutionary Computation* 15(2) (2011), pp. 267–281.

[124] D.J Wales and J.P Doyle. “Global optimization by basin-hopping and the lowest energy structures of Lennard-Jones clusters containing up to 110 atoms.” In: *J Phys Chem A* 101(28) (1997), pp. 5111–5116.

[125] M.E. Goldstein. “A unified approach to some recent developments in jet noise theory”. In: *Intl J. Aeroacoustics* 1(1) (2002), pp. 1–16.